Design of Active and Anisotropic Soft Matter

By

Peter C. Mushenheim

A dissertation submitted in partial fulfillment of

the requirements for the degree of

Doctor of Philosophy

(Chemical Engineering)

at the

UNIVERSITY OF WISCONSIN-MADISON

2015

Date of final oral examination: 7/9/2015

The dissertation is approved by the following members of the Final Oral Committee:

Nicholas L. Abbott, Professor, Chemical and Biological Engineering
Daniel J. Klingenberg, Professor, Chemical and Biological Engineering
David M. Lynn, Professor, Chemical and Biological Engineering
Brian F. Pfleger, Associate Professor, Chemical and Biological Engineering
Douglas B. Weibel, Associate Professor, Biochemistry

Design of Active and Anisotropic Soft Matter

Peter C. Mushenheim

Under the supervision of Professor Nicholas L. Abbott

at the University of Wisconsin-Madison

Abstract

The research described in this thesis reveals how the unique combination of properties that characterize an aqueous lyotropic chromonic liquid crystal (LC) phase can be exploited to create novel active and anisotropic soft materials. A series of studies aimed at creating and providing fundamental insight into the design of such novel soft matter systems is presented in this thesis. The thesis is organized into two parts.

The first part of this thesis aims to unmask how the anisotropic and viscoelastic environment defined by the nematic lyotropic chromonic LC changes the fundamental dynamic behaviors of motile bacteria. These studies, which are possible due to the biocompatibility of this aqueous LC phase, go beyond past studies of the dynamical and equilibrium behaviors of dispersions of synthetic microparticles in LCs to reveal a range of phenomena that emerge due to interplay between LC elasticity-mediated forces and bacterial flagella-derived propulsive forces. The insights developed in these investigations identify new methods for manipulating bacteria in technological contexts and reveal principles and future opportunities relating to the design of active and anisotropic soft material systems.

The second part of this thesis relates to the formation of anisotropic soft matter based on two different classes of emulsions. In the first, emulsions are prepared comprising two immiscible LC phases: micrometer-sized droplets of thermotropic LCs in a continuous lyotropic chromonic LC phase. As a result of a coupling between the orientations of the two nematic phases, these LC-in-LC emulsions are demonstrated to exhibit intriguing properties such as hierarchical ordering and the ability to respond dynamically to weak applied fields. In the second emulsion system, elastic stresses are shown to deform giant unilamellar vesicles (GUVs) prepared in a lyotropic chromonic LC into a range of elongated, non-spherical shapes following a quench from the isotropic phase to the nematic LC phase of the solution. The possibility to dynamically tune the curvature of GUVs in this system makes it an attractive experimental platform to use, for example, in biophysical investigations aimed at elucidating the role of membrane curvature on the localization of lipids within bacterial membranes.

Overall, these studies reveal fundamental insights that define new opportunities and provide guidance for the design of active and anisotropic materials based on lyotropic chromonic LCs.

Acknowledgements

I would like to acknowledge and thank all of the people that have contributed to my work here at the University of Wisconsin-Madison over the past five years. First, I would like to thank my advisor, Professor Nicholas L. Abbott. I am constantly struck by the passion, creativity, and intellectual depth that he displays in leading our group. It has been a privilege to work with and learn from him. I know that I exit graduate school a far better scientist due to his mentorship. I would like to thank all past and present members of the Abbott group for contributing to the work reported in this thesis, helping me to develop as a scientist, and for their friendship and camaraderie. In particular, I would like to acknowledge Dr. Daniel S. Miller, Dr. Rebecca J. Carlton, Dr. Lie Na Tan, Dr. Jacob T. Hunter, Dr. Joel S. Pendery, Emre Bukusoglu, Maggie Herron, Marco A. Bedolla Pantoja, Xiaoguang Wang, Reza Abbasi, Timothy J. Smith, Dan Abras, and Dr. Abhijit Dan. I also would like to acknowledge my collaborators from outside of the Abbott group, especially Professor Douglas B. Weibel and members of his group as well as Professor Saverio E. Spagnolie. In particular, I would like to thank my collaborator Rishi R. Trivedi for all of his contributions to the research reported in this thesis. I had the pleasure to work with and mentor two undergraduate students, Chaval Punyatanasakchai and Eddie B. Ramos Hernández, and I thank them for their time and assistance. I would like to thank the members of my final oral committee: Professor Nicholas L. Abbott, Professor Daniel J. Klingenberg, Professor David M. Lynn, Professor Brian F. Pfleger, and Professor Douglas B. Weibel. I also would like to thank my undergraduate research advisor Professor Hsueh-Chia Chang as well as my mentors Dr. Gilad Yossifon, Dr. Nishant Chetwani, Dr. Sagnik Basuray, and Dr. Satyajyoti Senapati for giving me a start working in a research laboratory and fostering in me a love for scientific research. Many of the times in Madison that I will remember most fondly were shared with my classmates and

friends, especially, Ben Wilson, Ashley Baltes, Mary Regier, Tyler Roberts, Aaron Fluitt, and Matthew Thomas. I hope that I will have the opportunity to see them all frequently in the future. I would like to thank my parents, Charles and Jane Mushenheim, my brother, Andrew and my sisters, Kristen and Sarah for their constant love and support throughout my life, and particular, during my years of graduate school. I am especially grateful for the excellent education that my parents provided to me and the joy in learning they instilled in me. Finally, I could have never completed this degree without my perfect fiancé, Megan Sennett. Five years ago, already very much in love and entirely committed to one another, we made the difficult decision to invest in our professional careers and accept positions in Chicago and Madison after completing college. Although this undoubtedly has represented a challenging and less than ideal situation for us from the start, our love for each other has grown over the course of countless hours of skype conversations and tens of thousands of miles of driving on weekends. I am so thankful to Megan for being so strong throughout these five years and for filling my life with such happiness and joy, even when we have so often been physically apart. She is everything to me and is my soulmate and I could not possibly be more excited and proud to marry her on the 25th of this month.

Table of Contents

List of Figures and Tables

Chapter 1: Introduction and Overview

1.1 Introduction

The goals of the research described in this thesis were to design and characterize novel active and anisotropic soft materials based on liquid crystals (LCs). Specifically, these studies exploit the unique combination of properties presented by the nematic phase of a lyotropic chromonic LC. Most importantly to the research described herein, this lyotropic chromonic LC is water-based (in contrast to more conventional "oily" thermotropic LCs that are commonly used in liquid crystal displays) and is characterized by long range ordering of columnar molecular aggregates, which leads the phase to exhibit optical and mechanical anisotropy. The first part of this thesis reports the impact of the complex anisotropic and viscoelastic environment defined by this biocompatible LC phase on the fundamental dynamic behaviors of motile, rod-shaped bacteria. While previous studies have characterized the equilibrium and dynamical behaviors of micrometer-sized synthetic colloids dispersed in LCs,[1–13] investigations of self-propelling bacteria, which serve as model "active" particles in this thesis, within LCs and at LC interfaces, reveal a rich range of phenomena reflecting interplay between LC elasticity-mediated forces and bacterial flagella-derived forces. The fundamental insights developed in these studies suggest methods and approaches for the manipulation of bacteria in ways that are not possible in isotropic fluids. The insights also define new opportunities for the design of active and anisotropic soft material systems. In addition, because bacteria commonly inhabit viscoelastic environments that exhibit long-lived anisotropic states, the studies reported in this thesis provide insight regarding the influence of elasticity and mechanical anisotropy on bacteria in these biological settings.

In the second part of this thesis, the same aqueous lyotropic chromonic LC phase is utilized for the creation of two novel LC emulsion systems. In the first, micrometer-sized droplets of thermotropic LCs were dispersed in an immiscible continuous phase defined by the aqueous lyotropic LC. Investigation of these LC-in-LC emulsions revealed the ordering of the two LC phases to be coupled through anisotropic van der Waals interactions, leading the droplets to adopt specific orientations within continuous lyotropic LC films and to respond dynamically to the application and removal of weak magnetic fields. In the second, giant unilamellar vesicles (GUVs) were created that both encapsulated and were encompassed by the lyotropic chromonic LC. While these vesicles exhibit spherical shapes when prepared in the isotropic phase of the solution, elastic stresses imparted by the nematic LC phase deform the GUVs upon quenching the solution, forcing them to adopt elongated, non-spherical shapes. The spatial variations in membrane curvature exhibited by these GUVs may make them particularly well-suited to function as synthetic model cell membranes in future biophysical studies.

The following section of this first chapter provides the reader with a brief introduction to LCs. Detailed descriptions of optical methods used to characterize LC films and interfaces in this thesis and an extensive review of relevant literature are withheld until Chapters 2 and 3, respectively. The third and final section of this chapter presents an overview of all chapters comprising the remainder of this thesis.

1.2 Introduction to Liquid Crystals

The liquid crystalline phase of matter is intermediate to a crystalline solid and an isotropic liquid, as mesogens in the LC phase are free to flow, yet still retain some degree of orientational order.[14–16] There are two overarching categories of LCs: thermotropic and lyotropic.

Thermotropic LCs consist of small, rod-shaped organic molecules, such as 4'-pentyl-4-cyanobiphenyl (5CB, Figure 1-1A), that exhibit liquid crystallinity in the absence of a solvent. As their name suggests, their phase behavior is dictated largely by temperature (Figure 1-1B). This type of LCs is commonly utilized in liquid crystal display (LCD) technologies. Lyotropic LCs, on the other hand, are mixtures that exhibit LC phase behavior that is dictated by both temperature and the concentrations of the components (Figure 1-1D). While conventional lyotropic LC phases typically are formed by solutions of amphiphilic molecules such as surfactants, another class of lyotropic LCs (which is frequently employed in the research reported in this thesis) is the so-called "lyotropic chromonic LCs". Lyotropic chromonic LC phases form when non-amphiphilic, polyaromatic molecules, such as disodium cromoglycate (DSCG, Figure 1-1C) are dispersed in a polar solvent (commonly water).[17] Chromonic LC phases form when the small molecules assemble into columnar aggregates as a result of strong pi-pi interactions and hydrophobic interactions (Figures 1-1E and 1-1F).[17] In contrast to the case of thermotropic LCs, where individual rod-shaped molecules serve as the constituents of the LC phase (or "mesogens"), in lyotropic chromonic LC phases, these columnar aggregates are the mesogens.

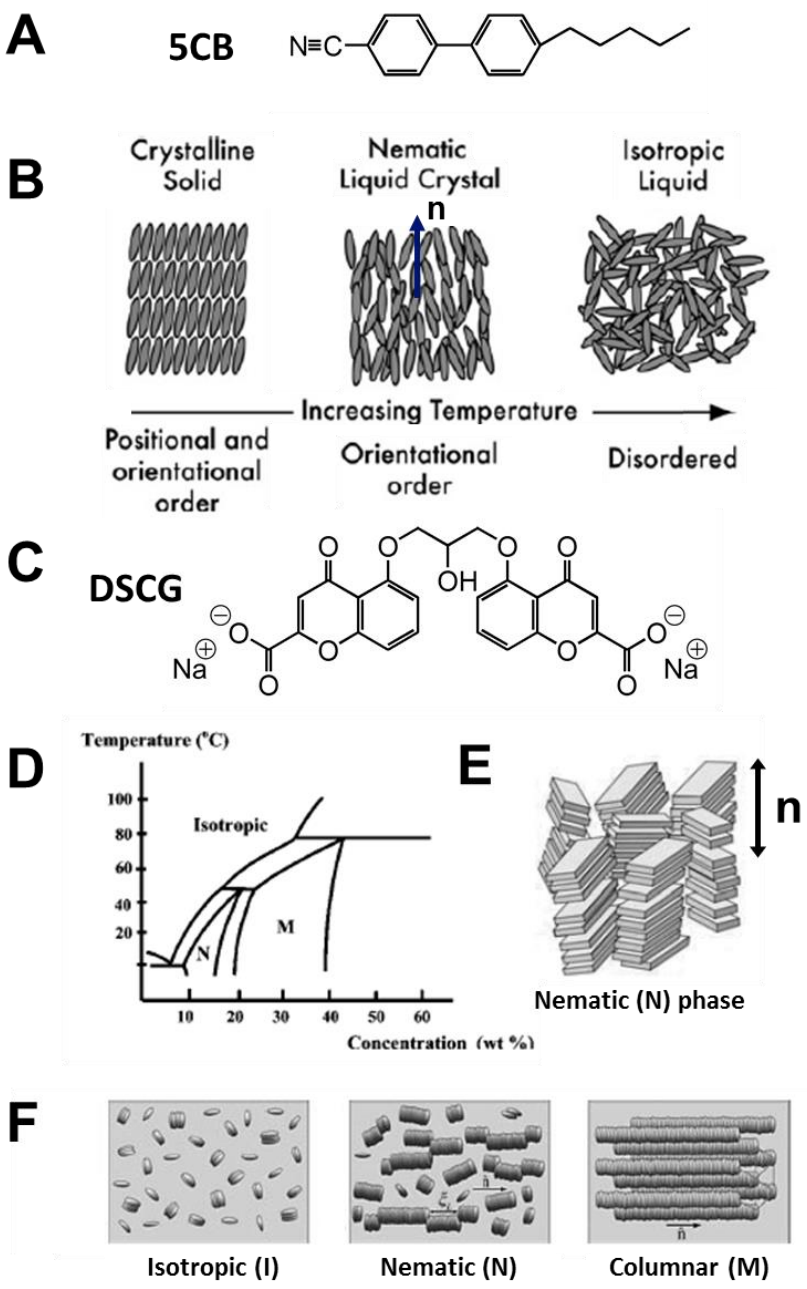

Figure 1-1. Introduction to thermotropic and lyotropic chromonic liquid crystals (LCs).

(A) Molecular structure of 4'-pentyl-4-cyanobiphenyl (5CB). (B) Schematic depiction of the phase behavior of a molecule that exhibits a thermotropic nematic LC phase. (C) Molecular structure of disodium cromoglycate (DSCG). (D) Phase diagram depicting the LC mesophases formed by aqueous dispersions of DSCG. (E) Schematic illustration of the columnar molecular aggregates that comprise the nematic phase of lyotropic chromonic LCs. (F) Schematic depiction of the organization of molecules in lyotropic chromonic LC phases. Reproduced with permission.[17,18]

The simplest LC phase, which can be formed by both thermotropic and lyotropic chromonic LCs is the nematic. In the nematic LC phase, mesogens orient along a common average direction given by the director, **n**, but exhibit no additional positional order. As will be described in additional detail in Chapters 2 and 3 of this thesis, the combination of long range ordering and high mobility of mesogens that characterize nematic LCs give rise to a number of key properties of this mesophase that differentiate it from, for example, isotropic liquids. These properties include elasticity, sensitive surface-induced ordering, and the ability to locally melt in order to form topological defects. In addition, nematic LCs exhibit anisotropic physical properties such as optical birefringence as well as dielectric and diamagnetic anisotropy. The research reported in Chapters 4 through 8 is enabled by these important features of nematic LCs.

1.3 Thesis Overview

Chapters 2 through 8 were prepared as separate publications and thus may be read independently. Chapter 2 describes optical methods used for characterization of LC phases that are employed in the research reported in this thesis. Chapter 3 is a literature review that details recent advances in the design of responsive and active soft materials based on LCs. The remaining chapters report on experimental research investigations and can be grouped into the two series of studies. Chapters 4 through 6 describe the dynamical behaviors of motile bacteria dispersed within and at the interfaces of biocompatible lyotropic LCs. Chapters 7 and 8 focus on the formation of novel LC emulsions incorporating lyotropic chromonic LC phases. Further descriptions of Chapters 2 through 8 are provided below.

Chapter 2 describes methods and underlying principles that can be used to characterize both the orientations assumed spontaneously by LCs at interfaces and the strength with which the

LCs are held in those orientations (so-called anchoring energies). The application of these methods to several different classes of LC interfaces is described, including solid and aqueous interfaces as well as planar and nonplanar interfaces (such as those that define a LC-in-water emulsion droplet). These methods, which enable fundamental studies of the ordering of LCs at polymeric, chemically functionalized, and biomolecular interfaces, are described in this chapter on a level that can be easily understood by a nonexpert reader such as an undergraduate or graduate student. We focus on optical methods because they are based on instrumentation that is found widely in research and teaching laboratories.

In Chapter 3, a review of literature in the area of the design of responsive and active soft materials using LCs is provided. LCs are widely known for their use in liquid crystal displays (LCDs). Indeed, LCDs represent one of the most successful technologies developed to date using a responsive soft material: an electric field is used to induce a change in ordering of the LC and thus a change in optical appearance. Over the past decade, however, research has revealed the fundamental underpinnings of potentially far broader and pervasive uses of LCs for the design of responsive soft material systems. These systems involve a delicate interplay of the effects of surface-induced ordering, elastic strain of LCs and formation of topological defects, and are characterized by a chemical complexity and diversity of nano- and micro-meter-scale geometry that goes well beyond that previously investigated. As a reflection of this evolution, the community investigating LC-based materials now relies heavily on concepts from colloid and interface science. In this context, this chapter describes recent advances in colloidal and interfacial phenomena involving LCs that are enabling the design of new classes of soft matter that respond to stimuli as broad as light, airborne pollutants, bacterial toxins in water, mechanical interactions with living cells, molecular chirality and more. Ongoing efforts hint also that the

collective properties of LCs (e.g., LC-dispersed colloids) will, over the coming decade, yield exciting new classes of driven or active soft material systems in which organization (and useful properties) emerge during the dissipation of energy.

Chapter 4 reports an investigation of dynamical behaviors of motile rod-shaped bacteria within anisotropic viscoelastic environments defined by lyotropic LCs. In contrast to passive microparticles (including non-motile bacteria) that associate irreversibly in LCs via elasticity-mediated forces, we report that motile *Proteus mirabilis* bacteria form dynamic and reversible multi-cellular assemblies when dispersed in a lyotropic LC. By measuring the velocity of the bacteria through the LC (8.8 ± 0.2 μm/s) and by characterizing the ordering of the LC about the rod-shaped bacteria (tangential anchoring), we conclude that the reversibility of the inter-bacterial interaction emerges from the interplay of forces generated by the flagella of the bacteria and the elasticity of the LC, both of which are comparable in magnitude (tens of pN) for motile *Proteus mirabilis* cells. We also measured the dissociation process, which occurs in a direction determined by the LC, to bias the size distribution of multi-cellular bacterial complexes in a population of motile *Proteus mirabilis* relative to a population of non-motile cells. Overall, these observations and others reported in this paper provide insight into the fundamental dynamic behaviors of bacteria in complex anisotropic environments and suggest that motile bacteria in LCs are an exciting model system for exploration of principles for the design of active materials.

Bacteria often inhabit and exhibit distinct dynamical behaviors at interfaces, but the physical mechanisms by which interfaces cue bacteria are still poorly understood. In Chapter 5, we use interfaces formed between coexisting isotropic and LC phases to provide insight into how mechanical anisotropy and defects in LC ordering influence fundamental bacterial behaviors. Specifically, we measure the anisotropic elasticity of the LC to change fundamental behaviors of

motile, rod-shaped *Proteus mirabilis* cells (3 μm in length) adsorbed to the LC interface, including the orientation, speed, and direction of motion of the cells (the cells follow the director of the LC at the interface), transient multicellular self-association, and dynamical escape from the interface. In this latter context, we measure motile bacteria to escape from the interfaces preferentially into the isotropic phase, consistent with the predicted effects of an elastic penalty associated with strain of the LC about the bacteria when escape occurs into the nematic phase. We also observe boojums (surface topological defects) present at the interfaces of droplets of nematic LC (tactoids) to play a central role in mediating the escape of motile bacteria from the LC interface. Whereas the bacteria escape the interface of nematic droplets via a mechanism that involved nematic director-guided motion through one of the two boojums, for isotropic droplets in a continuous nematic phase, the elasticity of the LC generally prevented single bacteria from escaping. Instead, assemblies of bacteria piled up at boojums and escape occurred through a cooperative, multicellular phenomenon. Overall, our studies show that the dynamical behaviors of motile bacteria at anisotropic LC interfaces can be understood within a conceptual framework that reflects the interplay of LC elasticity, surface-induced order, and topological defects.

In Chapter 6, we report on the organization and dynamics of bacteria (*Proteus mirabilis*) dispersed within lyotropic LC films confined by pairs of surfaces that induce homeotropic (perpendicular) or hybrid (homeotropic and parallel orientations at each surface) anchoring of the LC. By using motile vegetative bacteria (3 μm in length) and homeotropically aligned LC films with thicknesses that exceed the length of the rod-shaped cells, a key finding reported in this paper is that elastic torques generated by the LC are sufficiently large to overcome wall-induced hydrodynamic torques acting on the cells, thus leading to LC-guided bacterial motion near surfaces that orient LCs. This result extends to bacteria within LC films with hybrid anchoring,

and leads to the observation that asymmetric strain within a hybrid aligned LC rectifies motions of motile cells. In contrast, when the LC film thickness is sufficiently small that confinement prevents alignment of the bacteria cells along a homeotropically aligned LC director (achieved using swarm cells of length 10 – 60 μm), the bacterial cells propel in directions orthogonal to the director, generating transient distortions in the LC that have striking "comet-like" optical signatures. In this limit, for hybrid LC films, we find LC elastic stresses deform the bodies of swarm cells into bent configurations that follow the LC director, thus unmasking a coupling between bacterial shape and LC strain. Overall, these results provide new insight into the influence of surface-oriented LCs on dynamical bacterial behaviors and hint at novel ways to manipulate bacteria using confined LC phases that are not possible in isotropic solutions.

In Chapter 7, we report the formation and characterization of hierarchical ordering in systems comprised of micrometer-sized droplets of thermotropic nematic LCs dispersed in continuous nematic phases of a lyotropic chromonic LC (disodium cromoglycate (DSCG)). Significantly, we find the orientations of the two LC phases to be coupled, with nematic droplets of 4'-pentyl-4-cyanobiphenyl (5CB) exhibiting a bipolar configuration with an axis of symmetry aligned orthogonal to the far-field director of the DSCG phase. We determine that this coupling of orientations does not result from either anisometric LC droplet shape or interfacial ionic phenomena but rather is consistent with the influence of van der Waals interactions that arise from the anisotropic polarizabilities of nematic 5CB ($\Delta n = +0.18$) and DSCG ($\Delta n = -0.02$) phases. We also find that it is possible to rotate and uniformly align the nematic droplets by using a weak magnetic field ($\mathbf{B} \sim 0.3$ T). An analysis of the dynamics of relaxation of the orientations of the 5CB droplets following removal of the magnetic field reveals the DSCG and 5CB droplets to be coupled by energies of $\sim 10^4$ kT, consistent with a simple theoretical estimate

of the influence of anisotropic van der Waals interactions. We also observed the nematic 5CB droplets to form dimers and larger assemblies mediated by the elasticity of the nematic DSCG. Overall, these results reveal that LC-in-LC emulsions define a new class of hierarchically ordered soft matter in which both thermotropic and lyotropic LCs are coupled in their ordering.

In Chapter 8, we explore coupling between deformable objects and a structured fluid by using giant unilamellar vesicles (GUVs) prepared in an aqueous lyotropic chromonic LC phase. We report the GUVs to adopt anisometric shapes with aspect ratios up to 10 as a result of stresses arising from confinement within the LC. Specifically, we find two distinct populations of non-spherical GUVs (major axis legnths ranging from 2.5 μm to 50 μm) to form in our experiments: GUVs that are slightly elongated with approximately rounded poles (characterized by cusp angles of $\alpha > 130°$) and GUVs that are highly elongated and possess sharply cusped poles ($\alpha < 130°$). Whereas formation of the population of slightly elongated GUVs is consistent with LC elasticity-induced expansion of lipid membrane surface area up to 3% while GUV volume is conserved, our results suggest that efflux of LC encapsulated by GUVs, likely from transient pores in the membranes of strained vesicles, gives rise to the population of highly elongated GUVs. Moreover, an analysis of the equilibrium shapes of GUVs in our experiments reveals that the energy associated with stretching the GUV membrane is small relative to a surface energy due to an interfacial tension and suggests that a coupling between this surface energy and the LC elastic energy gives rise to the GUV shapes we observe. Overall, these results reveal that elastic stresses imparted by a nematic LC can dynamically deform the shapes of lipid membranes, and likely other flexible soft particles. This demonstrated coupling between LC elastic strain and strain within deformable particles defines new opportunities in the design of LC-based responsive and reconfigurable materials.

1.4 References

1. Loudet, J. C.; Hanusse, P.; Poulin, P. Stokes Drag on a Sphere in a Nematic Liquid Crystal. *Science* **2004**, 306, 1525.
2. Mondiot, F.; Loudet, J.-C.; Mondain-Monval, O.; Snabre, P.; Vilquin, A.; Würger, A. Stokes-Einstein Diffusion of Colloids in Nematics. *Phys. Rev. E* **2012**, 86, 010401.
3. Turiv, T.; Lazo, I.; Brodin, A.; Lev, B. I.; Reiffenrath, V.; Nazarenko, V. G.; Lavrentovich, O. D. Effect of Collective Molecular Reorientations on Brownian Motion of Colloids in Nematic Liquid Crystal. *Science* **2013**, 342, 1351–1354.
4. Lynch, M. D.; Patrick, D. L. Organizing Carbon Nanotubes with Liquid Crystals. *Nano Lett.* **2002**, 2, 1197–1201.
5. Lapointe, C.; Hultgren, A.; Silevitch, D. M.; Felton, E. J.; Reich, D. H.; Leheny, R. L. Elastic Torque and the Levitation of Metal Wires by a Nematic Liquid Crystal. *Science* **2004**, *303*, 652–655.
6. Tkalec, U.; Škarabot, M.; Muševič, I. Interactions of Micro-Rods in a Thin Layer of a Nematic Liquid Crystal. *Soft Matter* **2008**, 4, 2402–2409.
7. Mondiot, F.; Chandran, S. P.; Mondain-Monval, O.; Loudet, J.-C. Shape-Induced Dispersion of Colloids in Anisotropic Fluids. *Phys. Rev. Lett.* **2009**, 103, 238303.
8. Senyuk, B.; Smalyukh, I. I. Elastic Interactions between Colloidal Microspheres and Elongated Convex and Concave Nanoprisms in Nematic Liquid Crystals. *Soft Matter* **2012**, 8, 8729–8734.
9. Musevic, I.; Škarabot, M.; Tkalec, U.; Ravnik, M.; Žumer, S. Two-Dimensional Nematic Colloidal Crystals Self-Assembled by Topological Defects. *Science* **2006**, 313, 954–958.
10. Poulin, P.; Stark, H.; Lubensky, T. C.; Weitz, D. A. Novel Colloidal Interactions in Anisotropic Fluids. *Science* **1997**, 275, 1770–1773.
11. Škarabot, M.; Ravnik, M.; Žumer, S.; Tkalec, U.; Poberaj, I.; Babič, D.; Osterman, N.; Muševič, I. Interactions of Quadrupolar Nematic Colloids. *Phys. Rev. E* **2008**, 77, 031705.
12. Tasinkevych, M.; Mondiot, F.; Mondain-Monval, O.; Loudet, J.-C. Dispersions of Ellipsoidal Particles in a Nematic Liquid Crystal. *Soft Matter* **2014**, 10, 2047–2058.
13. Nych, A.; Ognysta, U.; Muševič, I.; Seč, D.; Ravnik, M.; Žumer, S. Chiral Bipolar Colloids from Nonchiral Chromonic Liquid Crystals. *Phys. Rev. E* **2014**, 89, 062502.
14. De Gennes, P. G. *The Physics of Liquid Crystals*; Clarendon Press: Oxford, England, 1974.
15. Chandrasekhar, S. *Liquid Crystals*; Cambridge University Press: Cambridge, 1977.
16. Collings, P. J.; Hird, M. *Introduction to Liquid Crystals: Chemistry and Physics*; Taylor & Francis: London, 1997.
17. Lydon, J. Chromonic Review. *J. Mater. Chem.* **2010**, 20, 10071–10099.
18. Park, H.; Lavrentovich, O. D. Lyotropic Chromonic Liquid Crystals: Emerging Applications. In *Liquid Crystals Beyond Displays: Chemistry, Physics, and Applications*; Li, Q., Ed.; John Wiley & Sons: Hoboken, NJ, 2012; pp 449–484.

Chapter 2: Introduction to Optical Methods for Characterizing Liquid Crystals at Interfaces*

2.1 Introduction

Measurements of the orientational ordering of liquid crystals (LCs) near interfaces enable fundamental studies of biological materials (e.g., lipid droplets found in certain types of mammalian cells),[1,2] the design of electro-optical devices (such as liquid crystal displays),[3] strategies for the hierarchical design of nanoscale materials (e.g., semiconducting nano-rods),[4,5] and the creation of LC-based materials that respond to specific chemical and biological cues.[6-8] The intent of this chapter is not to dig deeply into fundamental questions specific to any one of these contexts, but rather this chapter seeks to enable new researchers to study interfacial phenomena involving LCs by providing instruction in key experimental methods. We focus in particular on the use of optical methods because these are accessible in many research and teaching laboratories, and they can provide broadly useful information on both the average orientations of LCs and the strengths with which LCs are held in preferred orientations at interfaces. In this chapter, we also avoid providing extensive details regarding the preparation of experimental systems because they tend to be specific to a particular line of investigation and are described elsewhere.[6-26]

2.2 Organization of this Chapter

This chapter covers three classes of LC interfaces (where the LCs are formed from molecules such as those shown in Figure 2-1A). We briefly describe these LC interfaces below and refer to them in subsequent sections of this chapter.

The first class of LC interfaces is formed between a LC and a solid (Figure 2-1C). This is the most widely explored class of LC interfaces because of its use in electro-optical devices. (The planar solid surface typically comprises an electrode that is used to switch the orientation of the LC.) Materials that are commonly used to prepare such solid interfaces include polymers (e.g., sheared mechanically to align the polymer such that it serves as a molecular template that directs the orientation of the LC)[27,28] and inorganic compounds prepared by physical vapor deposition (such as silicon oxide or gold).[29,30] In the case of gold, the surface can be chemically functionalized using organosulfur compounds to generate a wide range of intermolecular interactions between the LC and the solid interface.[14,23,24,31,32] This latter system is particularly versatile and suitable for fundamental studies of the ordering of LCs at solid surfaces. At solid surfaces, the preferred orientation of the LC (easy axis) is defined by an azimuthal angle and a zenithal angle (Figure 2-1B). Typically, the azimuthal angle, ϕ, is defined with respect to a symmetry axis within the solid surface (e.g., the direction of deposition of an inorganic layer deposited by physical vapor deposition at an oblique angle of incidence). The zenithal angle, θ, is reported with respect to the surface normal.

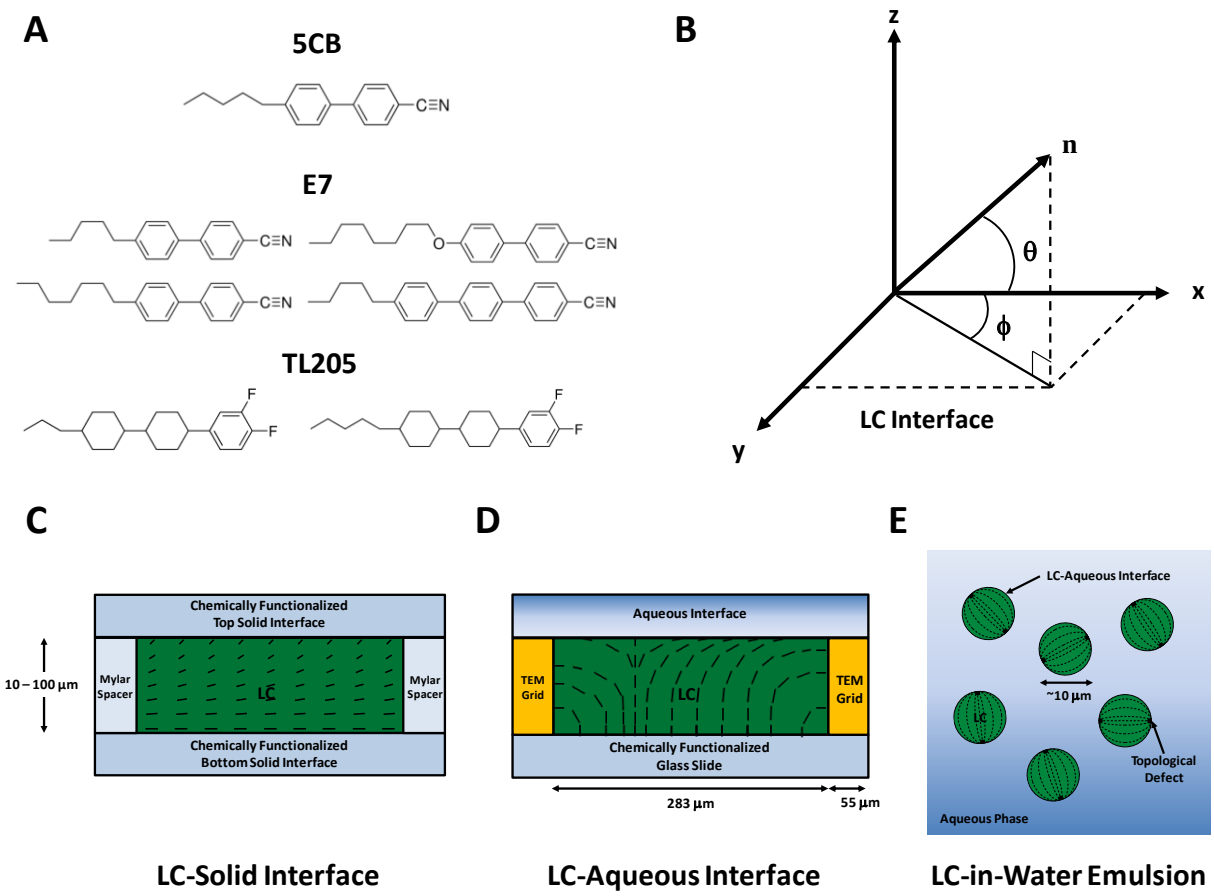

Figure 2-1. LC mesogens and common LC interfaces.

(A) Molecular structures of three common mesogens or mixtures of mesogens that form room-temperature nematic LC phases: 4-cyano-4'-pentylbiphenyl (5CB), E7 and TL205. Several physical properties of these LCs are displayed in Table S1 of the SI. (B) Definition of angles used to characterize the average orientation of a LC (director, *n*) near a flat interface. The azimuthal orientation is characterized by the azimuthal angle (ϕ) and the zenithal orientation is characterized by the zenithal angle (θ). (C-E) Schematic illustrations of three classes of LC interfaces that are discussed in this chapter. (C) LC-solid interface: LC is sandwiched between two chemically functionalized solid surfaces, each of which anchoring the LC in a preferred orientation. (D) LC-aqueous interface: LC is hosted within the pores of a grid supported on a chemically functionalized glass-slide and submerged under an aqueous solution to create a stable LC-aqueous interface. (E) LC-in-water emulsion: LC droplets are dispersed in an aqueous phase. Dashed lines indicate the director of the LC. Modified and reproduced with permission.[7]

We note that a common occurrence in an experiment involving a film of LC confined between two solid surfaces is that the easy axes of the LC differ at the two surfaces. In this situation (often referred to as a "hybrid" LC system), the orientation of the LC between the two surfaces is determined by the minimization of the anchoring and elastic energies of the film of LC (Figure 2-1C). The strains experienced by a LC include splay, bend, and twist, and an elastic constant (K) for each mode of deformation connects the strain to the free- energy density. (See Equation 2-2 and associated text below for additional detail.[3,33,34]) In this situation, it is common to consider a so-called extrapolation length, defined as $L \approx K/W$ for the case of planar films, where W is the orientation- dependent surface energy or anchoring energy per unit area.[34] In a planar film of LC, the extent to which the LC departs from the orientation of the easy axis depends on the ratio of the extrapolation length to the thickness of the LC film (d). For sufficiently thick films ($L/d \ll 1$), the orientation of the LC near an interface is close to the easy axis. Unless indicated otherwise, the planar films of LC discussed in this chapter satisfy this criterion.

The second class of planar interfaces involving LCs that can be characterized using the methods described in this chapter are those formed between LCs and aqueous phases.[7] As depicted in Figure 2-1D, the stabilization of this type of LC interface has to date been commonly achieved by using capillary forces generated by the placement of a grid onto a solid surface.[10] Within the pores of the grid, which have a width (typically ~300 μm) that is much larger than the thickness of the LC film (5−50 μm), an approximately planar interface can be formed between the LC and the aqueous phase. Particular experimental protocols must be followed, however, to obtain an approximately planar interface. For example, if excess LC is deposited within the pores of the grid, then the resulting LC interface will be curved due to formation of a meniscus, which

will impact the optical characterization of the interface (see below). Similar to the case of a LC−solid interface, the orientation of the LC at the aqueous interface is defined by azimuthal and zenithal angles (see above).

Finally, we comment that this chapter also addresses the characterization of LC droplets (Figure 2-1E), including LC droplets dispersed in an aqueous phase. This spherical geometry has particular relevance to the development of stimuli-responsive LC materials because confinement can lead to configurations of LC within the droplet that reflect a delicate balance of interfacial and elastic contributions to the free energy. One additional common feature of the droplet geometry is the formation of so-called topological defects in the LC. In brief, when LCs are confined within the approximately spherical volume of a droplet, in many instances it is not possible for the LC to satisfy the anchoring conditions at the droplet interface through the continuous strain of the LC (such as by some combination of twist, splay, and bend). In these situations, localized regions of the LC partially "melt" (i.e., exhibit low levels of orientational order relative to that of the bulk LC) to generate defects in the LC. The "cores" of the defects, although nanoscopic in size, possess refractive indices that differ substantially from that of the surrounding LC and thus can be characterized using optical methods. Common defects encountered in the droplet geometry include point defects and line defects, where the latter are frequently referred to as disclination lines. Additional discussion regarding defects in LCs can be found later in this chapter.

The remainder of this chapter is organized into four sections. First, we briefly outline procedures that can be used to prepare each of the three classes of experimental systems mentioned above. For details, we refer the reader to past publications.[6-26] Second, we describe the use of polarized light microscopy to provide qualitative information regarding the

orientations of LCs near interfaces. Third, we report optical methods that permit the quantitation of optical properties of LCs that in turn provide a quantitative measurement of, for example, the zenithal angle assumed by a LC at an interface. Fourth, we describe methods that permit the measurement of the anchoring energies of LCs. Finally, we briefly describe some unresolved challenges related to the preparation and characterization of LC interfaces. In each of these sections, we address the characterization of the three classes of experimental systems shown in Figures 2-1C through 2-1E.

2.3 Preparation of Experimental Systems

2.3.1 LC−Solid Interfaces

To study the orientation of a LC at a solid surface, it is common to form an optical cell within which the LC is confined between two solid surfaces (as shown in Figure 2-1C). The preparation of the system typically begins by the placement of thin sheets of a polymer film, often Mylar, of known thickness (typically 2−100 μm) along two edges of the bottom solid surface. Next, the top surface is inverted, aligned with the bottom surface, and placed on the spacers in a manner such that a cavity is defined between the two surfaces of interest. The edges that have the spacers are then clipped together (using “bulldog” or “binder” clips); alternatively, the cell can be sealed and held together using epoxy after the introduction of the LC. Next, both the LC in a glass syringe and the sample cell are heated to above the nematic-to-isotropic transition temperature (clearing temperature) of the LC, which can be achieved, for example, by the placement of the sample on a hot plate. The LC is then introduced into the cell by capillary action. We note that it is generally preferred to introduce the LC into an optical cell after heating it above the clearing temperature to avoid flow-induced alignment and “surface-memory” effects

that occur if the material is introduced while in the LC phase. If using labile organic interfaces (e.g., self-assembled monolayers formed on gold films), however, one also has to be careful that the heating of the system does not cause thermal degradation. Finally, the sample is moved to an optical microscope for characterization.

2.3.2 LC–Aqueous Interfaces

The preparation of an interface between an aqueous phase and a LC can be achieved by first adding a small amount (~0.2 μL) of a nematic LC to the pores of a copper- or gold-coated transmission electron microscopy (TEM) grid supported on a glass substrate.[10] The glass substrate is usually chemically functionalized to induce a preferential zenithal orientation of the contacting LC. Common treatments of the glass employ one of two silanes, octadecyltrichlorosilane (OTS) or dimethyloctadecyl[3- (trimethoxysilyl)propyl]ammonium chloride (DMOAP), either of which causes perpendicular (homeotropic) anchoring of most nematic LCs.[7, 10, 35] As mentioned above, the grids are used to generate capillary forces that lead to the formation of stable LC−aqueous interfaces. A typical grid used in such an experiment will have a lateral pore size of ~300 μm and a known thickness ranging from 5 to 50 μm. Prior to use, the grids should be rinsed sequentially with ethanol, methanol, and chloroform and dried overnight in an oven. After a grid is placed on the glass substrate, it is filled with LC to form a film with approximately the same thickness as the grid. Excess LC (which will create a curved interface) can be removed from the grid by touching the LC with an empty capillary tube. The glass substrate supporting the LC-filled grid is then held at a slight angle from the horizontal and immersed in an aqueous solution to form the interface between the LC and the aqueous solution. As noted above, curved LC−aqueous interfaces will be generated if the grid is significantly

overfilled or underfilled with LC. These situations are easily recognized by rings of interference colors that are observed upon imaging the sample between crossed polarizers using white light (described below). Finally, we note that the gold- and copper-coated surfaces of the TEM grids cause a homeotropic orientation of the LCs. However, the extent of this alignment (~10 μm) is small compared to the lateral size of the grid pores typically used in these experiments (~300 μm, Figure 2-3C).

2.3.3 LC-in-Water Emulsions.

The simplest method for preparing a LC-in-water emulsion involves the use of sonication and vortex mixing to disperse LC added to a bulk aqueous phase (e.g., 2 μL of LC in 1 mL of water).[21,25] When using conditions detailed in our past publication, this simple procedure results in a polydisperse population of LC droplets with diameters ranging from 1 to 20 μm.[25] A measurement of turbidity (using a UV−vis spectrophotometer) is a useful way to assess the end point of the sonication because, for a given volume of LC added to the bulk aqueous phase, emulsions with similar turbidities will possess similar size distributions of LC droplets. If precise control over the size of the LC droplets in the LC-in-water emulsion is desired, then one of several alternative methods of preparation can be employed. For example, monodisperse LC-in-water emulsions have been prepared by using polyelectrolyte multilayer capsules as templates[26] or by using microfluidics.[19] Finally, for optical characterization of a LC-in-water emulsion, a small volume of the emulsion (several microliters is usually sufficient) can be dispersed onto a supporting substrate (e.g., a glass microscope slide) and the sample can be placed onto the stage of a microscope. We note that glycerol is often added to the aqueous phase of LC-in-water

emulsions in order to increase the viscosity of the aqueous phase and thereby slow the diffusion of the LC droplets (for ease of observation by microscopy).

2.4 Qualitative Optical Characterization of LCs at Interfaces

Most LCs possess anisotropic optical properties, and thus many methods used to characterize the orientations of LCs revolve around the interaction of polarized light with the LCs. As detailed below, measurements of the polarization of light transmitted through LCs are commonly performed by placing a polarizer before and after a LC sample in the optical path of a microscope (Figure 2-2). To enable a discussion of polarized light microscopy, below we briefly describe how polarized light interacts with (uniaxial) LCs.

Polarized light propagating through a LC in a uniaxial nematic phase can experience two distinct refractive indices depending on the polarization of the light relative to the director of the LC (the direction the molecules of the LC tend to align on average): a refractive index parallel to the nematic director (ne, extraordinary refractive index) and a refractive index perpendicular to the director (no, ordinary refractive index) (Figure 2-2A).[33] The difference between these direction- dependent refractive indices is known as birefringence ($\Delta n = n_e - n_o$) and leads to two possible scenarios when a nematic LC is placed between a polarizer and an analyzer (oriented 90° with respect to the polarizer; crossed polarizers) and viewed in transmission mode using white light (Figures 2-2B through 2-2E). First, if the LC is oriented perpendicular to the bottom surface of the sample (Figure 2-2B) or if the azimuthal orientation of the LC is either 90° (Figure 2-2C) or 0° (Figure 2-2D) relative to the plane of polarization of the light passing through the bottom polarizer, then the light propagating through the LC will experience only one index of refraction (n_o or n_e) and the polarization of the light passing through the LC will remain

unchanged. Thus, upon exiting the LC, light will not pass through the crossed analyzer, resulting in a dark optical appearance of the material (Figures 2-2B through 2-2D). Second, if the azimuthal orientation of the LC is neither parallel nor perpendicular to the bottom polarizer (Figure 2-2E), then the light propagating through the LC will experience two indices of refraction and split into so-called ordinary and extraordinary rays with electric field vectors vibrating in different planes. The different refractive indices experienced by the two rays causes them to travel at different velocities, inducing a phase shift. In general, the rays are phase shifted such that the light emerges from the LC with an elliptical polarization. Thus, some light will pass through the analyzer, resulting in a bright optical appearance of the LC (Figure 2-2E). As will be discussed in detail below, the specific orientations of the LCs in the second scenario can give rise to a range of optical appearances of the LC samples.

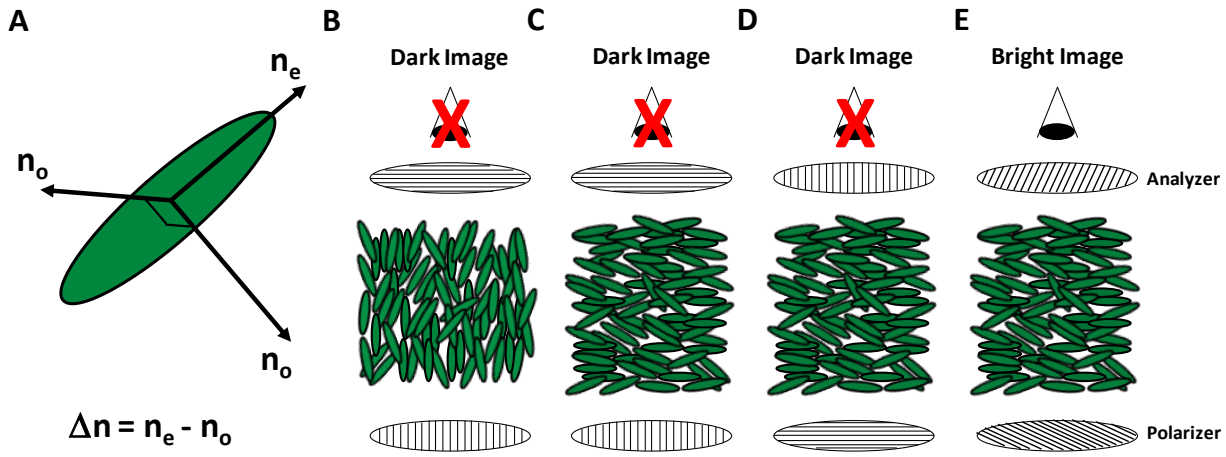

Figure 2-2. Polarized light microscopy of nematic LCs using orthoscopic illumination.
(A) Schematic illustration of the index ellipsoid of a uniaxial nematic LC. Two distinct refractive indices are evident - a refractive index parallel to the nematic director (n_e) and a refractive index perpendicular to the director (n_o). The difference between these refractive indices is known as birefringence ($\Delta n = n_e - n_o$). (B-D) Examples of orientations of LCs that, when viewed between crossed polarizers, exhibit a dark optical appearance. In B, the director of the LC is oriented parallel to the direction of propagation of the light through the LC. In C and D, the director of the LC is oriented in the plane of the sample with an azimuthal alignment that is either perpendicular (C) or parallel (D) to the incident polarizer. (E) When the

director of the LC is oriented in the plane of the sample but with an azimuthal orientation that lies between the polarizer and analyzer, the light transmitted through the LC gains an elliptical polarization leading. This leads to a bright optical appearance of the LC.

2.4.1 Orthoscopic Polarized Light Microscopy of LCs

2.4.1.1 Orthoscopic Polarized Light Microscopy of Planar Films of LC

An important consequence of the above-described birefringence of nematic LCs is that orthoscopic polarized light microscopy can be employed to characterize the orientational ordering of nematic LCs at interfaces.[6,7] This technique probes a LC sample with a beam of near-parallel rays of polarized light. To illustrate its utility in characterizing the orientational ordering of nematic LCs at interfaces, we focus on a system in which a thin planar film (slab geometry) of LC, tens of micrometers in thickness, is confined between a solid substrate and an aqueous phase (Figure 2-3). At the LC−aqueous interface, the zenithal orientation of the LC can be either homeotropic (perpendicular to the interface), planar (parallel to the interface), or tilted (at an acute angle to the interface). The bottom interface in Figure 2-3 is a reference interface, where the zenithal orientation of the LC is homeotropic (caused by treatment of a glass surface with a silane, see above). Each of the three zenithal orientations of the LC at the top interface will lead to distinct optical appearances of the LC film when viewed using polarized light microscopy. Below, we describe the optical appearance of the film for each of these zenithal orientations. We also comment that this discussion, although presented in the context of LC−aqueous interfaces, applies also to analysis of LCs between two solid surfaces.

When the zenithal orientation of the LC is parallel at the aqueous interface (so-called planar anchoring), the LC confined in the film will undergo splay and bend distortions (Figure 2-3B) to accommodate the competing anchoring conditions at opposing interfaces. This

configuration of the LC leads to a bright optical appearance of the film as a result of the in-plane birefringence of the LC (Figure 2-3A). It is important to note that, although the zenithal orientation of the LC is well-defined at the LC−aqueous interface in Figure 2-3A, the azimuthal orientation (preferred orientation of the LC in the plane of the interface) of the LC is influenced by interactions with the vertical surfaces of the TEM grid. As a result of the anchoring on the TEM grid, dark brushes that emanate from the edges of the film as well as defects (described in further detail below) are evident in the optical appearance of the LC film. The LC appears dark when the azimuthal orientation of the LC is locally parallel to either the polarizer or analyzer and bright when the LC adopts an intermediate azimuthal orientation. When the azimuthal orientation of a LC is degenerate, the appearance of the LC is often referred to as having a Schlieren texture.[33,36,37] Outside of the dark brushes, if the sample is illuminated using white light, the colors of the film of the LC are typically faint yellow, pink, or green (Figure 2-3A). These colors depend on the optical retardance of the LC film, which in turn is a function of the thickness of the film of LC as well as the LC orientation (also discussed in more detail below).

In contrast to the case of a planar orientation at the LC− aqueous interface, when the zenithal orientation of the LC is homeotropic, the orientation of the LC is uniformly perpendicular except near the vertical surfaces of the grid (Figure 2-3D). The perpendicular configuration of the majority of the LC leads to a dark optical appearance when the LC film is viewed between crossed polarizers (Figure 2-3C). The sample appears dark because, as described above, polarized light transmitted through the LC experiences only one index of refraction of the LC (the so-called ordinary refractive index). Thus, the polarization of the incident light will be preserved upon transmission through the sample, and the light will not be able to pass through the crossed analyzer. As noted above, the bright regions of the LC evident near the surfaces of

the grid are caused by a homeotropic orientation of the LC on the vertical surfaces of the grid. The influence of the grid on the LC only extends a distance horizontally from the grid surface that is comparable to the thickness of the LC film (~10 μm in Figure 2-3C).

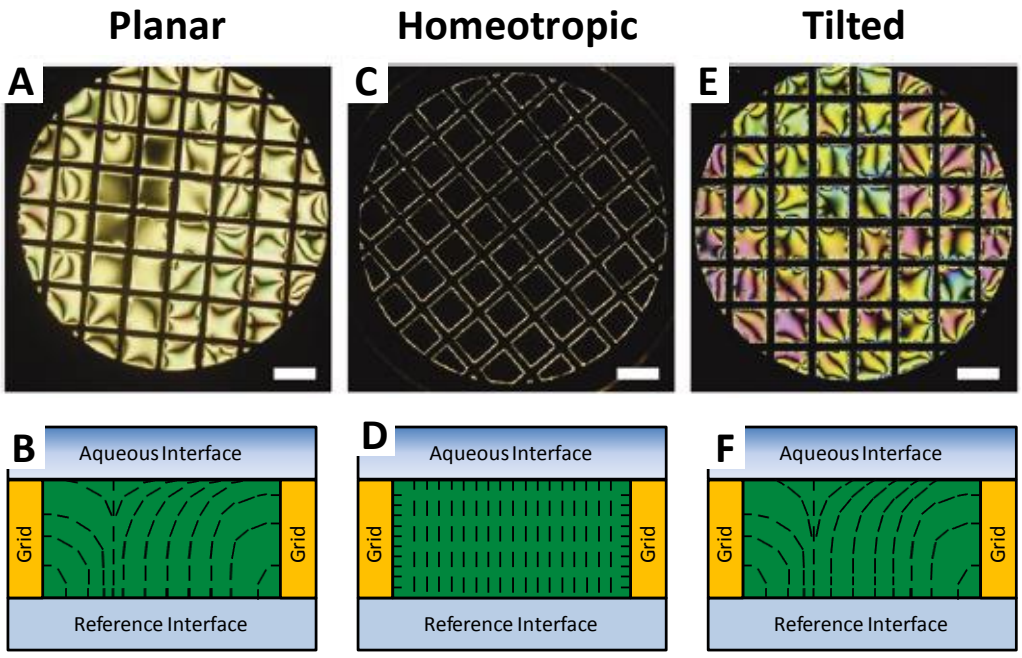

Figure 2-3. Polarized light micrographs (orthoscopic illumination) of micrometer-thick films of nematic 5CB anchored in three distinct orientations at LC-aqueous interfaces.
Optical images (crossed polarizers; A, C and E) and schematic illustrations of the director profiles (B, D and F) are shown. A and B correspond to planar anchoring, C and D correspond to homeotropic anchoring, and E and F correspond to tilted anchoring of the LC at the LC-aqueous interface. Scale bars are 300 μm. Modified and reproduced with permission.[†]

Finally, similar to the case of a planar orientation, when the orientation of the LC is tilted at the LC−aqueous interface, both splay and bend distortions will be present in the LC film (Figure 2-3F). In the regions of the LC where the azimuthal orientation of the LC is not influenced by the grid, the LC exhibits an appearance that is similar to a Schlieren texture (Figure 2-3E). However, as compared to the case of a planar orientation, a tilted orientation at the top interface leads to a lower optical retardance. This lower retardance leads to intense

coloration in regions outside of the dark brushes (Figure 2-3E). An analysis of the interference colors can provide quantitative information regarding the tilt angles of the LC at the interface (see below).

The experimental situation addressed in Figure 2-3 did not involve a twist deformation of the thin film of the LC. If a sample, when viewed between crossed polarizers, does not appear dark at some orientation between crossed polarizers, it is likely that a twist distortion is present in the sample. This situation can occur if the orientation of the LC is parallel to both the top and bottom interfaces yet the azimuthal orientation of the LC is different at both interfaces (Figure 2-9A). In this situation, if the azimuthal orientation of the LC at the bottom surface is aligned with the plane of polarization of the light passing through the bottom polarizer, then the LC will serve as a waveguide where the polarization of the light follows the twist of the nematic director. In later sections, we describe in detail how the rotation of a sample cell with a twist distortion can be used to quantify the azimuthal orientation of the LC at each interface (and thus also the twist angle of the LC in the sample).

As briefly mentioned above, the optical texture of a thin film of LC between crossed polarizers often possesses dark brush-like features (Figures 2-3A and 2-3E). These brushes typically emanate from defects present in the film. The defects can be either line defects (disclinations) extending throughout the bulk of the LC film or isolated point defects confined to the plane of observation. Under conditions that lead to a degenerate azimuthal orientation at the top interface of a thin film of LC (Figure 2-4A), two dark brushes emanate from the cores of disclinations whereas four dark brushes will emanate from the cores of isolated point defects.[36] The presence of disclinations in areas where two brushes originate can be confirmed by displacing either the top or bottom confining surface of the LC film. When either of the surfaces

is shifted, the centers with two brushes will leave a clear singular trace and the centers with four brushes will not.[36]

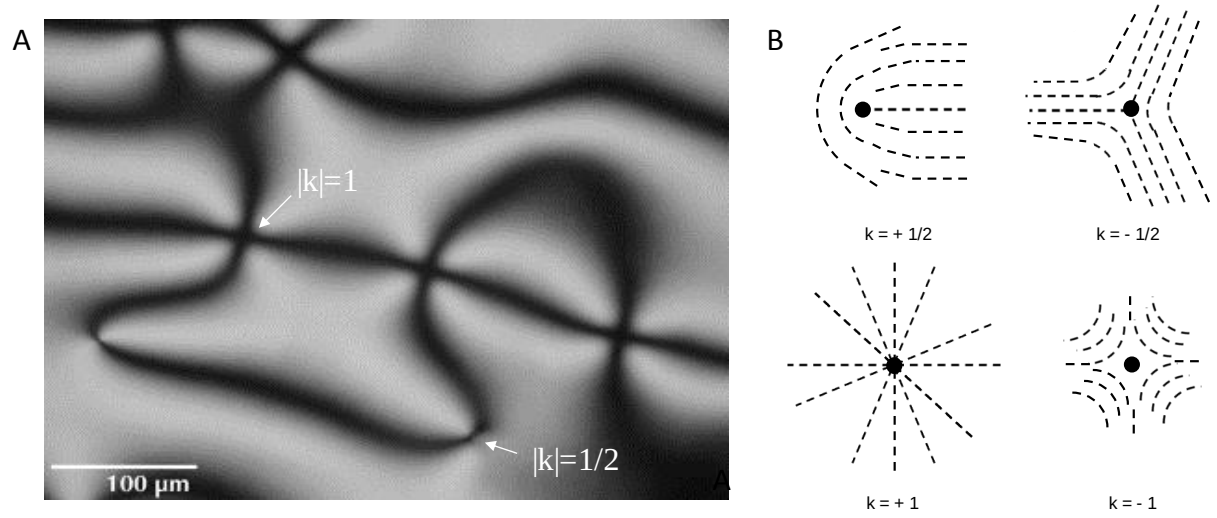

Figure 2-4. Topological defects in LCs.

(A) Polarized light micrograph of a Schlieren texture characteristic of a micrometer-thick film of LC with a degenerate planar alignment. Arrows indicate the positions of topological defects. (B) Schematic illustrations of director profiles around topological defects of indicated strength (*k*). (A) Modified and reproduced with permission.[50]

The number of brushes (*B*) emanating from the core of a defect can be used to assign the magnitude of the strength of a defect (|*k*|) according to the relationship $|k| = B/4$.[36] Physically, |*k*| defines the number of times the orientation of the nematic director rotates by $\pm 2\pi$ around the core of the defect (Figure 2-4B). In addition, the direction that the brushes rotate around a defect during an in-plane rotation of the film of LC can be used to define the sign of the defect. Clockwise rotation of the brushes around a defect corresponds to a positive defect, and counterclockwise rotation of the brushes corresponds to a negative defect. Figure 2-4B shows the director profiles around defects with different signs and strengths. Finally, we note that the type of defect can provide insight into the orientation of the LC at an interface. For example, in a film formed by spreading LC onto a solid substrate in air (with a perpendicular orientation of the LC

at the LC−air interface), the observation of a disclination line running through the central region of the film indicates that the zenithal orientation at the LC−solid interface is planar and the azimuthal orientation is uniform.[38] Furthermore, the direction that the disclination traverses the film is perpendicular to the azimuthal orientation of the LC at the LC−solid interface.

2.4.1.2 Orthoscopic Polarized Light Microscopy of LC-in-Water Emulsions.

The example presented above illustrates how orthoscopic polarized light microscopy can be used to make qualitative statements regarding the orientational ordering of nematic LCs at the flat interface of a micrometer-thick film. Although the orientational ordering of LCs at the interface of micrometer-sized droplets in a LC-in-water emulsion can also be elucidated through the use of orthoscopic polarized light microscopy,[3,6,7,18,21,25,33] key differences exist between the approaches typically used to determine the orientations of LCs at the interfaces of droplets as compared to planar films. In particular, the confinement of LCs to micrometer-sized droplets generates well-defined patterns of topological defects within the LCs.[3,39] The observation of these defects can be very useful when determining the orientations of the LC within droplets with light microscopy. As shown in Figure 2-5, the positions of topological defects in LC droplets and the organizations of the LC director around these defects (so-called "director configurations") result in distinct optical signatures when the LC droplets are viewed between crossed polarizers.

The positions of topological defects within the bulk or at the interfaces of LC droplets are governed by a subtle balance of surface anchoring and bulk elastic energies of the LC.[3,16,39] The relative importance of the two contributions to the droplet free energy is size-dependent, with the anchoring energy scaling with the square of the droplet radius and the elastic energy scaling in

proportion to the droplet radius. For the purpose of this chapter, we focus on the characterization of large LC droplets (>1 μm) with strong anchoring. The term strong anchoring implies that the surface chemistry at the droplet interface sets the orientation of the LC at this interface and the LC within the bulk of the droplet relaxes to a director configuration that minimizes the elastic energy of the LC. For a discussion of the influence of droplet size and weak anchoring on defect structures encountered in LC droplets, the reader is directed elsewhere.[3,16,39]

In contrast to systems containing flat films of LC, LC-in-water emulsions contain LC droplets that are diffusing (translating and rotating), resulting in the time-varying optical appearance of LC droplets. When LC droplets are characterized, it is useful to obtain multiple images of each LC droplet by using video microscopy. By imaging LC droplets in many different orientations, the full director profile of the LC confined within the droplet can be determined. In addition to diffusion, when the LC is denser than the confining aqueous medium (such as in the case of nematic 5CB in water), a second complication is that the LC droplets undergo sedimentation. Our past studies have established that the sedimentation of LC droplets onto solid surfaces (e.g., a glass microscope slide) can result in changes in the orientational ordering of the LC within the droplets.[20] Imaging of LC droplets should, therefore, be performed before a majority of the LC droplets contained in the emulsion have sedimented onto the supporting substrate (which often occurs within a few minutes of preparing a sample for observation). Finally, to ensure that the LC droplets were not perturbed by the supporting substrate, LC droplets that were at least 50 μm above the surface of the substrate and translating with velocities greater than 1 μm/s were selected for characterization in our past experiments. This distance (50 μm) is a conservative estimate based on our experimental observations and knowledge of the sizes of the LC droplets in the LC-in-water emulsions used in our studies

(diameters of 1 to 20 μm).[20,21,25] Hydrodynamic interactions between diffusing LC droplets and surfaces have not been studied in detail, although it is likely that the distance over which interactions occur will depend on the sizes of the droplets. As noted above, glycerol can also be added to the aqueous phases to increase the viscosity and slow sedimentation.

If the orientation of the LC at a droplet interface is tangential (i.e., locally planar), then the director may exhibit a so-called bipolar configuration within the droplet (Figures 2-5A through 2-5C). In a bipolar configuration, the droplet possesses two diametrically opposed point defects (called boojums; Figures 2-5A and 2-5B).[3] These point defects can be identified by their dark appearance in polarized light images (Figure 2-5B) but are more readily identified when the droplets are viewed using bright field microcopy because they scatter light, resulting in areas of high contrast compared to defect-free regions (Figure 2-5A).[18] Therefore, bright field microscopy is a useful and complementary tool to polarized light microscopy when characterizing the orientational ordering of LCs confined within micrometer-sized droplets. In brief, bright field microscopy is performed by imaging the sample following the removal of the analyzer in a polarized light microscope.

In regions of a droplet where the projected orientation of the LC is uniform along the optical path and either parallel or perpendicular to the polarizer or analyzer (crossed polarizers), the LC will appear dark. In other regions of the LC droplet, the LC will appear bright. Thus, in the polarized light micrograph of the bipolar droplet shown in Figure 2-5B the majority of the LC within the droplet appears bright. However, Figure 2-5B is only one of many appearances that a bipolar droplet can exhibit between crossed polarizers because the ordering of the LC within the bipolar configuration is not spherically symmetric. Polarized light micrographs of bipolar droplets viewed in many different orientations can be found in ref 3.

When the orientation at a LC droplet interface is homeotropic, one possible director configuration is a so-called radial configuration (Figures 2-5D through 2-5F). The radial configuration is characterized by a single point defect (or a very small disclination line in the shape of a ring) located at the center of the droplet.[3] A radial droplet possesses spherical symmetry, and thus its optical appearance is invariant upon rotation of the droplet. Finally, a polarized light micrograph of a radial droplet is characterized by a dark crosslike pattern as generated by the regions of the LC that are oriented either parallel or perpendicular to a polarizer (Figure 2-5E).

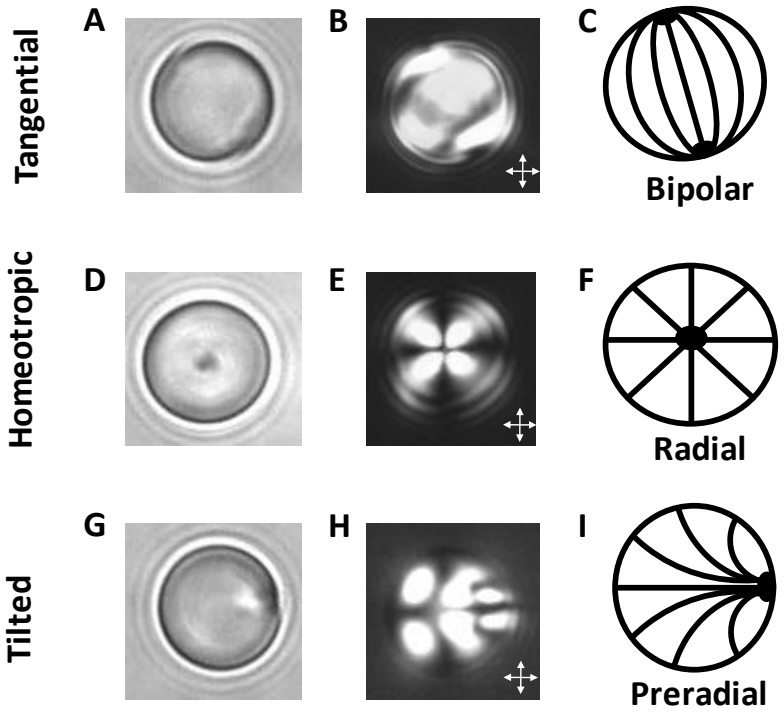

Figure 2-5. Orthoscopic bright field and polarized light micrographs of 8-μm-diameter droplets of nematic 5CB, shown as a function of the anchoring of the LC at the droplet interface.

Bright field micrographs (A, D, G), polarized light micrographs (crossed polarizer, B, E, H) and schematic illustrations of the director configurations (C, F, I) are shown, for tangential (A–C), homeotropic (D–F), and tilted (G–I) anchoring of the LC at the droplet interface. Reproduced with permission.[21]

When the orientation of the LC at a droplet interface is tilted, one possible director configuration is the so-called preradial configuration (Figures 2-5G through 2-5I). Similar to a radial configuration, the preradial configuration possesses a single point defect. However, this defect is located at the surface of the droplet rather than in the core of the droplet. Similar to a bipolar droplet, a preradial droplet does not possess the spherical symmetry characteristic of a droplet in a radial configuration, and thus many possible optical appearances are exhibited by preradial droplets, dependent on the plane of rotation of the droplets. Again, by imaging preradial droplets oriented in many different planes of rotation, the full director profile within the droplet can be characterized (Figure 2-5I).

Finally, we note that the LC droplet configurations described above represent one of many possible director configurations induced by a tangential, homeotropic, or tilted orientation of the LC at a droplet interface. The most stable director configuration for a given preferred orientation is dictated by the relative magnitudes of the elastic constants that characterize the different modes of strain within the LC droplets. The elastic constant for twist is typically smaller than the other elastic constants (for splay and bend), and thus twisted configurations of LC droplets are not uncommon. For an extensive catalog of possible director configurations for each anchoring condition, the reader is directed elsewhere.[3] Finally, in contrast to defects in planar films of LC, defects present in LC droplets are typically classified by a topological charge. This classification is somewhat more complex than assigning a strength to a defect in a planar film.[39]

2.4.2 Conoscopic Polarized Light Microscopy of Planar Films of LCs

The above sections describe how orthoscopic polarized light microscopy can be used to characterize the orientational ordering of nematic LCs at interfaces. Oftentimes, however, a complementary technique is necessary to provide an unambiguous determination of the orientation of the LC. For example, in the slab geometry, either a LC film with a uniform homeotropic orientation between confining interfaces (Figure 2-3D) or a film containing an isotropic phase of mesogens will appear dark when viewed using orthoscopic polarized light microscopy (Figures 2-6C and 2-6E). If the LC film is formed within the pores of a TEM grid, then a simple method to distinguish between these two states of a LC film is to observe the regions near the grid. As discussed in section 2.4.1.1, the regions of the LC films near the surfaces of the grids will appear bright (Figure 2-6C). In contrast to LC films with a uniform homeotropic alignment, an isotropic phase of mesogens will appear dark near the surfaces of the grids. More generally, however, conoscopic polarized light microscopy can be performed in conjunction with the orthoscopic examination to distinguish between homeotropic and isotropic states of a sample.

Figures 2-6A and 2-6B shows schematic illustrations of a polarized light microscope configured for orthoscopic and conoscopic observations, respectively. In contrast to orthoscopic examination, conoscopic examination requires, in addition to crossed polarizers, the insertion of a Bertrand lens and a substage condensing lens.[40] The substage condenser causes the sample to be illuminated by a cone of light rather than a column of light, and the Bertrand lens brings interference patterns resulting from the interaction of this cone of light with the LC film into the focal plane of the ocular lens of the microscope. The conoscopic examination of a thin film of LC in a uniform homeotropic alignment between confining interfaces will lead to an interference

pattern consisting of a dark cross overlying concentric rings (Figure 2-6D). In contrast, the conoscopic examination of an isotropic phase of mesogens will not generate an interference figure but rather will give rise to a dark optical appearance of the film (Figure 2-6F) because the polarization of the light transmitted though the isotropic film remains unchanged. If the LC is tilted slightly away from homeotropic, then the cross shown in Figure 2-6D will be displaced from the center of the image. Below we return to the analysis of conoscopic figures to provide quantitative information regarding the tilt of a LC away from the surface normal.

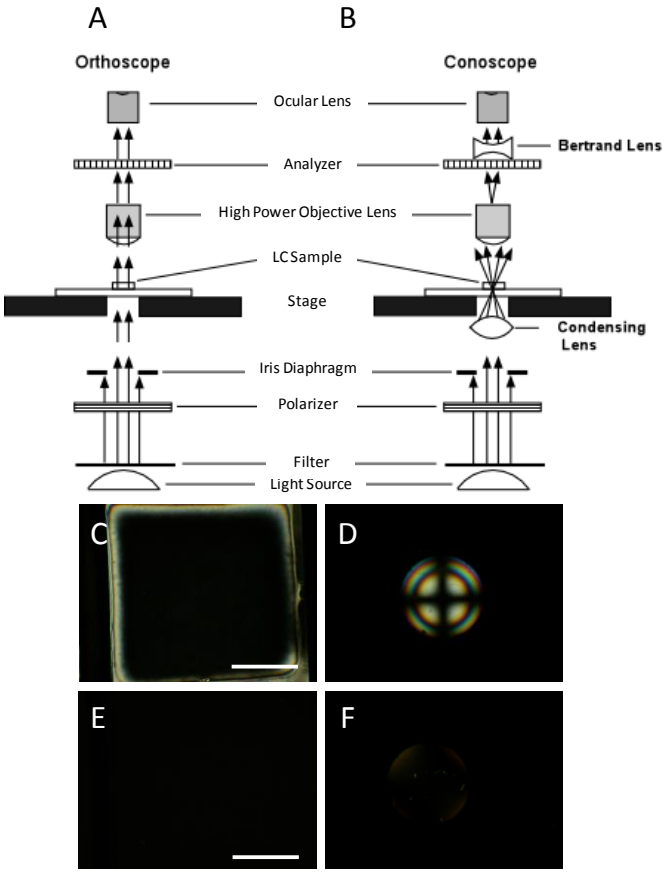

Figure 2-6. Orthoscopic and conoscopic optical microscopy.

Schematic illustrations (cross-sectional view) of the optical elements in a polarized light microscope when using (A) orthoscopic and (B) conoscopic illumination. (C) Orthoscopic and (D) conoscopic polarized light micrographs (crossed polarizers) of a LC film with a uniform homeotropic orientation. (E) Orthoscopic and (F) conoscopic polarized light micrographs (crossed polarizers) of a film of an isotropic phase of mesogens. Scale bars are 100 μm. Modified and reproduced with permission.[51]

We conclude this section by reminding the reader that a film of LC oriented in a uniform planar alignment between confining interfaces can also give rise to a dark optical appearance during orthoscopic examination with crossed polarizers. However, conoscopic examination is not necessary to distinguish between this situation and the previous two scenarios described above. Instead, if the film of LC is rotated at an angle between 0 and 90° relative to the polarizer, then the LC will exhibit a bright optical appearance (brightest at 45°). In contrast to a film containing LC in a uniform planar alignment, both a film with a uniform homeotropic alignment of the LC and a film of an isotropic material will remain dark at all angles of rotation of the sample.

2.5 Quantitation of the Orientations of LCs at Planar Interfaces

The experimental methods described above lead to qualitative information regarding the orientations of LCs at interfaces. (For example, they can indicate the presence of a tilt but do not provide the tilt angle.) In this section, we discuss optical methods that permit the quantitation of the orientations of LCs at interfaces. Obtaining quantitative information regarding the orientation of a LC at a surface, in general, requires a consideration of the director profile in a sample (that is, a description of the variation of the nematic director as a function of position throughout the sample). In this section, we will discuss the experimental methods that are used to infer both the zenithal and azimuthal orientations of LCs in thin films.

2.5.1 Quantitation of the Zenithal Orientations of LCs

First we consider the case of a LC film that exhibits a homeotropic orientation at a bottom (reference) surface. In this situation, as was shown in section 2.4.1.1, the zenithal orientation of the LC at the opposing top interface (i.e., planar, homeotropic, or tilted)

determines the optical appearance of the LC film (Figure 2-3). To quantify the orientation of the LC at the top interface of the LC film (θ_{top}, zenithal tilt angle), it is first necessary to determine both the thickness, *d*, and the optical retardance, Δr, of the LC film. Methods used to measure these two quantities are described below.

2.5.1.1 Measurement of LC Film Thickness, d

In some circumstances, where a precise measurement of θ_{top} is not required, it may be sufficient to approximate the thickness of a LC film by, for example, the thickness of a Mylar spacer[41] (slab geometry) or by the thickness of a TEM grid (aqueous—LC interface).[10] To obtain a precise measurement of the tilt angle of the LC, however, a measurement of LC film thickness will likely be required. As described below, the thickness of the LC film within a LC optical cell can be obtained through the use of a UV−vis spectrophotometer.

In the situation where a LC film is to be confined between two semireflective solid surfaces, the thickness can be measured using the interferogram generated when the cell is inserted into the light path in a UV−vis spectrophotometer (before the cell is filled with the LC or when the LC is heated to an isotropic phase). Once within the light path, the constructive and destructive interference of light partially reflected from the internal surfaces of the optical cell leads to the formation of a pattern of interference fringes. Specifically, the thickness is calculated by identifying the wavelengths of adjacent peaks (λ_i) in the interference pattern using the following equation

$$d = \frac{1}{2n}\left(\frac{1}{\frac{1}{\lambda_2} - \frac{1}{\lambda_1}}\right) \qquad (2\text{-}1)$$

where n is the index of refraction of the medium in the optical cell (for the case of an air-filled cell, $n = 1$).

When a LC film has a free interface (*e.g.*, an aqueous—LC interface), measuring the thickness of the LC film is not as straightforward as in the case of a LC film confined between two solid surfaces. In the former situation, one approach is to measure the LC film thickness by decorating the aqueous interface of the LC with a few microparticles and by scratching the surface of the supporting solid substrate (before contacting the LC with the surface).[21] By locating the focal plane of the microscope on the features on both interfaces of the LC and by calibrating the notches on the fine focus knob of the microscope, the distance between the two interfaces of the LC can be determined by moving the focus from the bottom surface to the top interface of the LC film. The theoretical accuracy of this method is limited by the numerical aperture (NA) of the objective used. (The limit of the out-of-plane resolution of a microscope objective is proportional to $1/NA^2$.) We estimate, in practice, that this method permits the determination of the LC film thickness within ±1 μm when using a 50× objective with NA = 0.5 (on an Olympus BX60 microscope).

2.5.1.2 Measurement of LC Film Optical Retardance, Δr

The optical retardance, Δr, of a LC film is the integrated effect of the LC birefringence and the optical path length experienced by light transmitted through the film. As described in section 2.4.1.1, upon entering a LC film with hybrid boundary conditions, light refracts into two components (ordinary and extraordinary rays) that travel at different velocities through the film. The relative phase shift between these two rays upon exiting the LC medium is referred to as the

optical retardance. As described below, this quantity can be measured through the use of a compensator, a Polscope, or it may also be estimated through the use of a Michel-Levy chart.

Compensators are instruments that shift the phase of light to exactly offset, or compensate for, the retardance of a birefringent sample. Although many different types of compensators exist and can be used to determine the retardance of a sample, here we discuss the Berek U-CTB compensator because it is a commonly used compensator. A Berek compensator consists of a birefringent calcite plate that can be precisely tilted to generate a desired (compensating) optical retardance (Figure 2-7). To use this instrument to determine the retardance of a LC film, one must first place the sample on a circular stage and examine the film between crossed polarizers using a polarized light microscope. It is then necessary to identify and focus on a region of the film where the LCs locally exhibit a uniform azimuthal orientation. The stage is then rotated until the observed region of the film attains extinction (i.e., appears dark). Note that if the confining interface does not give rise to an overall preferred azimuthal orientation, as is the case for the interface between a LC and water, then regions of local uniform azimuthal alignment can be conveniently identified by the location of dark brushes. Next, the stage is rotated clockwise 45° and clamped into place (Figure 2-7C). The Berek compensator crystal is then inserted into the optical path above the sample but beneath the analyzer with its drum initially set to 30°. Subsequently, the angle adjustment dial of the compensator is slowly rotated in one direction, which leads to the appearance of a number of brightly colored fringes passing through the sample. The dial should continue to be rotated until a single black fringe intersects the center of the field of view (Figure 2-7D). This angle (θ_1) is recorded from the compensator. The dial is then rotated in the opposite direction, past 30°, until a second black fringe appears at θ_2 (Figure 2-7E). If no colored fringes are observed during this process, then

rotate the stage counterclockwise 90°, reclamp it, and repeat the procedure described above. If a black fringe is still not observed to intersect the center of the field of view, it is possible that the retardation of the LC film exceeds that which is measurable by the Berek compensator. After the measurement of these angles, the angle $\theta = |\theta_1 - \theta_2|/2$ is calculated and used to determine the retardance of the LC film (each compensator is accompanied by a reference table that reports the retardance as a function of this angle, Figure 2-7B).

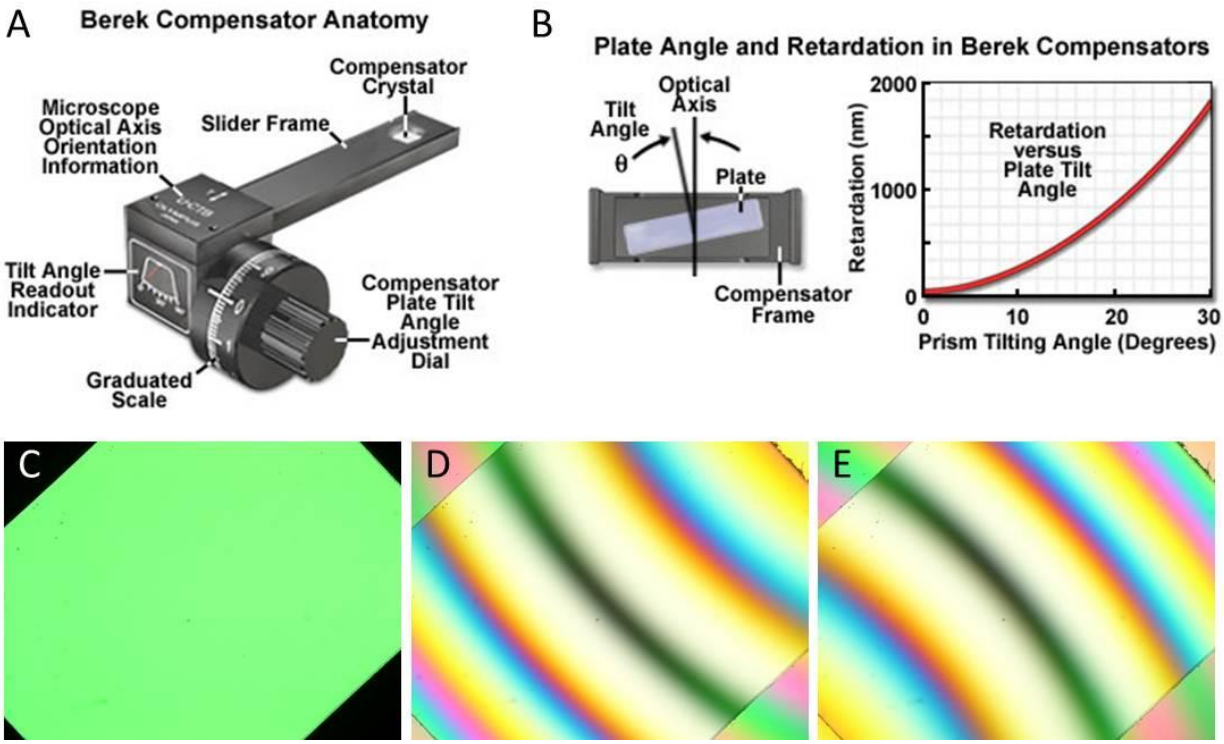

Figure 2-7. Measurement of optical retardance using a Berek compensator.

(A) Schematic illustration of a Berek compensator. (B) Illustration of the calcite crystal within a Berek compensator, and the tilting of the crystal to introduce compensating retardance into the optical path. (C) Polarized white light micrograph of a birefringent LC sample viewed between crossed polarizers when rotated by 45° from extinction. (D, E) Optical images following insertion of a Berek compensator into the optical path and subsequent rotation of the compensator dial, both forward (D) and backward (E), to locate a black fringe in the middle of the image. Reproduced with permission.[52]

An alternative way to measure the optical retardance of a LC film is through the use of a retardance mapping instrument such as the CRI PolScope.[15] This instrument operates by illuminating a sample with circularly polarized light (λ = 546.5 nm). After passing through the sample, the light is collected by a LC compensator and imaged through the use of a CCD camera. This instrument is capable of mapping the retardance of a sample over a large spatial area and can determine retardance values of between 0 and 273 nm (i.e., λ/2) to a precision of 0.02 nm. A limitation of this technique is that it cannot be used to measure the absolute value of the retardance of a sample when the retardance exceeds 273 nm. (The Polscope reports retardances above 273 nm with an ambiguity on the order of the retardation.) The Polscope is best utilized either for analyzing small spatial variations in the retardance of a sample or for calculating exact retardance values in cases when the approximate retardance of the sample is already known.

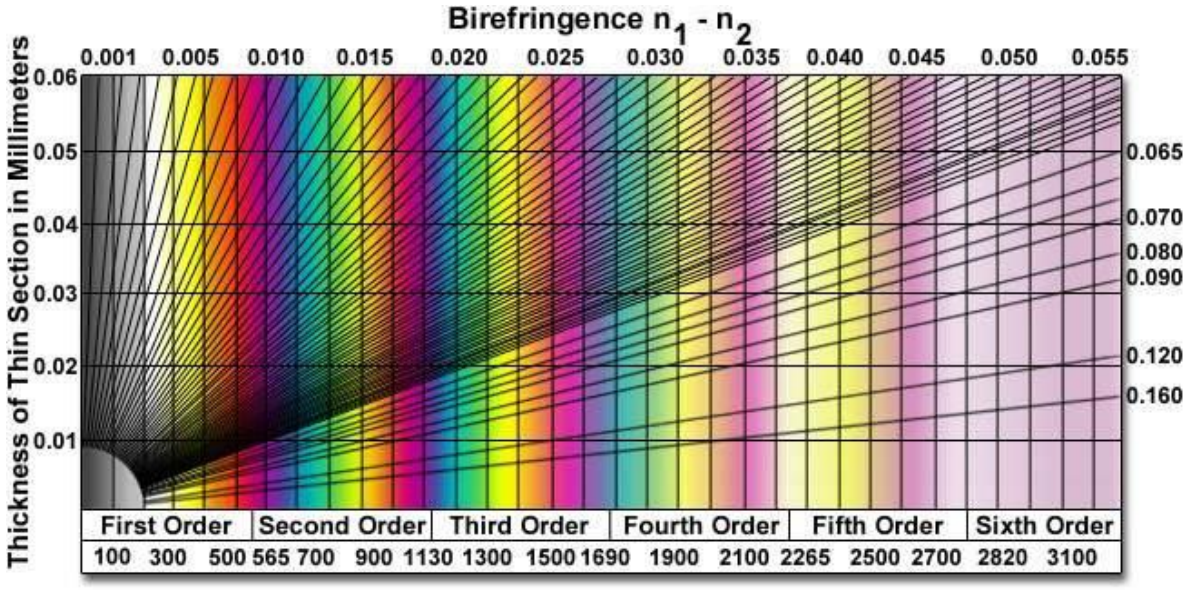

Figure 2-8. Michel-Levy color chart.

The chart relates sample thickness, optical retardance and effective birefringence of optically anisotropic materials to colors observed when using crossed polarizers and white light illumination. Optical retardance (in nm) is given at the bottom of the chart. Reproduced with permission.[53]

Finally, we comment that a comparison of the interference colors observed in a LC sample (when imaged between crossed polarizers using white light) with those found in a Michel-Levy chart (Figure 2-8) can be used to estimate the retardance of a thin film of LC. However, the precision of this method can be low, especially for high optical retardances (>1500 nm), because individual interference colors can correspond to broad ranges (~300 nm) of retardance values. The interference colors also become increasingly washed out at high orders. We note that the Michel-Levy chart can also be utilized to estimate the thickness of a LC film when the orientation of the LC is known.

2.5.1.3 Determination of the Zenithal (Tilt) Angle

As mentioned above, the zenithal orientation of a LC (θ_{top}) at the upper interface of a LC film can be determined from the measurements of the retardance and film thickness. The evaluation of θ_{top} is based on a model of the director profile across the thickness of the LC film, which is typically determined by the minimization of an expression for the elastic free energy of the thin LC film.[7,11,15] The elastic free energy density of a LC, as described by the Frank−Oseen expression, is

$$F_{\text{elastic}} = \frac{1}{2}\left[K_{11}(\nabla \cdot n)^2 + K_{22}(n \cdot \nabla \times n)^2 + K_{33}(n \times \nabla \times n)^2 - K_{24}\nabla \cdot \left(n \times \nabla \times n + n(\nabla \cdot n)\right)\right] \quad (2\text{-}2)$$

where n is the director of the LC and K_{11}, K_{22}, K_{33}, and K_{24} are the elastic constants for splay, twist, bend, and saddle-splay deformations, respectively.[34] An additional term containing K_{13}, the splay−bend elastic constant, is not included in Equation 2-2 because it contains higher-order derivatives of n. The term containing K_{24} is also often neglected, although it clearly plays an

important role in some geometries, including spherical LC droplets.[3,16,21,25] Finally, a one elastic constant approximation ($K_{11} = K_{22} = K_{33} = K$) of the full Frank–Oseen expression[3,34] is often used to simplify Equation 2-2 further, although we note that there are instances where this simplification does not capture the experimental behavior of the LC.[16,25] The use of the one-constant approximation reduces the expression for the elastic free energy density of the film to

$$F_{\text{elastic}}(\theta, \dot{\theta}) = \frac{1}{2} K \dot{\theta}^2 \qquad (2\text{-}3)$$

Minimization of the elastic free energy of the LC slab geometry leads to the result that the tilt of the LC varies linearly with position across the film

$$\theta(z) = \frac{z}{d}\left(\theta_{\text{top}} - \theta_{\text{bottom}}\right) + \theta_{\text{bottom}} \qquad (2\text{-}4)$$

For the situation where the orientation of the LC on the bottom substrate is strong and homeotropic ($\theta_{\text{bottom}} = 0°$), the relationship between the optical retardance of the LC film of thickness d and the tilt angle at the top interface (θ_{top}, measured from the surface normal) is given by

$$\Delta r \approx \int_0^d \left(\frac{n_{\text{o}} n_{\text{e}}}{\sqrt{n_{\text{o}}^2 \sin^2\left(\frac{z}{d}\theta_{\text{top}}\right) + n_{\text{e}}^2 \cos^2\left(\frac{z}{d}\theta_{\text{top}}\right)}} - n_{\text{o}} \right) \mathrm{d}z \qquad (2\text{-}5)$$

in which n_{o} and n_{e} are the indices of refraction perpendicular and parallel to the optical axis of the LC, respectively.[7,11,15] The solution of this equation to obtain the experimentally measured value of Δr yields θ_{top}. The interested reader is referred elsewhere to a detailed derivation of the equations for Δr and $\theta(z)$.[7]

To illustrate the relative precision of estimates of θ_{top} obtained using a compensator versus the Michel-Levy chart, we consider the following example. The retardance of a sample composed of a 20-μm-thick film of nematic 5CB (ne = 1.711 and no = 1.5296)[22] with strong

homeotropic orientation on the bottom reference surface was measured using a compensator in our laboratory to be Δr = 1055 ± 14 nm. The solution of Equation 2-5 for θ_{top} yields θ_{top} = 63.0 ± 0.5°. For comparison, from the Michel-Levy chart (Figure 2-8), it can be seen that such a film would possess pink interference colors when imaged between crossed polarizers using white light. However, the chart also shows that the pink interference color will be observed for all Δr values between ~1020 and 1100 nm. Therefore, if only the Michel-Levy chart was used to estimate θ_{top} in this particular sample, then θ_{top} could only be determined to lie between 61.7 and 64.6°.

Finally, we note that conoscopy can also be used to determine θ_{top}, particularly when the director is tilted only slightly from a homeotropic orientation. As noted above, the conoscopic examination of a thin LC film with uniform homeotropic alignment yields an interference figure consisting of a dark extinction cross overlying concentric rings in the center of the field of view. In the case of a LC film that tilts slightly from the homeotropic orientation, the dark cross will be shifted from the center of the field of view. The measurement of the position of the cross, when combined with a knowledge of the refractive indices of the LC, can be used to obtain α_o, the angle between the surface normal and the center of the interference figure through use of Mallard's equation

$$\frac{r}{R}\mathrm{NA} = \langle n \rangle \sin \alpha_o \qquad (2\text{-}6)$$

where r is the distance between the center of the field of view and the center of the cross, R is the radius of the field of view, NA is the numerical aperture of the objective, and $\langle n \rangle$ is the average refractive index of the sample.[44] The tilt angle is then given by

$$\theta_{top} = 90° - \alpha_o \qquad (2\text{-}7)$$

We refer the reader to a prior publication for a complete description of this method.[44]

2.5.2 Quantitation of Azimuthal Orientations of LCs

In this section, we describe how the azimuthal orientation of a LC can be quantified for the experimental situation in which the LC film is sandwiched between two contacting solid surfaces, each of which induces different azimuthal orientations in the LC. The distinct azimuthal orientation of the nematic LC at each of the two confining surfaces will lead, in general, to the formation of a twist distortion within the LC (Figure 2-9A). Depending on the azimuthal anchoring energy (W_a) at each of the confining surfaces and the elastic energy stored in the bulk resulting from the twist deformation, the LC director at one or both surfaces may depart from the easy axis.[14] Figure 2-9A depicts a case in which the easy axes of the LC at the two confining surfaces are aligned orthogonal to one another and a strong azimuthal orientation of the LC on the bottom reference surface prevents the LC director from deviating from the easy axis on the bottom surface.[6] However, weak anchoring of the director to the top surface allows the LC director to deviate from the top easy axis, decreasing the twist distortion across the film (characterized by the twist angle, Ψ).

The twisted nematic LC (TNLC) described above acts as a waveguide. Thus, polarized light propagating through the LC film follows the twist of the LC director provided the Mauguin condition, $\lambda \ll (n_e - n_o)P$, is satisfied,[34] where P, the pitch of the LC, is equivalent to $4d$ and d is the thickness of the film for a 90° twist.[34] This condition is satisfied in LC films that are tens of micrometers in thickness.

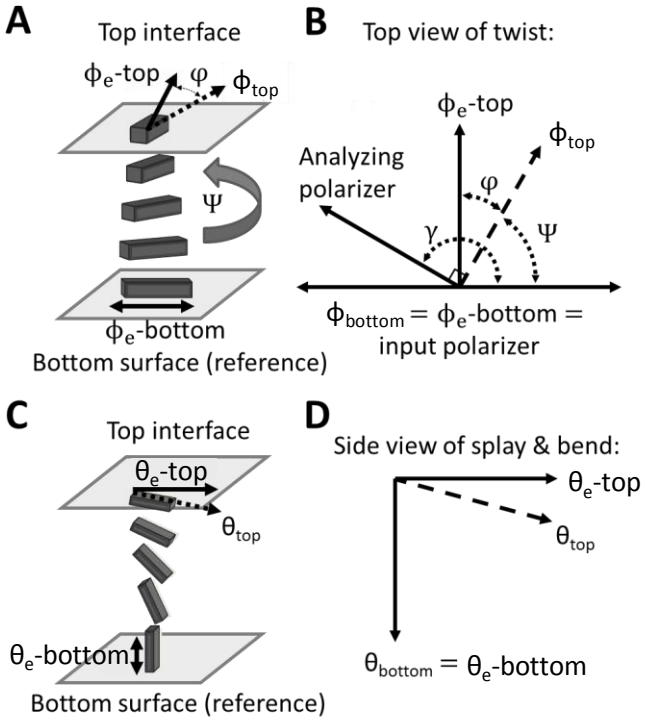

Figure 2-9. Experimental set-ups and angle diagrams used to determine azimuthal (A and B) and zenithal (C and D) anchoring energies.

(A) Schematic illustration of a twisted nematic LC (TNLC). (B) Diagram depicting the angles used to characterize the TNLC between two polarizers. The azimuthal orientation of the easy axis of the LC (defined by Φ_e) and the azimuthal orientation of the LC director (defined by Φ) are shown for both the top and bottom surfaces. (C-D) Schematic illustrations and corresponding definitions of angular displacements of the director in a LC film with planar-homeotropic hybrid anchoring conditions. The bottom surface is assumed to cause strong homeotropic anchoring and is used as a reference surface. The orientation of the easy axis of the LC at the top surface is characterized by the zenithal angle θ_e, and the orientation of the LC director is characterized by θ. Modified and reproduced with permission.[14]

With reference to Figure 2-9B, to determine Ψ, it is first necessary to determine the angle between the analyzer and source polarizer corresponding to the minimal transmission of polarized light (angle γ). A determination of γ requires that the easy axis of the LC on the bottom reference surface be aligned parallel to the input polarizer. This can be accomplished by the use of reference regions within the TNLC cell, corresponding to regions of the upper substrate that

have been patterned such that the easy axis is parallel to that of the reference surface.[24] Within these regions, the LC film will have a uniform zenithal and azimuthal alignment. However, even in the absence of these reference regions, the reference surface of a TNLC cell can be properly aligned because the complete extinction of transmitted light will be observed upon the rotation of the analyzer only when the easy axis of the reference surface is aligned parallel to the input polarizer. In this situation, the TNLC cell is placed on a microscope stage between crossed polarizers with the input polarizer facing the reference surface, and the sample is subsequently rotated between the stationary polarizers to minimize light transmitted through the sample. Subsequently, the analyzer is rotated to further minimize the light transmitted through the sample. Three iterations of this procedure are typically sufficient to obtain extinction.[24] This procedure can be conveniently performed by capturing optical images of the TNLC at regularly spaced intervals of the sample or analyzer orientation (Figure 2-10A). Image processing is then used to determine the mean luminosity of the LC in each image, and this data can be plotted as a function of analyzer position (Figure 2-10B). The magnitude of light transmitted through the twisted LC film can be fit to a function of the form[14,45]

$$f(x) = A\cos^2(x - x_o) \qquad (2\text{-}8)$$

to determine γ. The twist angle, Ψ, can then be obtained from γ using the angle diagram depicted in Figure 2-9B. For the case of interest, when the easy axes of the two confining substrates are orthogonal to one another, the relationship is

$$\Psi = \gamma - 90° \qquad (2\text{-}9)$$

where Ψ is constrained to be between -90 and $+90°$.[14,45]A generalization of this expression for TNLC cells in which the easy axes are not orthogonal can be found elsewhere.[14,45]

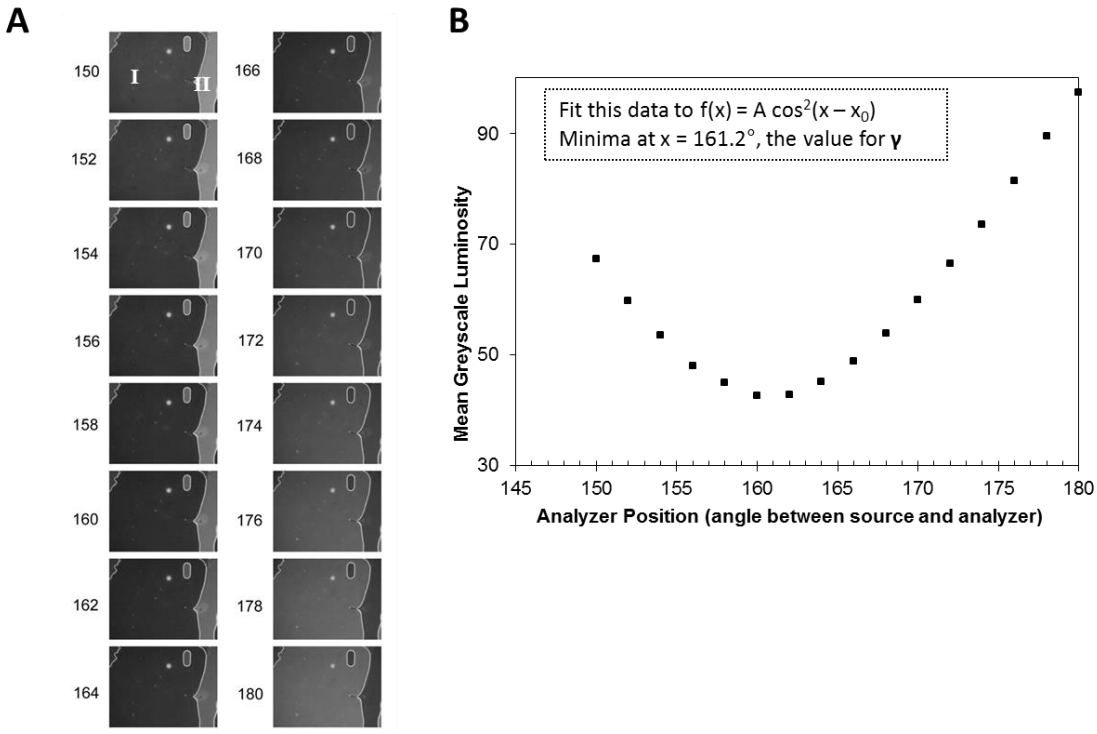

Figure 2-10. Measurement and analysis of the intensity of light transmitted through a twisted LC to determine the angle γ (definition in the text).

(A) Optical images (polarized white light) captured for the TNLC cell as a function of analyzer position (i.e., "crossed polarizers" correspond to 90°). (B) Mean luminosity of a domain within the LC sample, plotted as a function of analyzer position. The data was fit to a cosine squared function (inset) to provide an accurate determination of the minimum. The angle at which the minimum occurs corresponds to γ. Reproduced with permission.[14]

Finally, we note that a pixel-by-pixel quantitation of the twist angle within a TNLC cell (i.e., azimuthal orientation of LC on the top surface relative to the bottom surface) can also be performed using methods adapted from those described above.[23] For example, Figure 2-11 shows a high-resolution map polarized light micrographs.[23] We also note that the quantification of the orientations of LCs in spherical geometries (i.e., LC-in-water emulsions) is more difficult than in the slab geometry described above. In general, quantitative information about the orientations of LCs at the interfaces of LC droplets is obtained by comparing the optical textures of droplets

calculated from simulations to experimentally obtained polarized light micrographs.[3] We caution that the procedure is laborious and can be ambiguous.

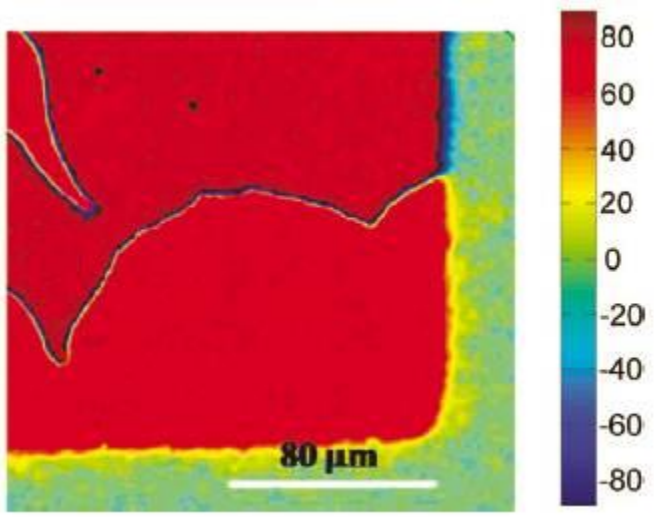

Figure 2-11. Optical map depicting spatial variation of the twist angle within a LC that is anchored on a chemically patterned surface.

The color chart shown at the right side of the figure indicates the twist angle. Measurement of the position-dependent twist angle of the LC can be used to image chemical patterns on surfaces (see text for details). Reproduced with permission.[23]

2.6. Measurements of Anchoring Energies

The measurement of the anchoring energy of a LC can provide fundamental insight into the intermolecular interactions responsible for the orientations of a LC at a particular interface, and it is also a technologically important quantity because it often determines the response of a LC to a stimulus (e.g., electric field) or adsorbate. In the context of using LCs to report interfacial phenomena, measurements of changes in the anchoring energy can be substantially more sensitive than measurements of changes in the easy axis.[9,14,23] Below, we describe methods that permit the measurement of anchoring energies at a variety of LC interfaces.

2.6.1 Quantification of Anchoring Energies of LCs at Planar Interfaces

A number of methods exist to measure the anchoring energy of a LC at an interface.[3,7,14,21,23-25,34] In general, the methods involve the application of a perturbation to the LC and the measurement of a response that is dictated by the anchoring energy. One common approach is to design the LC to be elastically strained (deformed in the bulk) such that the torque generated by the strain in the LC causes the LC to deviate from the easy axis at the surface of interest. The magnitude of the angular deviation of the LC from the easy axis permits an evaluation of the anchoring energy. We note that this approach requires a knowledge of the orientation of the easy axis of the LC. When characterizing LCs in slab geometries, the torque generated by a thick film will be small, and thus experiments performed with thick LC films (i.e., $d \approx 50$ μm) are typically used to determine the orientation of the easy axis of the LC. Conversely, measurements using thin LC films will yield orientations of the LC at the confining surfaces that deviate from the easy axes (because of the torque associated with the strain of the LC) and thus provide access to anchoring energies of LCs.

2.6.1.1 Governing Equations Used to Determine Anchoring Energies.

The orientation-dependent interfacial energy, f_{S}, of a LC is often described by the Rapini−Papoular expression,[7,46] namely,

$$f_{\mathrm{S}} = \frac{1}{2} W_{\mathrm{z}} \sin^2(\theta - \theta_{\mathrm{e}}) + \frac{1}{2} W_{\mathrm{a}} \sin^2(\phi - \phi_{\mathrm{e}}) \qquad (2\text{-}10)$$

where subscripts z and a denote zenithal and azimuthal quantities, respectively. We consider first an experiment performed in a thin film geometry that is designed to provide values for W_{z}. We then generalize the result to allow the determination of W_{a}. For simplicity, we assume that the

magnitude of the elastic constants for splay, bend, and twist are equal (the so-called one-constant approximation discussed above). The experimental system comprises a bottom confining surface (reference surface with strong anchoring) and a top surface at which the anchoring energy is to be determined. As described below, minimization of the free energy of the system using the one elastic constant expression for the elastic energy and the Rapini−Papoular expression for the interfacial energy at the top surface results in a simple expression for W on the top surface. In brief, Equations 2-3, 2-4, and 2-10 are inserted into the expression for the free energy of the LC film

$$F = \int_0^d F_{elastic}(\theta, \dot{\theta}) dz + \underbrace{f_{S1} + f_{S2}}_{F_{Surface}} \qquad (2 - 11)$$

to yield

$$F(\theta_{top}) = \int_0^d \frac{K}{2}\left(\frac{\theta_{top} - \theta_{bottom}}{d}\right)^2 dz + \frac{1}{2} W_z \sin^2(\theta_{top} - \theta_e) + f_{S2} \qquad (2 - 12)$$

where θ_{top} and θ_{bottom} are the zenithal angles defined by the director at the top and bottom interfaces, respectively (Figure 2-9), and θ_e defines the orientation of the easy axis of the LC at the top interface. The minimization of this free energy with respect to the orientation of the LC at the top interface yields the expression

$$W_z = \frac{2K(\theta_{top} - \theta_{bottom})}{d \sin\left(2(\theta_e - \theta_{top})\right)} \qquad (2 - 13)$$

For the measurement of the azimuthal anchoring energy, a twisted nematic LC cell is used. By using the twist elastic constant (i.e., $K = K_{22}$) and by redefining the angles in the system, we reach the commonly used torque balance expression ($\phi_{top} - \phi_{bottom} = \psi$ and $\phi_e - \phi_{top} = \varphi$, see Figure 2-9):[14,23]

$$W_{\mathrm{a}} = \frac{2K_{22}\psi}{d\sin(2\varphi)} \qquad (2\text{-}14)$$

2.6.1.2 Measurement Technique

To use Equation 2-14 to determine the azimuthal anchoring energy at a LC−solid interface, the thickness of the LC film (section 2.5.1.1) and the twist angle of the LC (section 2.5.2) are measured. Figure 2-12 shows the relationship among the LC film thickness, twist angle, and anchoring energy calculated using Equation 2-14 (using $K_{22} \approx 3.8$ pN).[24,47] From Figure 2-12, we make a couple of observations. First, the twist angle varies significantly with anchoring energy for values of W that are less than ~0.5 μJ/m^2 for thick films (d = 50 μm) and less than ~2 μJ/m^2 for thin films (d = 4 μm). For larger values of the anchoring energy, the torque generated by the elastic energy stored in the LC film is insufficient to cause easily measured deviations of the LC orientation from the easy axis at the interface. The range of anchoring energies that can be measured by this method is therefore relatively limited (0.5−2.0 μJ/m^2). Outside of this range of anchoring energies, the uncertainty associated with the measured anchoring energies will be larger because small changes in the twist angle correspond to large changes in the anchoring energy (Figure 2-12B).[24] Specifically, for a surface with an anchoring energy of 5 μJ/m^2, if characterized with a LC film with a thickness of 50 μm and a LC orientation measured with a precision of ±0.5°, the uncertainty in the anchoring energy would be approximately ±2 μJ/m^2.

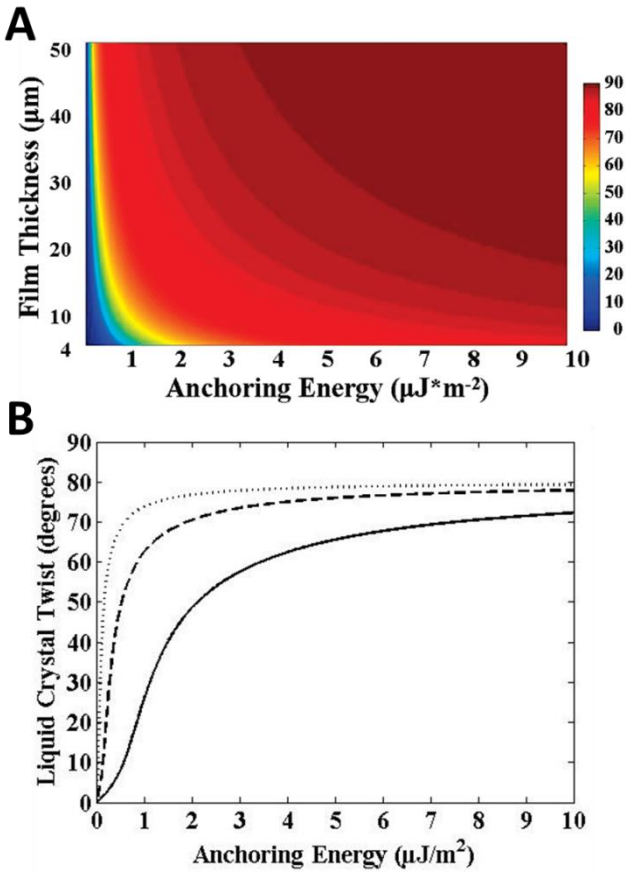

Figure 2-12. Twist angles of LCs calculated from the torque-balance equation (details in the text). Results shown are for 5CB and assume that the orientations of the easy axes (in plane of surface) at the confining surfaces are separated by 80°. (A) LC twist angles plotted as a function of anchoring energy and LC film thickness. (B) Plots of LC twist versus azimuthal anchoring energy for LC films thicknesses of 50 μm (dotted line), 16 μm (dashed line), and 4 μm (solid line). Reproduced with permission.[24]

An implementation of Equation 2-13 forms the basis of the measurement of the zenithal anchoring energy. To illustrate this method, we describe the measurement of the zenithal anchoring energy at a free interface of a LC film, such as the LC−aqueous interface. Here we assume that the anchoring of the LC at the bottom reference surface is strong and homeotropic. As with the example described above, it is first necessary to determine the thickness of the LC film (details in section 2.5.1.1). Next, the measurement of the retardance of the LC film is performed using a compensator (section 2.5.1.2). By solving Equation 2-5, it is possible to

determine the tilt of the LC at the LC−aqueous interface and, using Equation 2-13, to determine the zenithal anchoring energy. The challenges associated with this method include the measurement of the thicknesses of LC films with free interfaces (such as a LC−aqueous interface). For example, a LC film of thickness 7 ± 1 μm and measured retardance of 475 ± 10 nm leads to an estimate of W that lies between 2 and 16 μJ/m^2 (using K = 6 pN). When performing measurements of the anchoring energies of LCs at LC−aqueous interfaces, it is also important to understand that the pH and the ionic content of the aqueous phase play important roles in determining the anchoring energy.[12,13]

We end this section by commenting that the above analysis assumes that the film thickness (d) is large compared to the extrapolation length ($L/d \ll 1$, where L is the extrapolation length, defined in section 2.2, at the top surface). As described earlier, this means that the LC film thickness is large enough that it leads to relatively small deviations of the director from the easy axis. In experiments in which the LC film thickness is comparable to the extrapolation length at the top surface ($L/d \approx 1$) and the anchoring of the LC on the bottom surface is strong and homeotropic, the determination of the film thickness at which the entire film becomes homeotropic provides the basis of another method to estimate the anchoring energy of the LC at the top surface.

2.6.2 Anchoring Energies in LC-in-Water Emulsions

The determination of the anchoring energy of a LC at the aqueous interface of a LC droplet can be achieved by exploiting the elastic energies generated by the confinement of the LCs to the droplets. As mentioned in section 2.4.1.2, the relative importance of surface and elastic contributions to the free energy of a LC droplet is dependent on the size of the LC droplet.

This scaling can be used to determine anchoring energies based on observations of size-dependent ordering in LC droplets. For large droplets dispersed in an aqueous medium where the easy axis is tangential to the droplet interface, the surface energy will be dominant and LC droplets will assume a bipolar configuration. In contrast, for small droplets, the elastic energy of the LC in the volume of the droplet becomes dominant and causes a transition to a radial configuration (Figure 2-13).[16] By observing the size at which droplets spontaneously transition to radial ordering, one can estimate the anchoring energy at the LC−aqueous interface for the LC emulsion system. Specifically, as described elsewhere, the free energies of a bipolar droplet and a radial droplet (both with an easy axis tangential to the LC interface) can be approximated as[25]

$$F_{\mathrm{Bp}} = 5\pi K_{11} R - 2\pi K_{24} R \qquad (2\text{-}15)$$

$$F_{\mathrm{R}} = 8\pi K_{11} R - 4\pi K_{24} R + 2\pi W R^2 \qquad (2\text{-}16)$$

and by setting Equation 2-15 equal to Equation 2-16, we can write the anchoring energy as

$$W = \frac{K_{24} - \frac{3}{2} K_{11}}{R_c} \qquad (2\text{-}17)$$

where R_c is the size of the LC droplets at which the transition from radial to bipolar configurations takes place. Although this method appears to be straightforward to implement, we make three comments regarding its use. First, Equations 2-15 and 2-16 are approximate, and thus Equation 2-17 provides only an estimate of the anchoring energy. Second, it relies on a knowledge of K_{24}, and there is substantial variation in the estimates of this elastic constant in the literature. Third, for LC−aqueous interfaces, commonly encountered anchoring energies lead to values of R_c that can be below the resolution of an optical microscope. For example, we measured R_c to be 400 nm (using a 100× objective) for droplets of nematic 5CB in contact with

aqueous solutions. By using K_{11} = 6.4 pN and $K_{24} = 1.53K_{11}$, we arrived at an estimate of W of ~0.5 μJ/m^2.[16,25] Values of W higher than ~1 μJ/m^2 will involve even smaller values of R_c.

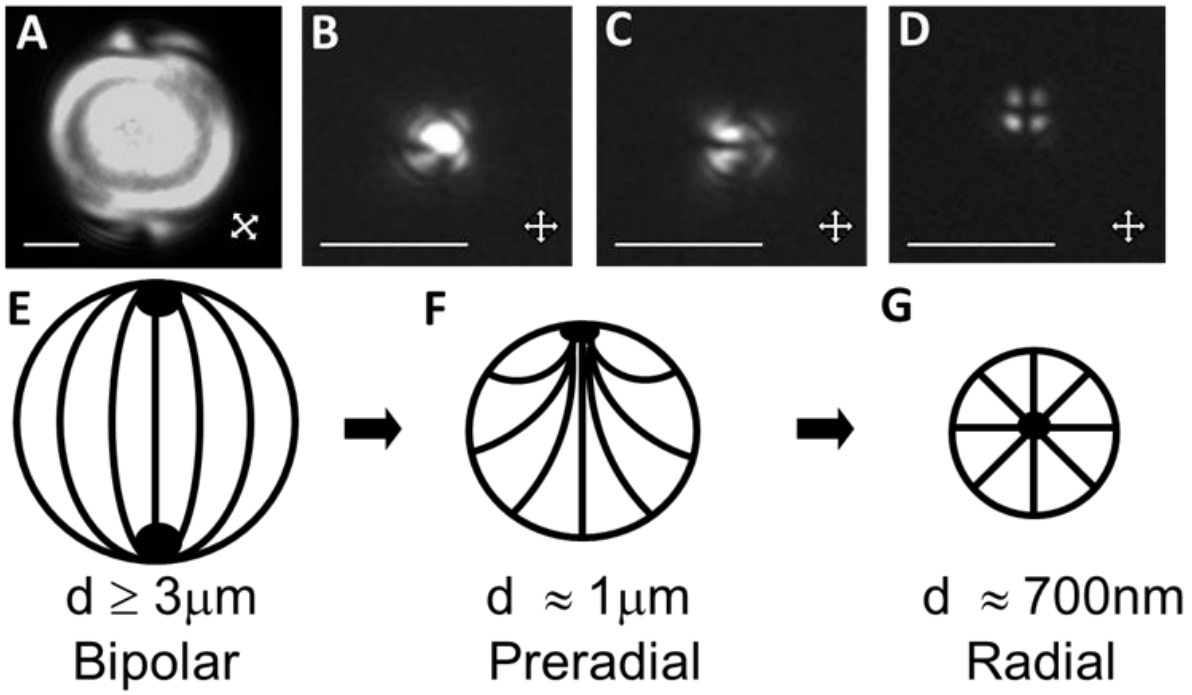

Figure 2-13. Optical micrographs and schematic illustrations of the configurations of LCs within LC droplets, shown as a function of LC droplet size (with constant surface chemistry).

(A-D) Polarized light micrographs (crossed polarizers) of 5CB droplets hosted within polymer capsules with diameters of (A) 8.0 ± 0.2 μm, (B, C) 1.0 ± 0.2 μm, or (D) 0.70 ± 0.08 μm. (E-G) Schematic illustrations of bipolar (E), preradial (F) and radial configurations (G) of LCs, corresponding to the micrographs in A, B and C, and D, respectively. Scale bars are 2 μm in A-C and 1 μm in D. Modified and reproduced with permission.[16]

2.7. Unresolved Challenges and Cautions

Before concluding this chapter, we briefly discuss some unresolved challenges and cautions related to the optical characterization of LC interfaces. We present the challenges with the hope that they might define topics of research for new researchers entering the field. The cautions are presented with the goal of alerting new researchers to some of the potential pitfalls when characterizing LC interfaces.

Our first comments involve the characterization of LC droplets. As discussed above, this area of research is a fertile one (for example, as the basis of biological sensors), yet the characterization of the interfaces of LC droplets remains relatively difficult. As noted in section 2.4.1.2, micrometer-sized LC droplets in LC-in-water emulsions typically translate with velocities greater than 1 μm/s both in and out of the focal plane of a microscope. This makes the imaging of LC droplets a challenge.[20,21,25] Past attempts by us and others to address this issue include the immobilization of LC droplets on chemically tailored solid surfaces.20 The immobilization of the LC droplets, however, perturbs the ordering of the LC within the droplets.[20] An alternative approach (as described above) is to add glycerol to the aqueous phase to increase the viscosity of the aqueous phase and thus slow the motion of the LC droplets. Although this approach does decrease the velocity of the droplets, it also has the potential to change interfacial phenomena occurring in LC-in-water emulsion systems (e.g., adsorbate-induced ordering transitions involving biological molecules) substantially. In addition, we emphasize that in general it is particularly difficult to obtain quantitative information about the orientations of LCs at the interfaces of droplets. Current procedures typically involve calculations of the optical appearance of droplets from the results of simulations and comparisons of the calculated optical appearance to experimentally obtained polarized light

micrographs. These procedures are laborious and can be ambiguous.[3] Overall, there exists an unmet need for the development of general and facile optical methods that permit the quantitative characterization of LC-in-water droplets. Advances in microfluidic technologies and associated single-particle optical techniques (e.g., flow cytometry) might form the basis of such techniques.

We also offer a few cautions for new researchers working in this field. The first caution relates to the purity (and stability) of LCs. LCs, although often provided by manufacturers at high purity, can degrade if not handled correctly (e.g., exposed to sunlight from a window).[49] The degradation of a small fraction of the molecules within a LC sample can quickly change the interfacial ordering of the LC if the degradation products are surface-active. Therefore, care must be taken to avoid the degradation of the LC or the introduction of impurities from materials that contact the LC (e.g., water that forms the basis of a LC−aqueous interface). A second caution that we offer here relates to the characterization of LC−aqueous interfaces. This is a so-called buried interface that is relatively difficult to characterize when decorated, for example, by a biological analyte such as a lipid that triggers an anchoring transition within the LC. A common approach is to add to the adsorbate a small amount of a fluorescent marker and perform fluorescence microscopy in parallel with both bright field and polarized light optical microscopy.[6,7,18,20,21] We and others have observed that the presence of fluorophores at the LC interface can substantially change the ordering of the LC.[7] The development of spectroscopic methods that do not require the use of labels and can be used to characterize buried interfaces (e.g., nonlinear optical methods) is a promising area of ongoing research.

2.8 Conclusions

This chapter presents an introductory-level description of widely accessible optical methods that can be used to characterize the orientations of LCs at interfaces. These methods can be used to characterize the orientations of LCs at planar interfaces (LC− solid and LC−aqueous) as well as the curved interfaces of LC- in-water emulsion droplets. All of the methods described in this chapter can be performed on a standard polarized light microscope with white-light illumination and a Bertrand lens. In addition, we describe optical methods that permit the measurement of the anchoring energies of LCs at interfaces. Such measurements can provide important insights into interfacial phenomena occurring at LC interfaces that do not give rise to changes in the easy axes of LCs. Overall, the methods described in this chapter enable studies of LC interfaces relevant to electro-optical devices, materials synthesis, biological liquid crystals, and the design of stimuli-responsive LC systems suitable for chemical and biological sensing.

Acknowledgements

This work was primarily supported by the NSF through DMR-1121288 (Materials Research Science and Engineering Center) and DMR-0425880, the Army Research Office (W911NF-11-1-0251 and W911NF-10-1-0181), and the National Institutes of Health (CA108467, CA105730, and 5T32GM08349). N.L.A. also acknowledges the support of research relevant to this review from the Department of Energy, Basic Energy Sciences, Biomaterials Program (DESC0004025).

2.9 Supporting Information

Physical properties of LCs

Property	5CB[b]	E7[c]	TL205[d]
K_{11} (pN)	6.3	11.7	17.3
K_{22} (pN)	3.9	8.8	-
K_{33} (pN)	8.3	19.5	20.4
T_{NI} (°C)	35	58	87.4
Δn	0.212	0.2255	0.2175
n_e	1.742	1.7472	1.7445
n_o	1.530	1.5217	1.527
Δε	20.1	14.1	5

Table 2-S1. Physical properties of the LCs displayed in Figure 2-1A of the main text (4-cyano-4'-pentylbiphenyl (5CB), E7 and TL205).[a]

[a]Notation: K_{11}, splay elastic constant; K_{22}, twist elastic constant; K_{33}, bend elastic constant; T_{NI}, nematic-to-isotropic clearing temperature; Δn, birefringence; n_e, extraordinary refractive index; n_o, ordinary refractive index; Δε, dielectric anisotropy.

[b]elastic constants from [54]; T_{NI} from [41, 55].

[c]elastic constants from [56, 57]; T_{NI} from [55].

[d]elastic constants courtesy of EMD group, *Merck* KGaA.; T_{NI} from [55].

[b,c,d]Δn, n_e, n_o, and Δε courtesy of EMD group, *Merck* KGaA.

2.10 References

*This chapter was originally published as an Instructional Review in the journal *Langmuir*. My contribution to this review was in writing section 2.5, discussing content of other sections, and assisting my co-authors in the proof reading of the manuscript and preparation of some of the figures.

†Figure 2-3:

1. Rothblat, G. H.; Rosen, J. M.; Insull, W.; Yau, A. O.; Small, D. M. Production of Cholesteryl Ester-Rich, Anisotropic Inclusions by Mammalian-Cells in Culture. *Exp. Mol. Pathol.* **1977**, 26, 318–324.
2. Stewart, G. T. Liquid Crystals of Lipid in Normal and Atheromatous Tissue. *Nature* **1959**, 183, 873–875.
3. Drzaic, P. S. *Liquid Crystal Dispersions*. World Scientific: Singapore ; River Edge, NJ, 1995; p 429.
4. Karanikolos, G. N.; Alexandridis, P.; Mallory, R.; Petrou, A.; Mountziaris, T. J. Templated Synthesis of ZnSe Nanostructures Using Lyotropic Liquid Crystals. *Nanotechnology* **2005**, 16, 2372–2380.
5. Yang, C. S.; Awschalom, D. D.; Stucky, G. D. Growth of CdS Nanorods in Nonionic AmphiphilicTriblock Copolymer Systems. *Chem. Mater.* **2002**, 14, 1277–1284.
6. Bai, Y.; Abbott, N. L. Recent Advances in Colloidal and Interfacial Phenomena Involving Liquid Crystals. *Langmuir* **2011**, 27, 5719–5738.
7. Lockwood, N. A.; Abbott, N. L. Self-Assembly of Surfactants and Phospholipids at Interfaces Between Aqueous Phases and Thermotropic Liquid Crystals. *Curr. Opin. Colloid Interface Sci.* **2005**, 10, 111–120.
8. Lowe, A. M.; Abbott, N. L. Liquid Crystalline Materials for Biological Applications. *Chem. Mater.* **2012**, 24, 746–758.
9. Bai, Y.; Abbott, N. L. Enantiomeric Interactions Between Liquid Crystals and Organized Monolayers of Tyrosine-Containing Dipeptides. *J. Am. Chem. Soc.* **2012**, 134, 548–558.
10. Brake, J. M.; Abbott, N. L. An Experimental System for Imaging the Reversible Adsorption of Amphiphiles at Aqueous-Liquid Crystal Interfaces. *Langmuir* **2002**, 18, 6101–6109.
11. Brake, J. M.; Mezera, A. D.; Abbott, N. L. Effect of Surfactant Structure on the Orientation of Liquid Crystals at Aqueous-Liquid Crystal Interfaces. *Langmuir* **2003**, 19, 6436–6442.
12. Carlton, R. J.; Gupta, J. K.; Swift, C. L.; Abbott, N. L. Influence of Simple Electrolytes on the Orientational Ordering of Thermotropic Liquid Crystals at Aqueous Interfaces. *Langmuir* **2012**, 28, 31–36.
13. Carlton, R. J.; Ma, C. D.; Gupta, J. K.; Abbott, N. L. Influence of Specific Anions on the Orientational Ordering of Thermotropic Liquid Crystals at Aqueous Interfaces. *Langmuir* **2012**, 28, 12796–12805.

14. Clare, B. H.; Guzman, O.; de Pablo, J. J.; Abbott, N. L. Measurement of the Azimuthal Anchoring Energy of Liquid Crystals in Contact with Oligo(ethylene glycol)-Terminated Self-Assembled Monolayers Supported on Obliquely Deposited Gold Films. *Langmuir* **2006**, 22, 4654–4659.
15. Gupta, J. K.; Abbott, N. L. Principles for Manipulation of the Lateral Organization of Aqueous-Soluble Surface-Active Molecules at the Liquid Crystal-Aqueous Interface. *Langmuir* **2009**, 25, 2026–2033.
16. Gupta, J. K.; Sivakumar, S.; Caruso, F.; Abbott, N. L. Size-Dependent Ordering of Liquid Crystals Observed in Polymeric Capsules with Micrometer and Smaller Diameter. *Angew. Chem. Int. Ed. Engl.* **2009**, 48, 1652–1655.
17. Gupta, J. K.; Tjipto, E.; Zelikin, A. N.; Caruso, F.; Abbott, N. L. Characterization of the Growth of Polyelectrolyte Multilayers Formed at Interfaces Between Aqueous Phases and Thermotropic Liquid Crystals. *Langmuir* **2008**, 24, 5534–5542.
18. Gupta, J. K.; Zimmerman, J. S.; de Pablo, J. J.; Caruso, F.; Abbott, N. L. Characterization of Adsorbate-Induced Ordering Transitions of Liquid Crystals within Monodisperse Droplets. *Langmuir* **2009**, 25, 9016–9024.
19. Khan, W.; Choi, J. H.; Kim, G. M.; Park, S. Y. Microfluidic Formation of pH Responsive 5CB Droplets Decorated with PAA-b-LCP. *Lab Chip* **2011**, 11, 3493–3498.
20. Kinsinger, M. I.; Buck, M. E.; Abbott, N. L.; Lynn, D. M. Immobilization of Polymer-Decorated Liquid Crystal Droplets on Chemically Tailored Surfaces. *Langmuir* **2010**, 26, 10234–10242.
21. Lin, I. H.; Miller, D. S.; Bertics, P. J.; Murphy, C. J.; de Pablo, J. J.; Abbott, N. L. Endotoxin-Induced Structural Transformations in Liquid Crystalline Droplets. *Science* **2011**, 332, 1297–1300.
22. Lockwood, N. A.; de Pablo, J. J.; Abbott, N. L. Influence of Surfactant Tail Branching and Organization on the Orientation of Liquid Crystals at Aqueous-Liquid Crystal Interfaces. *Langmuir* **2005**, 21, 6805–6814.
23. Lowe, A. M.; Bertics, P. J.; Abbott, N. L. Quantitative Methods Based on Twisted Nematic Liquid Crystals for Mapping Surfaces Patterned with Bio/chemical Functionality Relevant to Bioanalytical Assays. *Anal. Chem.* **2008**, 80, 2637–2645.
24. Lowe, A. M.; Ozer, B. H.; Bai, Y.; Bertics, P. J.; Abbott, N. L. Design of Surfaces for Liquid Crystal-Based Bioanalytical Assays. *ACS Appl. Mater. Inter.* **2010**, 2, 722–731.
25. Miller, D. S.; Abbott, N. L. Influence of Droplet Size, pH and Ionic Strength on Endotoxin-Triggered Ordering Transitions in Liquid Crystalline Droplets. *Soft Matter* **2012**, 9, 374–382.
26. Sivakumar, S.; Gupta, J. K.; Abbott, N. L.; Caruso, F. Monodisperse Emulsions through Templating Polyelectrolyte Multilayer Capsules. *Chem. Mater.* **2008**, 20, 2063–2065.
27. Chen, W.; Feller, M. B.; Shen, Y. R. Investigation of Anisotropic Molecular Orientational Distributions of Liquid-Crystal Monolayers by Optical 2nd-Harmonic Generation. *Phys. Rev. Lett.* **1989**, 63, 2665–2668.
28. Jerome, B. Surface Effects and Anchoring in Liquid Crystals. *Rep. Prog. Phys.* **1991**, 54, 391–451.
29. Goodman, L. A.; Mcginn, J. T.; Anderson, C. H.; Digeronimo, F. Topography of Obliquely Evaporated Silicon-Oxide Films and Its Effect on Liquid-Crystal Orientation. *IEEE Trans. Electron Devices* **1977**, 24, 795–804.

30. Skaife, J. J.; Brake, J. M.; Abbott, N. L. Influence of Nanometer-Scale Topography of Surfaces on the Orientational Response of Liquid Crystals to Proteins Specifically Bound to Surface-Immobilized Receptors. *Langmuir* **2001**, 17, 5448–5457.
31. Gupta, V. K.; Abbott, N. L. Azimuthal Anchoring Transition of Nematic Liquid Crystals on Self-Assembled Monolayers Formed from Odd and Even Alkanethiols. *Phys. Rev. E* **1996**, 54, R4540–R4543.
32. Luk, Y. Y.; Tingey, M. L.; Hall, D. J.; Israel, B. A.; Murphy, C. J.; Bertics, P. J.; Abbott, N. L. Using Liquid Crystals to Amplify Protein-Receptor Interactions: Design of Surfaces with Nanometer-Scale Topography that Present Histidine-Tagged Protein Receptors. *Langmuir* **2003**, 19, 1671–1680.
33. Collings, P. J. *Liquid Crystals:Nature's Delicate Phase of Matter*. 2nd ed.; Princeton University Press: Princeton, N.J., 2002; p 204.
34. de Gennes, P.-G. *The Physics of Liquid Crystals*. Clarendon Press: Oxford [Eng.], 1974; p 333.
35. Mullin, C. S.; Guyotsionnest, P.; Shen, Y. R. Properties of Liquid-Crystal Monolayers on Silane Surfaces. *Phys. Rev. A* **1989**, 39, 3745–3747.
36. Lavrentovich, O. D.; Buschow, K. H. J. Nematic Liquid Crystals: Defects. In *Encyclopedia of Materials Science and Technology*, Elsevier: Amsterdam; New York, 2001; Vol. 6, pp 6071–6076.
37. Nehring, J.; Saupe, A. On the Schlieren Texture in Nematic and Smectic Liquid Crystals. *J. Chem. Soc., Faraday Trans. 2* **1972**, 68, 1–15.
38. Lay, E. H.; Kirakosian, A.; Lin, J. L.; Petrovykh, D. Y.; Crain, J. N.; Himpsel, F. J.; Shah, R. R.; Abbott, N. L. Alignment of Liquid Crystals on Stepped and Passivated Silicon Templates Prepared in Ultrahigh Vacuum. *Langmuir* **2000**, 16, 6731–6738.
39. Lavrentovich, O. D. Topological Defects in Dispersed Liquid Crystals, or Words and Worlds Around Liquid Crystal Drops. *Liquid Crystals* **1998**, 24, 117–125.
40. Bloss, F. D. *An Introduction to the Methods of Optical Crystallography*. Holt: New York, N.Y., 1961; p 294.
41. Shah, R. R.; Abbott, N. L. Coupling of the Orientations of Liquid Crystals to Electrical Double Layers Formed by the Dissociation of Surface-Immobilized Salts. *J. Phys. Chem. B* **2001**, 105, 4936–4950.
42. Allender, D. W.; Crawford, G. P.; Doane, J. W. Determination of the Liquid-Crystal Surface Elastic-Constant K_{24}. *Phys. Rev. Lett.* **1991**, 67, 1442–1445.
43. Goyal, R. K.; Denn, M. M. Orientational Multiplicity and Transitions in Liquid Crystalline Droplets. *Phys. Rev. E* **2007**, 75, 021704.
44. Van Horn, B. L.; Winter, H. H. Analysis of the Conoscopic Measurement for Uniaxial Liquid-Crystal Tilt Angles. *Appl. Opt.* **2001**, 40, 2089–2094.
45. Fonseca, J. G.; Galerne, Y. Simple Method for Measuring the Azimuthal Anchoring Strength of Nematic Liquid Crystals. *Appl. Phys. Lett.* **2001**, 79, 2910–2912.
46. Rapini, A.; Papoular, M. Distortion d'une Lamelle Nematique sous champ Magnetique Conditions d'Ancrage aux Parois. *J. Phys. (Paris)* **1969**, 30, 54–56.
47. Toyooka, T.; Chen, G.; Takezoe, H.; Fukuda, A. Determination of Twist Elastic-Constant K-22 in 5CB by 4 Independent Light-Scattering Techniques. *Jpn. J. Appl. Phys. 1* **1987**, 26, 1959–1966.

48. Zou, J. H.; Bera, T.; Davis, A. A.; Liang, W. L.; Fang, J. Y. Director Configuration Transitions of Polyelectrolyte Coated Liquid-Crystal Droplets. *J. Phys. Chem. B* **2011**, 115, 8970–8974.
49. Park, J. S.; Jang, C. H.; Tingey, M. L.; Lowe, A. M.; Abbott, N. L. Influence of 4-cyano-4 '-biphenylcarboxylic Acid on the Orientational Ordering of Cyanobiphenyl Liquid Crystals at Chemically Functionalized Surfaces. *J. Colloid Interface Sci.* **2006**, 304, 459–473.
50. Lagerwall, J. P. F.; Scalia, G. A New Era for Liquid Crystal Research: Applications of Liquid Crystals in Soft Matter Nano-, Bio- and Microtechnology. *Curr. Appl. Phys.* **2012**, 12, 1387–1412.
51. Perkins, D.; Henke, K. R. *Minerals in Thin Section*. Prentice Hall: Upper Saddle River, N.J., 2000; p 125.
52. Davidson, M. W. The Berek Compensator. http://www.olympusmicro.com/primer/techniques/polarized/berekcompensator.html (November 5, 2012),
53. Hoffman, R.; Davidson, M. W. Michel-Levy Birefringence Chart. http://www.olympusmicro.com/primer/techniques/polarized/michel.html (November 5, 2012),
54. Bradshaw, M. J.; Raynes, E. P.; Bunning, J. D.; Faber, T. E. The Frank Constants of Some Nematic Liquid Crystals. *J. Phys (Paris)* **1985**, 46, 1513–1520.
55. Luk, Y. Y.; Campbell, S. F.; Abbott, N. L.; Murphy, C. J. Non-Toxic Thermotropic Liquid Crystals for Use with Mammalian Cells. *Liq. Cryst.* **2004**, 31, 611–621.
56. Ambrozic, M.; Formoso, P.; Golemme, A.; Zumer, S. Anchoring and Droplet Deformation in Polymer Dispersed Liquid Crystals: NMR Study in an Electric Field. *Phys. Rev. E* **1997**, 56, 1825–1832.
57. Wu, S. T.; Smith, W. H.; Lackner, A. M. Diamagnetic Anisotropy Measurements of Nematic Liquid Crystals. *Mol. Cryst. Liq. Cryst.* **1986**, 140, 83–93.

Chapter 3: Design of Responsive and Active (Soft) Materials using Liquid Crystals*

3.1 Introduction

LCs are condensed fluid phases that, for a given material, are thermodynamically stable at temperatures intermediate between those that give rise to crystalline solids and isotropic liquids (Figure 3-1A). LCs are classified as thermotropic when the temperature of the system alone determines the phase behavior; in contrast, lyotropic systems consist of compositions that require the addition of solvent to form a LC phase.[1] LC phases derive many of their unique properties from the long-range ordering of their constituent molecules, called mesogens.[1] For example, rod-like molecules such as pentyl cyanobiphenyl (5CB) (Figure 3-1B) exhibit an average orientation (termed the "director") in the nematic LC phase that is preserved over distances that are several orders of magnitude greater than molecular dimensions. The long-range ordering of mesogens in LCs imparts the bulk material with anisotropic mechanical properties as well as optical birefringence, which is commonly associated with crystalline solids. Unlike a crystalline solid, however, the mesogens are able to diffuse (via translation and rotation) at rates that are comparable to simple, isotropic liquids. This characteristic mobility allows the material to rapidly reorganize and communicate information across the bulk of the phase, which as will be discussed later in this chapter, enables new designs of responsive and potentially active materials.

The nematic LC described above is one of the simplest and best-studied LC phases. Many other exotic LC phases have been discovered over the past decade, including the recently reported "twist-bend" or "heliconical" nematic phase.[2-4] These new phases are formed from

molecules that have unusual shapes (and names). For example, in the case of bent-core LC phases, the molecules comprising the LC consist of rigid, banana-shaped mesogens (Figure 3-1C). For purposes of this chapter, we introduce only the so-called B4 phase, which forms when banana-shaped mesogens assemble into nanosheets that twist into chiral helical structures (Figure 3-1D).[5] In turn, these sheets aggregate into nanorods, which then form porous filaments.[5] It is worth noting that these chiral nanosheets arise despite the achiral nature of the constituent molecules. While this spontaneous breaking of symmetry leads to locally chiral structures, the material overall comprises a racemic mixture of domains of opposite handedness. Nonetheless, use of these materials has been proposed for the fabrication of non-linear optical devices and opto-electric responsive systems.[6-8]

Whereas the nematic and bent-core LCs described above are phases that arise from the properties and organization of a single type of mesogen, mixtures of mesogens (or mixtures of mesogens and non-mesogenic molecules) give rise to a wide range of interesting LC phases. For example, the addition of a chiral molecule (Figure 3-1E) to a nematic LC induces a helical twist perpendicular to the director (Figure 3-1F).[1] This chiral phase is referred to as a cholesteric LC. At a sufficiently high concentration of the chiral additive, and when the temperature of the LC is close to the nematic-isotropic transition temperature, the twist develops in two directions perpendicular to the director, giving rise to the formation of cylindrical structures that self-assemble into three-dimensional periodic lattices (Figures 3-1G and 3-1H).[9-11] This LC phase is termed a “blue phase” for historical reasons, but modern materials that form blue phases (BPs) may exhibit a range of colors depending on the wavelengths scattered by their constitutive lattice structures.[11] Interestingly, the interstitial spaces within blue phases, where three double-twist cylinders meet, is highly frustrated and the local order is greatly diminished relative to the bulk

LC.[10] These regions, called line defects or disclinations, possess high energy densities and impact the temperature range over which the BP forms (see below for additional discussion of defects). Much work has been devoted, therefore, to replacement of the high energy disclinations by polymers or nanoparticles with the goal of extending the range of temperatures over which blue phases are stable.[12,13]

Lyotropic LCs constitute another type of LC phase that can be formed by small amphiphilic or polyaromatic molecules upon addition of a solvent.[14,15] Lyotropic LC phases formed by dispersing polyaromatic, non-amphiphilic molecules in a solvent are referred to as "chromonics". Disodium cromoglycate (DSCG) (Figure 3-1I) is an example of a molecule that can form chromonic LC phases. When dissolved in water (at a given temperature), molecules of DSCG stack into columns that serve as mesogens, displaying nematic-like orientational order (Figures 3-1J and 3-1K).[15] This aqueous LC phase is particularly attractive for use in biological contexts. Recently, for example, it has been used as a biocompatible anisotropic medium in which to study the fundamental behaviors of motile bacteria,[16-20] as will be described in Chapters 4-6 of this thesis. Such studies are defining principles for the design of active materials based on LCs.

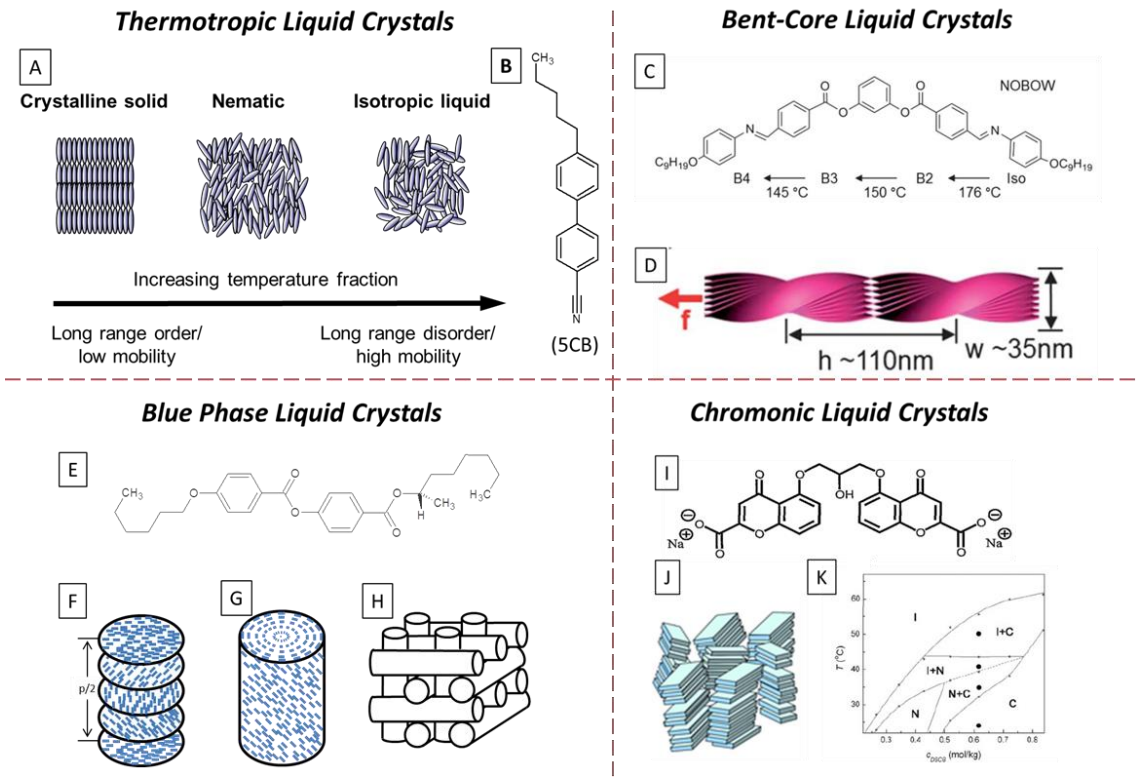

Figure 3-1. Examples of liquid crystals discussed in this chapter.

(A) Schematic illustration of the temperature-dependent phase behavior of thermotropic LCs. (B) Molecular structure of pentyl-cyanobiphenyl (5CB), a commonly studied mesogen that forms a nematic phase at room temperature. (C) Molecular structure of banana-shaped mesogens that form bent-core LC phases comprised of nanostructures, such as (D) helical nanofilaments. (E) Example of a chiral dopant (S-811) that forms a (F) cholesteric LC phase when added to a nematic LC. (G) Double-twist cylinders of cholesteric LCs form at high temperatures and concentrations of the chiral additive. (H) These cylinders, in turn, self-assemble into cubic lattices characteristic of blue phase LCs. (I) Molecular structure of disodium cromoglycate (DSCG), which forms a nematic phase in water. The DSCG molecules stack into columns (J) that exhibit long-range orientational (nematic) order. The resulting phase, called a chromonic LC, exhibits a phase behavior that depends on both the temperature and concentration of DSCG (K). Reproduced with permission.[8,15,21,†]

The examples described above serve to illustrate the chemical diversity of LCs. Interestingly, despite these striking differences in chemistry, LC phases exhibit unifying characteristics and behaviors that emerge from the long-range order and mobility of their mesogenic constituents. Here we summarize three key concepts relevant to all LCs, which

underlie the colloidal and interfacial phenomena described in the remainder of this chapter: (i) the so-called "surface anchoring" of LCs, (ii) the elasticity of LCs, and (iii) the formation of topological defects in LCs.

The phenomenon of surface anchoring, which refers to the surface-induced ordering of LCs, results from intermolecular interactions between LCs and a confining medium. In the absence of external fields, the lowest free energy orientation of the LC director is dubbed the "easy axis" (denoted as n_e in Figure 3-2A).[22,23] A perturbation to the orientation of a LC (e.g., application of an external field) that causes the director to deviate from the easy axis leads to an orientation-dependent increase in the free energy of the interface, which is often described by[24,25]

$$F_S = F_0 + \frac{1}{2} W_a sin^2(\theta_s - \theta_e) \qquad (3\text{-}1)$$

where F_S is the interfacial free energy, F_0 is the free energy of the interface corresponding to the easy axis, W_a is the anchoring energy (typically 10^{-3} – 10^{-2} mJ/m^2), and θ_s and θ_e are the angles defining the orientations of the surface director and easy axis, respectively (Figure 3-2A).[24,25] While Figure 3-2A depicts changes in the orientation of the LC with respect to the surface normal, it is common also for a surface to define an easy axis in the azimuthal direction.

The long-range orientational ordering of mesogens within LCs underlies the existence of the elastic properties of LCs. There are three fundamental modes of strain in LCs, twist, bend and splay (Figure 3-2B), although all modes of strain are not permitted for all LCs. The simplest description of the strain of LCs is the so-called Frank-Oseen equation for the free energy density[24-27]

$$F_e = \frac{1}{2} K_1 \left(\nabla \cdot \underline{n}\right)^2 + \frac{1}{2} K_2 \left(\underline{n} \cdot \nabla \times \underline{n}\right)^2 + \frac{1}{2} K_3 \left(\underline{n} \times \left(\nabla \times \underline{n}\right)\right)^2 \qquad (3\text{-}2)$$

where K_1, K_2, and K_3 are the splay, twist, and bend elastic constants, respectively (each typically in the order of 10^{-11} N).[24-26]

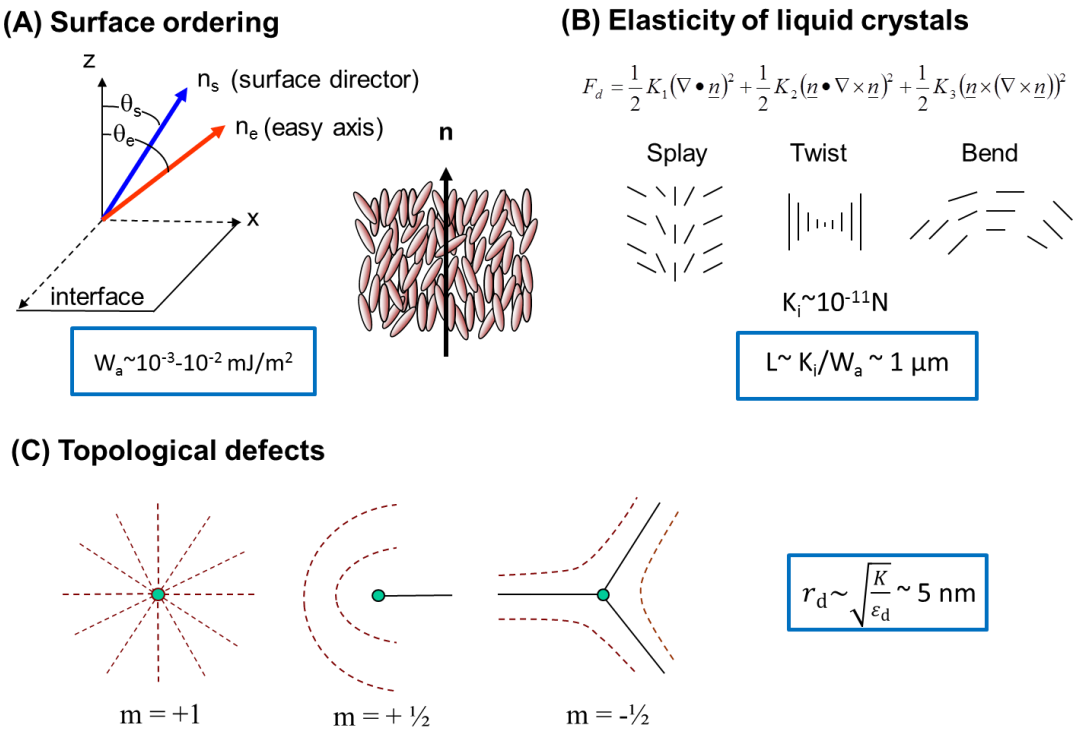

Figure 3-2. Properties of LC phases.

Schematic illustrations of (A) the director and easy axis of a LC anchored at a surface, (B) the three basic modes of deformation of a LC (splay, twist and bend) and an expression for F_d, the elastic free energy density, that results from these strains, and (C) three types of topological defects that can form in a LC. The left cartoon shows a point defect located at the center of a radially converging director field, and the center and right cartoons show cross-sections of line defects (disclinations). The line defects are oriented orthogonal to the plane containing the figure. The parameter m indicates the so-called strength of the defect.

The final key concept to introduce is that of a topological defect in a LC. When a LC is confined within certain geometries (e.g., inside a spherical cavity with perpendicular anchoring of the LC on the cavity wall), it is not possible to accommodate the surface-induced orientation (boundary condition) through a continuous strain of the LC. Under these conditions, regions of

the LC are generated in which the rate of strain of the LC is sufficiently high that the LC locally "melts".[27-32] Macroscopically, these regions correspond to singularities in the director profile. Microscopically, the "cores" of singular defects are nanoscopic regions within which the local orientational order of the LC has been substantially diminished. Some examples of geometries that give rise to defects are illustrated in Figure 3-2C. According to the above-described origin of defects, the energy of formation of a defect can be described as:

$$F_d = \int_{V_d} f_d dV_d \sim \frac{4}{3}\pi r_d^3 \epsilon_d \qquad (3-3)$$

where ϵ_d is the free energy density associated with local melting of the nematic phase to an isotropic phase and r_d is the estimate of the radius of the core of a defect. This process of local melting occurs when the free energy of melting the core is less energetically costly than straining the LC within the volume of the core. This latter term can be estimated as Kr_d where K is the elastic constant of the LC (assuming all three elastic constants are equal in magnitude; see Equation 3-2). A comparison of these two free energy terms yields an estimate of the size of the core of the defect[26,33]

$$r_d \sim \sqrt{\frac{K}{\epsilon_d}} \sim 5\ nm \qquad (3-4)$$

Significantly, the typical diameter of the core of a defect is approximately 10nm, thus topological defects within LCs create nanoscopic regions of the material with physical properties that are distinct from the bulk LC. The magnitude of the free energy of the core of a point defect is typically around 10^{-19} J.

Below we describe how the effects of surface anchoring, LC elasticity and topological defects combine in a range of experimental systems to produce a remarkable diversity of

colloidal and interfacial phenomena that underlie designs of responsive and active soft matter systems.

3.2 Interfacial Ordering of LCs

As described in the context of Figure 3-2A, LCs are remarkable for the fine scale of energetics that control their ordering at interfaces. Specifically, the orientation-dependent part of the interfacial energy (which effectively controls the orientational ordering of the LC) is typically around 10^{-2}-10^{-3} mJ/m^2. For comparison, the interfacial energy of an isotropic liquid ranges from 20 mJ/m^2 (for a non-polar liquid) to around 70 mJ/m^2 (for a hydrogen bonded liquid). The "surface-sensitivity" of LCs thus presents many opportunities for the design of responsive materials, particularly when combined with the advances in the synthesis of surfaces with well-defined structures and properties that have emerged over the past couple of decades.[34-36] In this section, we focus on the interfacial ordering of LCs at chemically functionalized interfaces and describe several advances in the design of responsive LC systems that have leveraged such interfaces. In contrast to interfaces used in LCDs, which possess a narrow range of chemistries (i.e., polyimides) and are passive, the work presented here demonstrates the opportunities that result from the design of surfaces that can be chemically or physically transformed in response to the delivery of a stimulus.

3.2.1 Stimuli-Responsive Surfaces

Chemically functionalized surfaces impose a preferred orientation on the LC through the interactions of the mesogens with the chemical functional groups displayed at the interface. In contrast to interfaces widely used in displays, in which anisotropic van der Waals interactions

dominate the orientation of the LC, the diversity of chemically functionalized interfaces explored over the past decade introduces a much wider range of interactions[24], including hydrogen bonding[37,38], electrical double layers[39], and metal ion-ligand coordination interactions[35]. Due to the long-range ordering exhibited by LCs, these surface interactions lead to changes in the ordering of the bulk of the material and thus can influence, for example, the optical properties of a micrometer-thick LC film. In this manner, LCs can serve as amplifiers and optical transducers of a range of intermolecular interactions at interfaces. This remarkable property of LCs also forms the basis of technological opportunities, including the creation of optical sensors for physical and chemical stimuli.

We use the term stimuli-responsive surfaces to describe surfaces with physical or chemical properties that change in response to an external stimulus or trigger, resulting in a change in the orientation of a contacting LC phase (Figure 3-3A). When the orientation of a LC changes from perpendicular (or homeotropic) to parallel (or planar) to the surface, or vice-versa, a dramatic optical response is observed when the film is viewed through crossed-polarizers (Figure 3-3B). For example, the shift from the "dark" to "bright" optical appearance depicted in Figure 3-3B accompanies an ordering transition within a LC film from a uniform homeotropic configuration (homeotropic anchoring at both interfaces confining the film) to a so-called "hybrid" configuration in which the LC is anchored parallel to one interface and homeotropic to the other. A bright optical appearance is observed in the latter case because polarized light experiences both indices of refraction of the nematic LC phase (as opposed to just one in a uniform homeotropic film), which leads to a change in polarization and the transmission of light through the analyzer (for additional details, see Chapter 2 of this thesis). Briefly, we discuss two

types of stimuli-responsive surfaces that can produce these types of ordering transitions within LC films: light-triggered surfaces and chemically triggered surfaces.

As an example of a light-triggered interface, we describe surfaces decorated with azobenzene. These light-triggered interfaces exploit the ability of azobenzene to undergo reversible *cis-trans* isomerization in response to UV/visible light (Figure 3-3C).[41,42] The resulting change in dipole that accompanies the change in conformation of azobenzene from *trans* to *cis* is able to trigger a contacting LC phase to switch from a homeotropic to planar orientation, or vice versa. Ichimura *et al.* were the first to demonstrate that azobenzene-containing polymers, when grafted onto glass surfaces to form monolayers, can trigger orientational transitions in LCs upon illumination with specific wavelengths of light.[43] They called these systems "command surfaces" because of the large amplification ($\sim 10^4$, defined as the number of molecules in the bulk LC that are controlled, on average, by each molecule on the surface) inherent in the response of the "obeying" LC phase to the "commanding" photoresponsive molecules on the surface. Subsequently, surfaces coated with azobenzene-functionalized polyimides, when irradiated with polarized light, were shown to permit control of the in-plane (azimuthal) orientation of LC films.[44] Alternatively, Seki *et al.* reported a method to prepare a layer of a photoresponsive material at a the free interface of an LC film, permitting LC alignment control without the need for chemical modification of the supporting substrate.[45] Building on these examples we mention that Takezoe and coworkers recently reported on a system of rod-shaped particles coated with light-responsive molecules that were dispersed in LCs.[46] When illuminated with light, the photo-induced change in anchoring of the LCs on the surface of the particles triggered a spontaneous reorientation of the rod-shaped particles. This study hints at novel designs of optically-driven colloidal materials.

Whereas the examples above address optically triggered changes in the orientations of LCs, stimuli-responsive interfaces that can be triggered by specific chemical species have also been explored. Chemically triggered interfaces bind targeted compounds via the presentation of chemical functionality from a surface and thereby produce an orientational transition in a nematic LC film (Figure 3-3D). Abbott et al. were the first to demonstrate the design of such surfaces, using nitrile-containing nematic LCs (e.g., 5CB) that formed coordination complexes with surfaces functionalized to present metal cations.[34] Exposure of the surface-oriented LCs to gases that contained parts-per-billion concentrations of organoamines or organophosphonates was observed to trigger ordering transitions in the LCs. It was established that the amine or phosphonate groups of the gas phase species formed coordination complexes with the metal cation on the surface, thus displacing the nitrile-containing mesogens from the surface coordination complexes.[34] This ligand exchange at the metal ion-decorated interface resulted in an orientational transition that was readily visualized. In contrast, exposure of the LC films to other compounds such as ethanol, acetone or water did not produce an optical response of the LC because these compounds were not able to displace the nitrile-containing mesogens coordinated with the metal ions.[34] These results demonstrated that competitive coordination interactions at chemically functionalized interfaces can form the basis of LC materials that respond selectively to specific compounds with high sensitivity. Subsequent work has built on these principles to demonstrate designs of LC materials that respond to the presence of nitrogen dioxide (NO_2), ammonia (NH_3), hydrogen sulfide (H_2S), etc.[47,48]

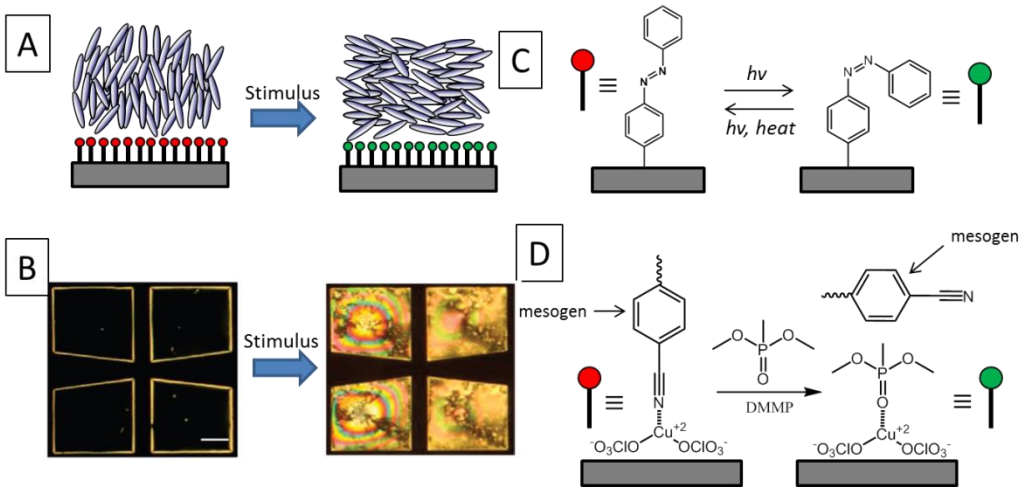

Figure 3-3. Stimuli-responsive LC films.

(A) Schematic illustration of a stimuli-responsive interface that triggers a change in the orientation of a LC. (B) The change in orientation of the LC leads to a distinct change in optical appearance of the LC when viewed between crossed-polars. (C) Schematic illustration of a surface decorated with azobenzene, which undergoes a UV light-induced isomerization (*trans*-to-*cis*) that triggers an orientational transition in a LC. (D) Schematic illustration of a chemically functionalized surface that triggers a change in orientation of a LC when a targeted compound binds to the surface. The surface shown in D presents Cu^{2+} ions, which orient a nitrile-containing mesogen through a coordination interaction. The targeted compound, dimethylmethylphosphonate (DMMP) binds to Cu^{2+} more strongly than the mesogen, and thus triggers an orientational transition in the LC through ligand displacement. Reproduced with permission.[35]

3.2.2 Chiral Interfaces

The examples presented in the previous section demonstrate that responsive LC systems can be designed using chemically functionalized surfaces that either reconfigure in response to illumination or binding of a targeted chemical species. Here we mention that the chirality of molecular adsorbates, and interfacial events that result in changes in chirality, also impact the orientation of LCs at interfaces. This sensitivity to the stereochemistry of adsorbates hints at a range of possible designs of responsive materials (e.g., materials that respond to the enantiomeric excess of a mixture of isomers generated in a chemical or biochemical reaction). Specifically, it

has been shown relatively recently that surfaces functionalized to present organized assemblies of chiral dipeptides can direct the azimuthal orientation of nematic LC films in a manner that is dependent on the chirality of the dipeptides.[37] In these studies, gold-coated substrates were prepared by vapor deposition at an oblique angle of incidence. This manner of deposition of the gold introduced a crystallographic texturing that led to the formation of organized monolayers of L-cysteine-L-tyrosine (L-Cys-L-Tyr) or D-cysteine-D-tyrosine (D-Cys-D-Tyr) (Figure 3-4A, B). Specifically, on L-Cys-L-Tyr-functionalized surfaces, the azimuthal alignment of the LC was rotated by +53° (in the plane of the surface) from the azimuthal direction of deposition of the gold during formation of the films. In contrast, for the surfaces presenting D-Cys-D-Tyr, the LC aligned in an azimuthal direction that defined an angle of -53° from the azimuthal direction of deposition of the gold. By varying the chemical functionality of the mesogens and immobilized amino acids, it was demonstrated that the response of the LC anchoring to the chirality of the adsorbates was caused by networks of hydrogen-bonds (the pattern of hydrogen bonds created by the network was dependent on the chirality of the amino acids) formed between the tyrosine-containing dipeptides grafted at the gold-coated substrates and the mesogens.[37]

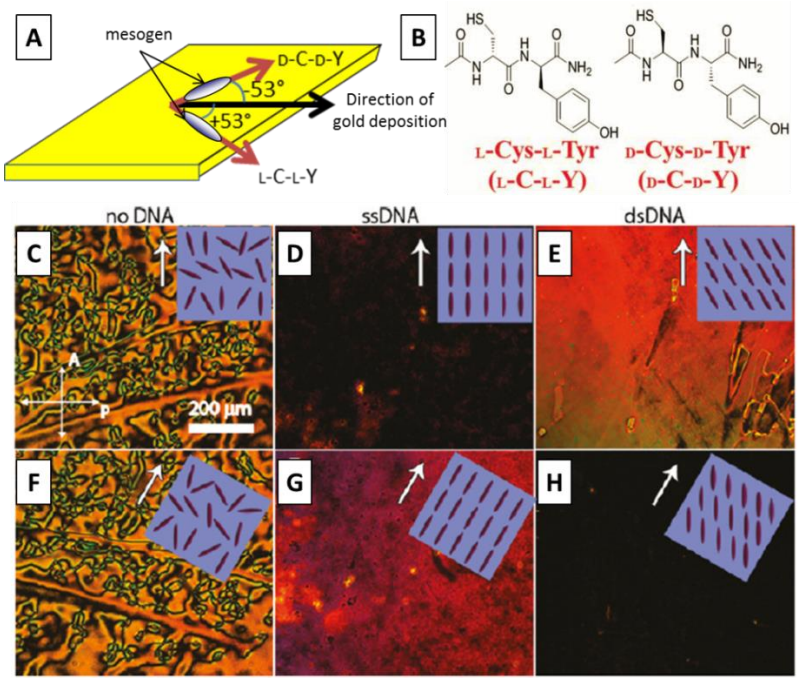

Figure 3-4. Orientations of LCs at chiral surfaces.

(A) Schematic illustration of the azimuthal orientation of nematic 5CB anchored on surfaces presenting the chiral dipeptides L-Cys-L-Tyr and D-Cys-D-Tyr. The chiral dipeptides are adsorbed to gold films deposited by physical vapor deposition at an oblique angle of incidence. The azimuthal direction of deposition of the gold is shown in the figure. A change in the chirality of the dipeptides results in a change in the orientation of the LC on the dipeptide-decorated surface. The molecular structures of the dipeptides are shown in (B). (C-H) Polarized light micrographs of nematic LCs oriented on bare surfaces or surfaces decorated with ssDNA or dsDNA. (C, F) surfaces dipped in buffer free of DNA, (D,G) surfaces decorated with ssDNA, imaged with the polarizers at two distinct orientations relative to the orientation of the ssDNA strands, (E, H) surfaces decorated with dsDNA, imaged with the polarizers at two distinct orientations relative to the orientation of the dsDNA strands. The white arrows show the orientation of DNA strands within the samples. Insets in (C-H) indicate the orientations of mesogens. Reproduced with permission.[36,37]

Chiral macromolecules with much greater complexity than the dipeptides mentioned above, such as DNA, can also affect the azimuthal alignment of nematic LCs. For example, Malone and Schwartz reported that 5CB exhibit distinct azimuthal orientations on surfaces

decorated with single-stranded (ss) DNA or double-stranded (ds) DNA molecules (Figures 3-4C through 3-4H).[36] Whereas the LC aligned parallel to extended strands of ssDNA, in contrast, the alignment of the LC was rotated away from the direction of extension of dsDNA molecules. Further analysis of this system led to the hypothesis that the interactions underlying the observed alignment of the LCs were steric in nature and dependent on the surface topography defined by the DNA molecules. Two key observations support this hypothesis, namely (i) the alignment of mesogens with distinct dipolar properties (5CB with a strong dipole and n-(4-methoxybenzylidene)-4-butylaniline (MBBA) with a weak dipole) were the same, and (ii) dense DNA coatings on the surfaces (DNA gels) did not align either 5CB or MBBA.[36,49] While additional measurements are needed to fully elucidate the mechanism that couples the LCs to the dsDNA, the chiral double helix formed by the dsDNA does appear to encode intermolecular interactions that are reported in the orientations of the LCs. Additional measurements performed with oligomers of DNA have also demonstrated the design of LC systems that respond dynamically to hybridization of DNA, thus providing principles for the design of responsive LC materials.[50] In particular, because DNA is modular and can be designed to respond to a range of biochemical targets, DNA-coupled LCs appear a promising area for future investigation.

3.2.3 Aqueous-LC Interfaces

The studies described above predominantly address responsive LC systems that are based on the ordering of LCs at chemically functionalized interfaces of solids. More recently, a number of studies of "free interfaces" of LCs have been reported.[24,51] Among the various free interfaces (air-LC; isotropic liquid-LC), one of the most exciting is the aqueous-LC interface. The aqueous-LC interface possesses several unique characteristics that differentiate it from solid-LC

interfaces. Specifically, (i) the aqueous-LC interface is soft and deformable, (ii) adsorbates can be transported to the aqueous-LC interfaces through the aqueous phase, and (iii) molecular species adsorbed at the aqueous-LC interface are highly mobile as compared to chemical species adsorbed on a solid surface. The latter point is particularly important because the high interfacial mobility of molecules at aqueous-LC interfaces permits their rapid reorganization in response to elastic stresses from within the LC films. This phenomenon is discussed in detail in Section 3.4 below, as it defines an exciting set of opportunities in which LCs can be used to direct the organization of interfacial adsorbates.[52]

Figure 3-5 shows an experimental geometry that has been used widely to create interfaces between LCs and aqueous phases, and to explore the response of the LCs to the presence of adsorbates at the interface. In brief, a LC film supported on a solid substrate is submerged into water or into an aqueous solution containing water-soluble adsorbates. In the absence of adsorbates (e.g., amphiphiles), when contacted by water, the orientation assumed by the nematic LC (e.g., 5CB, and many other nematic LCs) is typically planar but azimuthally degenerate. However, as adsorbates, such as surfactant molecules, diffuse from the aqueous solution to the LC interface, the interactions between the adsorbates and the mesogens (the interactions appear to be largely mediated by steric interactions that involve the tails of the adsorbates) change the orientations of the LCs (Figure 3-5A). As discussed above (Figure 3-3B), the resulting ordering transition can be easily visualized when the LC film is viewed between crossed-polarizers. By using this versatile system, a number of studies have shown that the orientational response of LCs can be used to follow the dynamics of adsorption and desorption of amphiphiles from this interface. For example, Gupta and Abbott showed that the surfactant dodecyltrimethylammonium bromide (DTAB) triggered a continuous decrease in the optical

retardance of a LC film exposed to increasing concentrations of surfactant (Figure 3-5B).[53] This change in optical retardance corresponds to a continuous tilting of the LCs at the aqueous-LC interface from planar to homeotropic orientations (Figure 3-5C).[53]

Biological and synthetic phospholipids, such as L-α-dilauroyl-phosphatidylcholine (L-DLPC), have also been shown to adsorb from solution onto the LC-aqueous interface and to cause an ordering transition in the LC.[51] Because phospholipids are the primary constituent of cell membranes and because they are known to reorganize when interacting with proteins and other biological species, this experimental system has formed the basis of a number of biomimetic designs of responsive LCs, where the LC responds to the interactions between the phospholipid (or more generally amphiphile) with a targeted biological species (e.g., enzyme that processes the phospholipid). Interestingly, and of relevance to the above discussion of the effects of the chirality of adsorbates on the orientations of LCs, recent work by Takezoe et al. using bent-core LCs (see Figures 3-1C and 3-1D) has revealed also that the chirality of DLPC molecules adsorbed at aqueous-LC interfaces can break the symmetry of the racemic mixture of chiral domains observed in the B4 phase (see Introduction).[54] Specifically, by using either D-DLPC or L-DLPC, the twisting of the helical ribbons of the B4 phase could be selected to be right-handed or left-handed (Figure 3-5D).[54]

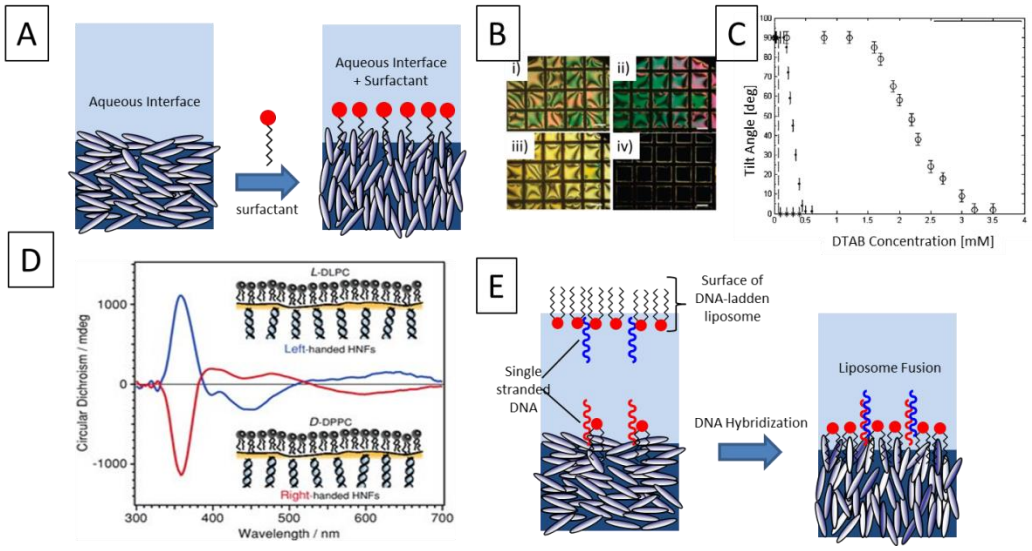

Figure 3-5. Adsorbate-induced orientations of thermotropic LCs at aqueous interfaces.
(A) Schematic illustration of the orientations of mesogens at the aqueous-LC interface prior to (left) and after (right) the adsorption of an amphiphilic molecule (surfactant) that triggers a transition from parallel to perpendicular orientations of the mesogens. (B) Optical images of aqueous-LC interfaces equilibrated against various aqueous concentrations of the surfactant dodecyltrimethylammonium bromide (DTAB). The concentrations of DTAB in the bulk aqueous phase are i) 0 mM, ii) 2.1 mM, iii) 2.7 mM and iv) 3.0 mM. (C) Quantification of the continuous, DTAB-triggered change in tilt angle of nematic 5CB at an aqueous-5CB interface. (D) Influence of the chirality of phospholipids on the ordering of bent-core LC phases near LC-aqueous interfaces. Circular dichroism measurements confirm that the chirality of the phospholipids induces an enantiomeric excess of chiral domains formed in a B4 phase. (E) Schematic illustration of the fusion of liposomes at a DNA-coated LC-interface. The hybridization of DNA strands in the liposome and those presented at the LC interface facilitates the fusion of the liposome, which leads to an ordering transition at the LC interface. Modified and reproduced with permission.[53-55]

Amphiphilic molecules that assemble at aqueous-LC interfaces form the basis of a wide range of opportunities for the design of responsive LCs. For example, Park and Abbott demonstrated a method for the formation of oligopeptide-decorated LC interfaces by covalently grafting oligopeptides to carboxylic acids presented by amphiphilic molecules adsorbed at the aqueous-LC interface.[56] Hydrolysis of the oligopeptides by a protease triggered an orientational

transition of the LC, demonstrating that this system could be used to report protease activity.[56] Similarly, Price and Schwartz demonstrated a method for preparation of aqueous-LC interfaces functionalized with ssDNA.[50] These surfaces induced an ordering transition in the LC when the ssDNA complements of the strands at the interface were introduced into the bulk aqueous solution.[50] Further work by the same group showed that these ssDNA-modified interfaces could be used to capture and report liposomes decorated with complementary ssDNA strands (Figure 3-5E).[55] Overall, these examples serve to illustrate the diversity of designs of LC materials based on LC-aqueous interfaces that respond to specific biochemical transformations. Related strategies have been demonstrated for the design of LC materials that respond to glucose, urea, cholesterol and other biological analytes.[57-59]

Whereas the examples provided above address the design of stimuli-responsive LC systems in the context of planar films of LC that contact aqueous phases, a range of additional experimental geometries and phenomena have been demonstrated using LC-aqueous interfaces. We describe two examples of these opportunities in Sections 3.4 and 3.5. In these sections, we sketch how LCs influence the phase behavior of nano- and micrometer sized species adsorbed at flat and curved aqueous-LC interfaces. In addition, we describe additional opportunities for the design of responsive, functional materials that arise due to the confinement of LCs within spherical droplets dispersed in water.

3.3 Colloidal Phenomena in LCs

As described in the previous section, the ordering of LCs at chemically functionalized interfaces (solid-LC or aqueous-LC) enables the design of a range of stimuli-responsive LC systems. In this section, we move to consider LCs at the highly curved surfaces of microparticles

and solid colloidal species. In these systems, the surface-induced ordering of LCs still plays a key role in determining the properties of the system. In addition, however, the elastic strain of the LCs around the particles and the associated formation of topological defects play additional key roles. We comment also that the particles in the LC are mobile, and thus stimuli (e.g., external fields or chemically-induced changes in surface anchoring) can lead to LC-mediated changes in the organization and dynamical properties of the systems. In this section, after discussing fundamental equilibrium and dynamical properties of colloidal dispersions in LCs, we highlight two examples that illustrate how these properties have been leveraged to define new opportunities for the design of active/driven soft material systems.

3.3.1 Colloidal Interactions in LCs

When microparticles or colloids are introduced into a nematic LC host, LCs in the vicinity of the particles are typically forced to deviate from the orientation set by the far-field director in a manner that simultaneously satisfies the anchoring condition at the particle surface (e.g., planar or homeotropic) and minimizes the resulting elastic strain within the LC phase. LCs accommodate micrometer-sized particles in this fashion because the energetic penalty associated with LCs straying from the lowest free energy orientation at the particle surface (which scales as $\sim W_a R^2$, where R is the radius of the particle) is generally greater than that associated with introduction of elastic distortions in the LC near the particle (which scales as $\sim KR$).[60] However, as a consequence of topological constraints, it is not possible for the LC, through continuous elastic strain, to accommodate the particles. This generally leads to the introduction of one (or more) topological defects. As discussed in the Introduction, topological defects form when the elastic energy density rises to a magnitude that is greater than the free energy density associated

with local "melting" of the LC – that is, within the core of a topological defect the orientational order is substantially lower than in the bulk of a LC. In Figures 3-6A through 3-6C, we present schematic illustrations that depict three common LC director profiles around microparticles. Tangential anchoring of LCs produces quadrupolar distortions in the LC with two diametrically opposed surface defects (so-called "boojums") (Figure 3-6A).[27] Homeotropic surface anchoring, on the other hand, typically gives rise to LC distortions with a dipolar symmetry (a so-called hyperbolic hedgehog point defect (Figure 3-6B)), although under specific conditions, distortions exhibiting quadrupolar symmetry with a "Saturn-ring" defect loop are formed (Figure 3-6C).[61]

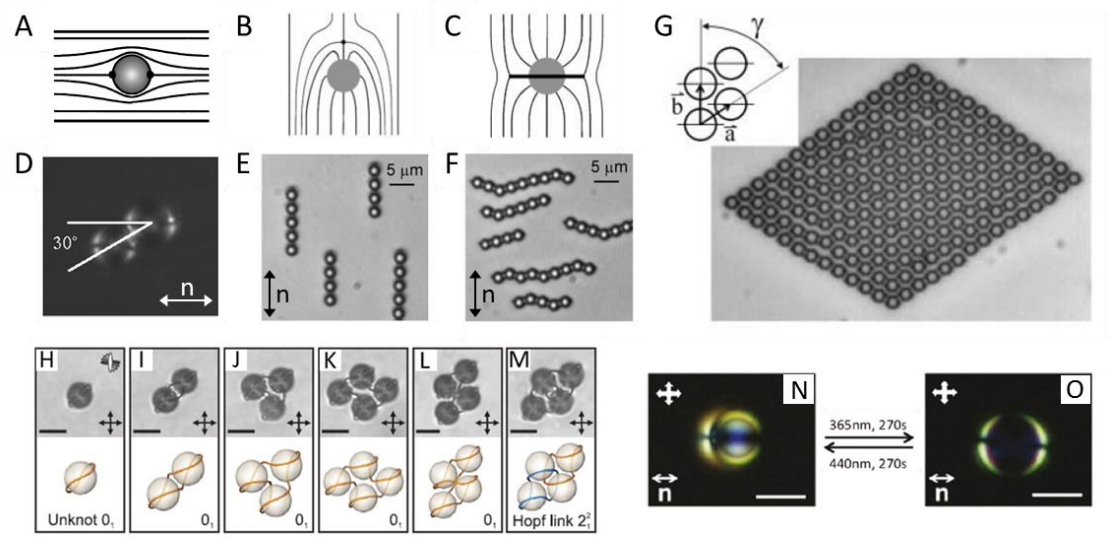

Figure 3-6. LC-mediated colloidal self-assembly.

(A-C) Schematic illustration of LC director profiles near particles dispersed in nematic LCs with either (A) tangential surface anchoring on the particles or (B,C) homeotropic anchoring on the particles. For the latter two cases, the LC exhibits an organization that possesses either dipolar (B) or quadrupolar (C) symmetry. The small dark circles (two in A and one in B) represent point defects, whereas the dark line in C represents a Saturn ring defect (line disclination). (D-F) Assemblies of particles that form as a consequence of interactions mediated by the LC director profiles shown in A-C, respectively. (G) Two-dimensional colloidal crystal formed by particles with Saturn ring defects. (H-M) Disclinations (line defects in the LC) can become fused or entangled in arrays of particles embedded within a chiral nematic LC to form non-trivial topological links and knots, such as the Hopf link in M. (N,O) Photoinduced

modulation of LC anchoring and defect structures formed around azobenzene-functionalized microparticles. Polarized light micrographs show a silica colloid with surface-bound azobenzene units dispersed in a nematic LC (E7) phase prior to (N) and following (O) UV irradiation. Scale bars are 5 μm in H-M and 2.5 μm in N and O. Reproduced with permission.[27,61-63]

The range of colloidal phenomena encountered in LCs is particularly rich and diverse, as the type of LC director distortion that forms around dispersed micrometer-sized particles (as described above) can significantly influence the dynamics and equilibrium states of the colloids. For instance, it has been demonstrated that the elastically strained regions of LC in the vicinity of particles give rise to anisotropic interparticle forces that drive colloidal self-assembly. The symmetries of these interparticle forces and the resulting self-assembled structures depend on the type of LC distortion around the particles. For example, microspheres with tangential anchoring form chains aligned at an angle of 30° from the far-field director (Figure 3-6D),[27] whereas microspheres with homeotropic anchoring assemble into either straight chains aligned parallel to the far-field director (Figure 3-6E) or kinked chains oriented perpendicular to the far-field director (Figure 3-6F) when the director distortions exhibit dipolar and quadrupolar symmetry, respectively.[61] Under the influence of cohesive energies that arise from the elasticity of LCs, and with the assistance of optical tweezers, colloids in LCs can be assembled into stable 2D or 3D structures, such as the 2D crystal formed by quadrupolar colloids with Saturn ring defects shown in Figure 3-6G.[61] Arrays formed by these particles are particularly interesting, as defects around individual particles can fuse or entangle in the arrays (Figures 3-6H and 3-6M), particularly when the colloids are dispersed in chiral LCs.[62] Moreover, we note that by functionalizing microspheres with photoresponsive molecules, such as molecules with azobenzene units described in the previous sections, it is possible to dynamically switch between tangential (Figure 3-6O) and homeotropic (Figure 3-6P) surface anchoring states by irradiating with UV

and visible light. This capability provides, for example, optical control of elasticity-mediated interparticle forces.[63] Finally, dispersion of colloidal particles with higher geometrical complexity[64-67] or that exhibit non-uniform surface anchoring[68] presents additional opportunities for the creation of self-assembled colloidal structures.

We end this section by noting again that the examples of LC-mediated interparticle interactions described above, and the resulting multiparticle organizations, are strongly dependent on the surface-induced ordering of the LC. Because reorganization of periodic structures such as those shown in Figure 3-6 can give rise to pronounced changes in the optical and electrical properties of materials, the integration of stimuli-responsive chemical functionality onto the surfaces of colloids that are dispersed in LCs appears a fertile future area of research for the design of responsive materials. Indeed, as described below in Section 3.4 (see Figure 3-10), chemoresponsive arrays of particles at LC-aqueous interfaces have been demonstrated.

3.3.2 Dynamics of Colloids in LCs

The diffusion of colloids dispersed in LCs differs from that in simple isotropic phases in two important ways. First, translational diffusion of colloids in LCs is anisotropic and the effective viscosity experienced by colloids depends on the direction of particle displacement relative to the orientation of the director in the far-field. Specifically, the diffusion coefficient of particles undergoing a displacement in a direction parallel to the LC director is typically higher than the diffusion coefficients measured for an orthogonal displacement (Figures 3-7A and 3-7B).[69-72] Moreover, for nanometer-sized particles, these diffusion coefficients have been shown to be influenced by the type of anchoring at the particle surface[71] because the local ordering of the LC changes the viscosities experienced by the colloids. Second, the diffusion of particles in

LCs measured on time scales less than or comparable to the characteristic relaxation time of director fluctuations (~0.1 – 10 s) is not only anisotropic but also is anomalous.[73] When undergoing anomalous diffusion, the mean squared displacement of the particles no longer scales linearly with time, but is either slower (subdiffusion) or faster (superdiffusion) (Figure 3-7C). Anomalous diffusive behavior emerges at these short time scales due to dynamic fluctuations in the orientational order of nematic LCs away from the average director profiles adopted around particles (Figures 3-6A and 3-6C). These fluctuations create elastic forces that transiently act on the particles and give rise to particle motion that can no longer be described by a simple diffusion process. Because these director fluctuations will be dependent on the LC-particle surface interactions, measurements of diffusive motions of particles may offer the basis of a sensitive and straightforward means of reporting chemical and physical events occurring at the surfaces of the particles.

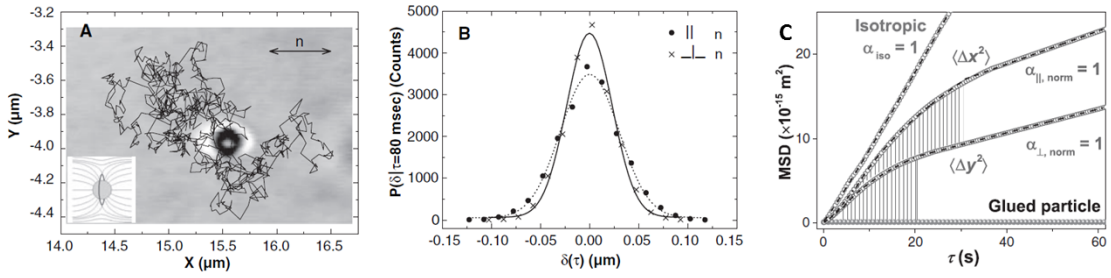

Figure 3-7. Anisotropic and anomalous diffusion of colloids in LCs.

(A, B) Anisotropic diffusion of a droplet of an isotropic liquid (about which a Saturn ring defect was formed) in nematic E7. A representative droplet trajectory is depicted in (A) and histograms of droplet displacements parallel and perpendicular to the nematic director (with Gaussian fits) are presented in (B). (C) Anomalous diffusion of a microparticle in a LC. Mean squared displacement of a silica colloid (homeotropic surface anchoring and dipolar distortions of the director) in a nematic phase of IS-8200 in directions parallel (x) and perpendicular (y) to the far-field LC director. Data for the same microsphere in the isotropic phase of IS-8200 is also shown. Reproduced with permission.[69,73]

3.3.3 Active Transport of Colloids in LCs

The dependence of interparticle interactions and colloidal transport processes on local LC order hints at many opportunities for the design of material that respond dynamically to changes in that local order. Such changes in order might be, for example, triggered by changes in the anchoring of the LC on the particle surface or via application of external fields. To illustrate the general opportunity in this area of research based on colloidal transport phenomena in LCs, we describe some recent experiments that have characterized changes in particle transport in LCs in response to externally applied fields. A particularly striking example is the phenomenon of LC-enabled electrophoresis (LCEEP) (Figure 3-8).[74,75] When particles are dispersed in isotropic solutions, the average motion of ionic species in the fluid in response to an applied field occurs in directions parallel or antiparallel to the polarity of the applied field. However, when a particle (either charged or neutral) dispersed in a LC generates a dipolar distortion of the director, application of a DC electric field in a direction orthogonal to the particle's dipole produces an electrophoretic motion in a direction parallel or antiparallel to the dipole (depending on the magnitude of the dielectric anisotropy of the LC) (Figures 3-8A and 3-8B). This LCEEP is caused by the breaking of the symmetry of the LC director profile in the vicinity of the particle, which leads to differences in the electroosmotic flows around the particle on either side of the plane indicated by the dashed line in Figures 3-8A and 3-8B. This explanation is further supported by the observation that when the distortions of the LC director around a particle instead are symmetric with respect to this plane, as is the case for a particle with a Saturn ring defect, no LCEEP occurs (Figure 3-8C). Notably, the direction of motion of dipolar particles due to LCEEP does not depend on the polarity of the applied electric field (Figures 3-8A and 3-8B). This allows unidirectional electrophoretic particle transport (in a direction set by the orientation

of each particle's dipole) to be achieved by LCEEP with an AC field, both in cases where an AC field is applied perpendicular (as in Figures 3-8A and 3-8B) or parallel to the orientation of the dipole (Figure 3-8D). LCEEP thus affords new and exciting possibilities for sensitive manipulation of the motion of colloids dispersed in LCs, and thus for the design of responsive or active materials, particularly in LC films designed with spatial variations in the director field.

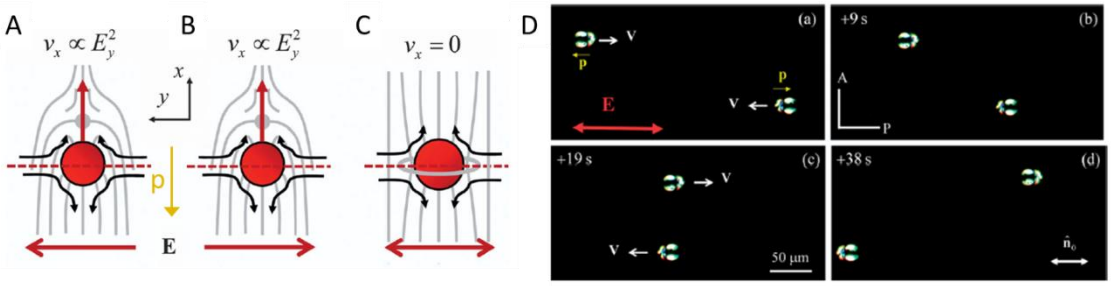

Figure 3-8. Electrophoresis of colloids in LCs.

(A, B) Schematic illustrations depicting LC-mediated electrophoresis of a colloid with dipolar symmetry in a nematic LC. The symmetry of electroosmotic flows around the particle is broken when an electric field is applied along the y axis, which induces electrophoretic motion of the particle in the x direction, anti-parallel to the orientation of the topological dipole defined by the LC. (C) For a particle with quadrupolar symmetry, no electrophoretic motion is observed when an electric field is applied in the y-direction. (D) Sequence of polarized light micrographs that depict LC-enabled electrophoresis of two silica microspheres that induce dipolar distortions of the director in a LC when an AC electric field is applied. The direction of the electrophoretic motion of each microsphere depends on the orientation of each microsphere's elastic dipole (p). Modified and reproduced with permission.[60]

Whereas the example above describes a field-driven response of a dispersion of particles in LC (e.g., electrophoresis), an emerging area of study addresses the situation where dissipative processes internal to the fluid (e.g., consumption of a fuel) drive transport processes. Specifically, the active transport of self-propelling particles, represented by rod-shaped motile bacteria with sizes comparable to the micrometer-sized synthetic particles described above, has also been shown to be significantly altered in the nematic phase of the biocompatible lyotropic

chromonic LC formed by aqueous solutions of disodium cromoglycate (DSCG). This particular active and anisotropic soft material system will be discussed in detail in Chapters 4-6 of this thesis.

Overall, dispersion of micrometer-sized particles (ranging from synthetic colloids to living bacteria) in LCs defines new opportunities for directing and dynamically tuning the spatial organization and self-assembly of the particles. The diversity of equilibrium and dynamic phenomena reflect the interplay of the effects of surface anchoring, elasticity, and defects, and suggests the basis of a multitude of designs of responsive materials based on colloidal dispersions in LCs. In addition, we note that these same properties of LCs present additional opportunities to control the transport of particles in LCs by application of external fields as well as to manipulate the dynamical behaviors of self-propelling "active" particles, including living cells.

3.4 Interfacial Behavior of Molecular and Colloidal Adsorbates

An earlier section of this chapter focused on how chemically functionalized interfaces of various types (e.g., photoresponsive or chemically reactive) can direct changes in the ordering of LCs to create responsive materials. In this section, we highlight the "inverse problem" wherein the order inherent to LC phases directs the organization of interfacial adsorbates. Because it is relatively easy to change the order within the bulk of a LC using an external field (such as an electric field of the type used in a LCD), the use of LC order to direct interfacial organization is a promising principle for the design of actively controlled and responsive materials. Indeed, the phenomenon of LC-directed organization of interfacial adsorbates can be viewed as a logistical

extension of the previous section in which the effects of LC order on the organization of colloidal species within the bulk of a LC was discussed.

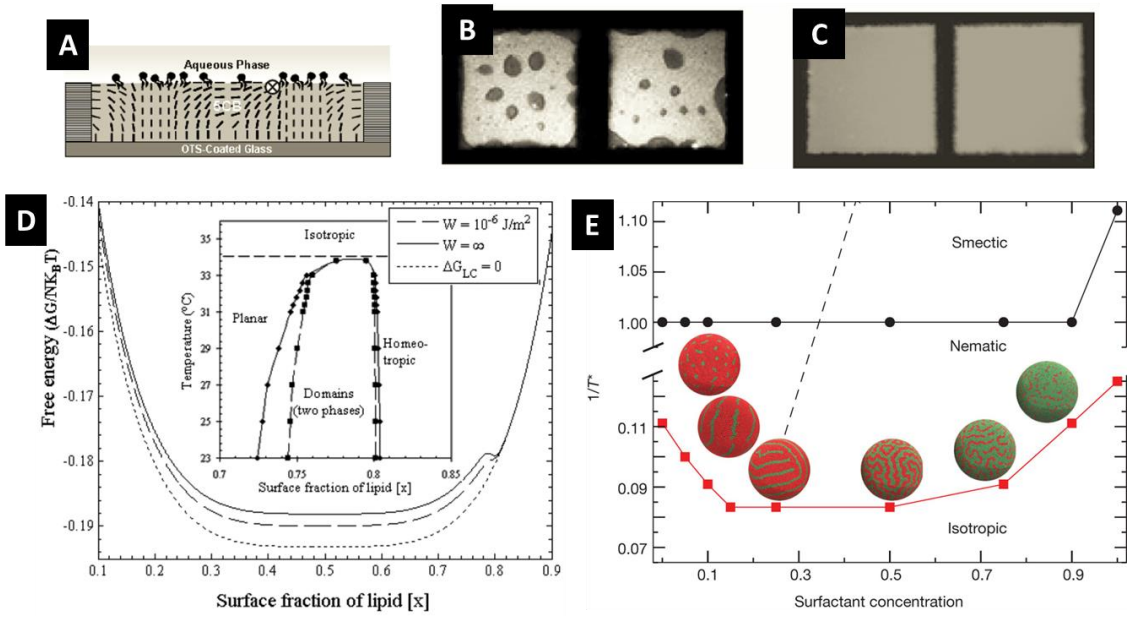

Figure 3-9. LC-driven phase separation of amphiphilic adsorbates.
(A) Schematic illustration of the phase separation of a monolayer of phospholipids at an aqueous-LC interface. The elastic energy stored in the strained state of the LC film triggers the phase separation. (B) Fluorescence micrograph of a phase separated monolayer of fluorescently-labeled phospholipid at the aqueous interface of a nematic 5CB film (32.0°C). (C) Fluorescence micrograph of the sample in (B) after heating the 5CB to form an isotropic phase (34.0°C). (D) Plot of dimensionless free energy versus mole fraction of lipid at aqueous-5CB interface in the presence and absence of elastic energy. The inset shows a phase diagram for the lipid monolayer, revealing phase separation induced by the elasticity of the LC. See text for details. (E) Phase diagram showing predictions (based on simulations) of the patterning of adsorbates on the surfaces of LC nanodroplets. Inset in the plot shows representative sketches of the adsorbates (green) at different surface concentrations. Reproduced with permission.[52,76]

The first example that we describe in this section addresses a phospholipid-decorated thin film of 5CB immersed in water (Figure 3-9A) and the role of the nematic order of the LC in directing the interfacial organization (phase behavior) of the phospholipids. In the nematic phase of 5CB, as shown in Figure 3-9B, it is apparent that lipid-lean and lipid-rich regions form at the

water-LC interface (based on the distribution of a fluorescent lipid probe). In contrast, in the isotropic phase of 5CB, following an increase in temperature of only a couple of degrees, the lipids are observed to cover the interface homogenously (Figure 3-9C). This experiment and others show that the ordering of the nematic LC influenced the assembly and lateral organization of the molecules adsorbed at these LC interfaces.[52,53] Here, the driving force for the phase separation of the surface adsorbed species, as depicted Figure 3-9A, is the elasticity of the LC film. In brief, the clustering of lipid on the interface of the LC results in the release of elastic energy stored in the initially strained state of the LC. A simple thermodynamic model was able to reproduce the phase behavior.[52,53] Figure 3-9D shows the free energy and the phase diagram of a monolayer of lipid supported on a film of LC predicted as a function of surface lipid fraction using the following expression:

$$\frac{\Delta G}{kT} = [n_1 lnx + (N - n_1)\ln(1-x) + \chi N x(1-x)] + \left[\frac{1}{2}\frac{K(T)}{D}\theta_S^2 + \frac{1}{2}W sin^2(\theta_S - \phi(x))\right]\frac{NA^*}{kT} \quad (3\text{-}4)$$

where n_1 is the number of lipid molecules at the interface, x is the fraction of surface lipid species relative to saturated monolayer coverage, A is the area per lipid, N is the number of adsorbed lipids at saturation, θ_S is the tilt angle of LC at the interface, ϕ is the easy angle of the LC, χ is a pairwise interaction parameter for adsorbed lipid molecules, $K(T)$ is the temperature-dependent LC elastic constant (one constant approximation), W is the anchoring strength coefficient, and D is the LC-film thickness. Examination of Figure 3-9D reveals that only in the presence of the nematic ordering is a miscibility gap predicted. This coupling between the strain within the LC and the interfacial phase behavior of adsorbates has been shown also to occur for soluble amphiphiles (such as cationic surfactants under conditions of high ionic strength[53]), indicating that it offers a versatile principle for the formation of patterned materials.

Significantly, because the interfacial phase behavior is coupled to elastic stresses, which in turn are dependent on the micrometer-scale geometry of the system, this coupling hints at future opportunities for the design of active and responsive materials based on control of shape on the micrometer-scale. Indeed, in complex biological systems such as bacteria, there is increasing evidence that such coupling between shape and elastic strain in liquid crystalline membranes is used to pattern molecules within membranes. We also comment that recent molecular-level simulations also predict that the orientational order and nematic elasticity of confined LC systems should lead to a rich range of interfacial phases on the surfaces of nanoscopic droplets of LCs (Figure 3-9E).[76]

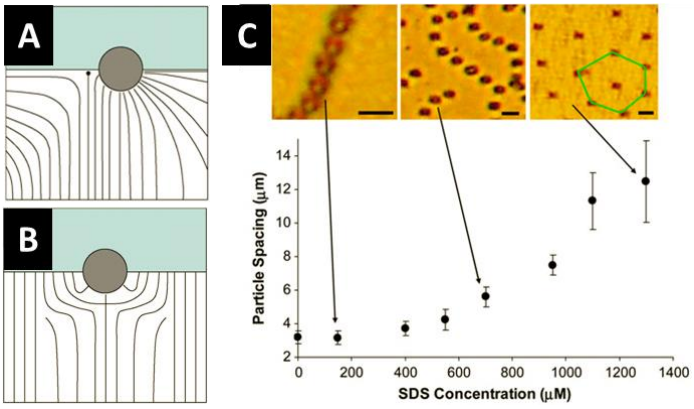

Figure 3-10. Chemoresponsive assemblies of microparticles at LC interfaces.
(A, B) Schematic illustrations of LC ordering around silica microparticles adsorbed at aqueous-LC interfaces. The LC is anchored in a homeotropic orientation of the surface of the microparticle, and the anchoring of the LC at the aqueous interface is either (A) planar or (B) homeotropic. (C) Change in organization of the microparticles triggered by the addition of a surfactant. The plot shows the center-to-center spacing of the particles as a function of the concentration of the surfactant sodium dodecylsulfate (SDS). Inset in (C) shows the bright field micrographs of particles at LC-water interface with the presence of 0.15, 0.7 and 1.3 mM SDS. Scale bars: 5 μm. Reproduced with permission.[77]

A second example of LC-directed interfacial ordering of adsorbates addresses solid particles adsorbed to LC interfaces. This example is particularly relevant to the design of responsive materials, as it was demonstrated that the ordering of microparticles could be manipulated reversibly via adsorption of amphiphiles at the LC interface, thus changing the type and orientation of the LC defect structure around particles.[77] As an example, we describe results obtained with microparticles with homeotropic LC anchoring. Each particle adsorbed at a LC-aqueous interface generates a point defect (Figures 3-10A and 3-10B). Depending on the orientation of LC at the aqueous interface, which was manipulated by varying the concentration of surfactants in aqueous media (sodium dodecylsulfate (SDS) in this example), the point defects were located either to the side (Figure 3-10A, planar LC anchoring at water interface) or below each microparticle (Figure 3-10B, homeotropic LC anchoring at water interface). Upon addition of SDS to the system, the organization of particles was observed to change reversibly between linear chains and hexagonal arrays of particles (Figure 3-10C).[77] This transition from one-dimensional to two-dimensional ordering was shown to result from the SDS-induced rotation of the topological dipole about the microparticles (Figure 3-10C). In addition, by varying the concentration of surfactant (orientation of the LC at the interface), the spacing of the particles within the linear assemblies could be varied.[77] Overall, this result provides proof of concept for the design of chemoresponsive arrays of particles at the interfaces of LC materials.

3.5 Emulsions of LCs

The interplay of surface anchoring, LC elasticity and topological defects is strongly dependent on the micrometer-scale geometry of LC systems. A particularly accessible and interesting system that reflects this interplay is based on spherical droplets of LCs dispersed in

aqueous phases. This section focuses on these so-called "nematic emulsions". We highlight two new findings to illustrate how confining LCs within droplets enables new opportunities for the design of responsive materials (in some cases, exquisitely responsive materials that are triggered by targeted species at picogram-per-milliliter concentrations in water).

3.5.1 Responsive Emulsions

At equilibrium, the ordering of LC within LC microdroplets dispersed in water reflects minimization of the above-described contributions of surface anchoring, bulk elastic deformations and topological defects to the free energy of the system.[78,79] For example, in pure water, LC droplets exhibit a so-called bipolar configuration, in which the LC aligns tangential to the droplet interface and two diametrically opposed point defects form at the droplet poles (Figure 3-11A). Similar to the surface-driven planar-to-homeotropic anchoring transition of planar LC films described above, adsorption of amphiphiles at the aqueous interfaces of LC droplets gives rise to a perpendicular orientation of the LC at the droplet interface, resulting in a so-called radial configuration with a single defect located at the center of the droplet (Figure 3-11A).[80-85] The balance of elastic, defect and surface energetics differs substantially in LC droplets relative to planar films of LCs, presenting opportunities for achieving unprecedented levels of responsiveness using LC droplets (see below for discussion).

Furthermore, several recent studies have revealed that amphiphiles can self-assemble *within* LC droplets to trigger ordering transitions. In this case, the ordering transition is driven by the formation of amphiphilic assemblies at the sites of topological defects (as opposed to conventional 'surface-driven ordering transitions' that involve changes in surface energetics).[86] Specifically, as shown in Figure 3-11C, bipolar-to-radial ordering transitions have been observed

in LC droplets dispersed in aqueous solution in the presence of bacterial endotoxin (lipid A portion displayed in Figure 3-11B) at picogram per milliliter concentrations, which is at least five orders of magnitude lower in concentration than that required to trigger surface-driven anchoring transitions in LC droplets. Confocal fluorescence microscopy confirmed that endotoxin was localized at the defect formed at the center of each LC droplet in a radial configuration (Figure 3-11D). Overall, these results indicate that the confinement of LCs in micrometer-sized droplets provides new principles for the design of remarkably responsive LC systems for targeting biological analytes. In addition, these results have motivated ongoing investigations of the self-assembly of amphiphiles in LCs, particularly in the nanoscopic environments defined by LC defects.

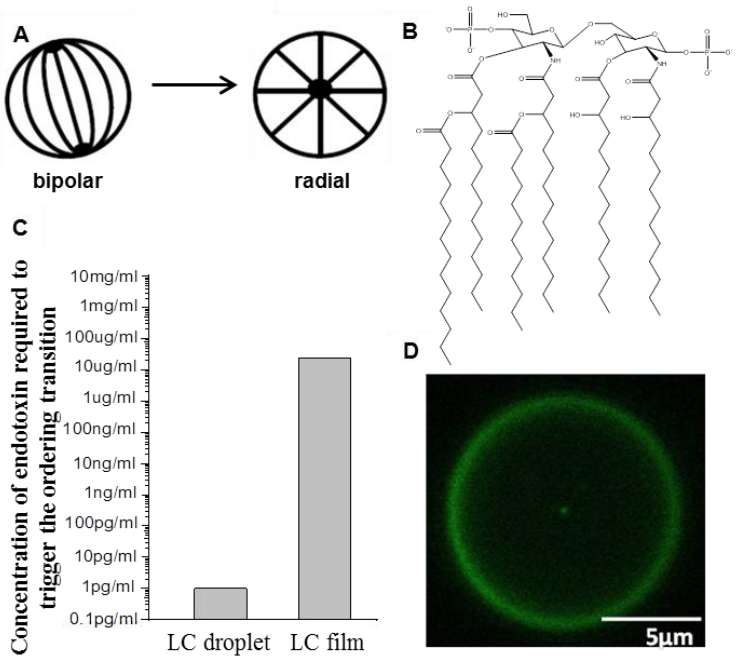

Figure 3-11. Ordering transitions in LC droplets triggered by picogram per milliliter concentrations of endotoxin.

(A) Schematic illustration of a bipolar configuration (left) and radial configuration (right) of a micrometer-sized droplet of a nematic LC. The bipolar configuration of the LC possesses two point defects located at the poles of the droplet. The radial configuration possesses a single point defect located

at the center of the droplet. (B) Molecular structure of lipid A, the glycolipid tail of endotoxin. (C) A comparison of the concentrations of endotoxin required to trigger an ordering transition in either (left) a micrometer-sized droplet of LC, or (right) a micrometer-thick film of a LC. The difference in concentration is approximately seven orders of magnitude, a reflection of the contrasting energetics of the two geometries (see text for details). (D) Confocal fluorescence micrograph showing localization of BODIPY-labeled endotoxin at the center of a 5CB droplet in the radial configuration. Modified and reproduced with permission.[86]

3.5.2 Templated Synthesis using LC Emulsion Droplets

It is increasingly recognized that colloids with non-spherical shapes and chemically heterogenous surfaces (e.g., so-called "patchy" particles) offer many opportunities to tune the functional properties of colloids (e.g., for drug delivery). Interest in these inhomogeneous particles is further motivated by their lack of symmetry, which leads to strong coupling (e.g., orientational coupling) to external fields. As such, they represent a promising set of building blocks for the creation of stimuli-responsive materials. The synthesis of such particles, however, remains a substantial challenge. Recently, LC droplets have been explored as a general and facile class of templates for the synthesis of spherical and non-spherical polymer particles with chemical patches, as shown in Figures 3-12A through 3-12F.[87,88] To synthesize such particles, micrometer-sized LC droplets (comprised of reactive liquid crystalline crosslinker RM257 and non-reactive 5CB) were prepared in the presence of colloidal particles (e.g., gold, silica, polystyrene, etc). After homogenization, the colloids were found to be preferentially positioned at the topological defects (point defects) that form at the north and south poles of the bipolar droplets (Figures 3-12B and 3-12C). By localizing at the sites of defects, the particles decrease the energetic cost associated with both diminished orientational order of molecules in the core of the defects and elastic deformations of LCs near the defects.[88] The surfaces of the colloids

protrude from the LC droplet, thus defining patches with a chemistry determined by the composition of the colloid. Subsequently, the positons of the colloids on the surfaces of LC droplets were preserved by photopolymerization. This procedure results in spherical particles consisting of a crosslinked polymeric network swollen with 5CB in which colloids remain attached at the poles. Finally, non-spherical patchy particles were prepared by extraction of 5CB from the above-described particles. Extraction of 5CB resulted in contraction of the polymerized particles in a direction perpendicular to the axis connecting the poles of the droplet. It was shown that colloids with a range of compositions and surface properties can be used in this procedure. Thus, the colloids can be tailored to introduce desired functional properties to the resulting patchy particles.[87]

The above strategy is, however, made more complex by the existence of multiple local energetic minima (i.e., two boojums), which can lead to kinetic traps for colloids on the droplet surfaces and result in heterogeneous populations of patchy particles.[87-90] For example, bipolar LC droplets with magnetic colloids adsorbed at both poles were observed to align in a bimodal distribution of orientations with droplets oriented under a weak external magnetic field (Figure 3-12H). To address this issue, a recent study used reversible switching of the internal configurations of LC droplets to drive the colloids to a single location on the LC droplet surfaces. As shown in Figure 3-12G, a transition triggered by adsorption of surfactants induces a long-range elastic force that sweeps adsorbed colloids to a unique location (the location of the single defect of the so-called “preradial” LC droplet configuration).[89] A subsequent reversal of this ordering transition results in a homogeneous population of bipolar LC droplets with colloids remaining at a single location (one of the boojum defects). Following this procedure, the

population of LC droplets responded in a homogeneous/uniform manner to the application of an applied magnetic field (Figure 3-12H).

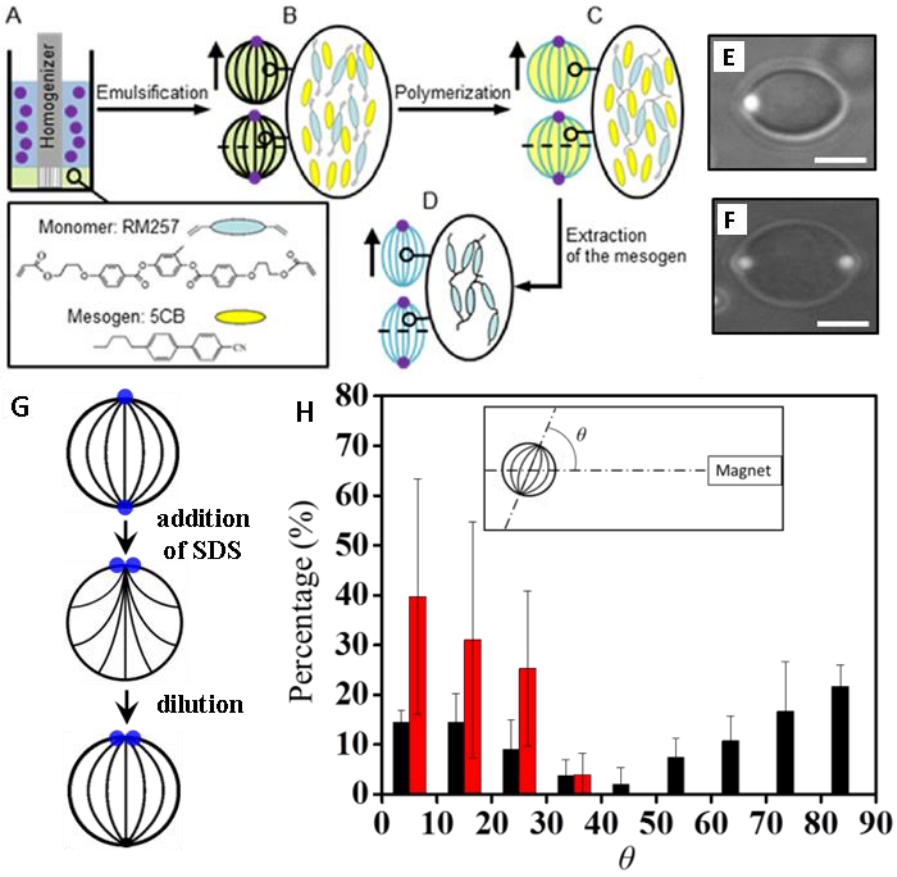

Figure 3-12. LC droplet-templated synthesis of anisometric and chemically "patchy" particles. Schematic illustration of the use of LC droplets for the synthesis of spherical and non-spherical particles with chemical patches: (A) Emulsification of LCs in water to form spherical droplets with bipolar configurations. In the bipolar configuration, the droplets possess a point defect at the north and south poles. (B) Formation of bipolar nematic droplets with either one or two fluorescent polystyrene (PS) colloids positioned at the poles. The colloids protrude from the surface of the LC droplets to create chemical patches. (C) Formation of spherical polymeric particles after photopolymerization of a bifunctional crosslinker RM257 dissolved into the LC. (D) Formation of non-spherical particles following extraction of the unreacted LC from the particles. (E, F) Combined bright field and fluorescent micrographs of lemon-shape particles presenting either one or two fluorescent PS colloids (chemical patches) at their poles, respectively. (G) Schematic illustration of synthesis of homogeneous populations of bipolar patchy LC droplets by reversible switching of LC order (through adsorption and desorption of SDS). (H) Magnetic-field-induced distribution of orientations of bipolar LC droplets with magnetic

colloids prior to (black data) or after (red) the treatment by SDS shown in G. Note that the treated population responded more uniformly to the application of the magnetic field. Reproduced with permission.[87,89]

In addition to the above-described studies in which colloids are positioned at defects on the surfaces of LC droplets, previous studies have revealed that colloids can also localize at defects in bulk LCs.[30,91-94] As described in Section 3.2, double twist cylinders in blue phase LCs arrange into lattice structures with high densities of defect lines (Figure 3-13A). Computer simulations have suggested that nanoparticles dispersed in blue phases can be trapped in the defect lines, and thus eliminate the energetic cost of the defect core as well as regions of high strain in the LC in the vicinity of the defect core, resulting in stabilization of blue phase (Figure 3-13B).[12,95] Overall, these studies provide new insight regarding the self-assembly of colloids at defects formed in LCs. Whereas blue phases are currently being explored as the basis of fast-switching displays (i.e., response to applied electric field), the rapid response of the blue phase suggests that this phase may also form the basis of materials that permit fast manipulation of the organization of colloids.

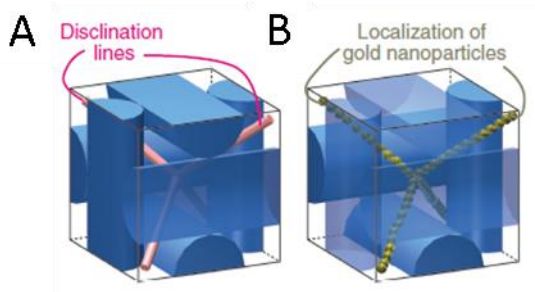

Figure 3-13. Stabilization of blue phases through localization of nanoparticles at defects.
(A) Schematic illustration of disclination lines formed within blue phases of LCs. (B) Schematic illustration of the positioning of nanoparticles at the disclinations. The cylinders represent the double-twist helical structure (see Fig. 1). Reproduced with permission.[95]

Finally, we note that formation and characterization of a new class of emulsion in which droplets of a thermotropic LC such as 5CB are dispersed within a continuous aqueous lyotropic chromonic LC phase will be described in Chapter 7 of this thesis.[96] The interesting properties of these LC-in-LC emulsions, in particular, their response to weak applied fields, suggest that LC systems comprised of coexisting LC phases represent a promising class of materials that respond to subtle perturbations.

3.6 LC Gels

The last topic that we address in this chapter revolves around LC-based gels. In contrast to particle-based gels formed in isotropic liquids, particle-based gels formed in LCs exhibit a range of interesting properties that arise from the responsiveness of the LC.[97] For example, LCs within the domains defined by the particle networks of the gel remain responsive to external stimuli, including biomolecules in aqueous media and gas phase analytes.[98,99] In addition, the use of photoactive dyes permits reversible control of the nematic-isotropic phase boundary, thus providing the basis of principles for actively tunable gels. In this section, we review a series of studies that have provided insight into the formation of LC gels and the factors that control their properties.

Past studies have shown that dispersions of colloidal particles in LCs can generate gels (colloid-in-LC gels or CLC gels) with solid-like properties and elastic moduli in the range of 100 Pa – 100 kPa via three pathways.[100-102] The first of these studies, initiated roughly a decade ago by Terentjev, Poon and coworkers[103] involved dispersing micrometer-sized poly(methyl methacrylate) (PMMA) colloids in the isotropic phase of a mesogen and subsequently cooling the system into the nematic phase. During slow cooling, colloids were expelled from advancing

nematic fronts following the nucleation and growth of nematic phase domains (expulsion is driven by the elastic free energy associated with the strain of the LC about the colloids) (Figure 3-14A).[100,104] The growth of the nematic domains was arrested upon jamming of colloids between the domains and the associated formation of a cellular microstructure, as shown in Figure 3-14B (green colored discontinuous nematic domains surrounded by a continuous particle-rich phase).[105]

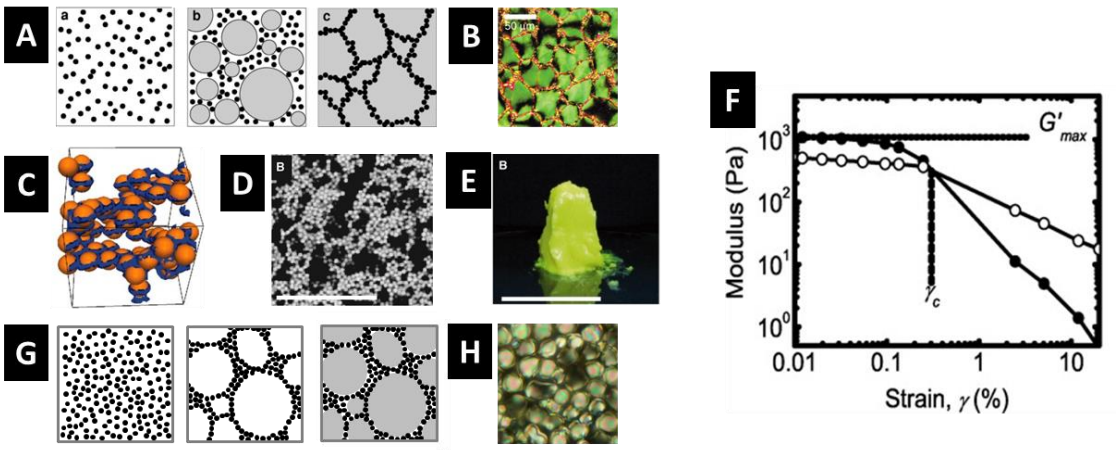

Figure 3-14. LC-based colloidal gels.

(A) Schematic illustration of the gelation pathway (left to right) proposed by Terentjev *et al.* in which nematic domains (grey) expel particles to form a jammed network. (B) Optical micrograph of the network of particles formed through the process shown in (A). (C) Results of a simulation of gelation that results from the entanglement of defect lines around particles, as reported by Wood et al. (orange spheres represent particles dispersed in a LC and blue rings represent defect lines) (D) Fluorescence micrograph showing a continuous network of particles formed by entanglement of disclinations. Scale bar is 20 μm. (E) Photograph of a LC gel at room temperature showing self-supporting behavior of the material (prepared as described in C). Scale bar is 1 cm. (F) Mechanical response of gel as a function of applied strain (28% by vol colloids; prepared as described in C). (G) A schematic illustration of a gelation pathway involving spinoidal decomposition of a colloidal dispersion in the isotropic phase of a mesogen, followed by subsequent formation of a nematic phase, as proposed by Bukusoglu et al. (H) Optical micrograph of the gel formed following the process described in (G). Scale bar is 40 μm. Reproduced with permission.[101-103,105]

A second pathway leading to gelation was described by Wood et al.[102] They demonstrated that mechanical shearing of micrometer-sized PMMA particles (that caused homeotropic alignment of LCs and so-called Saturn-ring defect lines (Figure 3-14C)) dispersed in LCs led to gelation at high loadings of particles (>15% vol.).[102] By using a combination of simulations and rheological measurements, they showed that the interparticle interactions leading to gelation arose from the entanglement of line defects (sharing of defects) generated about the particles. The composite material exhibited the mechanical properties of a self-standing, solid-like viscoelastic gel (Figures 3-14C through 3-14F, note that G'>G" at low frequencies).[102]

More recently, Bukusoglu et al. reported a third pathway leading to formation of LC gels. The pathway involved the spinodal decomposition and dynamic arrest of colloids (Figures 3-14G and 3-14H).[101] In this approach, the colloids were initially dispersed in the isotropic phase of the mesogen. Upon cooling, the colloids underwent a spinodal decomposition-type phase separation in the isotropic phase of the mesogen. The phase separation produced a continuous colloid-rich phase and a discontinuous colloid-lean phase. Subsequent to the formation of the colloidal network, a nematic to isotropic phase transition occurred in the colloid-lean regions of the system. Significantly, and in contrast to the first pathway leading to gel formation (see above), the LC-rich domains that formed in the gel were determined by the colloid-domain morphology that developed during the phase transition in the isotropic phase of the mesogens. With the addition of a third component, particles with diameters of hundreds of nanometers, this pathway has also provided new routes for ternary composites with hierarchical microstructures.[106]

As noted at the start of this section, colloid-based LC gels formed via the above-described pathways exhibit a range of interesting properties that arise from the responsiveness of the LC domains.[97] In contrast to the LC films described in Section 3.2 of this chapter, the LC

gels are self-supporting and for this reason have substantial technological promise. Recent studies have demonstrated that they can be combined with chemically functionalized interfaces to create stimuli-responsive gels.[98,99] In addition, because the stiffness of these materials results from interparticle forces mediated by the nematic order, and because photoactive dyes permit reversible control of the nematic-isotropic phase boundary, an exciting frontier of research involving colloid-based LC gels relates to the creation of materials with optically tunable mechanical properties. Because, for example, fundamental cell behaviors are dependent on their mechanical environment, and because the moduli of the LC gels are in a range (1-10 kPa) that is relevant to some mammalian cell lines[98], the possibility exists to make photoactive LC gels that can be used to dynamically control cell behaviors.

3.7 Concluding Remarks

This chapter describes the remarkable richness in equilibrium and dynamic behaviors of LCs that emerge from the interplay of the effects of surface-induced ordering, the elasticity of LCs and the formation of topological defects in LCs confined in complex geometries. This delicate balance of effects gives rise to a level of responsiveness in LC systems that is without precedent in other classes of materials, and thus it offers many opportunities to create new materials that can change their properties in response to subtle physical or chemical stimuli. It is also evident from this chapter that the design of these LC-based materials rely heavily on concepts from colloid and interface science and that the complexity of phenomena that result from the presence of an anisotropic solvent with viscoelastic properties creates many unresolved questions. Here we summarize a few of these problems:

i. Ionic phenomena, including electrical double layers. Historically, studies of LCs conducted in the context of LCDs have generally minimized the presence of ions in LCs due to their adverse effects on external electrical fields. However, when dealing with LC systems in contact with water or with interfaces decorated with ionic adsorbates, ions are present at high concentrations. Furthermore, the relatively high dielectric constants of many LCs (e.g., relative dielectric constants from 4-16 are common) promote disassociation of salts within LCs. The presence of ions in the bulk of LCs and near interfaces can give rise to a range of equilibrium and dynamic phenomena that are only now beginning to be explored. For example, electric fields formed within the diffuse part of electrical double layers at aqueous interfaces can generate torques on LCs that result in orientational transitions.[107] Moreover, the arrival of ionic surfactants at the interface likely modulates the double layer, a factor that is not generally considered in explanations of biomolecule- or surfactant-induced ordering transitions in LCs. In addition, as illustrated by recent measurements involving electrophoresis in LCs, electrokinetic processes in the anisotropic environment defined by a LC can give rise to complex colloidal transport phenomena.

ii. Specific ion effects. Whereas the above-described ionic effects can be largely described within the context of classical colloidal descriptions of electrical double layers and electrokinetic theory, an additional set of observations reveals that the specific identity of ions at aqueous-LC interfaces can have pronounced effects on LC ordering.[108] Based on complementary studies using monolayers of mesogens, the effects appear to involve ion-specific penetration into the interface, and thus perturbations to the ordering of LCs through a mechanism that is distinct from double

layers. No description of the mechanism exists, although it appears closely related to specific ion effects observed in bulk aqueous solution (which are also not understood).

iii. Chirality of interfaces. Several recent studies of chiral adsorbates at interfaces – including solid-LC interfaces and LC-aqueous interfaces - have revealed that the ordering of achiral LCs can be strongly influenced by the chirality of the adsorbates.[36,37] While the effects of chiral dopants in the bulk of LCs have been widely explored, the mechanisms through which chiral interfacial adsorbates influence the ordering of LCs have not been elucidated.

iv. Molecular structure and compositions of defects. As described in this chapter, on the basis of theory and simulation, it is generally accepted that the local order of mesogens within the cores of topological defects is low compared to the bulk LC. However, experimental characterization of the local order is limited. Furthermore, many LCs are comprised of mixtures of mesogens and it is not known to what extent the local compositions of defects differ from the bulk LC. These effects are likely to be pronounced in some mixtures of mesogens.

v. Spatial organization of adsorbates on LC nanodroplets. Recent experimental studies have revealed that elastic stresses within confined LC systems can regulate the phase behavior of adsorbates at the LC interface.[76] Specifically, micrometer-scale domains of lipids and surfactants were induced by the LC. Simulations involving nanodroplets of LC, however, suggest that a far richer range of interfacial phases of adsorbates are possible on LC interfaces. Experimental evidence of such phases has not yet been

found but might be observed through x-ray reflectivity or small angle neutron scattering measurements.

vi. The majority of studies reported in this paper involve optical measurements of the ordering of micrometer-sized LC phases. Non-linear optical measurements (second harmonic generation and infrared-visible sum frequency spectroscopy) at LC-solid interfaces have established that the order (and orientation) of the first layer of mesogens at an interface can differ substantially from the bulk LC phase.[109,110] To date, there are no published studies characterizing spectroscopically the orientational order at buried LC-aqueous interfaces. Such studies offer the potential to provide insight into the effects of, for example, specific ions on the orientations of LCs.

vii. Lateral organization of peptides and proteins at aqueous-LC interfaces. As discussed in this chapter, adsorbates at aqueous-LC interfaces exhibit high mobilities and thus can reorganize on experimental time-scales to trigger patterned orientational responses in LCs.[52] In this context, a number of past studies have revealed that proteins and peptides adsorbed at lipid-decorated LC-aqueous interfaces exhibit reproducible patterns (e.g., circular domains or fibrillar, fractal-like structures).[111] These observations suggest that interactions between peptides and proteins are forming lateral assemblies at the interface that reflect structural properties inherent to the adsorbates. The origins of these interactions, and the processes by which they give rise to lateral assemblies, are not understood.

viii. Influence of LC droplet size on internal ordering of LC. A number of studies have reported that the ordering of LCs within micrometer-sized droplets is strongly dependent on the size of the LC droplets.[79] In particular, although the easy axis of

nematic droplets at the LC-aqueous interface is tangential to the interface of the droplets, it has been observed that small LC droplets (typically around a micrometer in size) spontaneously exhibit a radial configuration (in the absence of an added adsorbate). Although it appears that saddle-splay strain in the LC may be able to provide an account of this change in ordering with the size of the LC droplets, a definitive explanation remains to be established.

Acknowledgements

This chapter describes work that has been supported by the National Science Foundation (under awards DMR-1121288 (MRSEC), CBET-1263970, DMR-1435195), the National Institutes of Health (CA108467), the Army Research Office (W911-NF-11-1-0251 and W911-NF-14-1-0140), and the Department of Energy (DE-SCS0004025)

3.8 References

*This chapter was originally submitted as an invited Review in the journal *Annual Reviews of Chemical and Biomolecular Engineering*. My contribution to this review was in writing Section 3.3, discussing content of other sections, and assisting my co-authors in the proof reading of the manuscript and preparation of some of the figures.

†Figure 3-1K: Reprinted from Park, H.; Lavrentovich, O. D. Lyotropic Chromonic Liquid Crystals: Emerging Applications. In *Liquid Crystals Beyond Displays: Chemistry, Physics, and Applications*; Li, Q., Ed.; pp 449-484, Copyright (2012), with permission from John Wiley & Sons.

1. de Gennes, P. G.; Prost, J. *The Physics of Liquid Crystals*; 2nd ed.; Oxford University Press: New York, 1995.
2. Borshch, V.; Kim, Y.-K.; Xiang, J.; Gao, M.; Jakli, A.; Panov, V. P.; Vij, J. K.; Imrie, C. T.; Tamba, M. G.; Mehl, G. H.; Lavrentovich, O. D. Nematic Twist-Bend Phase with Nanoscale Modulation of Molecular Orientation. *Nat. Commun.* **2013**, 4, 2635.
3. Chen, D.; Nakata, M.; Shao, R.; Tuchband, M. R.; Shuai, M.; Baumeister, U.; Weissflog, W.; Walba, D. M.; Glaser, M. A.; Maclennan, J. E.; Clark, N. A. Twist-Bend Heliconical Chiral Nematic Liquid Crystal Phase of an Achiral Rigid Bent-Core Mesogen. *Phys. Rev. E* **2014**, 89, 022506.
4. Cestari, M.; Diez-Berart, S.; Dunmur, D. A.; Ferrarini, A.; de la Fuente, M. R.; Jackson, D. J. B.; Lopez, D. O.; Luckfurst, G. R.; Perez-Jubindo, M. A.; Richardson, R. M.; Salud, J.; Timimi, B. A.; Zimmerman, H. Phase Behavior and Properties of the Liquid-Crystal Dimer 1",7"-bis(4-cyanobiphenyl-4'-yl) heptane: A Twist-Bend Nematic Liquid Crystal. *Phys. Rev. E* **2011**, 84, 031704.
5. Hough, L. E.; Jung, H. T.; Kruerke, D.; Heberling, M. S.; Nakata, M.; Jones, C. D.; Chen, D.; Link, D. R.; Zasadzinski, J.; Heppke, G.; Rabe, J. P.; Stocker, W.; Korblova, E.; Walba, D. M.; Glaser, M. A.; Clark, N. A. Helical Nanofilament Phases. *Science* **2009**, 325, 456–460.
6. Pintre, I. C.; Serrano, J. L.; Ros, M. B.; Martínez-Perdiguero, J.; Alonso, I.; Ortega, J.; Folcia, C. L.; Etxebarria, J.; Alicante, R.; Villacampa, B. Bent-Core Liquid Crystals in a Route to Efficient Organic Nonlinear Optical Materials. *J. Mater. Chem.* **2010**, 20, 2965–2971.
7. Otani, T.; Araoka, F.; Ishikawa, K.; Takezoe, H. Enhanced Optical Activity by Achiral Rod-Like Molecules Nanosegregated in the B4 Structure of Achiral Bent-Core Molecules. *J. Am. Chem. Soc.* **2009**, 131, 12368–12372.
8. Kim, H.; Lee, S.; Shin, T. J.; Cha, Y. J.; Korblova, E.; Walba, D. M.; Clark, N. A.; Lee, S. B.; Yoon, D. K. Alignment of Helical Nanofilaments on the Surfaces of Various Self-Assembled monolayers. *Soft Matter* **2013**, 9, 6185–6191.
9. Yang, D.; Crooker, P. Chiral-Racemic Phase Diagrams of Blue-Phase Liquid Crystals. *Phys. Rev. A* **1987**, 35, 4419–4423.
10. Meiboom, S.; Sethna, J. P.; Anderson, P. W.; Brinkman, W. F. Theory of the Blue Phase of Cholesteric Liquid-Crystals. *Phys. Rev. Lett.* **1981**, 46, 1216–1219.
11. Wright, D. C.; Mermin, N. D. Crystalline Liquids: The Blue Phases. *Rev. Mod. Phys.* **1989**, 61, 385–432.
12. Kikuchi, H.; Yokota, M.; Hisakado, Y.; Yang, H.; Kajiyama, T. Polymer-Stabilized Liquid Crystal Blue Phases. *Nat. Mater.* **2002**, 1, 64–68.

13. Karatairi, E.; Rožič, B.; Kutnjak, Z.; Tzitzios, V.; Nounesis, G.; Cordoyiannis, G.; Thoen, J.; Glorieux, C.; Kralj, S. Nanoparticle-Induced Widening of the Temperature Range of Liquid-Crystalline Blue Phases. *Phys. Rev. E* **2010**, 81, 041703.
14. Lee, H.; Labes, M. M. Phase Diagram and Thermodynamic Properties of Disodium Cromoglycate-Water Lyomesophases. *Mol. Cryst. Liq. Cryst.* **2007**, 91, 53–58.
15. Lydon, J. Chromonic Review. *J. Mater. Chem.* **2010**, 20, 10071–10099.
16. Mushenheim, P. C.; Trivedi, R. R.; Tuson, H. H.; Weibel, D. B.; Abbott, N. L. Dynamic Self-Assembly of Motile Bacteria in Liquid Crystals. *Soft Matter* **2014**, 10, 88–95.
17. Mushenheim, P. C.; Trivedi, R. R.; Weibel, D. B.; Abbott, N. L. Using Liquid Crystals to Reveal How Mechanical Anisotropy Changes Interfacial Behaviors of Motile Bacteria. *Biophys. J.* **2014**, 107, 255–265.
18. Zhou, S.; Sokolov, A.; Lavrentovich, O. D.; Aranson, I. S. Living Liquid Crystals. *Proc. Natl. Acad. Sci. U. S. A.* **2014**, 111, 1265–1270.
19. Sokolov, A.; Zhou, S.; Lavrentovich, O. D.; Aranson, I. S. Individual Behavior and Pairwise Interactions between Microswimmers in Anisotropic Liquid. *Phys. Rev. E* **2015**, 91, 013009.
20. Kumar, A.; Galstian, T.; Pattanayek, S. K.; Rainville, S. The Motility of Bacteria in an Anisotropic Liquid Environment. *Mol. Cryst. Liq. Cryst.* **2013**, 574, 33–39.
21. Kishikawa, K.; Sugiyama, T.; Watanabe, T.; Aoyagi, S.; Kohri, M.; Taniguchi, T.; Takahashi, M.; Kohmoto, S. Simple and Efficient Chiral Dopants to Induce Blue Phases and their Optical Purity Effects on the Physical Properties of Blue Phases. *J. Phys. Chem. B* **2014**, 118, 10319–10332.
22. Jerome, B. Surface Effects and Anchoring in Liquid Crystals. *Rep. Prog. Phys.* **1991**, 54, 391–451.
23. Gupta, V. K.; Abbott, N. L. Azimuthal Anchoring Transition of Nematic Liquid Crystals on Self-Assembled Monolayers Formed from Odd and Even Alkanethiols. *Phys. Rev. E* **1996**, 54, 4540–4543.
24. Lockwood, N. A.; Gupta, J. K.; Abbott, N. L. Self-Assembly of Amphiphiles, Polymers and Proteins at Interfaces between Thermotropic Liquid Crystals and Aqueous Phases. *Surf. Sci. Rep.* **2008**, 63, 255–293.
25. Collings, P. J.; Hird, M. *Introduction to Liquid Crystals Chemistry and Physics*; Taylor and Francis: London, 1997.
26. Lavrentovich, O. D. Topological Defects in Dispersed Liquid Crystals, or Words and Worlds around Liquid Crystal Drops. *Liq. Cryst.* **1998**, 24, 117–125.
27. Poulin, P.; Weitz, D. A. Inverted and Multiple Nematic Emulsions. *Phys. Rev. E* **1998**, 57, 626–637.
28. Guzman, O.; Kim, E. B.; Grollau, S.; Abbott, N. L.; de Pablo, J. J. Defect Structure around Two Colloids in a Liquid Crystal. *Phys. Rev. Lett.* **2003**, 91, 235509.
29. Poulin, P.; Stark, H.; Lubensky, T. C.; Weitz, D. A. Novel Colloidal Interactions in Anisotropic Fluids. *Science* **1997**, 275, 1770–1773.
30. Skarabot, M.; Ravnik, M.; Zumer, S.; Tkalec, U.; Poberaj, I.; Babic, D.; Musevic, I. Hierarchical Self-Assembly of Nematic Colloidal Superstructures. *Phys. Rev. E* **2008**, 77, 061706.
31. Koenig, G. M.; de Pablo, J. J.; Abbott, N. L. Characterization of the Reversible Interaction of Pairs of Nanoparticles Dispersed in Nematic Liquid Crystals. *Langmuir* **2009**, 25, 13318–13321.

32. Gu, Y.; Abbott, N. L. Observation of Saturn-Ring Defects around Solid Microspheres in Nematic Liquid Crystals. *Phys. Rev. Lett.* **2000**, 85, 4719–4722.
33. Loudet, J. C.; Barois, P.; Poulin, P. Colloidal Ordering from Phase Separation in a Liquid-Crystalline Continuous Phase. *Nature* **2000**, 407, 611–613.
34. Shah, R. R.; Abbott, N. L. Principles for Measurement of Chemical Exposure Based on Recognition-Driven Anchoring Transitions in Liquid Crystals. *Science* **2001**, 293, 1296–1299.
35. Hunter, J. T.; Pal, S. K.; Abbott, N. L. Adsorbate-Induced Ordering Transitions of Nematic Liquid Crystals on Surfaces Decorated with Aluminum Perchlorate Salts. *ACS Appl. Mater. Inter.* **2010**, 2, 1857–1865.
36. Malone, S. M.; Schwartz, D. K. Macroscopic Liquid Crystal Response to Isolated DNA Helices. *Langmuir* **2011**, 27, 11767–11772.
37. Bai, Y.; Abbott, N. L. Enantiomeric Interactions between Liquid Crystals and Organized Monolayers of Tyrosine-Containing Dipeptides. *J. Am. Chem. Soc.* **2012**, 134, 548–558.
38. Bai, Y.; Abbasi, R.; Wang, X.; Abbott, N. L. Liquid Crystals Anchored on Mixed Monolayers of Chiral versus Achiral Molecules: Continuous Change in Orientation as a Function of Enantiomeric Excess. *Angew. Chem. Int. Ed. Engl.* **2014**, 126, 8217–8221.
39. Shah, R. R.; Abbott, N. L. Coupling of the Orientations of Liquid Crystals to Electrical Double Layers Formed by the Dissociation of Surface-Immobilized Salts. *J. Phys. Chem. B* **2001**, 105, 4936–4950.
40. Miller, D. S.; Carlton, R. J.; Mushenheim, P. C.; Abbott, N. L. Introduction to Optical Methods for Characterizing Liquid Crystals at Interfaces. *Langmuir* **2013**, *29*, 3154–3169.
41. Bandara, H. M.; Burdette, S. C. Photoisomerization in Different Classes of Azobenzene. *Chem. Soc. Rev.* **2012**, 41, 1809–1825.
42. Beharry, A. A.; Woolley, G. A. Azobenzene Photoswitches for Biomolecules. *Chem. Soc. Rev.* **2011**, 40, 4422–4437.
43. Seki, T.; Sakuragi, M.; Kawanishi, Y.; Tamaki, T.; Fukuda, R.; Ichimura, K.; Suzuki, Y. "Command Surfaces" of Langmuir-Blodgett Films. Photoregulations of Liquid Crystal Alignment by Molecularly Tailored Surface Azobenzene Layers. *Langmuir* **1993**, 9, 211–218.
44. Gibbons, W. M.; Shannon, P. J.; Sun, S.-T.; Swetlin, B. J. Surface-Mediated Alignment of Nematic Liquid Crystals with Polarized Laser Light. *Nature* **1991**, 351, 49–50.
45. Fukuhara, K.; Nagano, S.; Hara, M.; Seki, T. Free-Surface Molecular Command Systems for Photoalignment of Liquid Crystalline Materials. *Nat. Commun.* **2014**, 5, 3320.
46. Eremin, A.; Hirankittiwong, P.; Chattham, N.; Nadasi, H.; Stannarius, R.; Limtrakul, J.; Haba, O.; Yonetake, K.; Takezoe, H. Optically Driven Translational and Rotational Motions of Microrod Particles in a Nematic Liquid Crystal. *Proc. Natl. Acad. Sci. U. S. A.* **2015**, 112, 1716–1720.
47. Sen, A.; Kupcho, K. A.; Grinwald, B. A.; Vantreeck, H. J.; Acharya, B. R. Liquid Crystal-Based Sensors for Selective and Quantitative Detection of Nitrogen Dioxide. *Sens. Actuators, B* **2013**, 178, 222–227.
48. Grinwald, B. A.; Robinson, S. E.; Burland, T. G.; Acharya, B. R. Liquid Crystal Sensors for Dosimetry and Rapid Sensing of Toxic Gases. Platypus Technologies, 2014.
49. Nakata, M.; Zanchetta, G.; Buscaglia, M.; Bellini, T.; Clark, N. A. Liquid Crystal Alignment on a Chiral Surface: Interfacial Interaction with Sheared DNA Films. *Langmuir* **2008**, 24, 10390–10394.

50. Price, A. D.; Schwartz, D. K. DNA Hybridization-Induced Reorientation of Liquid Crystal Anchoring at the Nematic Liquid Crystal/Aqueous Interface. *J. Am. Chem. Soc.* **2008**, 130, 8188–8194.
51. Brake, J. M.; Daschner, M. K.; Luk, Y. Y.; Abbott, N. L. Biomolecular Interactions at Phospholipid-Decorated Surfaces of Liquid Crystals. *Science* **2003**, 302, 2094–2097.
52. Gupta, J. K.; Meli, M. V.; Teren, S.; Abbott, N. L. Elastic Energy-Driven Phase Separation of Phospholipid Monolayers at the Nematic Liquid-Crystal-Aqueous Interface. *Phys. Rev. Lett.* **2008**, 100, 048301.
53. Gupta, J. K.; Abbott, N. L. Principles for Manipulation of the Lateral Organization of Aqueous-Soluble Surface-Active Molecules at the Liquid Crystal-Aqueous Interface. *Langmuir* **2009**, 25, 2026–2033.
54. Lee, G.; Carlton, R. J.; Araoka, F.; Abbott, N. L.; Takezoe, H. Amplification of the Stereochemistry of Biomolecular Adsorbates by Deracemization of Chiral Domains in Bent-Core Liquid Crystals. *Adv. Mater.* **2013**, 25, 245–249.
55. Noonan, P. S.; Mohan, P.; Goodwin, A. P.; Schwartz, D. K. DNA Hybridization-Mediated Liposome Fusion at the Aqueous Liquid Crystal Interface. *Adv. Funct. Mater.* **2014**, 24, 3206–3212.
56. Park, J.-S.; Abbott, N. L. Ordering Transitions in Thermotropic Liquid Crystals Induced by the Interfacial Assembly and Enzymatic Processing of Oligopeptide Amphiphiles. *Adv. Mater.* **2008**, 20, 1185–1190.
57. Khan, M.; Park, S. Y. Liquid Crystal-Based Proton Sensitive Glucose Biosensor. *Analytical Chemistry* **2014**, 86, 1493–1501.
58. Khan, M.; Kim, Y.; Lee, J. H.; Kang, I.-K.; Park, S.-Y. Real-Time Liquid Crystal-Based Biosensor for Urea Detection. *Anal. Methods* **2014**, 6, 5753–5759.
59. Zhu, Q.; Yang, K.-L. Amplification of Interference Color by Using Liquid Crystal for Protein Detection. *Appl. Phys. Lett.* **2013**, 103, 243701.
60. Lavrentovich, O. D. Transport of Particles in Liquid Crystals. *Soft Matter* **2014**, 10, 1264–1283.
61. Musevic, I.; Škarabot, M.; Tkalec, U.; Ravnik, M.; Žumer, S. Two-Dimensional Nematic Colloidal Crystals Self-Assembled by Topological Defects. *Science* **2006**, 313, 954–958.
62. Tkalec, U.; Ravnik, M.; Čopar, S.; Žumer, S.; Muševič, I. Reconfigurable Knots and Links in Chiral Nematic Colloids. *Science* **2011**, 2011, 62–65.
63. Chandran, S. P.; Mondiot, F.; Loudet, J. C. Photonic Control of Surface Anchoring on Solid Colloids Dispersed in Liquid Crystals. *Langmuir* **2011**, 27, 15185–15198.
64. Lapointe, C. P.; Mason, T. G.; Smalyukh, I. I. Shape-Controlled Colloidal Interactions in Nematic Liquid Crystals. *Science* **2009**, 326, 1083–1086.
65. Senyuk, B.; Liu, Q.; He, S.; Kamien, R. D.; Kusner, R. B.; Lubensky, T. C.; Smalyukh, I. I. Topological Colloids. *Nature* **2013**, 493, 200–205.
66. Liu, Q.; Senyuk, B.; Tasinkevych, M.; Smalyukh, I. I. Nematic Liquid Crystal Boojums with Handles on Colloidal Handlebodies. *Proc. Natl. Acad. Sci. U. S. A.* **2013**, 110, 9231–9236.
67. Tkalec, U.; Škarabot, M.; Muševič, I. Interactions of Micro-Rods in a Thin Layer of a Nematic Liquid Crystal. *Soft Matter* **2008**, 4, 2402–2409.
68. Conradi, M.; Ravnik, M.; Bele, M.; Zorko, M.; Žumer, S.; Muševič, I. Janus Nematic Colloids. *Soft Matter* **2009**, 5, 3905–3912.
69. Loudet, J. C.; Hanusse, P.; Poulin, P. Stokes Drag on a Sphere in a Nematic Liquid Crystal. *Science* **2004**, 306, 1525.

70. Smalyukh, I. I.; Kachynski, A. V.; Kuzmin, A. N.; Prasad, P. N. Laser Trapping in Anisotropic Fluids and Polarization-Controlled Particle Dynamics. *Proc. Natl. Acad. Sci. U. S. A.* **2006**, 103, 18048–18053.
71. Koenig, G. M.; Ong, R.; Cortes, A. D.; Moreno-Razo, J. A.; de Pablo, J. J.; Abbott, N. L. Single Nanoparticle Tracking Reveals Influence of Chemical Functionality of Nanoparticles on Local Ordering of Liquid Crystals and Nanoparticle Diffusion Coefficients. *Nano Lett.* **2009**, 9, 2794–2801.
72. Stark, H.; Ventzki, D. Stokes Drag of Spherical Particles in a Nematic Environment at Low Ericksen Numbers. *Phys. Rev. E* **2001**, 64, 031711.
73. Turiv, T.; Lazo, I.; Brodin, A.; Lev, B. I.; Reiffenrath, V.; Nazarenko, V. G.; Lavrentovich, O. D. Effect of Collective Molecular Reorientations on Brownian Motion of Colloids in Nematic Liquid Crystal. *Science* **2013**, 342, 1351–1354.
74. Lavrentovich, O. D.; Lazo, I.; Pishnyak, O. P. Nonlinear Electrophoresis of Dielectric and Metal Spheres in a Nematic Liquid Crystal. *Nature* **2010**, *467*, 947–950.
75. Lazo, I.; Lavrentovich, O. D. Liquid Crystal-Enabled Electrophoresis of Spheres in a Nematic Medium with Negative Dielectric Anisotropy. *Philos. Trans. R. Soc. London, Ser. A* **2013**, 371, 20120255.
76. Moreno-Razo, J. A.; Sambriski, E. J.; Abbott, N. L.; Hernandez-Ortiz, J. P.; de Pablo, J. J. Liquid-Crystal-Mediated Self-Assembly at Nanodroplet Interfaces. *Nature* **2012**, 485, 86–89.
77. Koenig, G. M.; Lin, I.; Abbott, N. L. Chemoresponsive Assemblies of Microparticles at Liquid Crystalline Interfaces. *Proc. Natl. Acad. Sci. U. S. A.* **2009**, 107, 3998–4003.
78. Miller, D. S.; Abbott, N. L. Influence of Droplet Size, pH and Ionic Strength on Endotoxin-Triggered Ordering Transistions in Liquid Crystalline Droplets. *Soft Matter* **2013**, 9, 374–382.
79. Miller, D. S.; Wang, X.; Abbott, N. L. Design of Functional Materials Based on Liquid Crystalline Droplets. *Chem. Mater.* **2014**, 26, 496–506.
80. Gupta, J. K.; Sivakumar, S.; Caruso, F.; Abbott, N. L. Size-Dependent Ordering of Liquid Crystals Observed in Polymeric Capsules with Micrometer and Smaller Diameters. *Angew. Chem. Int. Ed. Engl.* **2009**, 48, 1652–1655.
81. Gupta, J. K.; Zimmerman, J. S.; de Pablo, J. J.; Caruso, F.; Abbott, N. L. Characterization of Adsorbate-Induced Ordering Transitions of Liquid Crystals within Monodisperse Droplets. *Langmuir* **2009**, 25, 9016–9024.
82. Sivakumar, S.; Wark, K. L.; Gupta, J. K.; Abbott, N. L.; Caruso, F. Liquid Crystal Emulsions as the Basis of Biological Sensors for the Optical Detection of Bacteria and Viruses. *Adv. Funct. Mater.* **2009**, 19, 2260–2265.
83. Alino, V. J.; Tay, K. X.; Khan, S. A.; Yang, K. L. Inkjet Printing and Release of Monodisperse Liquid Crystal Droplets from Solid Surfaces. *Langmuir* **2012**, 28, 14540–14546.
84. Alino, V. J.; Pang, J.; Yang, K. L. Liquid Crystal Droplets as a Hosting and Sensing Platform for Developing Immunoassays. *Langmuir* **2011**, 27, 11784–11789.
85. Alino, V. J.; Sim, P. H.; Choy, W. T.; Fraser, A.; Yang, K. L. Detecting Proteins in Microfluidic Channels Decorated with Liquid Crystal Sensing Dots. *Langmuir* **2012**, 28, 17571–17577.
86. Lin, I.; Miller, D. S.; Bertics, P. J.; Murphy, C. J.; de Pablo, J. J.; Abbott, N. L. Endotoxin-Induced Structural Transformations in Liquid Crystalline Droplets. *Science* **2011**, 332, 1297–1300.

87. Mondiot, F.; Wang, X.; de Pablo, J. J.; Abbott, N. L. Liquid Crystal-Based Emulsions for Synthesis of Spherical and Non-Spherical Particles with Chemical Patches. *J. Am. Chem. Soc.* **2013**, 135, 9972–9975.
88. Whitmer, J. K.; Wang, X.; Mondiot, F.; Miller, D. S.; Abbott, N. L.; de Pablo, J. J. Nematic-Field-Driven Positioning of Particles in Liquid Crystal Droplets. *Phys. Rev. Lett.* **2013**, 111, 227801.
89. Wang, X.; Miller, D. S.; de Pablo, J. J.; Abbott, N. L. Reversible Switching of Liquid Crystalline Order Permits Synthesis of Homogenous Populations of Dipolar Patchy Microparticles. *Adv. Funct. Mater.* **2014**, 24, 6219–6226.
90. Wang, X.; Miller, D. S.; de Pablo, J. J.; Abbott, N. L. Organized Assemblies of Colloids Formed at the Poles of Micrometer-Sized Droplets of Liquid Crystal. *Soft Matter* **2014**, 10, 8821–8828.
91. Fleury, J.-B.; Pires, D.; Galerne, Y. Self-Connected 3D Architecture of Microwires. *Phys. Rev. Lett.* **2009**, 103, 267801.
92. Pires, D.; Fleury, J.-B.; Galerne, Y. Colloid Particles in the Interaction Field of a Disclination Line in a Nematic Phase. *Phys. Rev. Lett.* **2007**, 98, 247801.
93. Ravnik, M.; Alexander, G. P.; Yeomans, J. M.; Zumer, S. Mesoscopic Modelling of Colloids in Chiral Nematics. *Farad. Discuss.* **2010**, 144, 159–169.
94. Repnik, R.; Nita, V. P.; Kralj, S. Mixtures of Nanoparticles and Liquid Cystal Phases Exhibiting Topological Defects. *Mol. Cryst. Liq. Cryst.* **2012**, 560, 115–122.
95. Yoshida, H.; Tanaka, Y.; Kawamoto, K.; Kubo, H.; Tsuda, T.; Fujii, A.; Kuwabata, S.; Kikuchi, H.; Ozaki, M. Nanoparticle-Stabilized Cholesteric Blue Phases. *Appl. Phys. Express* **2009**, 2, 121501.
96. Mushenheim, P. C.; Abbott, N. L. Hierarchical Organization in Liquid Crystal-in-Liquid Crystal Emulsions. *Soft Matter* **2014**, 10, 8627–8634.
97. Agarwal, A.; Sidiq, S.; Setia, S.; Bukusoglu, E.; de Pablo, J. J.; Pal, S. K.; Abbott, N. L. Colloid-in-Liquid Crystal Gels that Respond to Biomolecular Interactions. *Small* **2013**, 9, 2785–2792.
98. Agarwal, A.; Huang, E.; Palecek, S.; Abbott, N. L. Optically Responsive and Mechanically Tunable Colloid-in-Liquid Crystal Gels that Support Growth of Fibroblasts. *Adv. Mater.* **2008**, 20, 4804–4809.
99. Pal, S. K.; Agarwal, A.; Abbott, N. L. Chemically Responsive Gels Prepared from Microspheres Dispersed in Liquid Crystals. *Small* **2009**, 5, 2589–2596.
100. Vollmer, D.; Hinze, G.; Ullrich, B.; Poon, W. C. K.; Cates, M. E.; Schofield, A. B. Formation of Self-Supporting Reversible Cellular Networks in Suspensions of Colloids and Liquid Crystals. *Langmuir* **2005**, 21, 4921–4930.
101. Bukusoglu, E.; Pal, S. K.; de Pablo, J. J.; Abbott, N. L. Colloid-in-Liquid Crystal Gels Formed via Spinodal Decomposition. *Soft Matter* **2014**, 10, 1602–1610.
102. Wood, T. A.; Lintuvuori, J. S.; Schofield, A. B.; Marenduzzo, D.; Poon, W. C. K. A Self-Quenched Defect Glass in a Colloid-Nematic Liquid Crystal Composite. *Science* **2011**, 334, 79–83.
103. Meeker, S. P.; Poon, W. C. K.; Crain, J.; Terentjev, E. M. Colloid–Liquid-Crystal Composites: An Unusual Soft Solid. *Phys. Rev. E* **2000**, 61, 6083–6086.
104. Vollmer, D.; Hinze, G.; Poon, W. C. K.; Cleaver, J.; Cates, M. E. The Origin of Network Formation in Colloid-Liquid Crystal Composites. *J. Phys. Condens. Matter* **2004**, 16, 227–233.

105. Petrov, P. G.; Terentjev, E. M. Formation of Cellular Solid in Liquid Crystal Colloids. *Langmuir* **2001**, 17, 2942–2949.
106. Diestra-Cruz, H.; Bukusoglu, E.; Abbott, N. L.; Acevedo, A. Hierarchical Microstructures Formed by Bidisperse Colloidal Suspensions within Colloid-in-Liquid Crystal Gels. *ACS Appl. Mater. Inter.* **2015**, 7, 7153–7162.
107. Carlton, R. J.; Gupta, J. K.; Swift, C. L.; Abbott, N. L. Influence of Simple Electrolytes on the Orientational Ordering of Thermotropic Liquid Crystals at Aqueous Interfaces. *Langmuir* **2012**, 28, 31–36.
108. Carlton, R. J.; Ma, C. D.; Gupta, J. K.; Abbott, N. L. Influence of Specific Anions on the Orientational Ordering of Thermotropic Liquid Crystals at Aqueous Interfaces. *Langmuir* **2012**, 28, 12796–12805.
109. Guyot-Sionnest, P.; Hsiung, H.; Shen, Y. R. Surface Polar Ordering in a Liquid Crystal Observed by Optical Second-Harmonic Generation. *Phys. Rev. Lett.* **1986**, 57, 2963–2966.
110. Feller, M. B.; Chen, D.; Shen, Y. R. Investigation of Surface-Induced Alignment of Liquid-Crystal Molecules by Optical Second-Harmonic Generation. *Phys. Rev. A* **1991**, 43, 6778–6792.
111. Daschner de Tercero, M.; Abbott, N. L. Ordering Transitions in Liquid Crystals Permit Imaging of Spatial and Temporal Patterns Formed by Proteins Penetrating into Lipid-Laden Interfaces. *Chem. Eng. Commun.* **2009**, 196, 234–251.

Chapter 4: Dynamic Self-Assembly of Motile Bacteria in Liquid Crystals*

4.1 Introduction

Bacteria adapt to a broad range of microenvironments with varied physical and chemical properties. Aspects of these microenvironments can impact the motility and viability of the microorganisms.[1] While bacteria most commonly inhabit isotropic microenvironments which possess direction-independent physical properties, some specialized bacteria including *Staphylococcus aureus, Neisseria gonorrhoeae,* β-hemolytic strains of *Streptococcus, Mycobacterium tuberculosis*, and *Pseudomonas aeruginosa* have been previously shown to colonize microenvironments possessing anisotropic properties (e.g., optical, mechanical, and diffusional), including those enriched in collagen, cellulose, chitin, synovial fluid, and the matrix of extracellular polymeric substances associated with bacterial biofilms.[2–5] How the anisotropy of these environments influences dynamic behaviors of bacteria, and in particular, intercellular interactions remains poorly understood.

In this paper, we address this topic by studying bacteria in model liquid crystalline materials. Liquid crystals (LCs) encompass a state of soft matter in which properties are typically anisotropic.[5] Unlike isotropic liquids, LCs exhibit long-range order and elasticity that enables energy to be stored at rest in strained states, and they form topological defects in confined systems.[5–8] These properties significantly influence the behavior of micrometer-sized synthetic particles (e.g., polystyrene or silica) when dispersed within a LC. For example, individual elongated microparticles are spontaneously oriented within nematic LC to minimize local elastic distortions that arise due to the preferential alignment of LC mesogens at the particle surface (so called "surface anchoring").[7,9] The specific orientation assumed by the particles relative to the

far-field director, which defines the average alignment of LC mesogens in the bulk, depends on the type of anchoring (e.g., tangential or perpendicular) at the particle surface. In addition, a series of recent studies have revealed that the elasticity of LCs can generate direction-dependent interparticle forces that lead to formation of complex, self-assembled structures of micrometer-sized particles in LCs including linear chains and two-dimensional arrays.[7–11] Such LC-mediated elastic forces can be very strong, commonly producing pair interaction potentials on the order of 10^2 to 10^3 kT and lead to the irreversible association of microparticles. Although interest exists in harnessing these forces to create self-assembled colloidal structures for use in photonics or in the design of metamaterials,[12] the strength of the anisotropic interparticle interactions often leads to the irreversible association of particles and kinetic traps (particle configurations which produce local free energy minima) and thus optical tweezers or other techniques are typically needed to guide the assembly process.

While the self-organization of 'passive' colloids in LCs has been well characterized, much less is known about the behaviors of 'active' particles[13,14] that propel themselves within LCs. Such an investigation is of particular interest because active particles may be able to generate forces of sufficient magnitude to overcome the irreversibility of many LC-mediated interparticle interactions (see above). Bacteria can be viewed as a promising class of active particles for these types of fundamental studies because, as we demonstrate, they can be genetically engineered to manipulate the magnitude of the propulsive force that they generate in LCs. Additionally, focusing on bacteria provides an opportunity to gain insight into the influence of elasticity of LCs on intercellular bacterial organization in anisotropic microenvironments.

Past studies have reported that the elasticity of anisotropic microenvironments can impact the orientation and motility of bacteria. Smalyukh *et al.* observed that the long axes of rod-

shaped *P. aeruginosa* cells oriented parallel to the direction of DNA alignment in a concentrated solution of aligned DNA chains.[15] They also found that cell motion was biased in this direction. These phenomena were hypothesized to arise from minimization of energy associated with elastic deformation of the nematic-like DNA biopolymer matrix. More recently, Kumar *et al.* have reported that elastic forces similarly induce *Escherichia coli* to move anisotropically when suspended in a nematic LC.[16] In this paper, we move beyond these past studies of isolated bacteria (i.e., single particles) by focusing instead upon the interplay of elasticity-mediated inter-bacterial forces and flagella-derived dissociative forces on the self-organization of multiple bacteria dispersed in a LC.

To investigate the above-described fundamental issues, we studied the behavior of *Proteus mirabilis* cells suspended in a lyotropic LC that creates an anisotropic viscoelastic microenvironment. *P. mirabilis* is a Gram-negative, rod-shaped γ-proteobacterium 2–3 μm in length that is commonly associated with urinary tract infections and the biofouling of catheters. Guided by environmental cues, *P. mirabilis* cells differentiate into long (~ 20 μm) swarmer cells having a characteristically high density of flagella that generate sufficient propulsive forces to enable movement through high viscosity fluids ($\mu \leq 8.34$ Pa·s), which is a phenotype that is thought to play a role in pathogenesis.[17] We hypothesized that these large propulsive forces might also permit the emergence of complex inter-bacterial behaviors in viscoelastic media such as LCs. Rather than working with swarmer cells per se, we studied *P. mirabilis* cells overexpressing the *flhDC* operon, which encodes the master regulator of flagellum biosynthesis, $FlhD_4C_2$. Overexpressing *flhDC* produces vegetative *P. mirabilis* cells (*P. mirabilis-flhDC*) that have a high density of flagella that resembles swarmer cells, and enables them to move through viscous fluids.[17] Focusing our studies on *P. mirabilis-flhDC* enabled us to recapitulate the

dominant phenotype of swarmers—movement through viscous environments—without the technical complexities of isolating and working with isogenic populations of these differentiated cells.

For our studies of *P. mirabilis-flhDC* in anisotropic environments, we used aqueous solutions of disodium cromoglycate (DSCG). DSCG (also known as cromolyn) is an example of a lyotropic LC. Aqueous DSCG solutions exhibit nematic LC phases within a particular range of compositions and temperatures due to formation of aggregates of stacked DSCG molecules.[18,19] Our choice of DSCG for these studies was primarily guided by its known biocompatibility with several types of cells and bacteria.[20,21] DSCG also has been characterized extensively, including the determination of its phase diagram,[18,22] birefringence,[23] and elastic constants.[24] In addition, synthetic LCs are particularly attractive model anisotropic fluids because it is possible to exert spatiotemporal control of the local LC alignment, e.g. through changes in boundary conditions or application of external fields.

4.2 Experimental Section

Bacterial strains and cell culture. *P. mirabilis* strain HI4320 was transformed with plasmid pflhDC to create *P. mirabilis-flhDC.* The plasmid pflhDC contained the *flhDC* genes from *P. mirabilis* inserted into pACYC184 (which contains a gene for chloramphenicol resistance). Empty vector pACYC184 (without *flhDC*) was transformed into HI4320 to obtain wild type vegetative *P. mirabilis*. Both strains were grown in chloramphenicol-resistance nutrient medium consisting of 1% (wt/vol) peptone (Becton, Dickinson, Sparks, MD), 0.5% (wt/vol) yeast extract (Becton, Dickinson), and 1% (wt/vol) NaCl (Fisher Scientific, Fairlawn, NJ) at 30°C in a shaking incubator.[17] Saturated overnight cultures were diluted 100-fold in 10 mL of fresh

nutrient medium and grown in 150 mL Erlenmeyer flasks at 30°C in a shaking incubator at 200 rpm. We observed that the highest swimming velocity of *P. mirabilis* cells occurred during stationary phase, hence we harvested cells at an absorbance (λ = 600 nm) of ~3.2 and centrifuged. The cells were then washed three times with an aqueous buffer for bacterial motility (0.01 M KPO_4, 0.067 M NaCl, 10^{-4} M EDTA, 0.1 M glucose, and 0.001% Brig-35, pH 7.0). To obtain non-motile *P. mirabilis* cells, the cells were treated with 4% glutaraldehyde for 3 h at 25°C after harvesting.

E. coli K-12 strain MG1655 (CGSC #8237) was grown in Luria-Bertani media (LB) (1% tryptone w/v, 0.5% yeast extract w/v, 1% NaCl w/v) at 37°C in a shaker incubator. Saturated overnight cultures were diluted 100-fold in 10 mL of fresh nutrient medium and grown in 150 mL Erlenmeyer flasks at 37°C in a shaking incubator at 200 rpm for 2 hours. After harvesting, these cells were washed as described above for *P. mirabilis*.

Lyotropic LC preparation. Disodium cromoglycate (DSCG) was purchased from Sigma-Aldrich (Milwaukee, WI) and used as received. Lyotropic LCs containing DSCG were prepared by mixing 15.3 wt% of DSCG with 84.7 wt% of aqueous motility buffer. The mixture was shaken for at least 12 h to ensure complete solubility and homogeneity. Prior to experimentation, the DSCG solution was heated at 65°C for 10 min to avoid possible time dependence of the properties of the mixture.[25,26] After cooling the solution to 25°C, a small volume of motility buffer containing bacteria was added to the DSCG mixture producing a final concentration of ~10^4 cells/μL. The final concentration of DSCG was 15.0 wt% in all experiments. At this concentration, DSCG forms a nematic LC phase below ~27°C and an isotropic phase above ~40°C with two-phase coexistence observed within the range of intermediate temperatures.[18,22]

Microscopy. We optically imaged cells using a Nikon Eclipse Ti inverted microscope equipped with crossed polarizers and a Photometics CoolSNAP HQ2 CCD camera (Tucson, AZ) using a Nikon Plan Apo λ, 100X/1.45 oil objective lens. Videos consisting of 400 frames were collected with the EM gain off and with a 100 ms exposure time (10 frames/sec). Images of cells were collected using Nikon NIS Elements software. For non-motile cells, bright field and crossed polar images were collected for the same field of view. A thermoplate (Tokai Hit, Fujinomiya, Japan) and 100X objective heater (Bioptechs, Butler, PA) were used to control the temperature of the samples during experiments. An Olympus BX60 microscope equipped with crossed polarizers was also used to analyze the imaging chambers. Images were captured using a digital camera (Olympus C-2040 Zoom) mounted on the microscope and set to an f-stop of 2.8 and a shutter speed of 1/125 sec.

Bacterial motility data analysis. Microscopy data for motile cells was analyzed using the MATLAB computing environment (MathWorks, Natick, MA) by identifying the centroid of each bacterium in successive frames and grouping those points together to create a cell trajectory. We combined the position of the cell at each interval in a cell track with the CCD frame rate to determine cell velocity. Using this script, we determined the length and position of each cell and the average cell velocity over the entire track. Tracks that were shorter than 25 frames were discarded. ImageJ software was used to calculate the angular dispersion of non-motile cell populations relative to the direction of rubbing, the distance between associated non-motile cells, and the angle with respect to the far-field director of multi-cellular complexes.

Rheology. An Advanced Rheometric Expansion System (ARES) (TA Instruments, Rheometric Scientific, Piscataway, NJ) with cone and plate type geometry (cone diameter 50 mm; cone angle 0.04 rad) was used to measure the effective viscosity of the DSCG solution. Steady shear rate sweeps were performed at room temperature at shear rates between 10^{-3} and 10^{3} s^{-1}. A gap of 0.0508 mm between the plate and the center of the cone was used such that DSCG solution fully filled the space between the plates, with excess material extended beyond the plates.

Statistical analysis. All experimentally determined values have been reported in the text and figures with associated standard errors.

4.3 Results

4.3.1 Anisotropic motion and orientation of *P. mirabilis-flhDC* cells in nematic DSCG

We first sought to confirm that the elasticity of the nematic LC phase of DSCG solutions (15 wt%) in aqueous motility buffer induced bacteria to move anisotropically, as has been reported previously for *E. coli*.[16] At this concentration, DSCG forms a nematic LC phase below ~27°C and an isotropic phase above ~40°C with coexistence of two phases at intermediate temperatures.[18,22] All of the experiments described in this manuscript were performed in 15 wt% DSCG. To prepare optical chambers for imaging bacterial cells suspended in DSCG solutions, we first rubbed a glass slide and a glass cover slip unidirectionally multiple times with tissue paper (Kimwipe). A small volume (~1 μL) of DSCG solution containing bacteria was subsequently confined between the two rubbed glass substrates in a cavity created using 6 μm-thick Mylar film (Figure 4-S1). Epoxy was used to seal the chamber and prevent water evaporation. The imaging chamber was prepared so the rubbed surfaces of the glass substrates

were both in contact with the DSCG solution and oriented such that the rubbing directions on the two substrates were antiparallel. The sample was briefly (~10 s) heated to 42°C into the isotropic phase of DSCG to mitigate any flow-induced alignment of the nematic LC before cooling back to room temperature. Using this technique, large regions (in excess of 100 μm × 100 μm) of the LC phase of DSCG (at 25°C) exhibited an orientation that was parallel to the surface with an azimuthal alignment in the direction of rubbing (Figure 4-S1). We confirmed that the alignment of the nematic LC in these regions was parallel to the direction of rubbing by inserting a quarter wave plate into the optical path of a microscope and analyzing the appearance of the sample between crossed polars.[27] Each imaging chamber was used within 3 h of its preparation. Bacteria were in contact with DSCG solutions for at least ten minutes prior to performing measurements of motility.

Initial experiments with *E. coli* strain MG1655 revealed limited motility in nematic phases of DSCG (average velocity $\overline{V} \sim 1.2 \pm 0.4$ μm/s), which made it challenging to differentiate between motile and non-motile cells. With few exceptions, past studies have demonstrated that many types of bacteria are unable to generate sufficient propulsive forces to move through fluids with $\mu > 0.06$ Pa·s (e.g. the motility of *Escherichia coli* strain KL227 ceases at $\mu = 0.06$ Pa·s).[28] Since *E. coli* MG1665 cells do not generate a large propulsive force in fluids of high viscosity such as lyotropic liquid crystals (and thus, we expected, would irreversibly aggregate in LCs), we instead investigated motile strains of *P. mirabilis* that were engineered to overexpress *flhDC* and enable cell motility in isotropic fluids with a dynamic viscosity, $\mu \leq 8.34$ Pa·s.[17] The aspect ratio of the engineered cells (k = L/2R) was ~ 3, closely matching vegetative *P. mirabilis* cells that did not overexpress *flhDC*. We measured the *P. mirabilis-flhDC* cells to move through DSCG solutions with a much higher velocity ($\overline{V} = 8.8 \pm 0.2$ μm/s) than both *E.*

coli cells and vegetative *P. mirabilis* cells that did not overexpress *flhDC* ($\overline{V}$ = 0.2 $\pm$ 0.1 μm/s) (Figure 4-1A). When we analyzed the motion of *P. mirabilis-flhDC* cells dispersed in nematic DSCG solution (see Video S1 in the online Supporting Information), we observed cells moving preferentially along the direction of LC alignment,[15,16] as illustrated by the offset representative trajectories shown in Figure 4-1B. The mean-square displacement for *P. mirabilis-flhDC* cells parallel to the nematic LC director (x-direction) was approximately two orders of magnitude greater than in the perpendicular direction (Figure 4-1D). In contrast, *P. mirabilis-flhDC* cells suspended in an isotropic DSCG solution (achieved by equilibrating the solution at 42°C) exhibited a comparable velocity of $\overline{V}$ = 8.1 $\pm$ 0.3 μm/s without a directional bias (Figures 4-1C and 4-1D; also see Video S2 in the online Supporting Information).

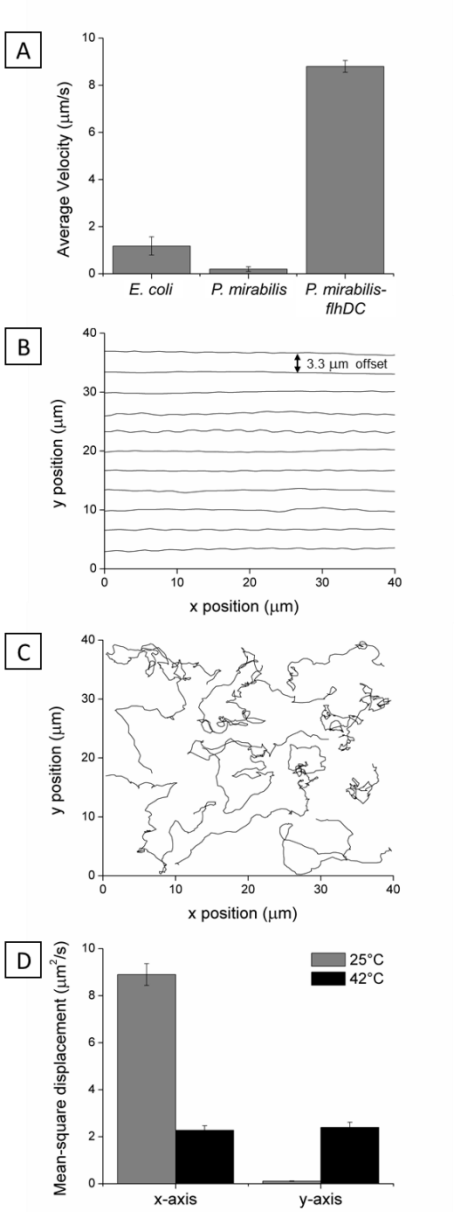

Figure 4-1. Anisotropic motion of bacteria in nematic LC.

(A) Average velocities of bacteria measured in nematic DSCG solutions (15 wt%) at 25°C. (B) Superimposed trajectories (offset from one another by 3.3 μm) of *P. mirabilis-flhDC* in nematic DSCG solutions at 25°C. The LC director was oriented along the x-axis (in the direction of rubbing of the glass slides). (C) Superimposed representative trajectories of *P. mirabilis-flhDC* in isotropic phases of DSCG at 42°C. (D) Plot of the mean-square displacement of *P. mirabilis-flhDC* calculated from analysis of 139 trajectories (25°C) and 75 trajectories (42°C). The velocities of *P. mirabilis-flhDC* cells in DSCG solution were comparable in magnitude at 25°C ($\overline{\mathbf{V}}$ = 8.8 ± 0.2 μm/s) and 42°C ($\overline{\mathbf{V}}$ = 8.1 ± 0.3 μm/s). Values are reported with associated standard errors.

To estimate the flagella-derived forces generated by the motile *P. mirabilis-flhDC* in nematic DSCG, we sought to determine the viscous drag force ($F_d = 6\pi\mu R\bar{V}$) which balances the propulsive force. Nematic LCs possess direction-dependent (Miesowicz) shear viscosities with the direction of lowest viscosity being parallel to the director.[29–31] In common thermotropic LCs, the Miesowicz viscosity corresponding to shear flow with velocity perpendicular to the director is often ~10× larger than the viscosity parallel to the director.[29] Because experimental determination of Miesowicz viscosities of lyotropic LCs is difficult as general and facile methods to manipulate the surface anchoring of lyotropic LC phases do not exist, we estimated the apparent viscosity experienced by the motile *P. mirabilis-flhDC* in nematic DSCG to be $\mu \sim 0.7$ Pa·s by comparing the average velocity in nematic DSCG to previous measurements of *P. mirabilis-flhDC* motility in solutions of known viscosity.[17] (We note that we also performed rheological measurements of the DSCG solution at 25°C and measured an effective viscosity of $\mu \sim 1$ Pa·s.) Employing $\mu = 0.7$ Pa·s as an approximation of the Miesowicz viscosity along the director, we estimate that $F_d \sim 60$ pN for the rod-shaped *P. mirabilis-flhDC* ($R = 0.5$ μm) cells moving at $\bar{V} = 8.8$ μm/s in nematic DSCG. Below we compare the magnitude of these flagella-derived propulsive forces to inter-bacterial forces generated by the elasticity of the LC.

Because the interactions between *P. mirabilis-flhDC* cells mediated by the elasticity of the LC are dependent on the anchoring of the LC on the surface of the bacteria and the resulting strain in the LC, we first characterized the anchoring of the LC on individual cells. To determine the anchoring of the LC on the bacteria, we characterized the distribution of orientations of non-motile *P. mirabilis-flhDC* cells in both the nematic and isotropic phases of DSCG solutions and characterized the ordering of nematic LC near the cells using polarized light microscopy. Treating *P. mirabilis-flhDC* cells with 4% glutaraldehyde rendered them non-motile. Non-motile

P. mirabilis-flhDC cells suspended in an isotropic DSCG solution exhibited no preferential orientational alignment (Figure 4-S2). In contrast, we measured the long axes of non-motile *P. mirabilis-flhDC* cells to preferentially align parallel to the far-field LC director in nematic DSCG (Figure 4-2A and 4-2D) and we observed four small regions with a bright optical appearance near the poles of each bacterium (Figure 4-2B), both which are consistent with tangential anchoring of the LC at the bacterial surface (Figure 4-2C). We also calculated that shear forces generated by motile bacteria should not perturb this local ordering of LC because the Ericksen number ($\mathrm{Er} = \mu\bar{V}\mathrm{R}/\mathrm{K}$) for the motion of *P. mirabilis-flhDC* cells in DSCG is < 1.[29] If the tangential surface anchoring of the LC on the surface of *P. mirabilis-flhDC* was strong, the orientation-dependent energy of interaction of the LC and the rod-shaped bacterium (length L = 3 μm, radius R = 0.5 μm) would be:[6,15,32,33]

$$U_{elastic} = 2\pi K\theta^2 L/\ln(2L/R), \qquad (4\text{-}1)$$

where θ is the angle (in radians) between the director of the LC and long-axis of the bacterium and K is the elastic constant of the LC (K = 10 pN)[24], where for simplicity the elastic constants for splay, twist, and bend are assumed to be equal in magnitude allowing the strain of the LC to be described by a single elastic constant. This analysis leads to the prediction that even slight deviations of the bacterial long axis from the nematic director would be highly unfavorable (e.g., $U_{elastic} \sim$ 90kT for θ = 4°). In contrast, we measured a significant number of bacteria to be oriented away from the far-field director (35% of cells in nematic DSCG were recorded with $\theta \geq$ 4°), suggesting that the tangential anchoring of the LC on the surface of the bacteria is likely weak [a conclusion which receives support from additional observations reported below; we note also that weak, tangential anchoring of DSCG at surfaces has been reported elsewhere[34,35]].

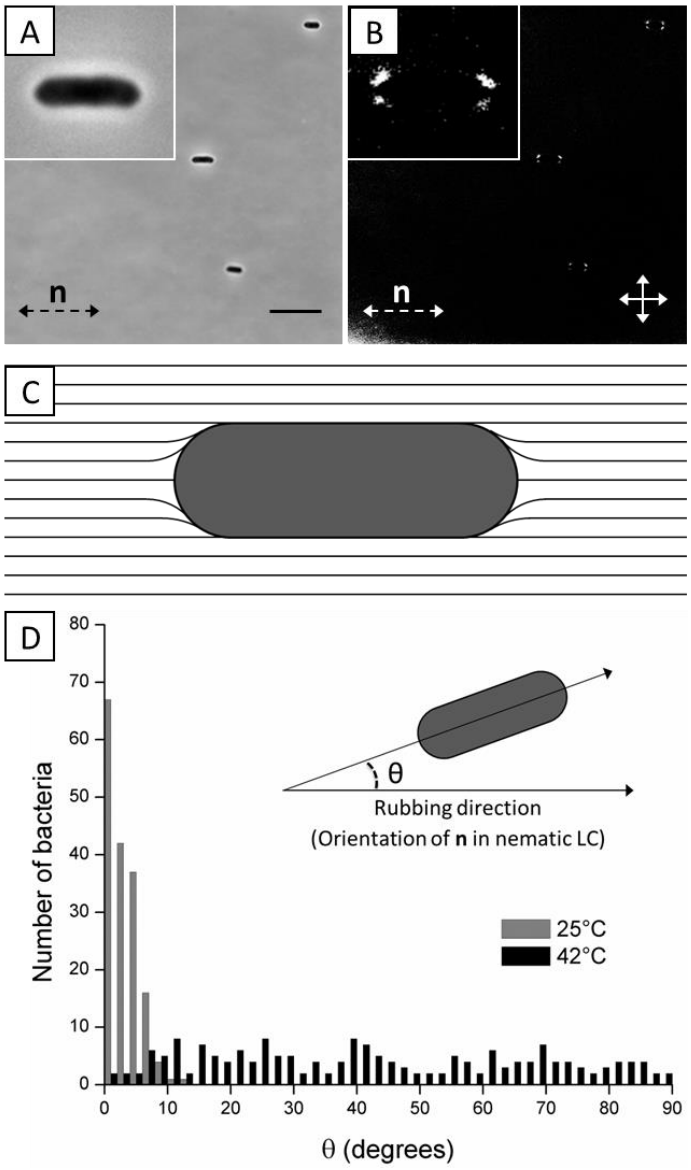

Figure 4-2. Configuration of LC around bacteria and resulting bacterial alignment.

(A, B) Bright field and crossed polars images, respectively, of non-motile *P. mirabilis-flhDC* cells dispersed in nematic DSCG solution at 25°C. The double-headed solid arrows in (B) indicate the positions of the polarizers while the double-headed dotted arrows depict the orientation of the LC director (n). (C) Schematic representation of the LC director profile that results from weak, tangential anchoring of the LC on the surface of *P. mirabilis-flhDC* cells. (D) Distribution of angles between the rubbing direction of the glass slides and the long axis of *P. mirabilis-flhDC* cells in DSCG solution at 25°C (nematic) and 42°C (isotropic). The scale bar in (A) is 10 μm. Values are reported with associated standard errors.

4.3.2 Interactions of bacteria mediated by LC

As noted above, past studies have demonstrated that the elasticity of LCs, and topological defects that form about passive particles in LCs, mediate particle-particle interactions that result in self-assembly of the particles.[7–11] For example, it has been demonstrated that spherical and ellipsoidal colloids with tangential surface anchoring form well-defined chains – for spherical colloids the vector that joins the particle centers is offset 30° from the far-field director.[36] We observed the above-described strain induced in the LC by non-motile and motile *P. mirabilis-flhDC* cells similarly leads to inter-bacterial forces that result in the formation of multi-cellular complexes. Figure 4-3A provides a sequence of snapshots which demonstrates the formation of a linear chain of two motile *P. mirabilis-flhDC* cells (see Video S3 in the online Supporting Information). At t = 3.7 s, the two bacteria, which had previously been swimming towards one another, associate together into a chain. This chain-like assembly then continues to move with a velocity similar to that of the faster individual component cell prior to the association event (Figure 4-3B). At later time points, the bacteria move within the LC together, retaining this state of association. We only observed the end-on-end association of *P. mirabilis-flhDC* cells in the nematic phase of the DSCG solution (they do not form within the isotropic phase). We also found that a small space remained between associated motile bacteria indicating the existence of a short-range repulsion. Limited by the resolution of our optical microscope, we estimate that the closest approach of the surfaces of the bacteria is approximately 0.3 μm. Although the origin of the repulsive interaction leading to this separation is unknown, it may arise from steric and/or electrostatic interactions between cells due to the presence of the lipopolysaccharide that decorates the outer leaflet of the bacterial membrane.

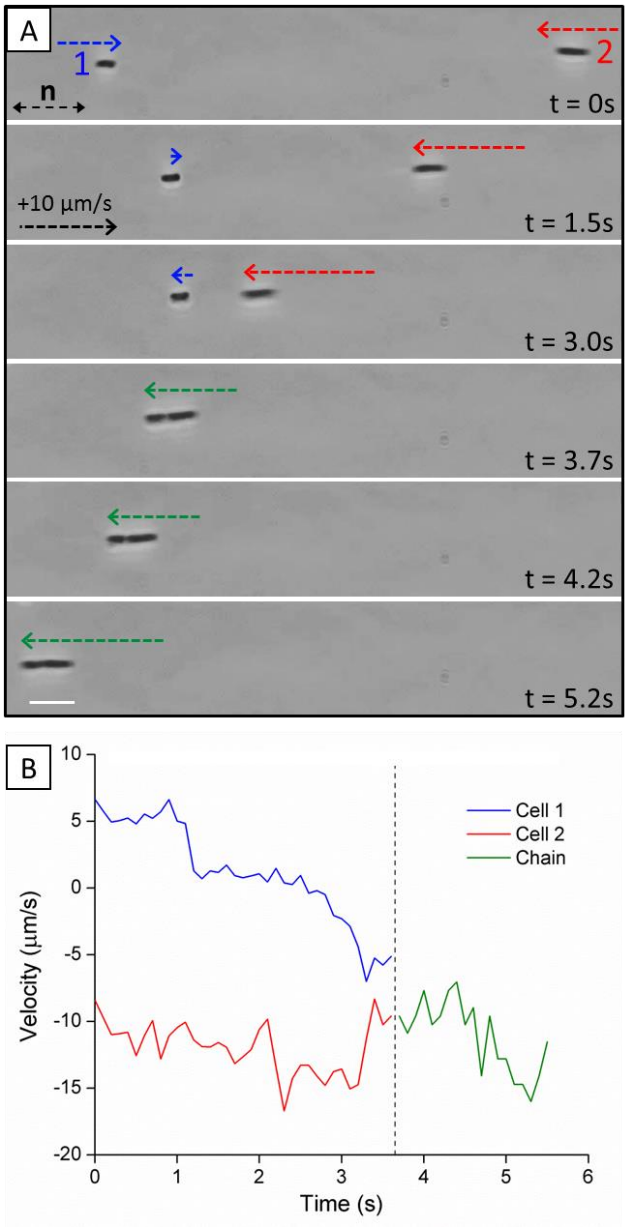

Figure 4-3. Dynamic association of motile bacteria in nematic LC.

(A) Sequence of images (bright field) showing end-on-end association of two motile *P. mirabilis-flhDC* cells in nematic DSCG solution (15 wt%) at 25°C. Dotted arrows indicate the velocity of the bacterial cells (see calibration in t = 1.5s). (B) Plot of the velocities of the *P. mirabilis-flhDC* cells shown in (A) before and after association into the chain. The scale bar in (A) is 5 µm.

The role of the elasticity of the LC in mediating the inter-bacterial interactions was confirmed by measurement of the relative orientations of the centroids of non-motile bacterial

cells within chains (Figure 4-4A). An angle of 5.5 ± 0.8° with respect to the far-field LC director was measured for chains of non-motile *P. mirabilis-flhDC* cells, consistent with theoretical predictions for elasticity-mediated interactions of ellipsoidal microparticles with tangential anchoring and aspect ratios matching *P. mirabilis-flhDC* cells.[9] We found that linear chains of motile *P. mirabilis-flhDC* cells were instead oriented at an angle of 3.3 ± 0.5° from the far-field director, an observation which likely reflects the drag forces generated by the motion of the swimming bacteria. Crossed-polar images confirm the quadrupolar symmetry of the nematic director near the surface of the non-motile bacteria within these chains (Figure 4-4B).

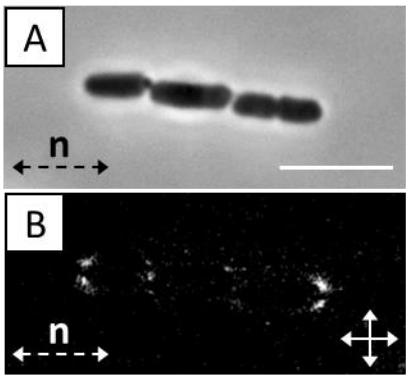

Figure 4-4. Multi-cellular assemblies formed in nematic LC.
(A) Bright field and (B) crossed polars images of a non-motile *P. mirabilis-flhDC* multi-cellular complex (trimer) in nematic DSCG solution (15 wt%) at 25°C. The scale bar in (A) is 5 μm.

Consistent with past studies of assemblies of passive particles, non-motile bacteria associated irreversibly in nematic DSCG solutions. In contrast, however, we frequently observed motile bacteria within multi-cellular assemblies to separate from each other with trajectories that followed the LC director (Figure 4-5A; also see Videos S4 and S5 in the online Supporting Information). We hypothesized that this dissociation of motile *P. mirabilis-flhDC* bacteria via flagella-derived forces would decrease the populations of multi-cellular assemblies (dimers,

trimers, and tetramers) found in LC suspensions of motile cells relative to non-motile cells. To test this idea, we prepared dispersions of both motile and non-motile *P. mirabilis-flhDC* cells in parallel at equal cell densities. Approximately 30 minutes after the addition of the concentrated bacteria solutions to DSCG and preparation of imaging chambers, we acquired images of more than 400 motile and non-motile bacteria. We quantified the number of single cells and cells within multi-cellular assemblies for each population (motile and non-motile) and scaled the final numbers to a population of 400 total cells. As seen in Figure 4-5B, we found that the population of motile monomers is higher by a factor of two relative to non-motile monomers, whereas the population of non-motile dimers is enriched relative to motile dimers. The role of flagella-derived forces in biasing the size-distribution of multi-cellular bacterial complexes is evidenced further in the populations of motile and non-motile trimers and tetramers in Figure 4-5B.

We estimated the magnitude of the LC-mediated attractive force acting between bacteria with surface anchoring energy W and quadrupolar distortions of the director as

$$F_{elastic} \propto C(W^2R^2/K)(2R/d)^6 \qquad (4-2)$$

where *d* is the distance between the surfaces of the two rod-shaped bacteria (0.3 μm, see above), and C is a coefficient of order one.[15,37,38] The parameter W (so-called "anchoring strength") quantifies how strongly LCs are held in a particular orientation at a surface. Guided by observations reported above indicating weak anchoring ($WR/K \sim 1$) of LCs on the surfaces of the bacteria [and reports of weak anchoring of DSCG at other interfaces[34,35]], we used $W \sim 10^{-5}$ J/m^2 to calculate $F_{elastic} \sim 10$ pN at d = 0.3 μm. Our observation that $F_{elastic}$ is comparable to our estimate of the propulsive forces generated by the flagella of *P. mirabilis-flhDC* cells [~60 pN, see above] provides additional support for the conclusion that the population of multi-cellular assemblies shown in Figure 4-5B (for motile bacteria) belong to non-equilibrium states

of the system that arise from the interplay of flagella-derived dissociative forces and elasticity-mediated attractive forces in the LC.

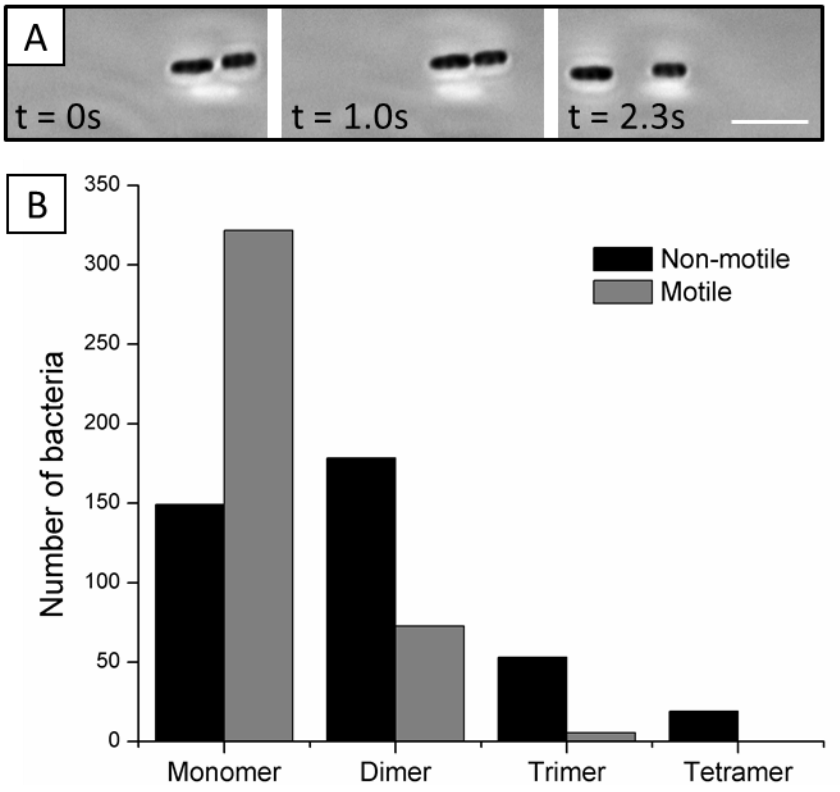

Figure 4-5. Reversible assembly of motile bacteria within LCs.
(A) Sequence of images (bright field) showing both the association and dissociation of two motile bacteria in nematic DSCG solution at 25°C. (B) Populations of bacteria in multi-cellular complexes formed in nematic DSCG solution by non-motile (black) and motile (gray) bacteria. (See text for experimental details.) The total number of cells in both populations is 400. The scale bar in (A) is 5 μm.

4.4 Discussion

Our results suggest that the elasticity of a nematic LC significantly influences both bacterial dynamics and organization. Not only do elasticity-mediated forces orient and direct the motion of isolated bacteria parallel to the director, as has been reported previously,[15,16] but additionally we find they induce the assembly of *P. mirabilis-flhDC* cells into linear chains. The

force (~60 pN) produced by motile *P. mirabilis-flhDC* cells to move within the viscous LC solution at $\overline{V} = 8.8 \pm 0.2$ μm/s is comparable in order of magnitude to the attractive LC inter-bacterial force (~10 pN), which facilitates the dissociation of multi-cellular complexes. Specifically, from our estimates of the magnitudes of these forces, we conclude that a *P. mirabilis-flhDC* cell can escape from elasticity-mediated interaction with another cell when a significant component of its flagella-derived propulsive force is directed opposite to the attractive elastic force. An unresolved question that emerges from our study is the extent to which the flagella-derived forces are changed when the bacteria are assembled into multi-bacterial complexes (as a consequence of the LC-mediated attractions). It is possible that the close proximity of bacteria within multi-cellular complexes (~0.3 μm spacing) may restrict the motion of flagella bundles (and propulsive forces) when bacterial motion is directed in opposition to the attractive elastic force. We note, for example, that following the formation of a linear chain of bacteria (Figure 4-3A), the cells continue to move at a speed and in a direction consistent with the fastest individual cell prior to the association event (Figure 4-3B). This observation may indicate that little propulsive force is generated by the second component cell in the direction of motion, which is opposite to the elastic attraction force.

We observed that the dissociation of motile *P. mirabilis-flhDC* cells using flagella-derived forces significantly influenced the population of individual cells and multi-cellular assemblies dispersed within LCs (Figure 4-5). Specifically, the reversibility of the elasticity-mediated inter-bacterial interaction for motile cells enriches monomers and depletes multi-cellular assemblies with respect to non-motile cells, which irreversibly associate with one another. We predict that the size distributions measured for motile bacteria suspended within the LC for longer periods will evolve, likely heightening the differences that we observed between

the populations of motile and non-motile cells. Alternatively, the relative abundance of multi-cellular complexes of motile bacteria can likely be tuned by manipulating the magnitude of the propulsive force they generate or by altering their size and shape (thus influencing the strength of the elastic attraction forces) using different species of bacteria or genetic engineering.

Finally, the results in this paper suggest several additional directions for research using motile bacteria suspended in LCs. Future investigations could focus on elastic interactions acting on bacteria at interfaces of LCs, interactions of bacteria with LC defects, and the use of external electric and magnetic fields to manipulate LCs and actively control bacterial behavior (e.g., to dynamically focus bacteria to a specific location in a system for analysis). In additional to producing fundamental information about the behavior of bacteria in anisotropic viscoelastic environments, these studies also may generate novel insight into the influence of anisotropy on bacteria in biological microenvironments.

4.5 Conclusions

In summary, this paper reports that motile *P. mirabilis-flhDC* cells form dynamic, reversible multi-cellular assemblies within the nematic phase of a lyotropic LC due to the interplay of elasticity-mediated forces and flagella-derived forces. While passive synthetic particles[7–11] as well as non-motile bacteria aggregate irreversibly when dispersed in a LC, we find the propulsive forces generated by the flagella of the *P. mirabilis-flhDC* cells are comparable in magnitude to LC-mediated attractive inter-bacterial forces (tens of pN) and can be used to overcome them. We observe that flagella-mediated dissociation significantly reduces the population of motile bacteria found in multi-cellular complexes relative to a population of non-motile cells. Overall, our observations provide new insight

into the manner in which elastic forces may also influence bacteria organization and dynamics within biological anisotropic viscoelastic microenvironments. In addition, our studies reveal that motile bacteria in LCs are a versatile system for investigations of self-organization that result from dissipative processes, for elucidation of general design principles for active soft matter (including systems containing synthetic particles driven by catalytic reactions[13,14]), and potentially for studies of the emergence of cooperative behaviors of populations of bacteria at high concentrations. In particular, we demonstrate that bacteria can be genetically engineered to manipulate the magnitude of the propulsive force that they generate in LCs to control, for example, the frequency with which they can escape elasticity-mediated inter-bacterial interactions. Based on our results, we envision that bacteria are well suited to serve as model 'active' particles with which to unmask dynamic phenomena that emerge from the interplay of local propulsive forces and anisotropic viscoelastic environments in LCs.

Acknowledgements

This work was supported by the National Science Foundation (under awards DMR-1121288 (MRSEC), CBET-0754921, and MCB-1120832), the National Institutes of Health (CA108467, AI092004, and 5T32GM08349), the Army Research Office (W911- NF-11-1-0251 and W911-NF-10-1-0181), and the United States Department of Agriculture (WIS01594).

4.6 Supporting Information

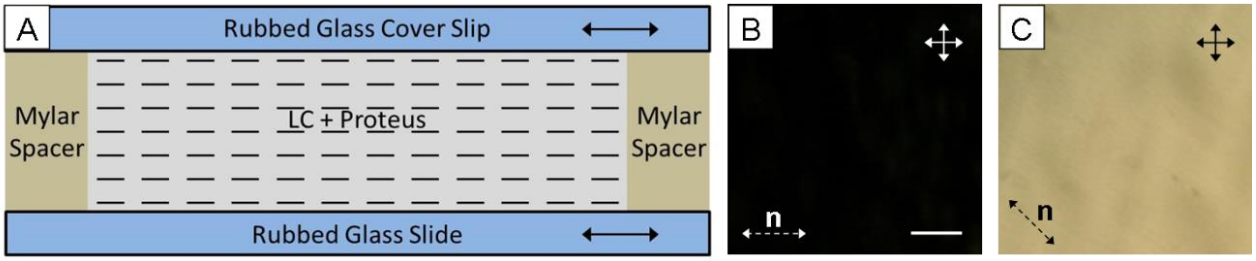

Figure 4-S1. Experimental setup.

(A) A schematic illustration depicting imaging chambers used to analyze bacterial cells in LC solutions. The double-headed arrows indicate the direction of rubbing along the surface of the glass slides. The LC director profile is indicated by the dotted lines. (B, C) Polarized light micrographs of the experimental cell aligned (B) parallel and (C) 45° to one of the crossed polarizers. We confirmed that the alignment of the nematic LC was parallel to the direction of rubbing by inserting a quarter wave plate into the optical path of a microscope and analyzing the appearance of the sample between crossed polars. The scale bar in (B) is 200 μm.

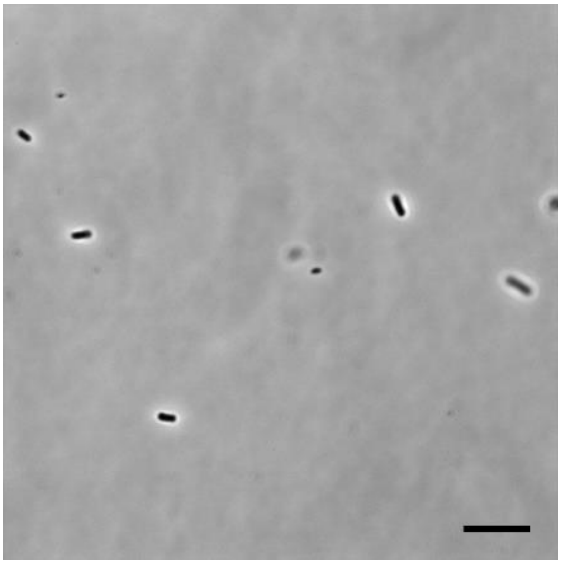

Figure 4-S2. Non-motile *P. mirabilis-flhDC* cells dispersed in an isotropic DSCG phase.

Bright field micrograph showing non-motile *P. mirabilis-flhDC* cells in an isotropic DSCG solution at 42°C. The scale bar is 10 μm.

Supplementary Video Captions

Supporting videos are available in the online SI (see DOI: 10.1039/c3sm52423).

Video S1. Bright field optical microscopy video showing anisotropic motion of *P. mirabilis-flhDC* cells in 15 wt% DSCG at 25°C (nematic phase). The LC director is aligned in the x-direction (horizontal direction of movie). Scale bar = 10 μm.

Video S2. Bright field optical microscopy video depicting isotropic motion of *P. mirabilis-flhDC* cells in 15 wt% DSCG at 42°C (isotropic phase). Scale bar = 5 μm.

Video S3. Bright field optical microscopy video which demonstrates the formation of a linear chain of two motile *P. mirabilis-flhDC* cells in 15 wt% DSCG at 25°C (nematic phase). Scale bar = 5 μm.

Video S4. Bright field optical microscopy video depicting the elasticity-mediated formation and subsequent dissociation of a linear chain of motile *P. mirabilis-flhDC* cells in 15 wt% DSCG at 25°C (nematic phase). Scale bar = 5 μm.

Video S5. Bright field optical microscopy video in which a linear chain of motile *P. mirabilis-flhDC* cells in 15 wt% DSCG at 25°C dissociates (nematic phase). Scale bar = 5 μm.

4.7 References

*This chapter was prepared as a Full Paper reporting original research in the journal *Soft Matter*. Rishi Trivedi contributed equally to performing and analyzing the experiments and preparing the manuscript. Hannah Tuson assisted in preliminary experiments and taught Rishi and I how to use the MATLAB bacteria tracking script.
Reprinted (adapted) with permission from: Mushenheim, P.C.; Trivedi, R. R.; Tuson, H. H.; Weibel, D. B. Abbott, N. L. Dynamic Self-Assembly of Motile Bacteria in Liquid Crystals. *Soft Matter* **2014**, 10, 88-95.

1. Fontes, D. E.; Mills, A. L.; Hornberger, G. M.; Herman, J. S. Physical and Chemical Factors Influencing Transport of Microorganisms through Porous Media. *Appl. Environ. Microbiol.* **1991**, 57, 2473–2481.
2. Shaw, T.; Winston, M.; Rupp, C. J.; Klapper, I.; Stoodley, P. Commonality of Elastic Relaxation Times in Biofilms. *Phys. Rev. Lett.* **2004**, 93, 098102.
3. Madoff, L. C.; Thaler, S. J.; Maguire, J. H. Infectious Arthritis. In *Harrison's Principles of Internal Medicine*; McGraw-Hill: New York, 2005; pp 2050–2055.
4. Flemming, H.-C.; Wingender, J. The Biofilm Matrix. *Nat. Rev. Microbiol.* **2010**, 8, 623–633.
5. Rey, A. D. Liquid Crystal Models of Biological Materials and Processes. *Soft Matter* **2010**, 6, 3402–3429.
6. Lapointe, C.; Hultgren, A.; Silevitch, D. M.; Felton, E. J.; Reich, D. H.; Leheny, R. L. Elastic Torque and the Levitation of Metal Wires by a Nematic Liquid Crystal. *Science* **2004**, 303, 652–655.
7. Tkalec, U.; Škarabot, M.; Muševič, I. Interactions of Micro-Rods in a Thin Layer of a Nematic Liquid Crystal. *Soft Matter* **2008**, 4, 2402–2409.
8. Musevic, I.; Škarabot, M.; Tkalec, U.; Ravnik, M.; Žumer, S. Two-Dimensional Nematic Colloidal Crystals Self-Assembled by Topological Defects. *Science* **2006**, 313, 954–958.
9. Mondiot, F.; Chandran, S. P.; Mondain-Monval, O.; Loudet, J.-C. Shape-Induced Dispersion of Colloids in Anisotropic Fluids. *Phys. Rev. Lett.* **2009**, 103, 238303.
10. Poulin, P.; Stark, H.; Lubensky, T. C.; Weitz, D. A. Novel Colloidal Interactions in Anisotropic Fluids. *Science* **1997**, 275, 1770–1773.
11. Škarabot, M.; Ravnik, M.; Žumer, S.; Tkalec, U.; Poberaj, I.; Babič, D.; Osterman, N.; Muševič, I. Interactions of Quadrupolar Nematic Colloids. *Phys. Rev. E* **2008**, 77, 031705.
12. Khoo, I. C.; Werner, D. H.; Liang, X.; Diaz, A. Nanosphere Dispersed Liquid Crystals for Tunable Negative-Zero-Positive Index of Refraction in the Optical and Terahertz Regimes. *Opt. Lett.* **2006**, 31, 2592–2594.
13. Paxton, W. F.; Kistler, K. C.; Olmeda, C. C.; Sen, A.; St Angelo, S. K.; Cao, Y.; Mallouk, T. E.; Lammert, P. E.; Crespi, V. H. Catalytic Nanomotors: Autonomous Movement of Striped Nanorods. *J. Am. Chem. Soc.* **2004**, 126, 13424–13431.
14. Paxton, W. F.; Sundararajan, S.; Mallouk, T. E.; Sen, A. Chemical Locomotion. *Angew. Chem. Int. Ed. Engl.* **2006**, 45, 5420–5429.

15. Smalyukh, I. I.; Butler, J.; Shrout, J. D.; Parsek, M. R.; Wong, G. C. L. Elasticity-Mediated Nematiclike Bacterial Organization in Model Extracellular DNA Matrix. *Phys. Rev. E* **2008**, 78, 030701.
16. Kumar, A.; Galstian, T.; Pattanayek, S. K.; Rainville, S. The Motility of Bacteria in an Anisotropic Liquid Environment. *Mol. Cryst. Liq. Cryst.* **2013**, 574, 33–39.
17. Tuson, H. H.; Copeland, M. F.; Carey, S.; Sacotte, R.; Weibel, D. B. Flagella Density Regulates Proteus Mirabilis Swarmer Cell Motility in Viscous Environments. *J. Bacteriol.* **2013**, 195, 368–377.
18. Hartshorne, N. H.; Woodard, G. D. Mesomorphism in the System Disodium Chromoglycate-Water. *Mol. Cryst. Liq. Cryst.* **1973**, 23, 343–368.
19. Lydon, J. Chromonic Review. *J. Mater. Chem.* **2010**, 20, 10071.
20. Cheng, L.-L.; Luk, Y.-Y.; Murphy, C. J.; Israel, B. A.; Abbott, N. L. Compatibility of Lyotropic Liquid Crystals with Viruses and Mammalian Cells That Support the Replication of Viruses. *Biomaterials* **2005**, 26, 7173–7182.
21. Shiyanovskii, S. V.; Lavrentovich, O. D.; Schneider, T.; Ishikawa, T.; Smalyukh, I. I.; Woolverton, C. J.; Niehaus, G. D.; Doane, K. J. Lyotropic Chromonic Liquid Crystals for Biological Sensing Applications. *Mol. Cryst. Liq. Cryst.* **2005**, 434, 587–598.
22. Lee, H.; Labes, M. M. Phase Diagram and Thermodynamic Properties of Disodium Cromoglycate-Water Lyomesophases. *Mol. Cryst. Liq. Cryst.* **1983**, 91, 53–58.
23. Nastishin, Y. A.; Liu, H.; Schneider, T.; Nazarenko, V.; Vasyuta, R.; Shiyanovskii, S. V; Lavrentovich, O. D. Optical Characterization of the Nematic Lyotropic Chromonic Liquid Crystals: Light Absorption, Birefringence, and Scalar Order Parameter. *Phys. Rev. E* **2005**, 72, 041711.
24. Nastishin, Y. A.; Neupane, K.; Baldwin, A. R.; Lavrentovich, O. D.; Sprunt, S. Elasticity and Viscosity of a Lyotropic Chromonic Nematic Studied with Dynamic Light Scattering. *Electron. Liq. Cryst. Commun.* **2008**, arXiv.org/abs/0807.2669.
25. Champion, J. V; Meeten, G. H. Conformation of Sodium Cromolyn in Aqueous Solution Using Light Scattering and Magnetic Birefringence. *J. Pharm. Sci.* **1973**, 62, 1589–1595.
26. Nastishin, Y. A.; Liu, H.; Shiyanovskii, S. V.; Lavrentovich, O. D.; Kostko, A. F.; Anisimov, M. A. Pretransitional Fluctuations in the Isotropic Phase of a Lyotropic Chromonic Liquid Crystal. *Phys. Rev. E* **2004**, 70, 051706.
27. Luk, Y.-Y.; Tingey, M. L.; Hall, D. J.; Israel, B. A.; Murphy, C. J.; Bertics, P. J.; Abbott, N. L. Using Liquid Crystals to Amplify Protein−receptor Interactions: Design of Surfaces with Nanometer-Scale Topography That Present Histidine-Tagged Protein Receptors. *Langmuir* **2003**, 19, 1671–1680.
28. Greenberg, E. P.; Canale-Parola, E. Motility of Flagellated Bacteria in Viscous Environments. *J. Bacteriol.* **1977**, 132, 356–358.
29. Stark, H.; Ventzki, D. Stokes Drag of Spherical Particles in a Nematic Environment at Low Ericksen Numbers. *Phys. Rev. E* **2001**, 64, 031711.
30. Koenig, G. M.; Ong, R.; Cortes, A. D.; Moreno-Razo, J. A.; de Pablo, J. J.; Abbott, N. L. Single Nanoparticle Tracking Reveals Influence of Chemical Functionality of Nanoparticles on Local Ordering of Liquid Crystals and Nanoparticle Diffusion Coefficients. *Nano Lett.* **2009**, 9, 2794–2801.
31. Abras, D.; Pranami, G.; Abbott, N. L. The Mobilities of Micro- and Nano-Particles at Interfaces of Nematic Liquid Crystals. *Soft Matter* **2012**, 8, 2026–2035.

32. Smith, C. J.; Denniston, C. Elastic Response of a Nematic Liquid Crystal to an Immersed Nanowire. *J. Appl. Phys.* **2007**, 101, 014305.
33. Brochard, F.; de Gennes, P. G. Theory of Magnetic Suspensions in Liquid Crystals. *J. Phys.* **1970**, 31, 691–708.
34. Nazarenko, V. G.; Boiko, O. P.; Park, H.-S.; Brodyn, O. M.; Omelchenko, M. M.; Tortora, L.; Nastishin, Y. A.; Lavrentovich, O. D. Surface Alignment and Anchoring Transitions in Nematic Lyotropic Chromonic Liquid Crystal. *Phys. Rev. Lett.* **2010**, 105, 017801.
35. Shiyanovskii, S. V.; Schneider, T.; Smalyukh, I. I.; Ishikawa, T.; Niehaus, G. D.; Doane, K. J.; Woolverton, C. J.; Lavrentovich, O. D. Real-Time Microbe Detection Based on Director Distortions around Growing Immune Complexes in Lyotropic Chromonic Liquid Crystals. *Phys. Rev. E* **2005**, 71, 020702.
36. Poulin, P.; Weitz, D. A. Inverted and Multiple Nematic Emulsions. *Phys. Rev. E* **1998**, 57, 626–637.
37. Smalyukh, I. I.; Lavrentovich, O. D.; Kuzmin, A. Z.; Kachynski, A. V.; Prasad, P. N. Elasticity-Mediated Self-Organization and Colloidal Interactions of Solid Spheres with Tangential Anchoring in a Nematic Liquid Crystal. *Phys. Rev. Lett.* **2005**, 95, 157801.
38. Smalyukh, I. I.; Kachynski, A. V; Kuzmin, A. N.; Prasad, P. N. Laser Trapping in Anisotropic Fluids and Polarization-Controlled Particle Dynamics. *Proc. Natl. Acad. Sci. U. S. A.* **2006**, 103, 18048–18053.

Chapter 5: Using Liquid Crystals to Reveal How Mechanical Anisotropy Changes Interfacial Behaviors of Motile Bacteria*

5.1 Introduction

Many bacteria live at interfaces.[1–11] The accumulation of bacteria at liquid-solid and liquid-air interfaces is an early step in the formation of bacterial communities that have a staggering impact on ecology,[1–5] industrial processing,[1,6,7] agriculture,[1,8,9] and human health.[1–3,5,10,11] In response to the growing significance attributed to bacteria in these niches, microbiologists have studied the mechanisms that influence cell movement, behavior, and assembly into multicellular structures at interfaces.[12–17] Much of this research has centered around biofilms on the surfaces of rigid solids due to the impact of these structures on human health, and the high costs associated with eradicating these microbial communities.[18–20] The extracellular matrix of biofilms[21–25] and other complex viscoelastic fluids in which bacteria live (e.g., synovial fluid, mucus, as well as fluids enriched in biopolymers such as collagen, chitin, and cellulose[15,26–31]) can possess local domains that exhibit long-lived anisotropic physical properties, particularly when they are exposed to shear or extensional flows. For instance, elastic relaxation times of bacterial biofilms, which commonly grow in flowing aqueous environments, have been measured to range from seconds to $>$10 min.[21–25] Thus, motile bacteria associated with biofilms[32] come into contact with extracellular polymeric substance domains that exhibit local alignment. However, virtually nothing is known about how anisotropy of an interfacial environment impacts fundamental bacterial behaviors. Significantly, the range of bacteria living in these anisotropic environments includes the biomedically important organisms *Mycobacterium tuberculosis*, *Neisseria gonorrhoeae*, *Pseudomonas aeruginosa*, *Staphylococcus*

aureus, and beta-hemolytic strains of *Streptococcus*.[24,28,31] Although previous investigators have studied bacteria at interfaces of isotropic liquids,[33–37] developing an understanding of the behavior and dynamics of bacteria at interfaces of anisotropic complex fluids, such as the liquid crystals (LCs) described in this work, has the potential to open a new window through which to view bacteria in environments that are relevant to biofilms, infections, and other fundamental and technological contexts.

In contrast to our lack of understanding of motile bacteria at the interfaces of complex fluids such as LCs, much more is known about the behavior at LC interfaces of synthetic micro-particles that are commensurate in size to bacteria.[38–45] Three key properties of LCs impact the equilibrium and dynamic interfacial behaviors of such micrometer-sized particles. First, because of the long-range ordering of molecules within LC phases, elastic strain of LCs about adsorbed microparticles gives rise to interparticle forces that have unusual symmetries.[38–42] These LC-mediated interparticle forces can generate hexagonal and chain-like two-dimensional interfacial assemblies. Second, LC phases possess anisotropic viscosities that influence the dynamics of localized particles, as indicated by the anisotropic diffusion of microparticles adsorbed to LC interfaces.[43] Third, topological defects that form at the surfaces of curved LC interfaces, such as LC droplets, possess high free energy densities and thus attract and localize microparticles.[44,45] Inspired by these past observations regarding synthetic microparticles at LC interfaces, we hypothesized that LC elasticity, viscosity, and topological defects would also likely impact fundamental behaviors of motile bacteria at LC interfaces.

In this work, we report the use of *Proteus mirabilis* as a model bacterium to study the dynamics of motile bacteria at interfaces of LCs, as it has been demonstrated previously that genetically manipulating flagella density on *P. mirabilis* can create cells that produce sufficient

flagella-derived propulsive forces to move through viscous fluids.[46] Specifically, *P. mirabilis* cells overexpressing flagella (that we refer to as *P. mirabilis* in this work) are rod-shaped with a length of ~3 μm and move at a velocity, $\bar{V} = 6.9 \pm 1.6$ μm/s through an aqueous polymer solution that has a kinematic viscosity (0.83 Pa·s)[46] comparable to the nematic LCs reported in this work. The interfaces used in our studies of *P. mirabilis* are formed between coexisting isotropic and nematic domains of aqueous solutions of disodium cromoglycate (DSCG) (Figure 5-1A). This use of DSCG interfaces extends previous studies of bacterial motility within the bulk phase of the LC.[47–49] Of particular relevance to this work, we recently reported that *P. mirabilis* cells align nematic DSCG phases parallel to their surfaces.[48] Minimization of the associated elastic strain of the LC resulted in orientations and motions of the rod-shaped cells along the nematic director.[48] We found also that the elasticity of the LC mediates attractive forces that assemble *P. mirabilis* cells into linear, multicellular structures. Formation of these structures was dynamic and reversible due to the interplay of flagella-derived propulsive forces and the elasticity-mediated attractive forces, both of which were comparable in magnitude for motile *P. mirabilis* cells (tens of pN).

The nematic-isotropic (N-I) interfaces used in our current study are defined by tactoids, which are elongated and cusped domains of either nematic LC in a continuous isotropic solution or isotropic phase domains dispersed in a continuous LC phase.[50–53] Such domains define a particularly interesting class of LC interfaces because their geometry leads to the generation of surface-localized topological defects (see below for additional discussion). Using this experimental system, we sought to determine whether bacteria would insert into the N-I interface of the tactoids and whether the orientational order (and associated anisotropic mechanical properties) of the nematic interface would guide the interfacial motility of cells. In addition,

inspired by observations (see above) of the association of microparticles with defects of LC droplets,[44,45] we aimed to explore how motile bacteria would be influenced by interfacial defects in the LC order. As described below, we find that the nematic elasticity of the LC combines with the presence of defects to define specific pathways by which bacteria can escape from nematic interfaces. We also show how this phenomenon can be tuned to control the capture and release of motile bacteria in LCs. We close this Introduction by noting that a recent publication by Zhou *et al.* reports an observation regarding the interaction of *Bacillus subtilis* cells with isotropic tactoids in nematic LC.[49] Below we contrast our findings with *P. mirabilis* to the observation with *B. subtilis* cells.

5.2 Experimental Section

Bacterial strains and cell culture. *P. mirabilis* strain HI4320 was transformed with plasmid pflhDC to create *P. mirabilis* cells overexpressing flagella. The plasmid pflhDC contained the *flhDC* genes from *P. mirabilis* inserted into pACYC184 (which contains a gene for chloramphenicol resistance). *P. mirabilis* cells were grown in chloramphenicol-resistance nutrient medium consisting of 1% (wt/vol) peptone (Becton, Dickinson, Sparks, MD), 0.5% (wt/vol) yeast extract (Becton, Dickinson), and 1% (wt/vol) NaCl (Fisher Scientific, Fairlawn, NJ) at 30°C in a shaking incubator.[46] Saturated overnight cultures were diluted 100-fold in 10 mL of fresh nutrient medium and grown in 150 mL Erlenmeyer flasks at 30°C in a shaking incubator at 200 rpm. We observed that the highest swimming velocity of *P. mirabilis* cells occurred during the stationary phase, hence we harvested cells at an absorbance (λ = 600 nm) of ~3.2 and concentrated them by centrifugation. The cells were washed three times with an aqueous buffer for bacterial motility (0.01 M KPO_4, 0.067 M NaCl, 10^{-4} M EDTA, 0.1 M

glucose, and 0.001% Brig-35, pH 7.0). To obtain non-motile *P. mirabilis* cells, the cells were treated with 4% glutaraldehyde for 3 h at 25°C after harvesting.

Lyotropic LC preparation. DSCG was purchased from Sigma-Aldrich (Milwaukee, WI) and used as received. Lyotropic LCs containing DSCG were prepared by mixing 15.3 wt% of DSCG with 84.7 wt% of aqueous motility buffer. The mixture was shaken for at least 12 h to ensure complete solubility and homogeneity. Before experimentation, the DSCG solution was heated at 65°C for 10 min to avoid possible time dependence of the properties of the mixture.[54,55] After cooling the solution to 25°C, a small volume of motility buffer containing bacteria was added to the DSCG mixture producing a final concentration of ~10^5 cells/mL. The final concentration of DSCG was 15.0 wt% in all experiments.

Preparation of imaging chambers. We created imaging chambers by adding a small volume (~1 µL) of DSCG solution on top of a glass slide between two sheets of 18 µm-thick Mylar film. A glass coverslip was placed on top of the Mylar and the chamber was sealed with epoxy to prevent water evaporation (see Figure 5-S1). We confirmed the direction of alignment of the nematic LC by inserting a quarter wave plate into the optical path of a microscope and analyzing the appearance of the sample between crossed polars.[56] Imaging chambers were used within 3 h of their preparation.

Microscopy. We imaged cells using a Nikon Eclipse Ti inverted optical microscope equipped with crossed polarizers and a Photometrics CoolSNAP HQ2 CCD camera (Tucson, AZ) using a Nikon Plan Apo l, 100X/1.45 oil objective lens. Videos were collected with the electron

multiplying gain off and with a 90 ms exposure time (11 frames/s). Images of cells were collected using Nikon NIS Elements software. A thermoplate (Tokai Hit, Fujinomiya, Japan) and 100X objective heater (Bioptechs, Butler, PA) were used to control the temperature of the samples during experiments. DSCG solutions were equilibrated at a particular temperature for at least 10 min before making observations and performing measurements of bacteria motility. An Olympus BX60 microscope equipped with crossed polarizers was also used to analyze the imaging chambers. Images were captured using a digital camera (Olympus C-2040 Zoom) mounted on the microscope and set to an f-stop of 2.8 and a shutter speed of 1/125 s.

Bacterial motility data analysis. Microscopy data for motile cells were analyzed using the MATLAB computing environment (The MathWorks, Natick, MA) by identifying the centroid of each bacterium in successive frames and grouping those points together to create a cell trajectory. These data were combined with the charge-coupled device frame rate to determine cell velocity.

Tactoid triple phase contact line measurement. Individual video frames were opened in ImageJ and the position of the triple phase contact line was determined using the Find Edges tool. Three consecutive traces of the triple phase contact line were performed to estimate its length.

Statistical Analysis. All experimentally determined values have been reported in the text and figures with associated standard errors unless otherwise noted.

5.3 Results

5.3.1 Capture and escape *of P. mirabilis* cells from the interfaces of nematic tactoids

We first sought to determine whether motile *P. mirabilis* cells would adsorb to interfaces formed between coexisting aqueous nematic and isotropic phases of 15 wt% DSCG in motility buffer. To this end, we prepared optical chambers containing 18 μm-thick DSCG films (see above) in which the nematic phase of DSCG was oriented parallel to the glass substrates and exhibited a degenerate azimuthal alignment. We observed the 15 wt% DSCG solution to form coexisting nematic and isotropic domains at temperatures between 29°C and 35°C. Specifically, after quenching samples from 40°C (isotropic phase) to 33°C, spindle-like domains of nematic phase with positive interface curvature and an elongated and cusped shape (tactoids) formed on the surface of the glass slides within a continuous isotropic phase (Figure 5-1B).[50–53] The prolate shape of the tactoids arises from a competition between the elasticity of the nematic phase and the interfacial tension between the nematic and isotropic phases.[57,58] As detailed elsewhere,[50–53] imaging of the nematic tactoids between crossed polars confirmed that the LC was anchored tangentially at the N-I interface and that two topological LC defects (boojums[50,59]) were located at the cusped poles near the triple phase (N-I-glass substrate) contact line. Although the elastic constant for twist (K_{22}) in nematic DSCG is an order of magnitude smaller than the elastic constants for splay (K_{11}) and bend (K_{33}),[60] we did not observe a twisted director profile within the sessile nematic tactoids, as evidenced by the extinction that occurs in the center of the tactoid when the major axis of the tactoid is aligned parallel with one of the polarizers (Figure 5-1B).[51,52,57,61,62] We also formed isotropic phase tactoids (in a continuous nematic phase) in our studies by heating a 15 wt% DSCG solution from 25°C (nematic phase) to 30°C (Figure 5-1C). We observed that both nematic and isotropic tactoid domains generally nucleated at and

remained attached to one of the glass substrates and following equilibration at either 33°C (nematic tactoids) or 30°C (isotropic tactoids) for several minutes, grew to a structure that was 30-µm in diameter along the major axis (Figure 5-1D). Unless otherwise noted, we restrict our observations to tactoids that had depth d < 18 µm, which is smaller than the gap between the glass substrates.

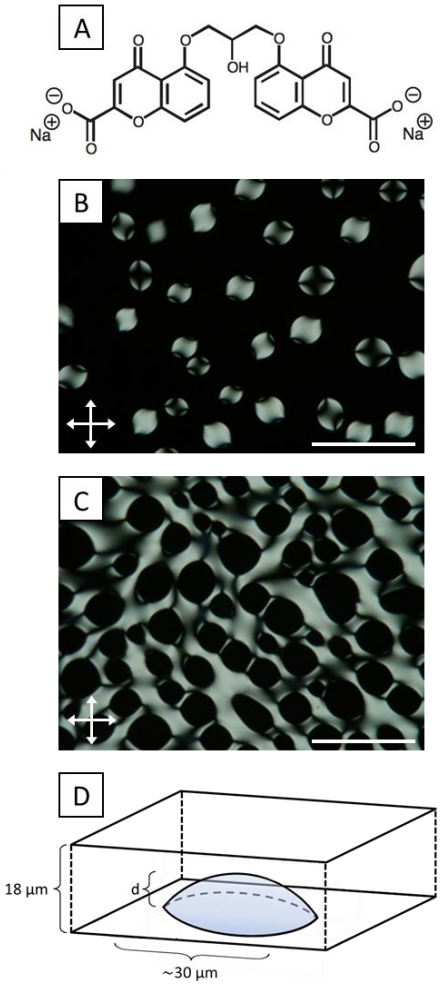

Figure 5-1. Formation of nematic and isotropic tactoids.

(A) Molecular structure of DSCG. (B and C) Crossed polar images of (B) nematic and (C) isotropic tactoids. The nematic tactoids formed in imaging chambers following cooling of an isotropic phase of 15 wt% DSCG solution from 40°C to 33°C; isotropic tactoids formed in imaging chambers following heating of a nematic phase DSCG solution from 25°C to 30°C. (D) Three-dimensional depiction of the shape adopted by sessile tactoids (both isotropic and nematic) in our experiments. Scale bars are 100 µm.

When *P. mirabilis* cells were dispersed uniformly in isotropic phases of DSCG at 40°C and then cooled to 33°C, we observed that the cells were excluded from the growing nematic domains (Figures 5-1B and 5-2A) and became concentrated in the continuous isotropic phase as well as proximate to the curved N-I interfaces of the tactoids. The *P. mirabilis* cells suspended within the bulk isotropic phase at 33°C moved without a directional bias with an average velocity of $\overline{V}$ = 17.6 ± 0.7 μm/s (N = 34), which is significantly faster than the velocity we measured previously for *P. mirabilis* cells in an isotropic phase of 15 wt % DSCG at 42°C ($\overline{V}$ = 8.1 ± 0.3 μm/s[48]) (Table 5-1). This difference in velocity is consistent with an increase in the viscosity of isotropic DSCG solutions with decreasing temperature[54] and an inverse relationship between *P. mirabilis* velocity and solution viscosity for μ < 9 mPa·s (See Table 5-1 for viscosities).[46] In contrast to the random movement of cells in the bulk isotropic phase, we observed bacteria near the surface of tactoids propelling themselves with clear directional bias along the N-I interface and the triple phase contact line with an average velocity of $\overline{V}$ = 17.1 ± 0.4 μm/s (N = 40) (Table 5-1). We discuss the magnitude of this interfacial velocity and origin of the biased motion below.

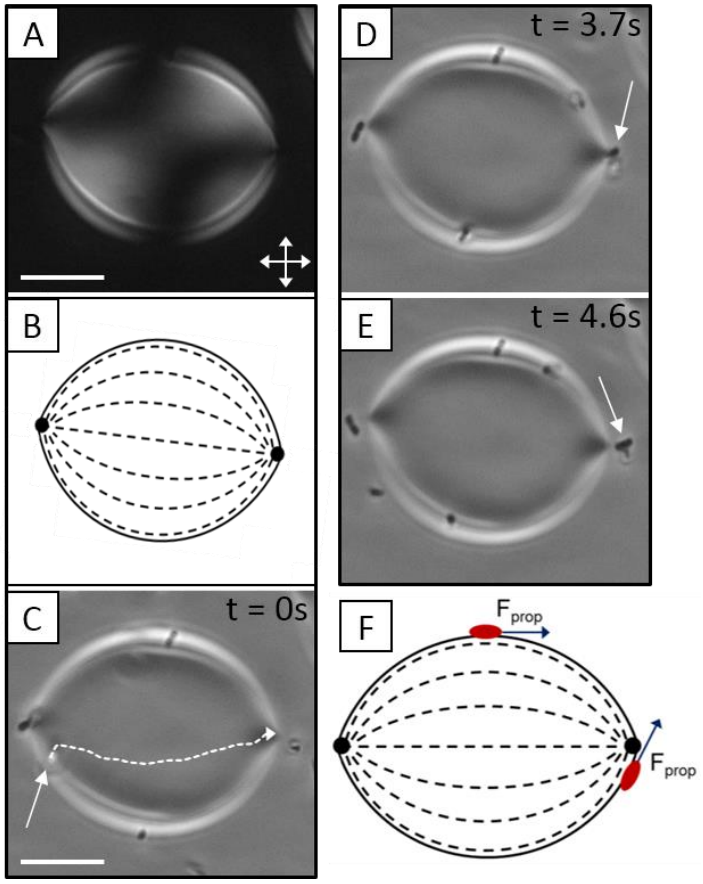

Figure 5-2. Guided motility and escape of a cell adsorbed to a nematic tactoid.

(A) Optical micrograph (crossed polars) of a nematic tactoid that formed within a continuous isotropic phase upon quenching a 15 wt% DSCG sample from 40°C to 33°C and that partially wets one of the glass surfaces of the imaging chamber. (B) Schematic representation of the LC director profile of the tactoid in (A). (C) Bright field micrograph of a nematic tactoid on which the trajectory of a motile P. mirabilis cell (depicted by an arrow) adsorbed to the N-I interface is indicated. (D and E) Bright field micrographs of a motile cell that escapes from the N-I interface at a boojum (topological defect at the cusped pole) of the tactoid. In (D), the cell is oriented toward the viewer. (F) Schematic diagram depicting the orientation of the flagella-derived propulsive force (F_{prop}) of motile bacteria adsorbed at various positions on the interface of a nematic tactoid. Scale bars are 10 μm.

Location	Temperature	Estimated Viscosity (mPa·s)	Velocity (μm/s)
Bulk nematic	25°C	700[a]	8.8 +/- 0.2[b]
Bulk nematic	30°C	650[a]	9.5 +/- 0.6
Bulk isotropic	33°C	9[c]	17.6 +/- 0.7
Bulk isotropic	42°C	2[c]	8.1 +/- 0.3[b]
N-I interface (isotropic tactoid)	30°C		16.7 +/- 0.5
N-I interface (nematic tactoid)	33°C		17.1 +/- 0.4

Table 5-1. Velocity of *P. mirabilis* in bulk DSCG phases and N-I interfaces.

[a] Estimated based on comparison of velocity of *P. mirabilis* cells in 15 wt% DSCG to previous measurements[46] of *P. mirabilis* motility in isotropic solutions of known viscosity.

[b] Data taken from [48].

[c] Estimated based on measurements of the shear viscosity of aqueous solutions of 14 wt% DSCG[54].

Limited by the resolution of our optical microscope, we were unable to initially determine whether the *P. mirabilis* cells near the N-I interface were inserted into the interface, such that they contacted both nematic and isotropic phases, or whether they remained suspended in the isotropic phase. We hypothesized that if they were inserted into the interface, *P. mirabilis* cells (which we reported previously anchor LCs tangentially[48]) would preferentially orient and move parallel to the local director at the interface of the tactoid due to the elasticity of the nematic phase. Figure 5-2C depicts the trajectory of a *P. mirabilis* cell that we observed to move along the N-I interface of a nematic tactoid. The cell depicted in Figure 5-2C moves out of the focal plane—located at the surface of a glass slide—as it moves along the interface of the sessile tactoid. A comparison of Figures 5-2B and 5-2C reveals that the trajectory of the cell follows the interfacial director profile of the tactoid (see Movie S1 in the online Supporting Information). We also determined the long axis of the motile bacterium to be oriented parallel to the LC

director. Analysis of additional bacterial trajectories near nematic tactoids yielded similar results (Figure 5-S2). In particular, we note that due to the quadrupolar symmetry of the tactoids, bacteria were guided by the LC director towards either of the boojum defects. Based on the directed motion of *P. mirabilis* at the interface of the tactoid, we concluded that the motile cells adsorb and insert into the N-I interface. We also observed non-motile bacteria (*P. mirabilis* cells treated with 4% glutaraldehyde) to adopt orientations parallel to the local nematic director when positioned at the interface of nematic tactoids (Figure 5-S3).

The strong adsorption of micrometer-sized particles to liquid-liquid interfaces is known to be driven, in part, by the interfacial tension between the two phases. To determine if the interfacial tension between the isotropic and nematic phases of the DSCG solution (γ_{NI}) is sufficiently large to drive the adsorption of the bacterial cells, we considered that the prolate shape of tactoids (with characteristic radius, R) arises from a balance between the elasticity of the bulk nematic phase (which scales as ~KR, where K is a one constant approximation of the LC elastic constant) and the energy of the N-I interface (which scales as $\gamma_{NI}R^2$).[51,57,58] For these bulk and surface energies to be comparable when R ~ 10^{-5} m (using K ~ 10 pN[60]), we estimate that γ_{NI} is ~ 10^{-6} J/m^2. This agrees with estimates of γ_{NI} for other lyotropic LCs including aqueous sols of vanadium pentoxide[57] (γ_{NI} ~ 10^{-6} J/m^2) and aqueous suspensions of cellulose crystallites[63] (γ_{NI} ~ 10^{-6} – 10^{-7} J/m^2) although a larger estimate (γ_{NI} ~ 10^{-4} J/m^2) has been reported previously for DSCG.[50] By modeling *P. mirabilis* cells as rod-shaped particles with a major axis 2*a* and minor axis 2*b*, and by noting the radius of curvature of the interface to be large compared to the cell, the interfacial area (A_{NI}) removed due to the presence of an adsorbed bacterium is given by $A_{NI} = \pi b^2 \sin^2\left[\cos^{-1}(1-h/b)\right]\left[1+\frac{4(a/b-1)}{\pi \sin\left[\cos^{-1}(1-h/b)\right]}\right]$, where *h* is the depth of immersion of the

bacterium in the nematic phase.[64] From this expression, we calculate the maximum area occupied by *P. mirabilis* to be 2.8 μm^2, thus leading to an upper bound on the contribution of γ_{NI} to the adsorption energy of 3×10^{-18} J/cell (~10^3 kT). This value is consistent with our observation of irreversible adsorption of non-motile *P. mirabilis* cells to the interfaces of nematic tactoids of DSCG.

Although we calculated *P. mirabilis* cells to be attached to the N-I interface with an adsorption energy of ~10^3 kT, we observed motile cells to be able to escape from the interface of nematic tactoids and enter the continuous isotropic phase. Figures 5-2C through 5-2E, show a representative example in which a motile cell adsorbs to a nematic tactoid and follows the director profile along the interface of the tactoid (Figure 5-2C) to arrive at one of the two cusped poles of the tactoid, where a boojum is present (Figure 5-2D). At the boojum, the cell escapes from the N-I interface into the isotropic phase (Figure 5-2E). Overall, we found that two-thirds (N = 170) of motile bacteria that escaped from the interface of nematic tactoids did so near a boojum. We hypothesize that this dominant mode of escape reflects the fact that i), motile bacteria are focused to the boojums by the convergence of the LC director profile (Figure 5-2B); and ii), a component of the flagella-derived force produced by cells (F_{prop}; estimated to be ~60 pN for *P. mirabilis* moving in bulk nematic DSCG[48]) is directed normal to the contact line near the boojum and thus can overcome forces associated with interfacial tension that hold cells at the interface (Figure 5-2F). These ideas are supported by additional observations reported below, which reveal motile bacteria to escape from the N-I interfaces of isotropic tactoids almost exclusively via boojums.

Whereas bacterial cells were able to escape from the N-I interface into the isotropic phase, we did not observe detachment of motile bacteria from the N-I interface into the interior

of the nematic tactoids in our experiments. We hypothesize that an energetic penalty associated with elastic strain of the nematic director around a cell, which occurs principally near the hemispherical poles of the bacteria,[48,65] is likely responsible for this observation and will tend to prevent escape of bacteria into the LC phase. We estimate the energy associated with the elastic strain of the LC around a cell on the interface as $E_{elastic} \sim Kb\, f(h/b)$, where $f(x)$ is a dimensionless function of the location of the cell at the interface.[40,66] For *P. mirabilis* and 15 wt% DSCG, we estimate K*b* to be 5×10^{-18} J, and conclude that the magnitude of this elastic energy penalty is comparable to the adsorption energy due to interface tension. We note that we estimate the energy associated with the extension of the N-I interface around an adsorbed cell due to capillary deformations to be only on the order of 10^{-20} J,[67] and thus small compared to the elastic energy associated with strain of the LC.

The previous conclusion that the energetic effects associated with elastic deformations around bacteria are comparable to interfacial tension leads us to also hypothesize that the nematic elasticity of the LC likely impacts the location of cells at N-I interfaces. Specifically, the elasticity of the LC should promote contact of the surface of the cells with the isotropic phase at the interface. Indeed, our measurement of *P. mirabilis* cells moving along the N-I interface with an average velocity similar to that in bulk isotropic phase at 33°C (Table 5-1) suggests that the majority of the surface of each cell is in contact with the isotropic phase.

5.3.2 Dynamics of *P. mirabilis* cells at the interfaces of isotropic tactoids

Based on the previous observations, we interpret the elasticity of the LC and the presence of topological defects to play key roles in influencing the interfacial behavior of bacteria. To further explore how these properties of the N-I interface impact *P. mirabilis* behaviors, we

created isotropic domains within a continuous nematic phase by heating 15 wt % DSCG solutions from 25°C (nematic phase) to 30°C (Figure 5-1C). The lateral size (~30 μm in diameter) and elongated, tactoidal shape of the isotropic domains resembled the nematic tactoids at 33°C described previously. However, tangential anchoring of the LC produced boojum defects just outside the N-I interface of the two cusped poles of the isotropic tactoids (Figures 5-3A and 5-3B). In addition, the morphologies of the isotropic domains that formed—particularly when they were in close proximity to one another (Figure 5-1C)—displayed considerably greater complexity than the nematic domains (Figure 5-1B) due to the strain present in the continuous nematic phase separating the isotropic domains. We found that isotropic domains with either one or three cusps nucleated from the cores of half-integer disclinations when heating from the nematic phase (50). Below, we describe experiments with motile bacteria interacting with sessile isotropic tactoids containing two cusps.

During the heating of DSCG solutions into the biphasic region, we observed motile *P. mirabilis* cells adsorb to the interface of the growing isotropic tactoid domains. Consistent with previous observations for *B. subtilis*,[49] the orientation and motion of the adsorbed motile *P. mirabilis* cells were constrained to be parallel to the orientation of the local director of the adjacent nematic phase (Figures 5-3B and 5-3C), similar also to motile bacteria adsorbed to nematic tactoids (Figure 5-2). Cells moved along the interface of isotropic tactoids with an average velocity of $\overline{V} = 16.7 \pm 0.5$ μm/s (N = 40). This velocity is similar to our measurement of bacterial motility at the interface of nematic tactoids (Table 5-1) and suggests that the interfacial environment experienced by *P. mirabilis* cells at the N-I interface (away from the cusps) is similar for the two types of tactoids.

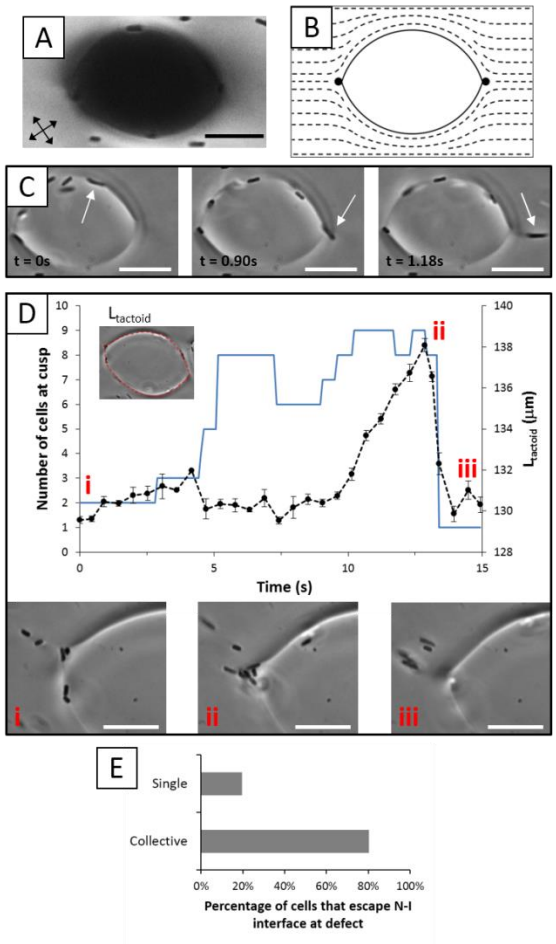

Figure 5-3. Escape mechanisms of motile bacteria from adsorption to an isotropic tactoid.

(A) Optical micrograph (crossed polars) of a sessile isotropic tactoid that forms within a continuous nematic phase after heating a 15 wt% DSCG sample from 25°C to 30°C. (B) Schematic representation of the LC director profile in the nematic phase. (C) Sequence of images (bright field) depicting the escape of a motile *P. mirabilis* cell (indicated by an arrow) from the interface of an isotropic tactoid into the continuous nematic phase at the cusped pole of the tactoid (adjacent to a boojum defect in the nematic phase). (D) Graph and sequence of images (bright field) depicting the accumulation of motile *P. mirabilis* cells near the cusped pole of an isotropic tactoid and their collective escape. In the graph, the number of cells localized at the cusp is given by the blue line, whereas measurements of $L_{tactoid}$, the triple phase (N-I-glass substrate) contact line of the tactoid are given by the black data points (with a dotted black line to guide the eyes). The force generated by trapped cells at the pole deforms the interface and extends the triple phase contact line. Ejection of the trapped cells into the nematic phase allows the interface to relax to its initial shape. (E) A plot of the frequency with which motile cells escape the N-I interface of isotropic tactoids near defect points as either single cells (as in (C)) or through a collective mechanism (as in (D)). Scale bars are 10 µm. Error bars represent standard deviations.

In contrast to our observations with nematic tactoids (motile cells did not detach from the N-I interface to enter the nematic phase), however, we observed motile *P. mirabilis* cells to escape the N-I interface of isotropic tactoids into the surrounding nematic phase. Escape of motile cells into the nematic phase primarily (~95%, N = 274) occurred at one of the two cusped poles of the tactoid, where boojums are located in the adjacent nematic phase (Figure 5-3B). We observed cell detachment to occur by at least two mechanisms. First, as shown by the sequence of micrographs in Figure 5-3C, we observed individual *P. mirabilis* cells adsorbed at the N-I interface to move toward one of the cusps of the isotropic tactoids, where they escaped (see Movie S2 in the online Supporting Information). Detachment of isolated cells from isotropic tactoids in this manner closely resembled our previous observations of the method of cell detachment from nematic tactoids (Figure 5-2) as well as the mechanism of single-cell escape from the interface of an isotropic tactoid observed for *B. subtilis*.[49]

However, we more frequently observed a second mechanism through which groups of motile *P. mirabilis* cells collectively escaped the interface of isotropic tactoids (Figure 5-3D, also see Movie S3 in the online Supporting Information). This event occurred when an adsorbed motile cell arrived at the cusp of an isotropic tactoid and appeared to get trapped by the boojum defect. Subsequently, additional cells that were directed toward the same cusp by the interfacial LC director profile were blocked in their escape by the first cell. This phenomenon led to the accumulation of an assembly of cells at the boojum. After several cells were trapped near the boojum, these cells along with additional motile cells that arrived at the cusp exerted a collective force on the interface of the tactoid that was observed to deform the N-I interface near the accumulated cells and lead to a growing, measurable extension of the triple phase contact line with time (Figure 5-3D). Ultimately, after the N-I interface near the cusp had been significantly

deformed, the arrival of one additional motile cell at the cusp was typically observed to initiate collective escape of the entire cluster of cells into the nematic phase. We measured the average colony size to lead to escape to be 4 cells, although as many as 10 or as few as 2 cells can also lead to escape. Free from the strain generated by the assembly of bacteria, the N-I interface relaxed back to its initial state and the process could be repeated. Overall, we found that motile *P. mirabilis* cells exited the N-I interface of isotropic tactoids much more frequently through this cooperative mechanism than as individual cells (Figure 5-3E). We also note that our observation of the trapping of motile bacteria at boojum defects near the cusps of isotropic tactoids closely resembles the partitioning of synthetic (e.g., polystyrene) microparticles to surface-associated defects of LC droplets.[44,45] This latter phenomenon is driven by replacement of the high-energy defect core and surrounding strained LC by the particle. We hypothesize that this same mechanism underlies the trapping of motile bacteria at defects described in this work. In support of this hypothesis, we observed that non-motile *P. mirabilis* cells, which adsorb irreversibly to isotropic tactoids, were also frequently localized at the cusps (Figure 5-S4). It is likely that elastic forces drive the localization of the non-motile cells to the boojum defects near the cusps.[44,45]

Although motile cells did not detach into the interior of nematic tactoids, we occasionally observed the detachment of motile cells into the interior of isotropic tactoids (Figure 5-S5). Together, these observations reflect the relative ease with which cells can detach from the N-I interface into the isotropic phase, likely due to several factors including the release of elastic strain accompanying cells at the interface (as opposed to introduction of additional strain associated with escape into the nematic phase) and the preferential wetting of adsorbed cells by the isotropic phase. To confirm this conclusion, we prepared two LC samples in parallel

containing equal densities of motile cells. One sample was heated from room temperature to 30°C to form isotropic tactoids, whereas the other was cooled from 40°C to 33°C to form nematic tactoids. After equilibration for 15 min, we imaged many tactoids in both samples and quantified the number of motile bacteria found adsorbed to the N-I interface. The tactoids that we analyzed were all of similar size (~30 μm in diameter). Inspection of Figure 5-4 reveals that cells were only concentrated on the interface of the isotropic tactoids (see also Figure 5-S6). Additional observations confirmed that motile *P. mirabilis* cells have a much shorter residence time on the N-I interface of nematic tactoids relative to isotropic tactoids. These differences provide added support for the conclusion that the elasticity of the nematic phase generates a barrier for bacterial detachment and that, in the presence of this barrier, bacteria escape is largely limited to a structured pathway that involves director-guided motion to boojums through which the cells exit using a force generated by a multicellular assembly.

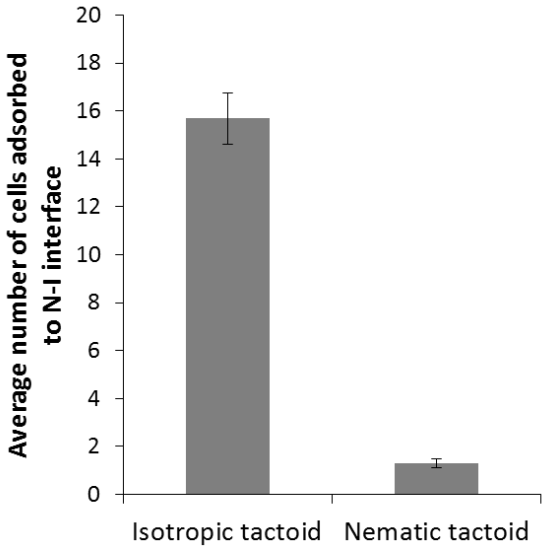

Figure 5-4. Temporal accumulation of motile bacteria at the interface of isotropic tactoids.
Average number of cells adsorbed to nematic tactoids (at 33°C) (N = 35) and isotropic tactoids (at 30°C) (N = 37) following a 15 min equilibration period at the indicated temperature. The tactoids were of similar size: ~30 μm in diameter. Error bars represent standard errors.

5.3.3 Capture and release of motile bacteria by using nematic elasticity and topological defects

Our observations of the infrequency with which bacteria escape from the N-I interface of isotropic tactoids into the nematic phase—particularly when not proximate to a topological defect—led us to explore if it is possible to corral motile *P. mirabilis* within large isotropic domains of a 15 wt% DSCG solution at 30°C by quenching the solution from the isotropic phase into the biphasic region rather than heating from the nematic (the latter was shown in Figure 5-3). We also hypothesized that the probability of encountering a topological defect would be dependent on domain size and thus release of bacteria from isotropic corrals might be tuned via control of the size of domains. To test this concept, we heated a suspension of cells in DSCG to 40°C and subsequently quenched the sample to 30°C. As the DSCG solution entered the biphasic region during cooling, motile cells were excluded from nucleating nematic phase tactoids. While the sample was equilibrated at 30°C, the nematic tactoids grew in size and coalesced, trapping isotropic phase domains (Figures 5-5A through 5-5C). These isotropic domains were initially larger (~60 μm in diameter) than the sessile tactoid domains described previously (Figures 5-1 and 5-3) and contacted the glass substrates on both sides of the 18-μm tall chamber. As these large isotropic domains formed, the inward-directed motion of the N-I interface pushed high densities of cells forward and trapped them within or at the domain interface (Figure 5-5A, also see Movie S4 in the online Supporting Information). For example, we observed that >80 cells were captured within the 60 μm-wide isotropic domain near the plane of focus depicted in Figure 5-5A, representing an enhancement in the local concentration of the bacteria (Figure 5-5D).

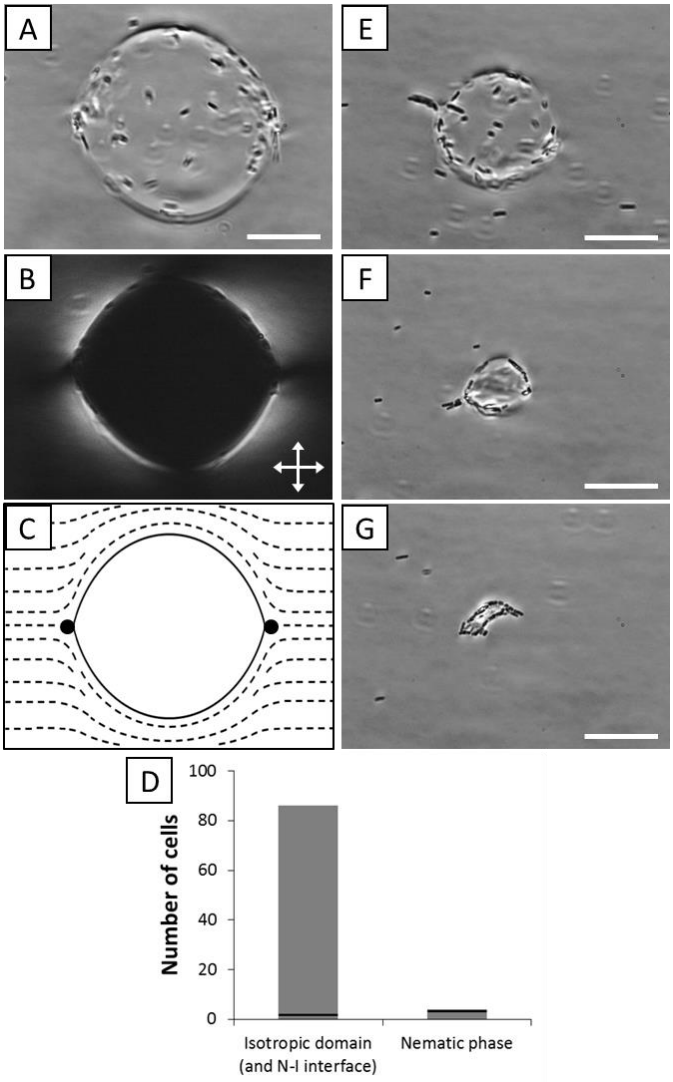

Figure 5-5. Temperature-controlled capture and release of bacteria from an isotropic domain.
(A) Bright field micrograph of an isotropic domain (diameter ~60 μm) that forms upon quenching a 15 wt% DSCG sample from 40°C to 30°C and spans the 18 μm-thick imaging chamber. (B) Corresponding crossed polars optical micrograph. (C) Schematic representation of the director profile corresponding to a cross section of the isotropic domain imaged in (A) and (B). (D) Number of cells trapped by the isotropic domain depicted in A and in the nematic phase encompassing it. Cells both in and out of the focal plane are counted. The black, horizontal lines indicate the number of cells expected to be in the isotropic and nematic domains within the field of view as calculated based on the total concentration of cells (~10^5 cells/mL) in the suspension. (E–G) Bright field micrographs of the isotropic sample after cooling to 29.5°C, 29.2°C, and 29°C, respectively. Rafts of cells collectively escape into the nematic phase in (E) and (F), whereas an aggregate of cells forms as the isotropic domain in (G) nearly disappears. Scale bars are 20 μm.

Due to the orientation of the director profile in the adjacent nematic phase (see Figure 5-5C), motile cells were largely constrained to circular trajectories when adsorbed to the interface of the nearly cylindrical isotropic domains with diameters of 35 μm or larger. The large size and nearly circular cross section of these isotropic domains (such as the one depicted in Figure 5-5A) prevented most of the cells from escaping into the nematic phase. The cells were, in effect, corralled by the elasticity of the surrounding nematic phase. The few escape events that did occur took place proximate to one of the two LC surface defects in the nematic phase near the poles of the spanning isotropic domains (Figure 5-5C), which are either boojums or cross sections of disclination lines.

By adjusting the temperature of the sample, we were able to tune the size of the isotropic corrals in which cells were confined. Specifically, over the course of 20 min, we slowly lowered the temperature of the sample from 30°C to 29°C and observed the isotropic domain to reduce in size and transform into a sessile droplet (Figures 5-5E and 5-5F). We found that by decreasing the area of the interface between the nematic and isotropic phases, *P. mirabilis* cells more frequently encountered the topological defects at the cusped regions at the N-I interface and escaped in greater numbers. For example, in the specific experiment highlighted in Figure 5-5, when the isotropic domain was ~30 μm in diameter (Figure 5-5E), we observed that 20 cells escaped into the nematic phase over the course of 1 min, representing an increase in escape frequency of nearly 4 times over when the domain was between 35 and 60 μm in diameter. This increase in escape frequency may also reflect changes in the morphology of the N-I interface near the LC surface defects that occur as the isotropic domain becomes smaller and transforms into a sessile state (with two boojums, similar to Figure 5-3).

Over the course of the experiment, not all of the cells escaped from the isotropic domain. We hypothesize that this is the result of the rate of shrinkage of the isotropic domain exceeding the rate at which bacteria escape via the cusps at the chosen experimental conditions. When the temperature of our sample reached 29°C, we observed the cells that remained adsorbed to the interface of the shrinking isotropic domain to ultimately form a small multicellular aggregate (Figure 5-5G). Individual cells seldom escaped from aggregates formed in this manner, as the close packing of cells may reduce their ability to generate flagella-derived propulsive forces. Past studies have reported that cooling DSCG samples from the biphasic region into the homogeneous nematic phase can shrink isotropic domains to disclination cores that remain stable even when positioned deep within the nematic phase.[50] The disclination cores serve as the sites of nucleation of isotropic tactoids upon reheating. We also observed an isotropic tactoid to reform at the site of the bacterial aggregate in Figure 5-5G upon reheating.

5.4 Discussion

The results presented in this work reveal that interfacial environments defined by anisotropic phases have a profound impact on fundamental behaviors of motile bacteria. Our observations have broad implications for studies aimed at understanding microbes in a range of ecologically and pathogenically relevant microenvironments that are known or suspected to be anisotropic. Specifically, we have found that motile *P. mirabilis* cells adsorbed at interfaces between coexisting nematic and isotropic phases of a biocompatible lyotropic LC are oriented by the elasticity of the LC, resulting in strongly biased motion of motile bacteria along the interfacial director profile of tactoids. Additional evidence of the influence of the nematic elasticity of the N-I interface can be found in our observations of multicellular behaviors (Figure 5-6). In

particular, we observed *P. mirabilis* cells to assemble into linear chains induced by LC elasticity at the N-I interface (Figures 5-6B and 5-6C). These chains were observed to be dynamic and reversible consistent with the interplay between LC elasticity-mediated forces and flagella-derived propulsive forces[48] (Figures 5-6D and 5-6E). These observations suggest that elastic strain associated with anisotropic interfacial environments can orient rod-shaped bacteria and lead to new, to our knowledge, classes of interbacterial interactions that are absent in isotropic interfacial environments.

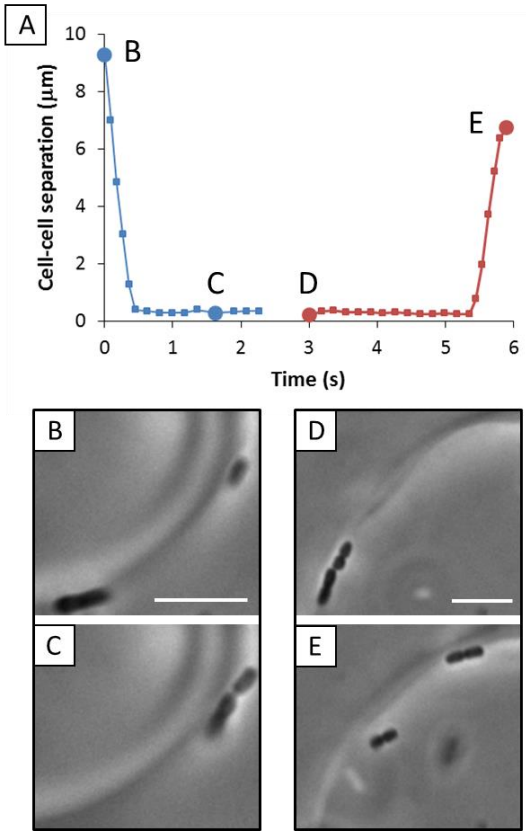

Figure 5-6. Reversible formation of multicellular assemblies at the N-I interface.
(A) Estimated minimum separation distance as a function of time between (B and C) two motile *P. mirabilis* cells that undergo LC elasticity-mediated end-on-end association and between (D and E) two motile *P. mirabilis* cells that dissociate from a chain-like assembly. Scale bars are 5 µm.

Another key influence of the elasticity of the nematic phase on the behavior of the bacteria at the N-I interface was evident in the statistics of bacterial populations found at the interfaces of isotropic versus nematic tactoids. Specifically, we observed the elastic energy penalty associated with strain of the LC about the cells in the nematic phase to substantially influence the probability of escape from nematic and isotropic domains. Moreover, the barrier created by the elastic energy penalty resulted in the cells adopting a cooperative mechanism of escape that involved formation of transient colonies at the poles of isotropic do- mains. This set of observations suggests that individual bacteria present at an interface between an isotropic and anisotropic microenvironment in a biofilm, for example, will tend to preferentially exit the interface into the isotropic domain. However, formation of multicellular assemblies may enable the bacteria to inhabit the anisotropic domain.

One of the most interesting findings of our study relates to the role that topological defects play in mediating the escape of bacteria from the N-I interface, particularly escape into bulk nematic phases. We observed escape from isotropic tactoids to occur most commonly through a collective mechanism that involved three distinct steps: i), director-guided motion of motile cells to a boojum; ii), trapping of individual bacteria at the boojum; iii), cooperative escape of an assembly of bacteria from the boojum once a critical colony size was formed. This collective phenomenon is in contrast to that observed for escape from the N-I interface into the isotropic phase of DSCG. Although the predominant mechanism of escape was still via a boojum, individual bacteria were able to dissociate from the potential well caused by the defect. In addition, non-motile bacteria were observed to associate irreversibly at the boojums of tactoids (Figure S4-4), similar to passive synthetic particles. More broadly, these results suggest that defects present in anisotropic native environments in which bacteria live, whether transient

or equilibrium in nature, likely play a central role in dictating fundamental behaviors, including collective dynamic behaviors, of the cells.

In a recent publication, Zhou *et al.* describe an observation of a single *B. subtilis* cell moving along the interface of an isotropic tactoid in a nematic LC before escaping attachment to the interface into the LC at the cusp of the tactoid.[49] We note that this observation contrasts with our own conclusions obtained with *P. mirabilis* cells in which we quantified the statistics of escape and found escape from isotropic tactoids to be most commonly mediated by the cooperative multicellular mechanism described previously (Figure 5-3E). We also note that Zhou *et al.* do not report evidence of elasticity-mediated interactions between *B. subtilis* cells as we reported previously in bulk LCs,[48] suggesting that *P. mirabilis* and *B. subtilis* cells differ in fundamental ways in terms of their behavior in LCs and at LC interfaces. Additionally, although both *P. mirabilis* and *B. subtilis* move at similar velocities through nematic DSCG (8.8 ± 0.2 μm/s and 8 ± 3 μm/s, respectively[48,49]), *B. subtilis* cells likely generate greater propulsive forces because they are approximately twice as long as *P. mirabilis*. Thus, although we have found that flagella-derived propulsive forces and elasticity-mediated forces are comparable in magnitude for *P. mirabilis* cells in DSCG,[48] the relative magnitude of these forces appears to be different for *B. subtilis*.

We end this discussion by noting that the influence of nematic elasticity and topological defects on dynamic interfacial behaviors of bacteria, as reported in this work, also suggests the basis of new, to our knowledge, approaches to manipulating bacteria in a technological context. We show, for example, that it is possible to use nematic elasticity of LCs to corral motile cells within isotropic domains in a continuous nematic phase and to alter the frequency with which cells escape through the topological defects of the domains via tuning of the sizes of the domain.

In future studies, we envision spatially targeted heating of a suspension of cells in DSCG (e.g., using Joule heating from an embedded wire or by dispersing dye molecules in the sample and employing a focused beam of light) to dynamically control the localization and release of bacteria.

5.5 Conclusion

Overall, our observations provide fundamental insight into how anisotropy, nematic elastic forces, and topological defects can substantially change the behaviors of motile bacteria at interfaces between isotropic and anisotropic microenvironments in ways that are not observed at interfaces between isotropic phases. Not only do we find that the dynamics of individual cells are altered at anisotropic LC interfaces, as demonstrated by the guided motion of cells along the nematic director and interactions of cells with boojums, but we also uncover multicellular phenomena that emerge, including the organization of cells into chains and the formation and cooperative escape of large assemblies of cells from interfaces of isotropic domains. These studies open a new window through which to view the behavior of bacteria in conditions that recapitulate key physical properties of native bacterial environments and also suggest new opportunities to achieve temporal and spatial control over bacteria.

Acknowledgements

This work was supported by the National Science Foundation (under awards DMR-1121288 (MRSEC), CBET-0754921, and MCB-1120832), the National Institutes of Health (CA108467, AI092004, and 5T32GM08349), the Army Research Office (W911-NF-11-1-0251 and W911-NF-14-1-0140), and the United States Department of Agriculture (WIS01594).

5.6 Supporting Information

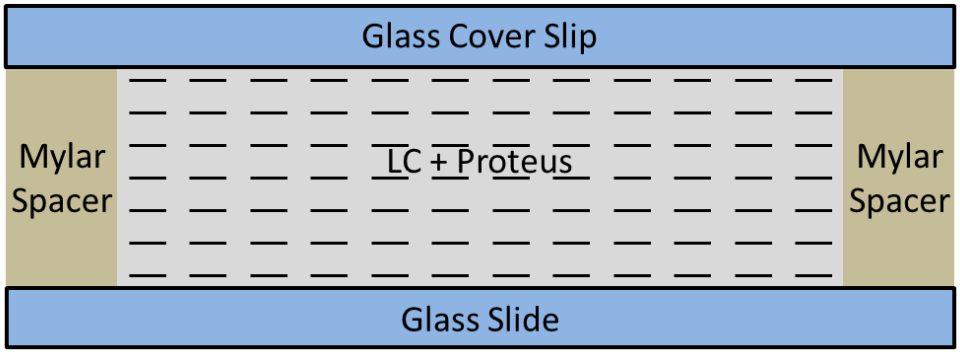

Figure 5-S1. Experimental setup.

A schematic illustration depicting imaging chambers used to analyze bacterial cells in LC solutions. The LC director profile of nematic DSCG at 25°C (in a region of the sample exhibiting uniform polar and azimuthal alignment) is indicated by the dotted lines.

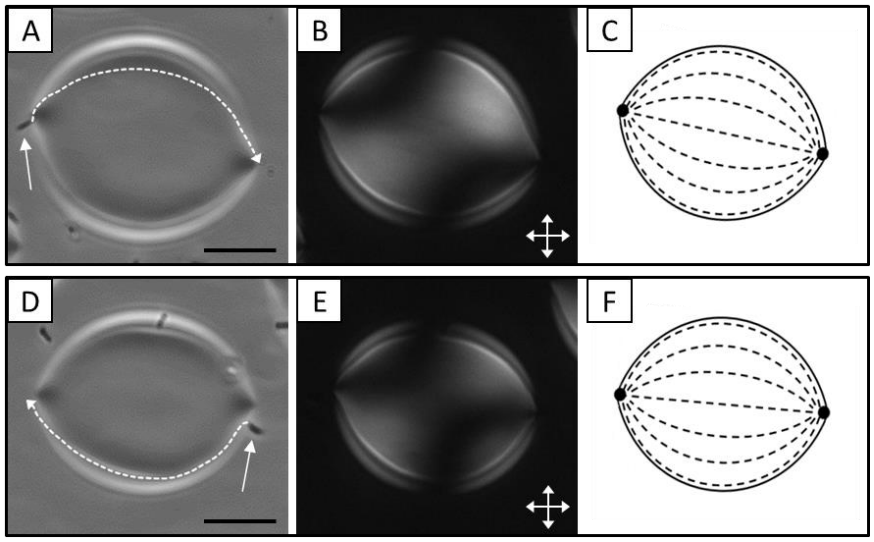

Figure 5-S2. Additional examples of LC elasticity-induced guided motility of cells adsorbed to nematic tactoids.

Two examples (A–C and D–F) of the motility of *P. mirabilis* cells adsorbed to the interface of nematic tactoids. (A and D) Bright field micrographs of nematic tactoids on which the trajectories of motile *P. mirabilis* cells (indicated by arrows) adsorbed to the N-I interface are indicated. (B and E) Corresponding crossed polars images. (C and F) Schematic representations of the LC director profiles of the tactoids in (B) and (E), respectively. Scale bars are 10 µm.

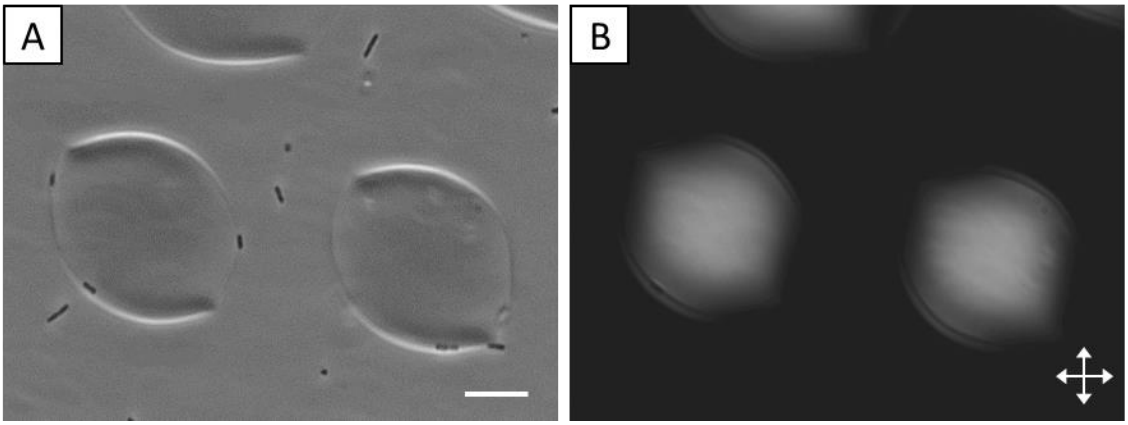

Figure 5-S3. Orientations of non-motile bacteria adsorbed to nematic tactoids.

(A) Bright field and (B) crossed polars images, respectively, of non-motile *P. mirabilis* cells adsorbed at the interface of nematic tactoids that formed on a glass substrate following cooling of an isotropic phase of DSCG (15 wt%) from 40°C to 33°C. The scale bar is 10 μm.

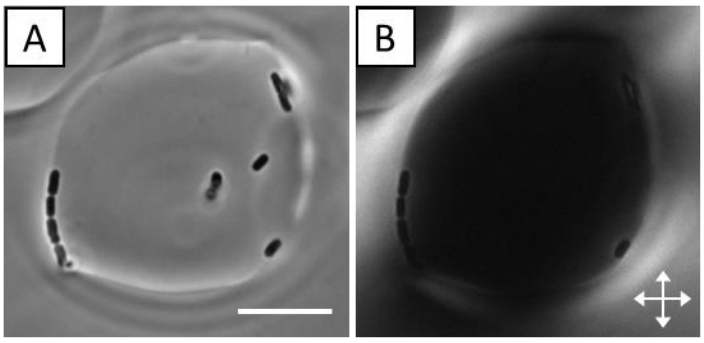

Figure 5-S4. Trapping of non-motile cells at the boojum associated with an isotropic tactoid.

(A) Bright field and (B) crossed polars micrographs of non-motile *P. mirabilis* cells adsorbed at the N-I interface of an isotropic tactoid. Scale bars are 10 μm.

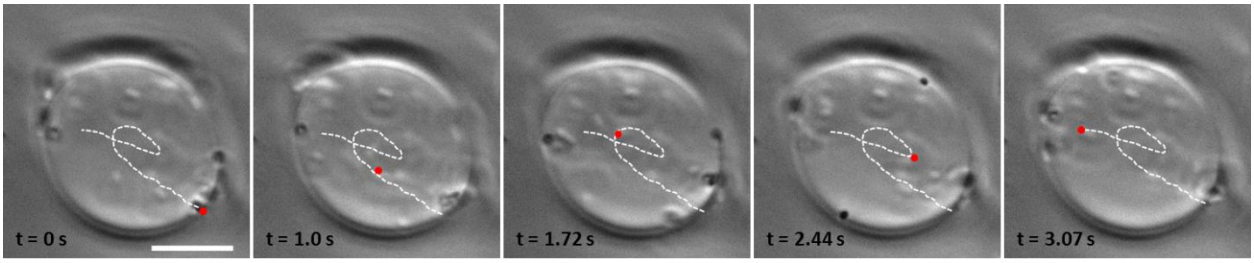

Figure 5-S5. Escape of an adsorbed motile cell into the interior of an isotropic tactoid.
Sequence of bright field micrographs that depicts the trajectory of a motile *P. mirabilis* cell, initially adsorbed to the interface of an isotropic tactoid, which escapes into the interior of the tactoid. The trajectory of the cell (indicated by a red dot) is depicted in the images. The random motion of the cell suggests that it is not adsorbed to the N-I interface. The scale bar is 10 µm.

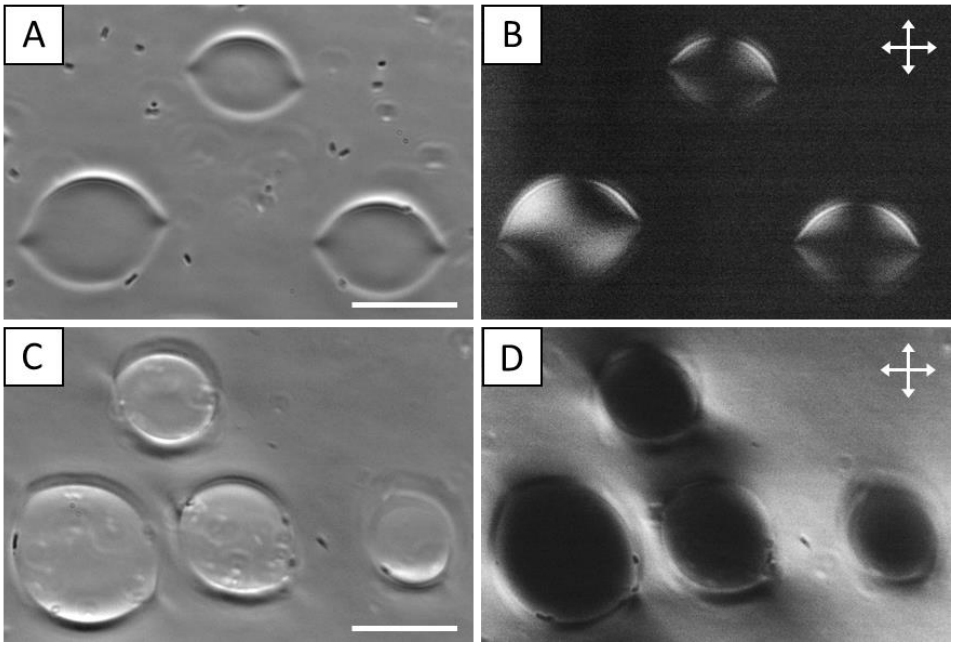

Figure 5-S6. Temporal accumulation of motile bacteria at the interface of isotropic tactoids.
(A and B) Bright field and crossed polars images, respectively of motile *P. mirabilis* cells dispersed in DSCG solution quenched to 33°C that contains nematic tactoids encompassed by isotropic phase solution. (C and D) Bright field and crossed polars images, respectively of motile *P. mirabilis* cells dispersed in DSCG solution heated to 30°C that contains isotropic tactoids surrounded by a continuous nematic phase. All images were obtained following 15 min of equilibration at the specified temperatures. Scale bars are 20 µm.

Supplementary Movie Captions

Supporting movies are available in the online SI (found at http://www.cell.com/biophysj/biophysj/supplemental/S0006-3495%2814%2900466-4).

Movie S1. Bright field optical microscopy movie in which the trajectories of motile *P. mirabilis* cells adsorbed to the N-I interface of a nematic tactoid largely map out the interfacial director profile of the tactoid. Additionally, bacteria can be observed escaping the interface at the cusped poles of the tactoids where a boojum is present. Scale bar = 10 μm.

Movie S2. Bright field optical microscopy movie in which a single motile *P. mirabilis* cell adsorbed to the N-I interface of an isotropic tactoid escapes into the continuous nematic phase at the cusped pole of the tactoid, which is adjacent to a boojum defect in the nematic phase. Scale bar = 10 μm.

Movie S3. Bright field optical microscopy movie that shows accumulation of motile *P. mirabilis* adsorbed to the N-I interface of an isotropic tactoid at the cusp-shaped pole. The large aggregate of cells collectively escape into the continuous nematic phase. Scale bar = 10 μm.

Movie S4. Bright field optical microscopy movie that shows the accumulation of motile *P. mirabilis* within and at the N-I interface of a large isotropic domain that spans the entire thickness of the experimental cell. This isotropic domain formed by quenching the 15 wt% DSCG solution from 40°C to 30°C. Scale bar = 20 μm.

5.7 References

*This chapter was prepared as a Full Paper reporting original research in the journal *Biophysical Journal*. Rishi Trivedi assisted me in performing and analyzing the experiments and preparing the manuscript.

1. Lens, P.; Moran, A. P.; Mahony, T.; Stoodley, P.; O'Flaherty, V. *Biofilms in Medicine, Industry and Environmental Biotechnology: Characteristics, Analysis and Control*; Lens, P., Moran, A. P., Mahony, T., Stoodley, P., O'Flaherty, V., Eds.; IWA Publishing: London, 2003.
2. Parsek, M. R.; Singh, P. K. Bacterial Biofilms: An Emerging Link to Disease Pathogenesis. *Annu. Rev. Microbiol.* **2003**, 57, 677–701.
3. Hall-Stoodley, L.; Costerton, J. W.; Stoodley, P. Bacterial Biofilms: From the Natural Environment to Infectious Diseases. *Nat. Rev. Microbiol.* **2004**, 2, 95–108.
4. Hallam, N. B.; West, J. R.; Forster, C. F.; Simms, J. The Potential for Biofilm Growth in Water Distribution Systems. *Water Res.* **2001**, 35, 4063–4071.
5. Oostdijk, E. A. N.; de Smet, A. M. G. A.; Blok, H. E. M.; Thieme Groen, E. S.; van Asselt, G. J.; Benus, R. F. J.; Bernards, S. A. T.; Frénay, I. H. M. E.; Jansz, A. R.; de Jongh, B. M.; Kaan, J. A.; Leverstein-van Hall, M. A.; Mascini, E. M.; Pauw, W.; Sturm, P. D. J.; Thijsen, S. F. T.; Kluytmans, J. A. J. W; Bonten, M. J. M. Ecological Effects of Selective Decontamination on Resistant Gram-Negative Bacterial Colonization. *Am. J. Respir. Crit. Care Med.* **2010**, 181, 452–457.
6. Chmielewski, R. A. N.; Frank, J. F. Biofilm Formation and Control in Food Processing Facilities. *Compr. Rev. Food Sci. Food Saf.* **2003**, 2, 22–32.
7. Shi, X.; Zhu, X. Biofilm Formation and Food Safety in Food Industries. *Trends Food Sci. Technol.* **2009**, 20, 407–413.
8. Johansson, J. F.; Paul, L. R.; Finlay, R. D. Microbial Interactions in the Mycorrhizosphere and Their Significance for Sustainable Agriculture. *FEMS Microbiol. Ecol.* **2004**, 48, 1–13.
9. Evans, F. F.; Rosado, A. S.; Sebastián, G. V; Casella, R.; Machado, P. L. O. A.; Holmström, C.; Kjelleberg, S.; van Elsas, J. D.; Seldin, L. Impact of Oil Contamination and Biostimulation on the Diversity of Indigenous Bacterial Communities in Soil Microcosms. *FEMS Microbiol. Ecol.* **2004**, 49, 295–305.
10. Guarner, F.; Malagelada, J.-R. Gut Flora in Health and Disease. *Lancet* **2003**, 361, 512–519.
11. Flint, H. J.; Duncan, S. H.; Scott, K. P.; Louis, P. Interactions and Competition within the Microbial Community of the Human Colon: Links between Diet and Health. *Environ. Microbiol.* **2007**, 9, 1101–1111.
12. DiLuzio, W. R.; Turner, L.; Mayer, M.; Garstecki, P.; Weibel, D. B.; Berg, H. C.; Whitesides, G. M. *Escherichia coli* Swim on the Right-Hand Side. *Nature* **2005**, 435, 1271–1274.

13. Lauga, E.; DiLuzio, W. R.; Whitesides, G. M.; Stone, H. A. Swimming in Circles: Motion of Bacteria near Solid Boundaries. *Biophys. J.* **2006**, 90, 400–412.
14. Berke, A.; Turner, L.; Berg, H.; Lauga, E. Hydrodynamic Attraction of Swimming Microorganisms by Surfaces. *Phys. Rev. Lett.* **2008**, 101, 038102.
15. Lauga, E.; Powers, T. R. The Hydrodynamics of Swimming Microorganisms. *Reports Prog. Phys.* **2009**, 72, 096601.
16. Lemelle, L.; Palierne, J.-F.; Chatre, E.; Place, C. Counterclockwise Circular Motion of Bacteria Swimming at the Air-Liquid Interface. *J. Bacteriol.* **2010**, 192, 6307–6308.
17. Morse, M.; Huang, A.; Li, G.; Maxey, M. R.; Tang, J. X. Molecular Adsorption Steers Bacterial Swimming at the Air/water Interface. *Biophys. J.* **2013**, 105, 21–28.
18. Flemming, H.-C. Biofouling in Water Systems--Cases, Causes and Countermeasures. *Appl. Microbiol. Biotechnol.* **2002**, 59, 629–640.
19. Del Pozo, J. L.; Patel, R. The Challenge of Treating Biofilm-Associated Bacterial Infections. *Clin. Pharmacol. Ther.* **2007**, 82, 204–209.
20. Høiby, N.; Bjarnsholt, T.; Givskov, M.; Molin, S.; Ciofu, O. Antibiotic Resistance of Bacterial Biofilms. *Int. J. Antimicrob. Agents* **2010**, 35, 322–332.
21. Klapper, I.; Rupp, C. J.; Cargo, R.; Purvedorj, B.; Stoodley, P. Viscoelastic Fluid Description of Bacterial Biofilm Material Properties. *Biotechnol. Bioeng.* **2002**, 80, 289–296.
22. Shaw, T.; Winston, M.; Rupp, C. J.; Klapper, I.; Stoodley, P. Commonality of Elastic Relaxation Times in Biofilms. *Phys. Rev. Lett.* **2004**, 93, 098102.
23. Hohne, D. N.; Younger, J. G.; Solomon, M. J. Flexible Microfluidic Device for Mechanical Property Characterization of Soft Viscoelastic Solids such as Bacterial Biofilms. *Langmuir* **2009**, 25, 7743–7751.
24. Flemming, H.-C.; Wingender, J. The Biofilm Matrix. *Nat. Rev. Microbiol.* **2010**, 8, 623–633.
25. Pavlovsky, L.; Younger, J. G.; Solomon, M. J. In Situ Rheology of *Staphylococcus* epidermidis Bacterial Biofilms. *Soft Matter* **2013**, 9, 122–131.
26. Hwang, S.; Litt, M.; Forsman, W. Rheological Properties of Mucus. *Rheol. Acta* **1969**, 8, 438–448.
27. Tam, P. Y.; Katz, D. F.; Berger, S. A. Non-Linear Viscoelastic Properties of Cervical Mucus. *Biorheology* **1980**, 17, 465–478.
28. Madoff, L. C.; Thaler, S. J.; Maguire, J. H. Infectious Arthritis. In *Harrison's Principles of Internal Medicine*; McGraw-Hill: New York, 2005; pp 2050–2055.
29. Stokes, J. R.; Davies, G. A. Viscoelasticity of Human Whole Saliva Collected after Acid and Mechanical Stimulation. *Biorheology* **2007**, 44, 141–160.
30. Haward, S. J.; Odell, J. A.; Berry, M.; Hall, T. Extensional Rheology of Human Saliva. *Rheol. Acta* **2011**, 50, 869–879.
31. Rey, A. D. Liquid Crystal Models of Biological Materials and Processes. *Soft Matter* **2010**, 6, 3402–3429.
32. Houry, A.; Gohar, M.; Deschamps, J.; Tischenko, E.; Aymerich, S.; Gruss, A. Bacterial Swimmers That Infiltrate and Take over the Biofilm Matrix. *Proc. Natl. Acad. Sci. U. S. A.* **2012**, 109, 13088–13093.
33. Mudd, S.; Mudd, E. B. H. The Penetration of Bacteria through Capillary Spaces. IV. A Kinetic Mechanism in Interfaces. *J. Exp. Med.* **1924**, 40, 633–645.
34. Mudd, S.; Mudd, E. B. H. Certain Interfacial Tension Relations and the Behavior of Bacteria in Films. *J. Exp. Med.* **1924**, 40, 647–660.

35. Rosenberg, M.; Gutnick, D.; Rosenberg, E. Adherence of Bacteria to Hydrocarbons: A Simple Method for Measuring Cell-Surface Hydrophobicity. *FEMS Microbiol. Lett.* **1980**, 9, 29–33.
36. Rosenberg, M. Bacterial Adherence to Hydrocarbons: A Useful Technique for Studying Cell Surface Hydrophobicity. *FEMS Microbiol. Lett.* **1984**, 22, 289–295.
37. Kang, Z.; Yeung, A.; Foght, J. M.; Gray, M. R. Hydrophobic Bacteria at the Hexadecane-Water Interface: Examination of Micrometre-Scale Interfacial Properties. *Colloids Surf. B. Biointerfaces* **2008**, 67, 59–66.
38. Lin, I.-H.; Koenig, G. M.; de Pablo, J. J.; Abbott, N. L. Ordering of Solid Microparticles at Liquid Crystal-Water Interfaces. *J. Phys. Chem. B* **2008**, 112, 16552–16558.
39. Koenig, G. M.; Lin, I.-H.; Abbott, N. L. Chemoresponsive Assemblies of Microparticles at Liquid Crystalline Interfaces. *Proc. Natl. Acad. Sci. U. S. A.* **2010**, 107, 3998–4003.
40. Smalyukh, I.; Chernyshuk, S.; Lev, B. I.; Nych, A. B.; Ognysta, U.; Nazarenko, V. G.; Lavrentovich, O. D. Ordered Droplet Structures at the Liquid Crystal Surface and Elastic-Capillary Colloidal Interactions. *Phys. Rev. Lett.* **2004**, 93, 117801.
41. Nazarenko, V. G.; Nych, A. B.; Lev, B. I. Crystal Structure in Nematic Emulsion. *Phys. Rev. Lett.* **2001**, 87, 075504.
42. Gharbi, M. A.; Nobili, M.; In, M.; Prévot, G.; Galatola, P.; Fournier, J.-B.; Blanc, C. Behavior of Colloidal Particles at a Nematic Liquid Crystal Interface. *Soft Matter* **2011**, 7, 1467–1471.
43. Abras, D.; Pranami, G.; Abbott, N. L. The Mobilities of Micro- and Nano-Particles at Interfaces of Nematic Liquid Crystals. *Soft Matter* **2012**, 8, 2026–2035.
44. Mondiot, F.; Wang, X.; de Pablo, J. J.; Abbott, N. L. Liquid Crystal-Based Emulsions for Synthesis of Spherical and Non-Spherical Particles with Chemical Patches. *J. Am. Chem. Soc.* **2013**, 135, 9972–9975.
45. Whitmer, J. K.; Wang, X.; Mondiot, F.; Miller, D. S.; Abbott, N. L.; de Pablo, J. J. Nematic-Field-Driven Positioning of Particles in Liquid Crystal Droplets. *Phys. Rev. Lett.* **2013**, 111, 227801.
46. Tuson, H. H.; Copeland, M. F.; Carey, S.; Sacotte, R.; Weibel, D. B. Flagella Density Regulates *Proteus mirabilis* Swarmer Cell Motility in Viscous Environments. *J. Bacteriol.* **2013**, 195, 368–377.
47. Kumar, A.; Galstian, T.; Pattanayek, S. K.; Rainville, S. The Motility of Bacteria in an Anisotropic Liquid Environment. *Mol. Cryst. Liq. Cryst.* **2013**, 574, 33–39.
48. Mushenheim, P. C.; Trivedi, R. R.; Tuson, H. H.; Weibel, D. B.; Abbott, N. L. Dynamic Self-Assembly of Motile Bacteria in Liquid Crystals. *Soft Matter* **2014**, 10, 88–95.
49. Zhou, S.; Sokolov, A.; Lavrentovich, O. D.; Aranson, I. S. Living Liquid Crystals. *Proc. Natl. Acad. Sci. U. S. A.* **2014**, 111, 1265–1270.
50. Kim, Y.-K.; Shiyanovskii, S. V; Lavrentovich, O. D. Morphogenesis of Defects and Tactoids during Isotropic-Nematic Phase Transition in Self-Assembled Lyotropic Chromonic Liquid Crystals. *J. Phys. Condens. Matter* **2013**, 25, 404202.
51. Prinsen, P.; van der Schoot, P. Shape and Director-Field Transformation of Tactoids. *Phys. Rev. E* **2003**, 68, 021701.
52. Nastishin, Y. A.; Liu, H.; Schneider, T.; Nazarenko, V.; Vasyuta, R.; Shiyanovskii, S. V; Lavrentovich, O. D. Optical Characterization of the Nematic Lyotropic Chromonic Liquid Crystals: Light Absorption, Birefringence, and Scalar Order Parameter. *Phys. Rev. E* **2005**, 72, 041711.

53. Van Bijnen, R. M. W.; Otten, R. H. J.; van der Schoot, P. Texture and Shape of Two-Dimensional Domains of Nematic Liquid Crystals. *Phys. Rev. E* **2012**, 86, 051703.
54. Nastishin, Y. A.; Liu, H.; Shiyanovskii, S. V.; Lavrentovich, O. D.; Kostko, A. F.; Anisimov, M. A. Pretransitional Fluctuations in the Isotropic Phase of a Lyotropic Chromonic Liquid Crystal. *Phys. Rev. E* **2004**, 70, 051706.
55. Champion, J. V; Meeten, G. H. Conformation of Sodium Cromolyn in Aqueous Solution Using Light Scattering and Magnetic Birefringence. *J. Pharm. Sci.* **1973**, 62, 1589–1595.
56. Luk, Y.-Y.; Tingey, M. L.; Hall, D. J.; Israel, B. A.; Murphy, C. J.; Bertics, P. J.; Abbott, N. L. Using Liquid Crystals to Amplify Protein−receptor Interactions: Design of Surfaces with Nanometer-Scale Topography That Present Histidine-Tagged Protein Receptors. *Langmuir* **2003**, 19, 1671–1680.
57. Kaznacheev, A. V; Bogdanov, M. M.; Taraskin, S. A. The Nature of Prolate Shape of Tactoids in Lyotropic Inorganic Liquid Crystals. *J. Exp. Theor. Phys.* **2002**, 95, 57–63.
58. Kaznacheev, A. V; Bogdanov, M. M.; Sonin, A. S. The Influence of Anchoring Energy on the Prolate Shape of Tactoids in Lyotropic Inorganic Liquid Crystals. *J. Exp. Theor. Phys.* **2003**, 97, 1159–1167.
59. Volovik, G. E.; Lavrentovich, O. D. Topological Dynamics of Defects: Boojums in Nematic Drops. *Sov. Phys. JETP* **1983**, 58, 1159–1166.
60. Nastishin, Y. A.; Neupane, K.; Baldwin, A. R.; Lavrentovich, O. D.; Sprunt, S. Elasticity and Viscosity of a Lyotropic Chromonic Nematic Studied with Dynamic Light Scattering. *Electron. Liq. Cryst. Commun.* **2008**, arXiv.org/abs/0807.2669.
61. Prinsen, P.; van der Schoot, P. Parity Breaking in Nematic Tactoids. *J. Phys. Condens. Matter* **2004**, 16, 8835–8850.
62. Tortora, L.; Lavrentovich, O. D. Chiral Symmetry Breaking by Spatial Confinement in Tactoidal Droplets of Lyotropic Chromonic Liquid Crystals. *Proc. Natl. Acad. Sci. U. S. A.* **2011**, 108, 5163–5168.
63. Chen, W.; Gray, D. G. Interfacial Tension between Isotropic and Anisotropic Phases of a Suspension of Rodlike Particles. *Langmuir* **2002**, 18, 633–637.
64. Binks, B. P.; Horozov, T. S. *Colloidal Particles at Liquid Interfaces*; Binks, B. P., Horozov, T. S., Eds.; Cambridge University Press: Cambridge, 2006.
65. Smalyukh, I. I.; Butler, J.; Shrout, J. D.; Parsek, M. R.; Wong, G. C. L. Elasticity-Mediated Nematiclike Bacterial Organization in Model Extracellular DNA Matrix. *Phys. Rev. E* **2008**, 78, 030701.
66. West, J. L.; Glushchenko, A.; Liao, G.; Reznikov, Y.; Andrienko, D.; Allen, M. Drag on Particles in a Nematic Suspension by a Moving Nematic-Isotropic Interface. *Phys. Rev. E* **2002**, 66, 012702.
67. Loudet, J. C.; Pouligny, B. How Do Mosquito Eggs Self-Assemble on the Water Surface? *Eur. Phys. J. E. Soft Matter* **2011**, 34, 76.

Chapter 6: Effects of Confinement, Surface-Induced Orientations and Strain on Dynamical Behaviors of Bacteria in Thin Liquid Crystalline Films*

6.1 Introduction

When dispersed within nematic liquid crystals (LCs), micro- and nanoparticles (e.g., polystyrene or silica) exhibit a range of dynamical and equilibrium behaviors that reflect the long-range orientational order and elasticity of the LC phase. For example, microparticles diffuse anisotropically and anomalously,[1–3] anisometric microparticles orient preferentially with respect to the nematic director,[4–8] and interparticle forces mediated by the elasticity of the LC induce the self-assembly of particles.[6–13] These phenomena, which have been observed for microparticles dispersed in both thermotropic[6,9–11] and lyotropic[7,12,13] LCs, reflect the strain induced in the LC phase by the presence of the particles.[14–20]

Whereas the above-mentioned studies involved synthetic 'passive' colloids dispersed in LCs, a series of recent studies have revealed that LC-mediated torques and stresses also manifest in the fundamental dynamical behaviors of living bacteria dispersed in LCs. Bacteria, which are commensurate in size to synthetic microparticles, can be dispersed in a non-toxic nematic lyotropic chromonic LC phase formed by aqueous solutions of disodium cromogylcate (DSCG) and generate flagella-derived forces that self-propel the bacteria through the LC.[21–25] Specifically, by using LC films with planar anchoring, motile, rod-shaped bacteria were observed to move parallel to the confining surfaces and to follow the nematic director (both in bulk LCs[21–23] and at isotropic-LC interfaces[24]) due to LC elastic forces and anisotropic effective

viscosities in the LC. Non-motile *Proteus mirabilis* cells also were found to orient along the direction of LC alignment as a consequence of tangential LC anchoring at the cell surface.[22] Moreover, an interplay between LC-mediated intercellular forces and flagella-derived forces was shown to give rise to additional dynamic phenomena, including formation of reversible, linear multicellular assemblies[22] and collective phenomena in concentrated dispersions of bacteria[23]. In addition to providing insight into the manner in which bacteria are influenced by anisotropic viscoelastic microenvironments encountered in biological systems (e.g., aligned mucus or biopolymer solutions[26–29]), these past studies demonstrate that motile bacteria can serve as model 'active' particles in fundamental studies of anisotropic soft matter.

The interplay of LC elasticity-mediated forces and flagella-derived forces uncovered in the above-described studies with planar surface anchoring of LCs hinted to us that a potentially much broader range of behaviors of motile bacteria might emerge from changes in the alignment (and non-uniform alignment) of LCs containing bacteria. In this paper, we report an investigation of how the organization and dynamics of bacteria are altered in thin LC films confined by surfaces that cause either uniform homeotropic (perpendicular) or so-called "hybrid" anchoring of the LC (in which there is homeotropic LC anchoring at one substrate and planar anchoring at the other). Specifically, whereas a surface-induced hydrodynamic torque resulting from bacterial flagella-derived forces typically reorients and causes the motion of motile bacteria in a direction parallel to a confining surface of an isotropic solution,[30,31] we sought to determine if elastic torques generated by a homeotropically aligned LC would be sufficiently large to align and direct the motion of bacteria perpendicular to a surface (overcoming hydrodynamic, wall-induced torques). Our results support the hypothesis that elastic torques generated by surface-oriented LCs do dominate the dynamical behaviors of bacteria near LC interfaces. Indeed, based

on this conclusion, we demonstrate that spatially varying profiles of the LC director, induced by confining LC films between two surfaces that anchor the LC in distinct orientations (hybrid LC films), can rectify the motion of bacteria.

In the second part of this paper, we confine bacteria in LC systems such that the small size of the LC domain does not permit the bacteria to assume an orientation that is parallel to the director. Specifically, we explore the limit where bacteria are long compared to the thickness of a homeotropic LC film. We show that, in this limit, the cells orient and move in directions orthogonal to the far-field director. Interestingly, self-propulsion of bacteria in this case creates transient distortions in the LC in the wake of each cell that have striking "comet-like" optical appearances. In addition, in this limit, we show that elastic stresses in the strained LC are sufficiently large to bend the bacteria. Interestingly, these results and others presented in this paper suggest that lyotropic LCs and bacterial systems can be mechanically matched, thus revealing a complexity in dynamical coupling (based on changes in shape of the bacteria) that has not previously been reported.

The studies reported here used motile *Proteus mirabilis* cells. *P. mirabilis* is a rod-shaped, motile, Gram-negative bacterium that can move through viscous fluids (via a "pushing" mechanism); genetic engineering of the cells has been performed to overexpress flagella and thus enable *P. mirabilis* to move rapidly through viscous environments.[32] Previously, we demonstrated that engineered vegetative *P. mirabilis* cells (~ 3 μm in length) are motile within nematic DSCG phases.[22,24] In addition, however, *P. mirabilis* is a particularly intriguing bacterium, because in response to certain environmental cues, vegetative *P. mirabilis* cells differentiate into long (10 μm – 60 μm), multinucleate "swarm cells".[32] The density of flagella

on these swarm cells is comparable to that on engineered vegetative cells overexpressing flagella, enabling the swarm cells to also move within highly viscous fluids, as well.[32]

6.2 Experimental Section

Bacterial strains and cell culture. *P. mirabilis* strain HI4320 was transformed with plasmid pflhDC to create vegetative *P. mirabilis* cells overexpressing flagella. The plasmid pflhDC contained the *flhDC* genes from *P. mirabilis* inserted into pACYC184 (which contains a gene for chloramphenicol resistance). *P. mirabilis* cells were grown in chloramphenicol-resistance nutrient medium consisting of 1% (wt/vol) peptone (Becton, Dickinson, Sparks, MD), 0.5% (wt/vol) yeast extract (Becton, Dickinson), and 1% (wt/vol) NaCl (Fisher Scientific, Fairlawn, NJ) at 30°C in a shaking incubator.[32] Saturated overnight cultures were diluted 100-fold in 10 mL of fresh nutrient medium and grown in 150 mL Erlenmeyer flasks at 30°C in a shaking incubator at 200 rpm. We observed that the highest swimming velocity of *P. mirabilis* cells occurred during stationary phase, hence we harvested cells at an absorbance (λ=600 nm) of ~3.2 and concentrated them by centrifugation. The cells were washed three times with an aqueous buffer for bacterial motility (0.01 M KPO_4, 0.067 M NaCl, 10^{-4} M EDTA, 0.1 M glucose, and 0.001% Brig-35, pH 7.0).

Harvesting *P. mirabilis* swarm cells. *P. mirabilis* swarm cells were obtained according to previously published methods.[32] Briefly, we prepared swarm agar plates by pipetting 50 ml of 1.5% (wt/vol) hot swarm agar into 150- by 15-mm petri dishes. After the agar plates solidified, excess liquid was removed from the surface by storing the plates in the laminar flow hood for 20 min with the covers of the dishes ajar. To differentiate *P. mirabilis* vegetative cells into swarm

cells, a swarm agar plate was inoculated with 4 μL of a suspension of 4×10^5 vegetative *P. mirabilis* cells/mL. The plate was then incubated at 30°C at 90% relative humidity in a static incubator for 15 h. Following this incubation period, swarm cells were harvested from the smooth leading edge of a migrating colony of *P. mirabilis* cells using a 1 μL-calibrated inoculation loop.

Lyotropic LC preparation. Disodium cromoglycate (DSCG) was purchased from Sigma-Aldrich (Milwaukee, WI) and used as received. Lyotropic LCs containing DSCG were prepared by mixing 15.3 wt% of DSCG with 84.7 wt% of aqueous motility buffer. The mixture was shaken for at least 12 h to ensure complete solubility and homogeneity. Prior to experimentation, the DSCG solution was heated at 65°C for 10 min to avoid possible time dependence of the properties of the mixture.[33,34] After cooling the solution to 25°C, a small volume of motility buffer containing bacteria (either vegetative or swarm cells) was added to the DSCG mixture producing a final concentration of ~10^5 cells/μL. The final concentration of DSCG was 15.0 wt% in all experiments.

Growth of graphene monolayers via chemical vapor deposition (CVD). Monolayers of graphene were grown on Cu foils (Alfa Aesar, Ward Hill, MA) as the growth catalyst. The foils were pre- cleaned with acetic acid (Fisher) for 15 min to remove contaminants and native oxides then rinsed in DI water (×3) before being dried with an air-gun. The cleaned Cu foils were then annealed for 30 min at 1030°C in 95% argon + 5% hydrogen (340 sccm flowrate) to remove trace surface contaminants and also to reduce the surface roughness of the foil before initiating the growth process. The growth was conducted at 1030°C with 95% argon + 5% methane (0.300

sccm) and 95% argon + 5% hydrogen (340 sccm) for 3 h in a 28 mm diameter quartz tube. The manufactured graphene on Cu foils were stored in a N_2 glovebox to prevent the oxidation of the graphene and the copper surfaces. All the graphene monolayers used for the experiments were manufactured from the same batch for consistency and the initial Raman scattering D-band (1347 cm^{-1}) to G-band (1585 cm^{-1}) intensity ratio (Figure 6-S1), quantifying the defect density in the atomic membrane, varied as 0.04 ± 0.025 for the entire batch used for this study indicating a low density of defects.

Transfer of graphene onto HMDS-coated glass substrates. Graphene monolayers grown via CVD were transferred onto glass substrates coated with hexamethyldisilazane (HMDS) (Alfa Aesar). The transfer was completed using a commonly employed sacrificial polymer (PMMA – poly(methyl methacrylate)) method, similar to as previously reported.[35,36] CVD-graphene on copper was over-coated with PMMA (M.W. = 950k, 2% in chlorobenzene) by spin-coating at 2,000 rpm. The samples were placed in copper etchant ammonium persulfate (25% Transene Company, Inc. APS-100 + 75% DI water) and then bath-ultrasonicated for 15 min to remove the bottom-facing graphene layer. The samples were left overnight (~10 h) in the etchant for the copper to completely etch. Post-etch, the floating PMMA on graphene was scooped out from the APS solution and re-floated in DI water (×3) to rinse any residual copper etchant. The samples were then dispersed in 5% HF in DI water for 60 min to remove trace silica particles that might have deposited from the CVD system during the growth, following which they were rinsed in DI water (×3). From the final DI water bath, the samples were scooped onto HMDS-coated glass substrates and spin-dried at 8,000 rpm for 2 min to remove water trapped between the graphene sheet and the substrate. To remove the PMMA layer, the samples were placed in room-

temperature acetone baths (×2) for 20 min after which they were rinsed in isopropanol for 2 min to wash away any residual acetone. Finally, they were dried using an air-gun.

Characterization and analysis of graphene. Raman spectroscopy was performed with a MicroRaman DXRxi (Thermo Scientific) to characterize graphene monolayers grown on HMDS-coated glass substrates. A 532 nm laser with power = 3 mW, raster-scan frequency = 0.025 Hz and scan area = 50 μm x 50 μm was used to generate spatially-resolved maps for all samples. The maps were spatially-averaged and normalized to the G-band intensity to obtain the final Raman spectra. The laser spot size was focused to ~500 nm, and a mapping pixel size of 1 μm x 1 μm was used. Raman spectroscopy confirmed the presence of monolayers of graphene both before and after contact with a 15 wt% DSCG solution (Figure 6-S1).

Preparation of imaging chambers. We created imaging chambers by adding a small volume (~1 μL) of 15 wt% DSCG solution on top of a glass slide between two sheets of Mylar film (10 – 18 μm-thick). A glass cover slip was placed on top of the Mylar and the chamber was sealed with epoxy to prevent water evaporation. To create uniform homeotropic LC films, two graphene-coated substrates were used to confine the DSCG solution.[37] In contrast, for hybrid LC films, only one of the two bounding glass substrates was coated with graphene.

Optical characterization of nematic DSCG phases. The orientation of the nematic phase of the 15 wt% DSCG solution in experimental imaging chambers was determined using plane-polarized light in transmission mode on an Olympus BX60 microscope equipped with crossed

polarizers. All images were captured using a digital camera (Olympus C-2040 Zoom) mounted on the microscope and set to an f-stop of 2.8 and a shutter speed of 1/125 sec.

Microscopy. We imaged cells using a Nikon Eclipse Ti inverted optical microscope equipped with crossed polarizers and a Photometics CoolSNAP HQ2 CCD camera (Tucson, AZ) using a Nikon Plan Apo λ, 100X/1.45 oil objective lens and a Nikon S Plan Fluor ELWD 40X/0.6 objective. Videos were collected with the EM gain off and with a 90 ms exposure time (11 frames/sec). Images of cells were collected using Nikon NIS Elements software.

6.3 Results and Discussion

LC film orientation \ Bacteria cell type	L ~ 3 µm	L ~ 10 µm – 60 µm
d ~ 10 µm (Graphene / Graphene)	6.3.1	6.3.2
d ~ 18 µm (Bare Glass / Graphene)	6.3.3	6.3.4

Table 6-1. Experimental conditions investigated in this study.
Small vegetative *P. mirabilis* cells dispersed in uniform homeotropic films are investigated in Section 6.3.1; long *P. mirabilis* swarm cells dispersed in homeotropic films in Section 6.3.2; vegetative cells in LC films with hybrid anchoring conditions in Section 6.3.3; and swarm cells dispersed in hybrid LC films in Section 6.3.4.

6.3.1 Homeotropic LC film; $L_{bacteria} < d_{film}$

We first characterized the manner in which vegetative *P. mirabilis* cells ($L_{bacteria} \sim 3$ μm) orient and move when dispersed in nematic LC films ($d_{film} \sim 10$ μm) confined between two graphene-coated substrates that give rise to a uniform homeotropic alignment of the LC (Table 6-1). While we have previously demonstrated that these motile cells orient and move parallel to the LC director in planar LC films as a result of elastic stresses that orient the cells[22], it is well-established that hydrodynamic stresses significantly influence the behavior of motile bacteria proximate to a solid substrate. Specifically, in isotropic solutions, bacteria that swim via a "pushing" mechanism and establish a dipolar flow field (such as *P. mirabilis*) are attracted to surfaces by hydrodynamic interactions.[30,31] The bacteria are induced to assume an orientation in which the swimming cells align parallel to the surface due to velocity gradients in the flow field that arise in the near-surface region.[30,31] This reorientation of the cell typically occurs over a time scale of seconds when cells approach within a few micrometers of a solid substrate.[30] Inspired by these past studies, we hypothesized that vegetative cells in a homeotropic LC film and proximate to one of the confining substrates might, in contrast, adopt an orientation perpendicular to the substrate if the torque due to the elasticity of the LC ($\Gamma_{elastic}$) is sufficient in magnitude to suppress the surface-induced hydrodynamic torque ($\Gamma_{hydrodynamic}$) (Figure 6-1A).

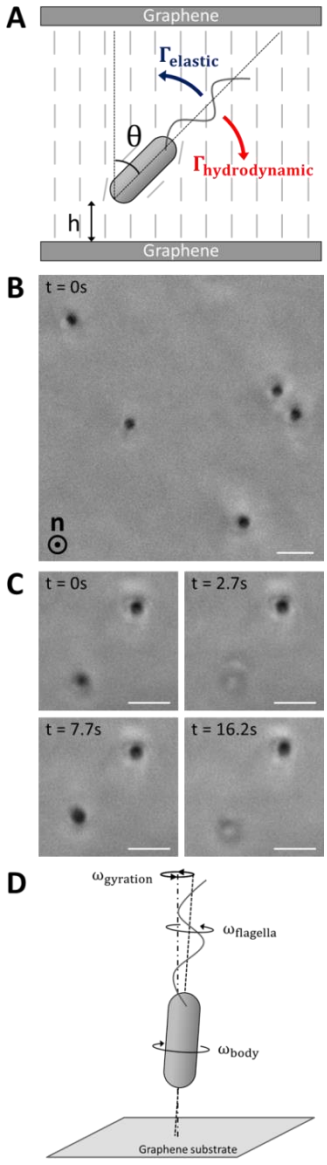

Figure 6-1. Alignment and motility of vegetative *P. mirabilis* cells in homeotropic LC films.

(A) Schematic representation of the elastic ($\Gamma_{elastic}$) and hydrodynamic ($\Gamma_{hydrodynamic}$) torques acting on a motile bacterium in a homeotropic LC film. (B) Phase contrast micrograph depicting the orientation of cells within a homeotropic LC film. The nematic director is oriented along the axis orthogonal to the plane of the page. (C) Sequence of phase contrast micrographs depicting a cell that moves back and forth across the thickness of the homeotropic film. The plane of focus remains fixed near one of the graphene-coated substrates in the micrographs. (D) Schematic (side view) depicting the handedness of the rotation of the cell body (ω_{body}) and flagella ($\omega_{flagella}$) about the axis defined by the long axis of the cell body as well as the handedness of the gyration ($\omega_{gyration}$) of the cell observed experimentally about an axis normal to the graphene-coated substrate. Scale bars = 3 μm.

To explore this hypothesis, we first dispersed motile vegetative *P. mirabilis* in an isotropic aqueous solution confined within a ~10 μm-thick experimental imaging chamber. We observed in this case that the motion of the bacteria was confined predominantly within planes parallel to the substrates, consistent with previous studies (see Video S1 in the online Supporting Information). Next, we dispersed vegetative cells within nematic DSCG and confined this mixture between two graphene-coated substrates separated by ~10 μm. We observed regions of the LC to adopt a uniform homeotropic orientation over the course of tens of minutes,[37] as confirmed by the observation of two crossed isogyres upon insertion of a sub-stage condenser and a Bertrand lens above the stage (Figure 6-S2).[38] In contrast to our observations of motile bacteria in isotropic solutions, we found that motile *P. mirabilis* cells (in addition to non-motile cells) oriented approximately parallel to the direction of LC alignment within the homeotropic regions (i.e., perpendicular to the graphene-coated substrates) (Figure 6-1B).

To determine whether the motile vegetative *P. mirabilis* were aligning perpendicular to the bounding substrates in uniform homeotropic DSCG films as a result of elastic forces, we calculated the relative magnitudes of Γ_{elastic} and $\Gamma_{\text{hydrodynamic}}$ acting on the vegetative cells. Specifically, we calculated the elastic torque as[39,40]

$$\Gamma_{\text{elastic}} \sim \frac{4\pi K \theta L_{\text{bacteria}}}{\ln(2L_{\text{bacteria}}/R)}, \qquad (6\text{-}1)$$

where K is the elastic constant of the LC (K ~ 10 pN for nematic DSCG[41]), R is the radius of a bacterium (R = 0.5 μm for *P. mirabilis*), and θ is the angle between the orientation of the long axis of the cell and the orientation of the far-field LC director. We estimated the hydrodynamic torque as

$$\Gamma_{\text{hydrodynamic}} \sim f_r \, \Omega, \qquad (6\text{-}2)$$

where Ω is the rate (in rad/s) at which surface-induced hydrodynamic stresses cause rod-shaped bacteria to reorient and f_r is the frictional drag coefficient associated with this rotation (see Supporting Information for details). In the absence of other applied torques, Ω is estimated by[30]

$$\Omega \sim -\frac{3p\cos\theta\sin\theta}{64\pi\eta h^3}, \qquad (6-3)$$

where p is the strength of the hydrodynamic force dipole, η is the viscosity, h is the distance of the bacterium away from the surface, and θ defines the angle between the cell long axis and the surface normal. For a swimming bacterium, the dipole strength can be approximated as $p \sim \eta V L_{tot}^2$,[30] where V is the linear velocity of the bacterium and L_{tot} is the total length of the bacterium (including both cell body and flagella). To compare the magnitudes of these two torques, we employed L_{tot} = 10 μm (a quantity that is optically measured using distortions in the LC induced by the flagella rotating behind motile bacteria[23] (see Video S2 in the online Supporting Information)), η ~ 0.7 Pa·s as an effective viscosity of nematic 15 wt% DSCG[22], and V = 8.8 μm/s as a typical velocity of vegetative *P. mirabilis* in nematic DSCG.[22] In the limit of small θ (in which the ratio $\Gamma_{elastic}/\Gamma_{hydrodynamic}$ is independent of θ), we calculate that the elastic torque associated with deviations of the alignment of a vegetative cell away from the far-field director (θ = 0°) near a graphene-coated substrate (h = 2 μm) exceeds the wall-induced hydrodynamic torque ($\Gamma_{elastic}/\Gamma_{hydrodynamic} \sim 6$). Although our estimate of $\Gamma_{hydrodynamic}$ does not account for the anisotropic viscosities of nematic LCs,[1,3,41,42] the relative magnitudes of $\Gamma_{hydrodynamic}$ and $\Gamma_{elastic}$ support our interpretation of our experimental observations in terms of the dominating influence of LC elastic torques (which overcome the influence of surface-induced hydrodynamic torques). This represents a striking departure from the typical behavior of motile rod-shaped cells near a solid substrate when dispersed in an isotropic solution.

Because we concluded that motile vegetative *P. mirabilis* cells were strongly oriented by elastic forces in homeotropic LC films, we next investigated their approach and collision with the substrates. Experimentally, we observed motile cells to remain localized for extended lengths of time (over the duration of our observations - tens of minutes) adjacent to one of the two graphene-coated substrates. The cell bodies of the five cells depicted in Figure 6-1B, for example, are dynamically positioned in a single plane proximate to one of the substrates. We judged that unidirectional flagella-derived forces were primarily responsible for this accumulation of bacteria near the bounding substrates. We note, however, that we occasionally observed vegetative cells to move back and forth along the LC director from one graphene-coated substrate to the other (Figure 6-1C; also see Video S3 in the online Supporting Information). We hypothesize that these cells are able to reverse direction due to flagella bundles that extend from both cell poles, as the elasticity of the nematic LC suppresses "tumbling" that typically reorients bacterial motion in isotropic solutions.[25]

Limited by the resolution of our optical microscope, it was difficult to establish whether the cells contacted the graphene-coated substrates by varying the focal plane, although we measured cells to regularly approach to within 1 μm from the substrates. However, we were able to conclude that bacteria did not physically adhere to the graphene-coated substrates but instead were likely dynamically positioned near the surfaces by hydrodynamic flows[31,43,44] as we observed the cell bodies of bacteria near a substrate to gyrate around an axis normal to the substrate (Figure 6-1D; also see Video S4 in the online Supporting Information). The handedness of the gyration matched that of the rotating flagella bundles (counter-clockwise when viewed from behind the cell) and proceeded at angular velocities between 1 – 2 rev/s (see Video S5 in the online Supporting Information). We measured the cell bodies of gyrating cells to deviate up

to 3° away from the surface normal (see Supporting Information for details). Using Equation 6-1, we estimate that an elastic torque as large as $\Gamma_{elastic} \sim 8$ pN·μm acts on the gyrating bacteria, a torque that must be balanced by rotation of the bacterial flagella. We also observed gyrating bacteria in homeotropic DSCG films with thicknesses of ~ 30 μm, suggesting this phenomenon is not simply an effect of confinement of the bacteria in LC films with $d_{film} \sim L_{bacteria}$. We note that this gyration resembles the "wobbling" of bacterial cell bodies that can occur in an isotropic solution when the long axis of a cell body and the axis of the helical flagella bundle are not collinear.[45–47]

6.3.2 Homeotropic LC film; $L_{bacteria} > d_{film}$

The results of the experiments described above establish that rod-shaped bacteria orient and move parallel to the LC director in homeotropic LC films when $L_{bacteria} < d_{film}$. Next, we investigated bacteria dispersed in a homeotropic LC film in the limit of $L_{bacteria} > d_{film}$ such that steric constraints (i.e., thickness of the LC film) prevent the body of the bacterium from orienting parallel to the LC. Specifically, we dispersed *P. mirabilis* swarm cells with lengths ranging from 10 – 60 μm within homeotropic LC films approximately 10 μm thick. In contrast to vegetative cells, we found that swarm cells oriented and moved through homeotropic nematic DSCG films in directions orthogonal to the nematic director with a velocity of $\overline{V}_{\perp} = 7.5 \pm 0.3$ μm/s (N = 97; standard error reported) (Figure 6-2A; also see Video S6 in the online Supporting Information). This velocity is lower than that measured for swarm cells moving parallel to the director (i.e., bacteria in uniform planar DSCG films; $\overline{V}_{\parallel} = 11.1 \pm 0.5$ μm/s (N = 34)) (see Video S7 in the online Supporting Information), consistent with the motile bacteria experiencing a higher effective shear viscosity when moving orthogonal to the director.[1–3] In support of this

interpretation, we note that the ratio of the diffusion coefficients of micrometer-sized silica particles in the nematic phase of a 13 wt% DSCG solution is $D_{\parallel}/D_{\perp} \sim 1.5$,[3] and that $\overline{V}_{\parallel}/\overline{V}_{\perp}$ for swarm cells is comparable to this value. In addition, we note that the magnitude of the flagella-derived forces produced by bacteria may differ when the cells are oriented either parallel or orthogonal to the far-field director due, for example, to differences in the orientation of the flagella bundle relative to the cell body caused by interaction with the LC.[25]

By varying the position of the focal plane of the microscope, we determined that swarm cells (both motile and non-motile) were localized typically (but not always, see below) at or near the midplane of the homeotropic LC films (for LC films with $d_{film}<L_{bacteria}$). This observation is consistent with repulsive LC elastic forces (due to homeotropic and tangential anchoring of the LC on the graphene-coated surface and bacteria, respectively; see Figure 6-2J) preventing swarm cells from approaching the graphene-coated substrates.[48–50] This observation also is a particularly interesting one because attachment to surfaces is the first step in the colonization of surfaces by bacteria (e.g., in forming biofilms). These results hint that LC materials may be useful in mediating bacteria-surface interactions to minimize attachment.

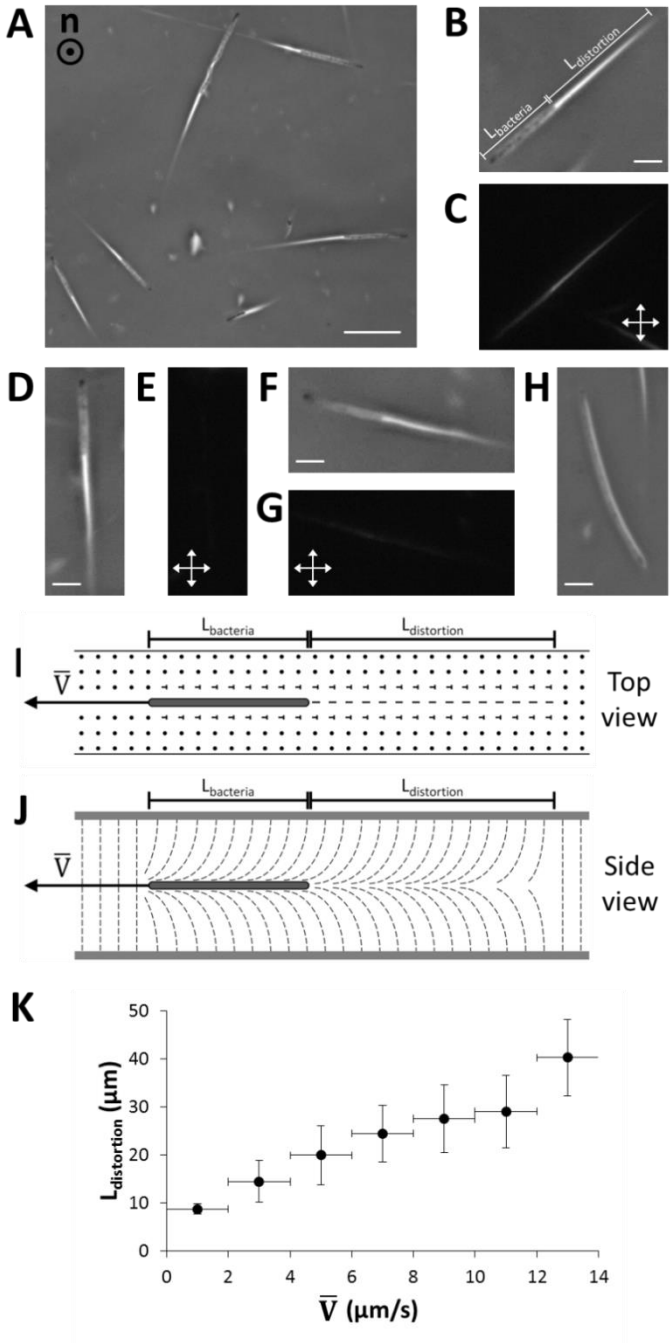

Figure 6-2. Motility of *P. mirabilis* swarm cells in homeotropic LC films.

(A) Phase contrast micrograph of motile swarm cells within a homeotropic LC film. The nematic director is oriented along the axis orthogonal to the plane of the page. The swarm cells move in directions orthogonal to the director, inducing distortions in the alignment of the LC in their wake. (B-G) Pairs of phase contrast micrographs (B and C, D and E, F and G) of swarm cells in homeotropic LC films taken either (B, D, F) without or (C, E, G) with crossed polarizers inserted into the optical path. In B, the length

of the swarm cell body ($L_{bacteria}$) and the wake of distorted LCs ($L_{distortion}$) are denoted. (H) Phase contrast micrograph of a stationary swarm cell in a homeotropic LC film. (I and J) Schematics (I – top view; J – side view) depicting the distortion in the LC film induced by motion of swarm cells perpendicular to the director (with velocity $\overline{V}$). (K) Plot of $L_{distortion}$ as a function of $\overline{V}$ measured for 97 swarm cells in homeotropic LC films. Horizontal error bars represent intervals over which data are binned while vertical error bars represent standard deviation. Scale bar in A = 20 μm; scale bars in B, D, F and H = 5 μm.

We also observed that self-propulsion of swarm cells generated "wakes" that had a striking comet-like optical appearance when visualized using phase contrast microscopy due to the birefringence of the nematic DSCG (Figure 6-2A; also see Video S6 in the online Supporting Information). Although previously it was demonstrated that rotation of bacterial flagella transiently strains uniform planar DSCG films over a length scale of a few micrometers[23], the distortions produced by swarm cells in our experiments appear to have a different origin, as we commonly measured these distortions to extend tens of micrometers behind the cell body and flagella of each swarm cell. These distortions in the LC film were long-lived, as the LC was observed to relax back to its original uniform homeotropic orientation over a time scale of seconds. By employing $\eta \sim 0.7$ Pa·s and $K \sim 10^{-11}$ N for nematic 15 wt% DSCG[22,41] and using a characteristic length scale of the distortions of $d_{film}/2 \sim 5$ μm, we estimated that τ, the elastic relaxation time scale ($\tau \sim \eta d_{film}^{2}/4K$)[51] is on the order of seconds ($\tau \sim 2$s), consistent with our experimental observations.

To obtain additional insight into the origin of the comet-like "tails," we analyzed the motions of the swarm cells both with and without crossed polarizers (Figures 6-2B through 6-2G). With crossed polarizers inserted, we found the brightness of the comet-like tails to depend on the direction of cell motion relative to the orientation of the polarizers. Specifically, whereas the wake exhibited a bright optical intensity when cells moved at an angle relative to both polarizers, appearing to reach a maximum for cells translating at approximately 45° with respect

to each polarizer (Figure 6-2C), the wakes were scarcely visible when cells moved nearly parallel to either polarizer (Figures 6-2E and 6-2G). We note that we did not observe comparable optical signatures extending from the poles of non-motile swarm cells (Figure 6-2H). These observations suggest that the motion of a swarm cell orthogonal to the homeotropically aligned nematic DSCG (in the far-field) induces a transient strain (bend and splay) within the LC, as depicted schematically in Figures 6-2I and 6-2J. We measured a linear relationship to exist between the length of the LC wake ($L_{distortion}$) and the average velocity ($\overline{V}$) of each cell (Figure 6-2K), consistent with $L_{distortion}$ being determined by how far a swarm cell travels over the course of τ, the time scale that characterizes the elastic relaxation of the LC (see above).

The orientation of the LC within the wake, which relaxes over time τ, likely reflects either or both the anchoring of the LC at the surface of the cell body, and shear alignment of the LC due to the motion of the DSCG induced by the bacteria. Even in the absence of motion of the cells, as noted above and shown in Figure 6-2J, the anchoring of the DSCG on the surface of the bacterial cell will induce the orientation of the LC observed within the core of the wake. In addition, however, we note that shear forces produced by the motion of the swarm cells could also lead to shear alignment of the LC in the absence of the above-described anchoring of the LC on the surface of the bacteria. This mechanism is supported by an estimate of the ratio of viscous to elastic torques, characterized by the Ericksen number ($Er = \eta d_{film}\overline{V}/2K$)[51], which is > 1 in our experiments.

We hypothesized that transient strain in the LCs induced by a moving swarm cell might also influence the motion of a second, trailing swarm cell. Consistent with this hypothesis and in support of our general physical picture proposed above, we found that when two swarm cells swam in close proximity to one another in a homeotropic LC film (in the same plane relative to

the graphene-coated substrates), the trajectory of one cell, upon encountering the wake of the other cell, assumed the trajectory of the first cell (Figure 6-3; also see Video S8 in the online Supporting Information).

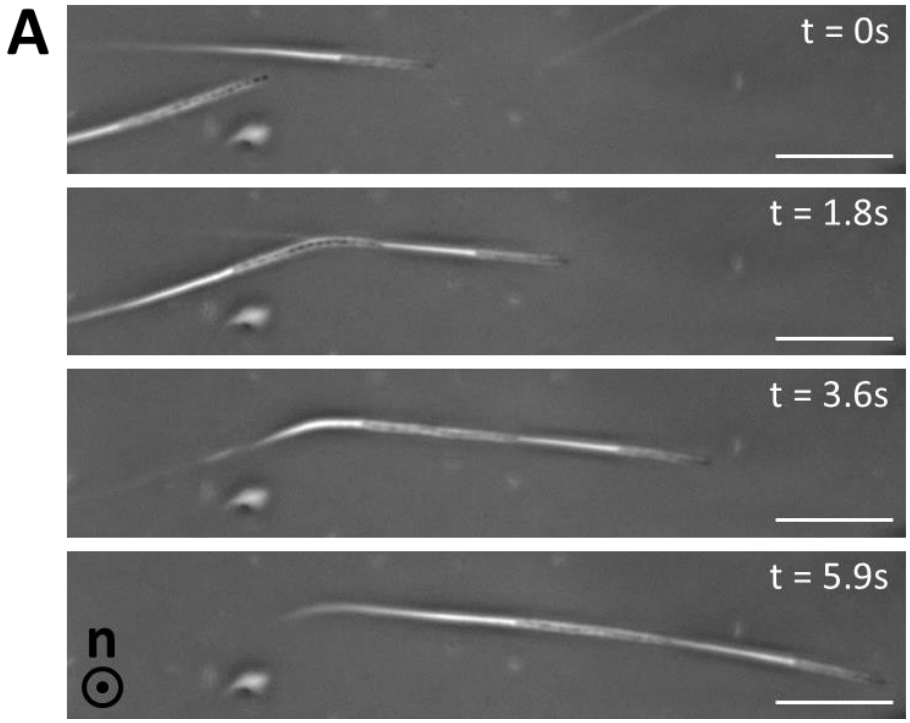

Figure 6-3. Interaction between two *P. mirabilis* swarm cells in a thin homeotropic LC film. Sequence of phase contrast micrographs depicting the motion of two *P. mirabilis* swarm cells within a homeotropic LC film. The trajectory of one of the cells is altered upon colliding with the wake of distorted LCs left by the other cell. Scale bars = 20 μm.

Although we typically observed *P. mirabilis* swarm cells were positioned at or near the midplane of uniform homeotropic LC films, we also occasionally found motile swarm cells instead located in a plane closer to one of the two bounding graphene-coated substrates. In these cases, we found the bodies of the swarm cells to be bent along their lengths and observed the swarm cells to swim in tight, circular trajectories within the plane parallel to the substrates (Figure 6-4). Moreover, when we analyzed these circular trajectories, we determined that they

always appeared counterclockwise when the cell was positioned near the graphene-coated substrate furthest from the objective of our inverted microscope (Figure 6-4A; also see Video S9 in the online Supporting Information) and clockwise when the cell was instead located near the substrate closer to the objective (Figure 6-4B; also see Video S10 in the online Supporting Information). These observations are consistent with previous reports of the emergence of circular cellular trajectories when bacteria dispersed in an isotropic solution swim near a solid surface.[31,52] These circular trajectories are caused by a wall-induced torque that arises from the motion of the cell body and the helical flagella bundle. They exhibit a specific handedness due to the chiral propulsion mechanism of the bacteria. Interestingly, however, we note that we did not observe *P. mirabilis* cells (either vegetative or swarm) to exhibit similar wall-induced circular trajectories when confined in nematic DSCG films exhibiting a uniform planar alignment. In this case, it appears that the elastic torque from the nematic LC is sufficient to suppress this wall-induced torque (analogous to the elastic suppression of vegetative cells from reorienting parallel to graphene-coated substrates when dispersed in homeotropic LC films, as described above).

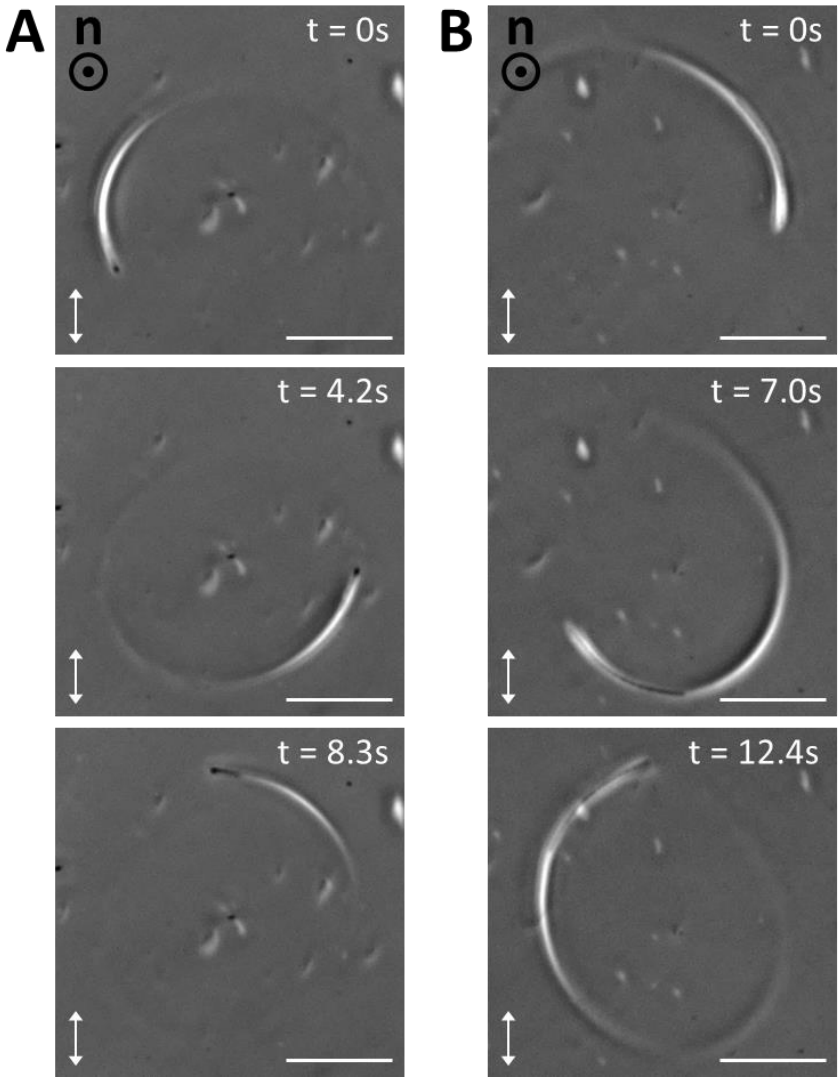

Figure 6-4. Circular trajectories of swarm cells in a homeotropic LC film.

(A, B) Sequences of micrographs (phase contrast with a single polarizer inserted) showing examples of the (A) counter-clockwise and (B) clockwise trajectories of motile swarm cells that arise when the cells are proximate to one of the two graphene-coated substrates in a homeotropic LC film. Scale bars = 20 μm.

6.3.3 Hybrid LC film; $L_{bacteria} < d_{film}$

A key conclusion that emerges from the above studies is that the LC elastic torques acting on bacteria near surfaces can be sufficiently large to dominate hydrodynamic interactions

that commonly govern the dynamics of bacteria in isotropic solvent systems near surfaces. To explore if the dominant influence of LC elastic stresses on bacterial dynamics near surfaces extends to situations where the director profile is non-uniform, next, we created nematic DSCG films with hybrid anchoring conditions by confining the LC between a graphene-coated substrate and a bare glass slide (Figure 6-S3). In these films, the out-of-plane orientation of the LC rotates by $\pi/2$ while going from one substrate to the other. We verified that nematic DSCG films adopted this hybrid configuration by confirming (i) the extinction of transmitted light as the sample was rotated between crossed polarizers and (ii) that interference colors observed at positions of minimum extinction of the sample corresponded to lower optical retardance values than for uniform planar films of the same thickness (Figure 6-S3). Consistent with this strained configuration of the LC director profile, when we dispersed small vegetative *P. mirabilis* cells within hybrid LC films, we observed that they aligned perpendicular to the graphene-coated substrate when proximate to it and parallel to the bare glass substrate when instead close to it (Figure 6-S4).

Most significantly, as shown in Figure 6-5, we found that when the bacteria were located in a region of the hybrid DSCG film ($d_{film} \sim 18$ μm) with a uniform in-plane orientation, the overall motion of bacteria was directed parallel to $\boldsymbol{p}$, a vector defined by the orientation of the bend and splay distortions in the hybrid film (as shown in Figure 6-5B) (see Video S11 in the online Supporting Information). Specifically, bacteria near the bare glass substrate within the hybrid LC film moved along the substrate in the direction parallel to $\boldsymbol{p}$. In contrast, when a cell with flagella bundles extending from both poles reversed its direction of motion such that it was directed anti-parallel to $\boldsymbol{p}$, the splay in the LC directed the bacterium across the thickness of the LC film towards the graphene-coated substrate, where the cell assumed an orientation

approximately perpendicular to the surface. Once held in this orientation, the motion of the cell ceased until it again reversed direction, moved back towards the bare glass substrate, and then continued moving parallel to ***p***. The net effect of this coupling between the strain of the LC and the bacteria was a rectification of the bacterial motion. Whereas rectification of bacterial motion has been achieved in isotropic solutions using microfluidic channels with special geometric features,[53,54] our results reveal that the elastic strain stored within the hybrid configuration of a nematic LC film tens of micrometers thick can also be leveraged to guide the overall motion of bacteria. Our results also demonstrate the elastic torques generated by complex and non-uniform LC director profiles also dominate hydrodynamic interactions of bacteria near surfaces.

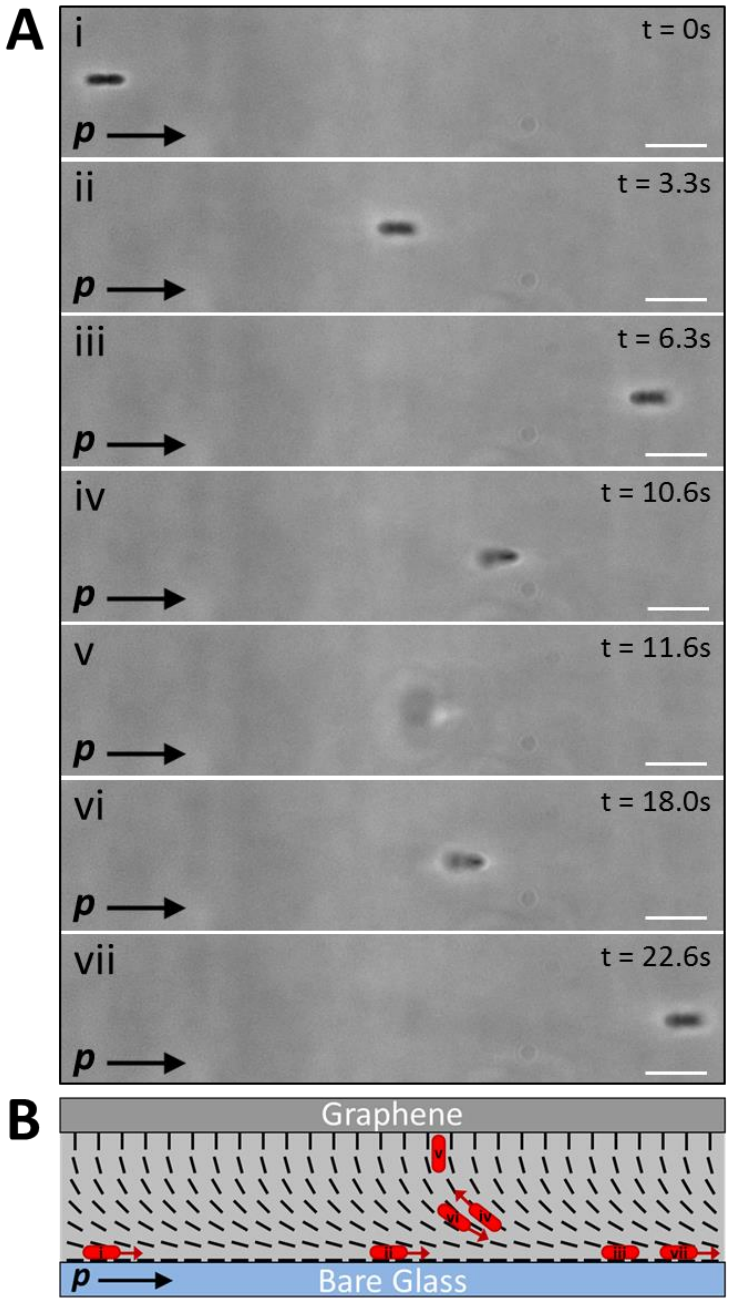

Figure 6-5. Rectification of vegetative *P. mirabilis* cell motion in a hybrid LC film.

(A) Sequence of phase contrast micrographs depicting the motion of a vegetative *P. mirabilis* cell within a hybrid LC film (11 µm thick). The plane of focus remains fixed near the bare glass substrate throughout the experiment. (B) Schematic representation of the director profile within the LC film along with the approximate location and direction of motion (indicated by red arrows) of the bacterium in each snapshot in A. In A and B, ***p*** indicates the orientation of the bend and splay distortions within the hybrid LC film. Scale bars = 5 µm.

6.3.4 Hybrid LC film; $L_{bacteria} > d_{film}$

Past studies by us and others have observed bacteria dispersed in LCs to behave as rigid entities. However, the results shown in Figure 6-4 clearly demonstrate that hydrodynamic interactions between the bacteria and surfaces can bend the bodies of swarm cells. To explore whether elastic stresses associated with strained LCs can also deform the bodies of a swarm cells, we explored LC films in which bend and splay distortions were present (in the limit $L_{bacteria} > d_{film}$). Our initial observations focused on swarm cells in hybrid DSCG films in which the direction of motion of the swarm cells was anti-parallel to $\boldsymbol{p}$. In this situation, we observed the leading end of a swarm cell to follow the $\pi/2$ rotation of the LC director across the thickness of the film, and upon reaching the graphene-coated substrate, trapped the swarm cell in a deformed configuration in which the cell body approximately followed the director within the hybrid LC film (Figure 6-6; also see Video S12 in the online Supporting Information). From this result, we conclude that the body of a *P. mirabilis* swarm cell is sufficiently soft that elastic stresses imparted by the LC phase can deform the cell body.

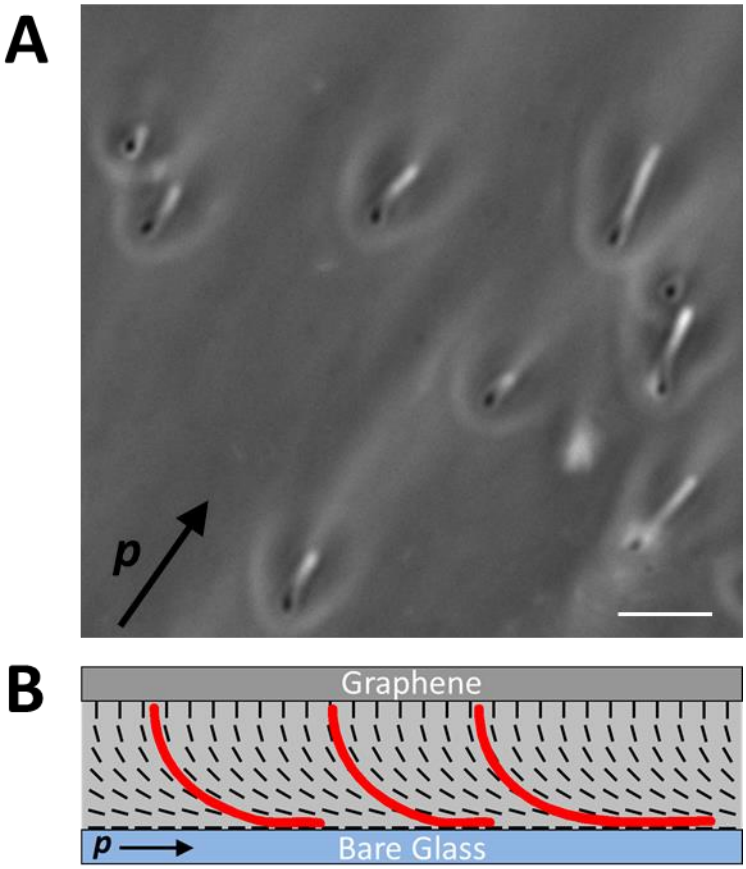

Figure 6-6. Deformation of *P. mirabilis* swarm cells in hybrid LC films.
(A) Phase contrast micrograph of *P. mirabilis* swarm cells dispersed within an 18 μm thick hybrid LC film (plane of focus near graphene-coated substrate). (B) Schematic representation of the director profile within the LC film along with the approximate configurations of the swarm cells. In A and B, ***p*** indicates the orientation of the bend and splay distortions within the hybrid LC film. Scale bar = 10 μm.

To examine further this conclusion, we compared the relative energetic cost of bending a swarm cell in a hybrid LC film (E_{cell}) to that associated with straining LCs locally around a bacterium not aligned with the far-field director (E_{LC}). We estimate the cell bending energy by the expression

$$E_{cell} = \frac{1}{2} E I L_{bend} \kappa^2, \qquad (6-4)$$

where *E* is the Young's modulus, I is the second moment of inertia, L_{bend} is the arc length of and κ is the mean curvature of the deformed segment of the bent swarm cell.[55] Employing typical values for our system, we estimate $E_{cell} \sim 1 \times 10^{-17}$ J for a swarm cell with L_{bend} = 28 μm in a hybrid LC film 18 μm thick (see Supporting Information for details).

To compare the magnitude of the LC elastic energy to this value of E_{cell}, we use the expression[39]

$$E_{LC} = 2\pi LK\theta^2/\ln(2L/R). \qquad (6-5)$$

Equation 6-5 is the energetic cost associated with realigning a swarm cell of length L and radius R an angle of θ away from the far-field director in a uniformly aligned LC film. For a swarm cell with L = L_{bend} = 28 μm and R = 0.5 μm and using K = 10 pN, we calculate $E_{LC} \sim E_{cell}$ when $\theta \sim$ 11°. This calculation suggests that LC elastic stresses should be sufficient in magnitude to deform the body of a swarm cell, consistent with our experimental observations. Moreover, this preliminary result suggests that hybrid LC films may be useful for measurement of cell mechanical properties, particularly since the amount of strain stored in the LC films can be modulated by either changing the thickness of the film or the temperature or composition of the lyotropic chromonic LC phase (in order to alter the magnitude of the elastic constants)[41,56].

6.4 Conclusions

In summary, our study reveals new dynamical behaviors of bacteria confined within thin homeotropic and hybrid nematic LC films, and provides insight into the origins of those behaviors. A key conclusion of our study is that elastic torques generated by the LC are sufficiently large to overcome wall-induced hydrodynamic torques, thus leading to LC-guided bacterial motion near surfaces that orient LCs. The dominating role of the elastic torques on the

near-surface behaviors of the bacteria are evident in our studies with homeotropically aligned LCs (the bacteria adopted orientations perpendicular to the surface) and in hybrid aligned films (the bacteria followed the spatial variation in the director profile, thus exhibiting rectified motion). In addition, it is evident in comparisons of the behavior of swarm cells in LC films in the limit $L_{bacteria} > L_{film}$; as shown in Figure 6-4, when the LC is aligned perpendicular to the surface, hydrodynamic interactions dominate the circular, in-plane motion of the cells because the LC exerts no torque (that influences in-plane motion); in contrast, when the LC is aligned in the plane of the surface, the LC-mediated torque results in trajectories of the cells that following the orientation of the director.

A second key conclusion of our study is that elastic stresses associated with non-uniform director profiles are sufficient to cause the deformation of the bacterial cell bodies when using long swarm cells. While we (Figure 6-4) and others[57] have reported previously that hydrodynamic interactions can lead to changes in cell shape, the observations in Figure 6-6 are the first to suggest that LC elastic stresses can deform cells. Indeed, our observations in Figure 6-6 suggest that the cell body largely follows the director profile in LC films with hybrid anchoring. This coupling between cell shape and LC director profile suggests that descriptions of the dynamical behaviors of bacteria in LCs will, in general, need to consider the shape of the cells as a dependent variable of the system.

Overall, the findings reported in this paper also suggest the basis of new methods and approaches for manipulation of bacteria in technological contexts. For example, we show that rectification of bacteria motion is possible in hybrid LC films and that, unlike isotropic solution, this phenomenon is achieved in nematic LCs without the need for special geometric features present on the walls confining the fluid. Thus, it may represent a versatile new means to facilitate

quantification and spatial localization of bacteria. Alternatively, by varying the magnitude of the elastic stresses acting on elongated bacteria in hybrid films and determining the resulting configurations adopted by the cells, strained LCs might be used to report the mechanical properties of bacteria (e.g., bending stiffness). In addition, we end by commenting that the dynamical response of the LC to the motions of bacteria (e.g., the transient distortions of the LC produced by swarm cells moving in directions orthogonal to the LC director field) might also be used to measure physical properties of nematic LCs.

Acknowledgements

This work was supported by the National Science Foundation (under awards DMR-1121288 (MRSEC), CBET-1263970, MCB-1120832, and CMMI-1129802), the National Institutes of Health (CA108467), the Army Research Office (W911-NF-11-1-0251 and W911-NF-14-1-0140), and the United States Department of Agriculture (WIS01594).

6.5 Supporting Information

Calculation of the rotational drag coefficient for vegetative *P. mirabilis* cells

Modeling vegetative *P. mirabilis* cells as prolate spheroids with semi-major axis a and semi-minor axis b, we estimated the frictional drag coefficient associated with the rotation of the cell around one of its minor axes using the expression $f_r = \frac{4(1-p^4)}{3p^2[aS(2-p^2)-2]} C_o$.[58] In this expression, $p = b/a$, $S = \frac{2}{a}(1-p^2)^{-1/2} \ln\left[\frac{\left[1+(1-p^2)^{1/2}\right]}{p}\right]$, and $C_o = 8\pi a^3 p^2 \eta$ is the coefficient for rotational frictional drag for a sphere with a volume equal to the volume of the ellipsoid. Employing a = 1.5 μm, b = 0.5 μm, and an effective viscosity of $\eta \sim 0.7$ Pa s for the nematic DSCG phase, we estimate $f_r \sim 1.5 \times 10^{-17}$ kg m^2 s^{-1}.

Measurement of the angle of alignment adopted by gyrating vegetative bacteria near graphene-coated substrates

Videos (200 frames long) of vegetative cells gyrating near graphene-coated substrates in uniform homeotropic and hybrid films were collected at different planes of focus separated by 1 μm. The Mosaic ParticleTracker 2D/3D plugin[59] for ImageJ then was used to plot trajectories of the approximately circular cross-sections of the gyrating cells, as depicted in Figure 6-S5. By determining the average radius of these trajectories collected for an individual gyrating cell at different planes of focus, trigonometric relations could be used to estimate the average angle (ϕ in Figure 6-S5) formed between the long axis of the vegetative cell and the surface normal.

Estimation of E_{cell} for swarm cells dispersed in a hybrid LC film

To estimate the energetic cost (E_{cell}) of bending a swarm cell of length L in a hybrid LC film of thickness d in the limit of $L > d$, we model the cell as a rod-shaped shell that has thickness w and radius R and use $E_{cell} = \frac{1}{2} E I L_{bend} \kappa^2$.[55] In this expression, E is the Young's modulus, I is the second moment of inertia, L_{bend} is the arc length of the bent cell, and κ is the mean curvature of the cell.[55] For a thin, hollow cylinder of thickness w, $I = \frac{1}{4}\pi[R^4 - (R-b)^4] \approx \pi R^3 w$.[60] We assume that if a swarm cell deforms such that its orientation is always parallel to the local director in a LC film of thickness d with hybrid anchoring conditions, the mean curvature of the deformed segment of the swarm cell is given by $\kappa \sim \frac{1}{d}$. Given this curvature, the deformed length of the swarm cell in the hybrid film (in which the out-of-plane orientation of the LC rotates by $\pi/2$ going from the graphene-coated substrate to the bare glass substrate) is $L_{bend} \sim \frac{\pi}{2} d$ (see Figure 6-S6). Inserting these expressions into the equation for E_{cell}, we arrive at $E_{cell} = \frac{\pi^2 R^3 w E}{4d}$. Employing typical values in our system of $R \sim 0.5$ μm and $d \sim 18$ μm, an estimate of the thickness of the peptidoglycan layer of *P. mirabilis* (which imparts rigidity to the cell body) of $w \sim 10$ nm[61], and an estimate for the Young's modulus of the highly flagellated *P. mirabilis-flhDC* swarm cell of $E \sim 8.743 \times 10^4$ Pa (personal communication from Weibel lab), we estimate $E_{cell} \sim 1 \times 10^{-17}$ J.

Gyration of vegetative *P. mirabilis* cells in hybrid LC films

We found that vegetative *P. mirabilis* cells dispersed in hybrid films also had a tendency to become dynamically positioned near the graphene-coated substrate, similar to the case of homeotropic LC films described in the main text. As a result, we observed that over the course of

an experiment, cells dispersed in hybrid LC films tended to accumulate near the graphene-coated substrate. Each cell positioned near the graphene-coated substrate gyrated about an axis normal to the substrate with a handedness matching that of its rotating flagella bundle (see Video S13 in the online Supporting Information). However, while we measured the angular velocity of the cell bodies to be comparable to that measured in homeotropic films ($\sim 1 - 2$ rev/s), we determined the cell body to commonly deviate at larger angles (up to 6°) away from the surface normal. We hypothesize that the combined effects of changes in the orientation of the far-field director profile over the length of the cell body and bending of the bacterial flagella due to the bend and splay in the LC are likely responsible for the pronounced deviation of the orientation of the cell body away from the surface normal measured in hybrid films.

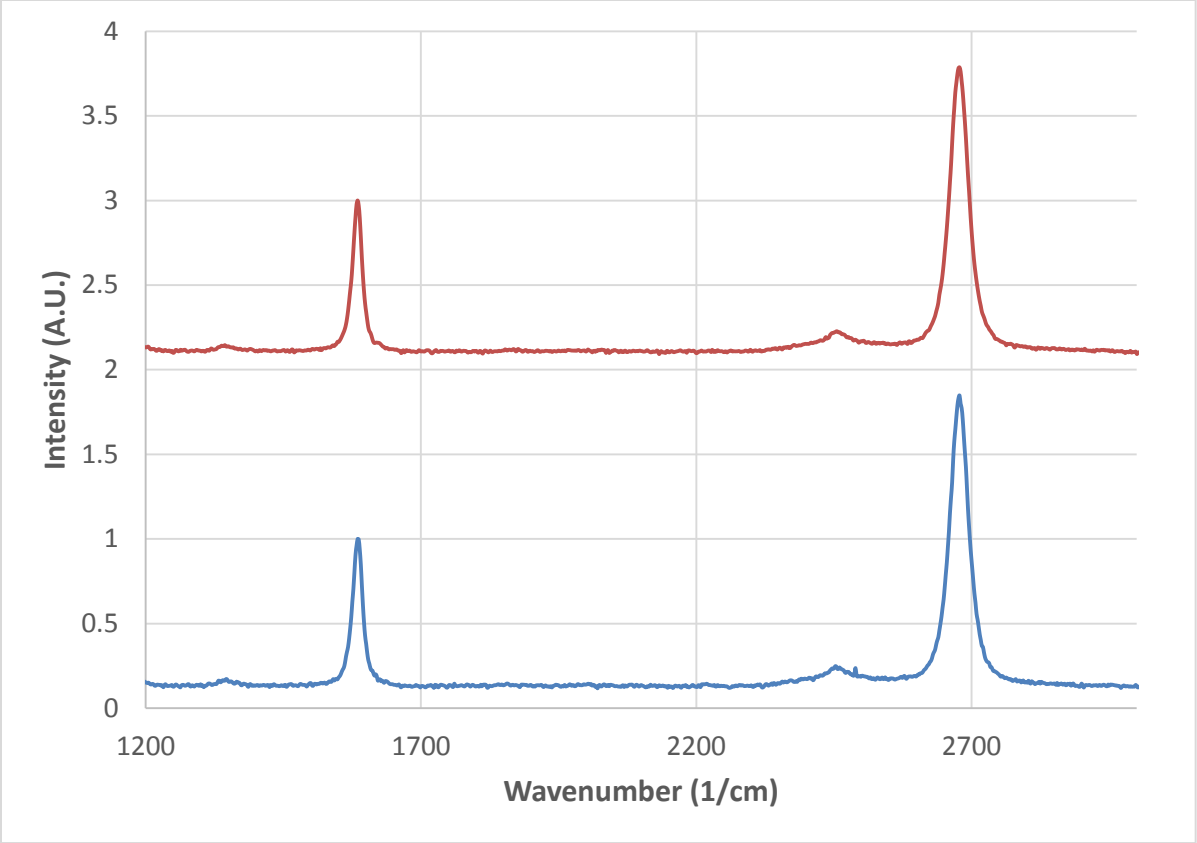

Figure 6-S1. Spatially-averaged Raman spectra (normalized to the G-band intensity) of a graphene-coated substrate collected both before (blue) and after (red) contact with a 15 wt% DSCG solution for 30 min.

The DSCG solution was removed from the surface of the graphene-coated substrate before the second spectrum was collected. A typical Raman spectra for graphene consists of three major bands, namely the D, G and 2D bands at ~1347 cm^{-1}, ~1585 cm^{-1} and 2680 cm^{-1} (for a 532 nm excitation wavelength).[62] In our spectra, the ratio of $I_{2D}/I_G > 1$ confirms the presence of a monolayer of graphene.[62] In addition, the ratio of I_D/I_G is directly proportional to the defect density, with values < 0.1 considered to indicate high quality graphene monolayers grown via chemical vapor deposition (CVD). In our spectra, taken both before and after application of the DSCG solution, we calculated I_D/I_G to be ~ 0.04. This indicates (i) a very low defect density in the as-manufactured graphene layer and (ii) that no additional defects were introduced during the application and removal of the LC.

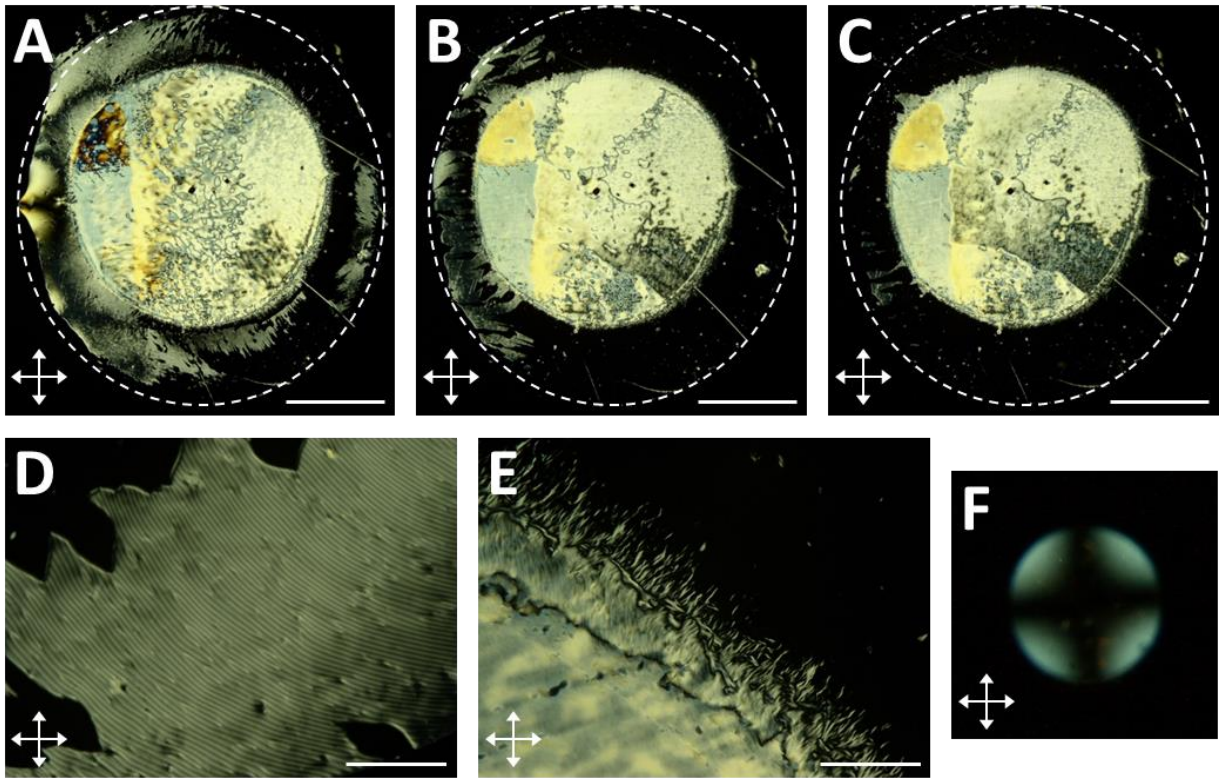

Figure 6-S2. Evolution of homeotropic orientation in a nematic phase DSCG film.

(A-C) Polarized light (crossed polars) micrographs of nematic phase DSCG film (~ 18 μm thick) confined between two graphene-coated substrates taken (A) 20 min, (B) 60 min, and (C) 120 min after preparation of the optical imaging chamber. Dotted white lines superimposed on the images indicate the approximate extent of the LC film. The optical imaging chamber was prepared by sandwiching 1.2 μL of DSCG in the nematic phase between the graphene-coated substrates and sealing with epoxy, using Mylar spacers to set the film thickness. Regions of the LC film in an outer annulus of the film transition to a homeotropic orientation over the initial 120 min and retain this homeotropic orientation for days following. The central region of the film (even after days) was not observed to transition to a homeotropic orientation. (D) Polarized light (crossed polars) micrograph of the transient stripe texture observed in the outer annulus of the LC film as the LC transitions to a uniform homeotropic orientation. Image acquired 25 min after preparation of the optical imaging chamber. (E) Polarized light (crossed polars) micrograph of the transition region observed between the outer annulus exhibiting homeotropic orientation and the inner region that does not. Image acquired 37 min after preparation of the optical imaging chamber. (F) Conoscopic image acquired in the outer annulus of DSCG, confirming uniform homeotropic orientation. Image acquired 70 min after preparation of the optical imaging chamber. Scale bars in A-C = 2 mm; scale bars in D,E = 5 μm.

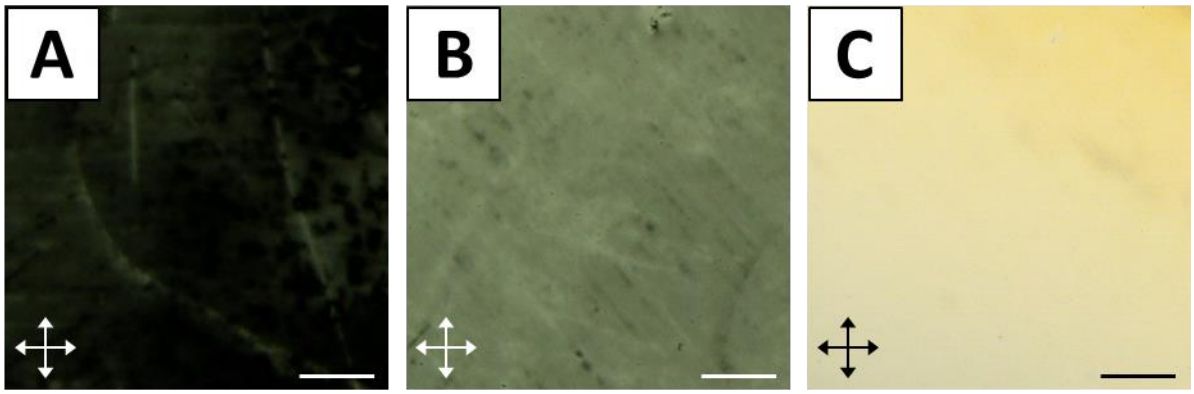

Figure 6-S3. Optical characterization of a hybrid LC film.

(A,B) Polarized light (crossed polarizers) micrographs of a region of a hybrid anchored LC film (~ 18 μm thick) exhibiting approximately uniform azimuthal alignment. The sample is rotated such that the direction of azimuthal alignment of the LC is oriented either (A) parallel or (B) 45° relative to the orientation of one of the polarizers. (C) Polarized light (crossed polarizers) micrograph of a uniform planar LC film (~ 18 μm thick) in which the director is oriented 45° relative to the orientation of one of the polarizers. Scale bars = 200 μm.

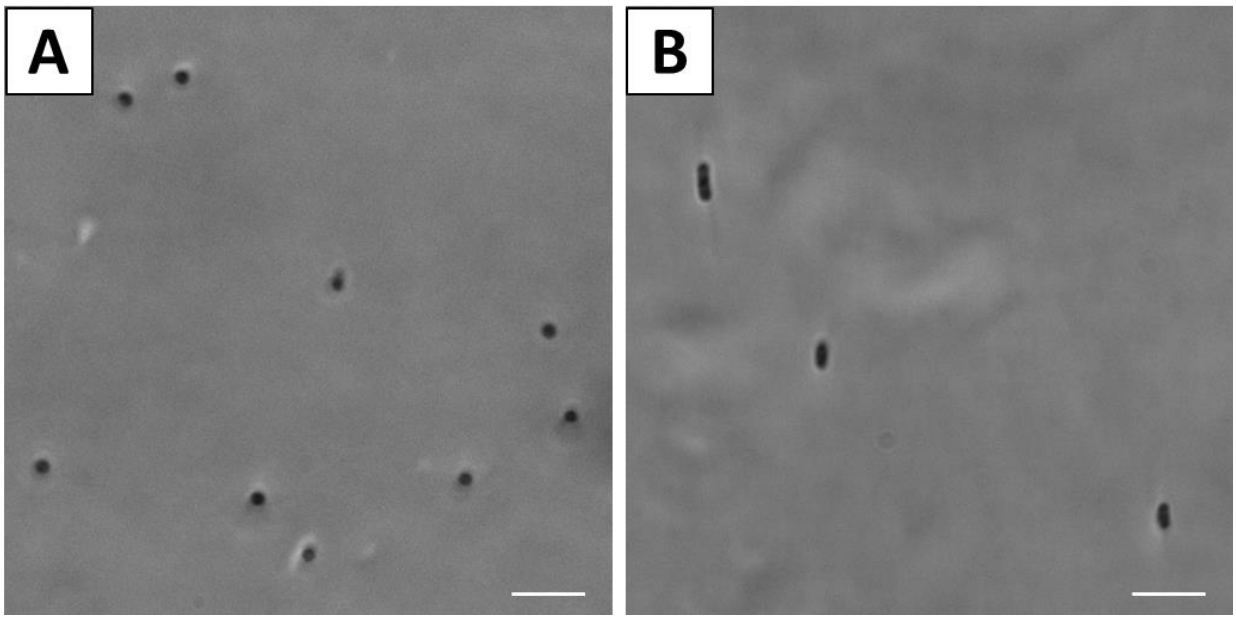

Figure 6-S4. Orientations of vegetative *P. mirabilis* cells in a hybrid LC film.

Phase contrast microscopy images of vegetative *P. mirabilis* cells dispersed within a hybrid LC film (~ 18 μm thick) in a plane (A) near to the graphene-coated substrate and (B) near to the bare glass substrate. Scale bars = 5 μm.

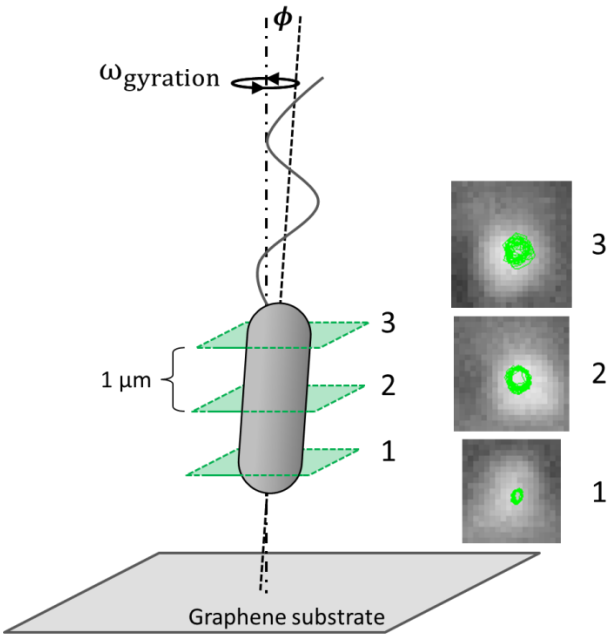

Figure 6-S5. Measurement of the orientations adopted by gyrating vegetative *P. mirabilis* cells. Schematic and representative trajectories (each 200 frames long) collected at different planes of focus (each separated by 1 µm) of a gyrating vegetative cell near a graphene-coated substrate within a hybrid DSCG film.

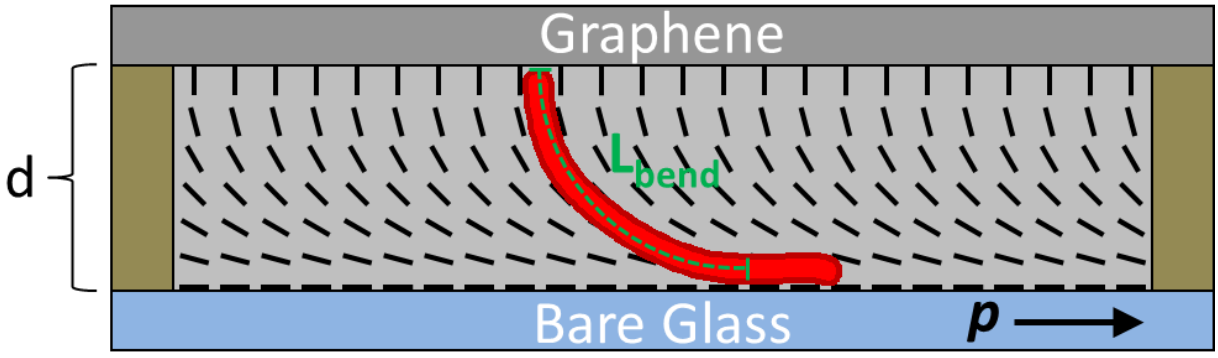

Figure 6-S6. Schematic depicting the configuration adopted by a *P. mirabilis* swarm cell in a thin hybrid LC film in the limit of L > d.

Supplementary Video Captions

Following the publication of this manuscript, supporting videos will be available in the online SI.

Video S1. Phase contrast microscopy video of the motion of vegetative *P. mirabilis* cells dispersed in isotropic aqueous motility buffer between glass substrates in a cavity ~10 um thick.

Video S2. Phase contrast microscopy video of the motion of a vegetative *P. mirabilis* cell dispersed in a planar DSCG film created using two bare glass substrates. Due to the birefringence of the LC, distortions produced by the rotating flagella can be visualized in the wake of the bacterium.

Video S3. Phase contrast microscopy video of vegetative *P. mirabilis* cells dispersed in a uniform homeotropic DSCG film created using two graphene-coated substrates that orient parallel to the LC director (perpendicular to the graphene substrates). One cell is observed to move back and forth through the thickness of the LC film.

Video S4. Phase contrast microscopy video in which vegetative *P. mirabilis* cells in a uniform homeotropic DSCG film near one of the graphene substrates align approximately parallel to the far-field LC director and gyrate in tight circular trajectories (in a counterclockwise fashion when viewed from above the substrate) around an axis normal to the substrate.

Video S5. Phase contrast microscopy video in which a vegetative *P. mirabilis* cell in a uniform homeotropic DSCG film near one of the graphene substrates orients at a small angle with respect to the far-field LC director and gyrates in tight circular trajectories (in a counterclockwise fashion when viewed from above the substrate) around an axis normal to the substrate. Distortions in the LC induced by the rotating flagella bundle of the cell also can be observed.

Video S6. Phase contrast microscopy video of *P. mirabilis* swarm cells moving within a homeotropic DSCG film in directions orthogonal to the far-field director.

Video S7. Phase contrast microscopy video in which *P. mirabilis* swarm cells align and move parallel to the nematic director when dispersed in uniform planar DSCG films confined between bare glass slides.

Video S8. Phase contrast microscopy video of two motile *P. mirabilis* swarm cells moving within a homeotropic LC film. The transient strain in the LCs produced in the wake of one of the motile swarm cells leads to a change in the direction of motion of the second swarm cell.

Video S9. Phase contrast microscopy video (taken with a single polarizer inserted into the light path oriented in the vertical direction) of the motility of a *P. mirabilis* swarm cell within a homeotropic LC film and near to the graphene substrate farther from the objective. Viewed from above the graphene substrate, the cell appears to move in counterclockwise circles.

Video S10. Phase contrast microscopy video (taken with a single polarizer inserted into the light path oriented in the vertical direction) of the motility of a *P. mirabilis* swarm cell within a homeotropic LC film and near to the graphene substrate closer to the objective. Viewed from in front of the graphene substrate, the cell appears to move in clockwise circles.

Video S11. Phase contrast microscopy video showing rectification of the motion of a vegetative *P. mirabilis* cell in a hybrid LC film.

Video S12. Z-stack of images (phase contrast) of *P. mirabilis* swarm cells that have cell bodies that are extended through the thickness of a hybrid LC film.

Video S13. Phase contrast microscopy video of a vegetative *P. mirabilis* cell in a hybrid DSCG film positioned near the graphene substrate. The cell aligns approximately parallel to the local LC director and moves in tight circular trajectories (in a clockwise fashion when viewed from in front of the substrate) around an axis perpendicular to the substrate. Distortions in the LC induced by the rotating flagella bundle of the cell, which bends through the thickness of the LC film, also can be observed.

6.6 References

*This chapter was prepared as a Full Paper reporting original research submitted to the journal *Soft Matter* at the time of publication of this thesis. Rishi Trivedi assisted me in performing and analyzing the experiments and preparing the manuscript. Susmit Singha Roy prepared and characterized graphene substrates.

1. Loudet, J. C.; Hanusse, P.; Poulin, P. Stokes Drag on a Sphere in a Nematic Liquid Crystal. *Science* **2004**, 306, 1525.
2. Mondiot, F.; Loudet, J.-C.; Mondain-Monval, O.; Snabre, P.; Vilquin, A.; Würger, A. Stokes-Einstein Diffusion of Colloids in Nematics. *Phys. Rev. E* **2012**, 86, 010401.
3. Turiv, T.; Lazo, I.; Brodin, A.; Lev, B. I.; Reiffenrath, V.; Nazarenko, V. G.; Lavrentovich, O. D. Effect of Collective Molecular Reorientations on Brownian Motion of Colloids in Nematic Liquid Crystal. *Science* **2013**, 342, 1351–1354.
4. Lynch, M. D.; Patrick, D. L. Organizing Carbon Nanotubes with Liquid Crystals. *Nano Lett.* **2002**, 2, 1197–1201.
5. Lapointe, C.; Hultgren, A.; Silevitch, D. M.; Felton, E. J.; Reich, D. H.; Leheny, R. L. Elastic Torque and the Levitation of Metal Wires by a Nematic Liquid Crystal. *Science* **2004**, 303, 652–655.
6. Tkalec, U.; Škarabot, M.; Muševič, I. Interactions of Micro-Rods in a Thin Layer of a Nematic Liquid Crystal. *Soft Matter* **2008**, 4, 2402–2409.
7. Mondiot, F.; Chandran, S. P.; Mondain-Monval, O.; Loudet, J.-C. Shape-Induced Dispersion of Colloids in Anisotropic Fluids. *Phys. Rev. Lett.* **2009**, 103, 238303.
8. Senyuk, B.; Smalyukh, I. I. Elastic Interactions between Colloidal Microspheres and Elongated Convex and Concave Nanoprisms in Nematic Liquid Crystals. *Soft Matter* **2012**, 8, 8729–8734.
9. Musevic, I.; Škarabot, M.; Tkalec, U.; Ravnik, M.; Žumer, S. Two-Dimensional Nematic Colloidal Crystals Self-Assembled by Topological Defects. *Science* **2006**, 313, 954–958.
10. Poulin, P.; Stark, H.; Lubensky, T. C.; Weitz, D. A. Novel Colloidal Interactions in Anisotropic Fluids. *Science* **1997**, 275, 1770–1773.
11. Škarabot, M.; Ravnik, M.; Žumer, S.; Tkalec, U.; Poberaj, I.; Babič, D.; Osterman, N.; Muševič, I. Interactions of Quadrupolar Nematic Colloids. *Phys. Rev. E* **2008**, 77, 031705.
12. Tasinkevych, M.; Mondiot, F.; Mondain-Monval, O.; Loudet, J.-C. Dispersions of Ellipsoidal Particles in a Nematic Liquid Crystal. *Soft Matter* **2014**, 10, 2047–2058.
13. Nych, A.; Ognysta, U.; Muševič, I.; Seč, D.; Ravnik, M.; Žumer, S. Chiral Bipolar Colloids from Nonchiral Chromonic Liquid Crystals. *Phys. Rev. E* **2014**, 89, 062502.
14. Lavrentovich, O. D. Transport of Particles in Liquid Crystals. *Soft Matter* **2014**, 10, 1264–1283.
15. Lapointe, C. P.; Mason, T. G.; Smalyukh, I. I. Shape-Controlled Colloidal Interactions in Nematic Liquid Crystals. *Science* **2009**, 326, 1083–1086.
16. Senyuk, B.; Evans, J. S.; Ackerman, P. J.; Lee, T.; Manna, P.; Vigderman, L.; Zubarev, E. R.; van de Lagemaat, J.; Smalyukh, I. I. Shape-Dependent Oriented Trapping and Scaffolding of Plasmonic Nanoparticles by Topological Defects for Self-Assembly of Colloidal Dimers in Liquid Crystals. *Nano Lett.* **2012**, 12, 955–963.

17. Chandran, S. P.; Mondiot, F.; Mondain-Monval, O.; Loudet, J. C. Photonic Control of Surface Anchoring on Solid Colloids Dispersed in Liquid Crystals. *Langmuir* **2011**, 27, 15185–15198.
18. Škarabot, M.; Ravnik, M.; Žumer, S.; Tkalec, U.; Poberaj, I.; Babič, D.; Muševič, I. Hierarchical Self-Assembly of Nematic Colloidal Superstructures. *Phys. Rev. E* **2008**, 77, 061706.
19. Nazarenko, V. G.; Nych, A. B.; Lev, B. I. Crystal Structure in Nematic Emulsion. *Phys. Rev. Lett.* **2001**, 87, 075504.
20. Tkalec, U.; Ravnik, M.; Čopar, S.; Žumer, S.; Muševič, I. Reconfigurable Knots and Links in Chiral Nematic Colloids. *Science* **2011**, 333, 62–65.
21. Kumar, A.; Galstian, T.; Pattanayek, S. K.; Rainville, S. The Motility of Bacteria in an Anisotropic Liquid Environment. *Mol. Cryst. Liq. Cryst.* **2013**, 574, 33–39.
22. Mushenheim, P. C.; Trivedi, R. R.; Tuson, H. H.; Weibel, D. B.; Abbott, N. L. Dynamic Self-Assembly of Motile Bacteria in Liquid Crystals. *Soft Matter* **2014**, 10, 88–95.
23. Zhou, S.; Sokolov, A.; Lavrentovich, O. D.; Aranson, I. S. Living Liquid Crystals. *Proc. Natl. Acad. Sci. U. S. A.* **2014**, 111, 1265–1270.
24. Mushenheim, P. C.; Trivedi, R. R.; Weibel, D. B.; Abbott, N. L. Using Liquid Crystals to Reveal How Mechanical Anisotropy Changes Interfacial Behaviors of Motile Bacteria. *Biophys. J.* **2014**, 107, 255–265.
25. Sokolov, A.; Zhou, S.; Lavrentovich, O. D.; Aranson, I. S. Individual Behavior and Pairwise Interactions between Microswimmers in Anisotropic Liquid. *Phys. Rev. E* **2015**, 91, 013009.
26. Shaw, T.; Winston, M.; Rupp, C. J.; Klapper, I.; Stoodley, P. Commonality of Elastic Relaxation Times in Biofilms. *Phys. Rev. Lett.* **2004**, 93, 098102.
27. Flemming, H.-C.; Wingender, J. The Biofilm Matrix. *Nat. Rev. Microbiol.* **2010**, 8, 623–633.
28. Tam, P. Y.; Katz, D. F.; Berger, S. A. Non-Linear Viscoelastic Properties of Cervical Mucus. *Biorheology* **1980**, 17, 465–478.
29. Haward, S. J.; Odell, J. A.; Berry, M.; Hall, T. Extensional Rheology of Human Saliva. *Rheol. Acta* **2011**, 50, 869–879.
30. Berke, A.; Turner, L.; Berg, H.; Lauga, E. Hydrodynamic Attraction of Swimming Microorganisms by Surfaces. *Phys. Rev. Lett.* **2008**, 101, 038102.
31. Lauga, E.; Powers, T. R. The Hydrodynamics of Swimming Microorganisms. *Reports Prog. Phys.* **2009**, 72, 096601.
32. Tuson, H. H.; Copeland, M. F.; Carey, S.; Sacotte, R.; Weibel, D. B. Flagella Density Regulates *Proteus mirabilis* Swarmer Cell Motility in Viscous Environments. *J. Bacteriol.* **2013**, 195, 368–377.
33. Nastishin, Y. A.; Liu, H.; Shiyanovskii, S. V.; Lavrentovich, O. D.; Kostko, A. F.; Anisimov, M. A. Pretransitional Fluctuations in the Isotropic Phase of a Lyotropic Chromonic Liquid Crystal. *Phys. Rev. E* **2004**, 70, 051706.
34. Champion, J. V; Meeten, G. H. Conformation of Sodium Cromolyn in Aqueous Solution Using Light Scattering and Magnetic Birefringence. *J. Pharm. Sci.* **1973**, 62, 1589–1595.
35. Roy, S. S.; Bindl, D. J.; Arnold, M. S. Templating Highly Crystalline Organic Semiconductors Using Atomic Membranes of Graphene at the Anode/Organic Interface. *J. Phys. Chem. Lett.* **2012**, 3, 873–878.

36. Li, X.; Zhu, Y.; Cai, W.; Borysiak, M.; Han, B.; Chen, D.; Piner, R. D.; Colombo, L.; Ruoff, R. S. Transfer of Large-Area Graphene Films for High-Performance Transparent Conductive Electrodes. *Nano Lett.* **2009**, 9, 4359–4363.
37. Jeong, J.; Han, G.; Johnson, A. T. C.; Collings, P. J.; Lubensky, T. C.; Yodh, A. G. Homeotropic Alignment of Lyotropic Chromonic Liquid Crystals Using Noncovalent Interactions. *Langmuir* **2014**, 30, 2914–2920.
38. Bloss, F. D. *An Introduction to the Methods of Optical Crystallography*; Holt, Rinehart and Winston: New York, NY, 1961.
39. Smith, C. J.; Denniston, C. Elastic Response of a Nematic Liquid Crystal to an Immersed Nanowire. *J. Appl. Phys.* **2007**, 101, 014305.
40. Smalyukh, I. I.; Butler, J.; Shrout, J. D.; Parsek, M. R.; Wong, G. C. L. Elasticity-Mediated Nematiclike Bacterial Organization in Model Extracellular DNA Matrix. *Phys. Rev. E* **2008**, 78, 030701.
41. Zhou, S.; Neupane, K.; Nastishin, Y. A.; Baldwin, A. R.; Shiyanovskii, S. V; Lavrentovich, O. D.; Sprunt, S. Elasticity, Viscosity, and Orientational Fluctuations of a Lyotropic Chromonic Nematic Liquid Crystal. *Soft Matter* **2014**, 10, 6571–6581.
42. Stark, H.; Ventzki, D. Stokes Drag of Spherical Particles in a Nematic Environment at Low Ericksen Numbers. *Phys. Rev. E* **2001**, 64, 031711.
43. Drescher, K.; Leptos, K. C.; Tuval, I.; Ishikawa, T.; Pedley, T. J.; Goldstein, R. E. Dancing *Volvox* : Hydrodynamic Bound States of Swimming Algae. *Phys. Rev. Lett.* **2009**, 102, 168101.
44. Petroff, A. P.; Wu, X.-L.; Libchaber, A. Fast-Moving Bacteria Self-Organize into Active Two-Dimensional Crystals of Rotating Cells. *Phys. Rev. Lett.* **2015**, 114, 158102.
45. Lowe, G.; Meister, M.; Berg, H. C. Rapid Rotation of Flagellar Bundles in Swimming Bacteria. *Nature* **1987**, *325*, 637–640.
46. Rowe, A. D.; Leake, M. C.; Morgan, H.; Berry, R. M. Rapid Rotation of Micron and Submicron Dielectric Particles Measured Using Optical Tweezers. *J. Mod. Opt.* **2003**, 50, 1539–1554.
47. Chattopadhyay, S.; Moldovan, R.; Yeungt, C.; Wu, X. L. Swimming Efficiency of Bacterium *Escherichia coli*. *Proc. Natl. Acad. Sci. U. S. A.* **2006**, 103, 13712–13717.
48. Fukuda, J.; Lev, B. I.; Yokoyama, H. Effect of Confining Walls on the Interaction between Particles in a Nematic Liquid Crystal. *J. Phys. Condens. Matter* **2003**, 15, 3841–3854.
49. Vilfan, M.; Osterman, N.; Čopič, M.; Ravnik, M.; Žumer, S.; Kotar, J.; Babič, D.; Poberaj, I. Confinement Effect on Interparticle Potential in Nematic Colloids. *Phys. Rev. Lett.* **2008**, 101, 237801.
50. Fukuda, J.; Žumer, S. Confinement Effect on the Interaction between Colloidal Particles in a Nematic Liquid Crystal: An Analytical Study. *Phys. Rev. E* **2009**, 79, 041703.
51. Kleman, M.; Lavrentovich, O. D. *Soft Matter Physics: An Introduction*; Lam, L., Guyon, E., Stanley, H., Langevin, D., Eds.; Partially Ordered Systems; Springer-Verlag New York: New York, NY, 2003.
52. Lauga, E.; DiLuzio, W. R.; Whitesides, G. M.; Stone, H. A. Swimming in Circles: Motion of Bacteria near Solid Boundaries. *Biophys. J.* **2006**, 90, 400–412.
53. Galajda, P.; Keymer, J.; Chaikin, P.; Austin, R. A Wall of Funnels Concentrates Swimming Bacteria. *J. Bacteriol.* **2007**, 189, 8704–8707.

54. Hulme, S. E.; DiLuzio, W. R.; Shevkoplyas, S. S.; Turner, L.; Mayer, M.; Berg, H. C.; Whitesides, G. M. Using Ratchets and Sorters to Fractionate Motile Cells of *Escherichia coli* by Length. *Lab Chip* **2008**, 8, 1888–1895.
55. Landau, L. D.; Lifshitz, E. M. *Theory of Elasticity*, 3rd ed.; Pergamon Press, 1986.
56. Zhou, S.; Cervenka, A. J.; Lavrentovich, O. D. Ionic-Content Dependence of Viscoelasticity of the Lyotropic Chromonic Liquid Crystal Sunset Yellow. *Phys. Rev. E* **2014**, 90, 042505.
57. Amir, A.; Babaeipour, F.; Mcintosh, D. B.; Nelson, D. R.; Jun, S. Bending Forces Plastically Deform Growing Bacterial Cell Walls. *Proc. Natl. Acad. Sci. U. S. A.* **2014**, 111, 5778–5783.
58. Koenig, S. H. Brownian Motion of an Ellipsoid. A Correction to Perrin's Results. *Biopolymers* **1975**, 14, 2421–2423.
59. Sbalzarini, I. F.; Koumoutsakos, P. Feature Point Tracking and Trajectory Analysis for Video Imaging in Cell Biology. *J. Struct. Biol.* **2005**, 151, 182–195.
60. Wang, S.; Arellano-Santoyo, H.; Combs, P. A.; Shaevitz, J. W. Actin-like Cytoskeleton Filaments Contribute to Cell Mechanics in Bacteria. *Proc. Natl. Acad. Sci. U. S. A.* **2010**, 107, 9182–9185.
61. Martin, J.-P.; Fleck, J.; Mock, M.; Ghuysen, J. The Wall Peptidoglycans of *Neisseria perflava*, *Moraxella glucidolytica*, *Pseudomonas alcaligenes* and *Proteus vulgaris* Strain P18. *Eur. J. Biochem.* **1973**, *38*, 301–306.
62. Ferrari, A. C.; Meyer, J. C.; Scardaci, V.; Casiraghi, C.; Lazzeri, M.; Mauri, F.; Piscanec, S.; Jiang, D.; Novoselov, K. S.; Roth, S.; Geim, A. K. Raman Spectrum of Graphene and Graphene Layers. *Phys. Rev. Lett.* **2006**, 97, 187401.

Chapter 7: Hierarchical Organization in Liquid Crystal-in-Liquid Crystal Emulsions*

7.1 Introduction

Over the past several decades, liquid crystals (LCs) confined within either direct or inverted emulsions have been widely explored as a new class of anisotropic soft matter.[1–7] In direct emulsions, the LCs are confined within micrometer-sized droplets dispersed within a continuous isotropic phase. The ordering of thermotropic LCs within droplets of direct emulsions has been shown to be influenced by the anisotropic elasticity of the LCs, the presence of topological defects, and interfacial interactions that can arise from hydrogen bonding, van der Waals forces, and electrical double layers.[1,4,7–9] More recently, lyotropic chromonic LCs (LCLCs), which form nematic or hexagonal columnar phases through face-to-face stacking of plank-like, polyaromatic molecules into columnar aggregates in aqueous solutions,[10,11] have also been characterized within emulsion droplets dispersed in immiscible isotropic oils.[12–15] These emulsions are, in some cases, distinguished from their thermotropic droplet-based counterparts by the formation of faceted LC droplets.[15] Alternatively, in the case of inverted LC emulsions, droplets of an isotropic phase (e.g., oil or aqueous solution) have been dispersed within a continuous LC phase.[3,5,16–19] In these studies, the elasticity and topological defects of LCs have been shown to generate interdroplet forces that drive the isotropic droplets into complex structures including linear chains and hexagonal arrays.[5,16,18,19] While initial studies largely focused on characterization of isotropic droplets in thermotropic LCs, recently it has been demonstrated that LCLC elasticity-mediated forces also induce self-assembly of micrometer-sized colloids[20] and living bacteria[21].

In this paper, we move beyond these past studies involving a single LC phase (dispersed or continuous) to investigate dispersions comprised of two immiscible LC phases. Specifically, we focus on droplets of nematic thermotropic LCs dispersed in an immiscible nematic LCLC (15 wt% disodium cromoglycate – DSCG) phase. Our investigation of these "LC-in-LC emulsions" was motivated by a number of fundamental questions, particularly the question of whether the ordering of the LCs in the two phases would be coupled through interactions mediated by, for example, anisometric droplet shapes, or alternatively interfacial interactions (surface anchoring). In addition, we sought to explore how nematic LC droplets would interact and self-assemble when dispersed within the LCLC.

7.2 Experimental Section

Materials. 4'-pentyl-4-cyanobiphenyl (5CB) was obtained from EM Sciences (New York, NY). N-(4-methoxybenzylidene)-4-butylaniline (MBBA), disodium cromoglycate (DSCG), glycerol, and phosphate-buffered saline (PBS) (0.01 M phosphate, 0.138 M NaCl, 0.0027 M KCl, pH 7.4) were purchased from Sigma-Aldrich (St. Louis, MO). Polyimide was obtained from HD Microsystems (Parlin, NJ). 1-methyl-2-pyrrolidinone, silicone oil, Fisher's Finest Premium Grade glass slides and cover glass were purchased from Fisher Scientific (Pittsburgh, PA). Deionization of a distilled water source was performed with a Milli-Q system (Millipore, Bedford, MA) to give water with a resistivity of 18.2 MΩ cm.

Lyotropic LC preparation. Lyotropic LCs containing DSCG were prepared by mixing 15 wt% of DSCG with 85 wt% of PBS. The mixture was shaken for at least 12h to ensure complete

solubility and homogeneity. Prior to the preparation of emulsions, the DSCG solution was heated at 65°C for 10 min as described elsewhere.[22,23] At this concentration, DSCG forms a nematic LC phase below ~32°C and an isotropic phase above ~40°C. Two-phase coexistence is observed within the range of intermediate temperatures.

Preparation of LC-in-LC emulsions. LC-in-LC emulsions were formed by sequential sonication and vortexing of mixtures of ~1 μL of 5CB (or MBBA) and ~100 μL of 15 wt% DSCG (in PBS). Five cycles consisting of 10s of vortexing followed by 10s of sonication in a bath held at 55°C were performed. Emulsions containing isotropic silicone oil droplets were prepared in the same manner. Emulsions were analyzed within 4h of their preparation.

Assembly of experimental imaging chambers. To create imaging chambers that induced a uniform azimuthal alignment of the nematic DSCG, we first rubbed a polyimide-coated glass slide and glass cover slip unidirectionally 30 times with a velvet cloth. A small volume (~4.5 μL) of LC-in-LC emulsion was then drawn between the two polyimide-coated glass substrates in a cavity created using two sheets of Mylar film (~60 μm in thickness). The two polyimide-coated glass substrates were oriented such that the rubbing directions of the two substrates were antiparallel. Following assembly, the chamber was immediately sealed with epoxy to prevent water evaporation. The imaging chamber was then heated into the isotropic phase of DSCG for 30s. Approximately 10 – 20 min after cooling the sample back to room temperature, the nematic DSCG film exhibited a planar orientation with largely uniform azimuthal alignment in the direction of rubbing of the polyimide-coated substrates.

Optical characterization of LC-in-LC emulsions. The configurations adopted by dispersed thermotropic LC droplets within continuous nematic lyotropic LCs were investigated using an Olympus IX71 inverted microscope (Center Valley, PA) equipped with a 100× oil-immersion objective and crossed polarizers. Bright field and polarized light micrographs of the LC-in-LC emulsions were collected with a Hamamatsu 1394 ORCAER CCD camera (Bridgewater, NJ) connected to a computer and controlled through SimplePCI imaging software (Compix, Inc., Cranberry Twp., NJ). Slow translational diffusion of LC droplets within the viscous nematic DSCG solution ($\mu \sim 0.7$ Pa·s)[21] enabled us to easily capture both bright field and crossed polars micrographs of individual droplets. Only droplets that were freely translating within the nematic DSCG and not adsorbed to one of the polyimide-coated glass substrates were imaged and analyzed, as contact with surfaces has been previously demonstrated to influence the configurations adopted by LC droplets.[24]

7.3 Results and Discussion

As detailed in the Experimental Section, we prepared emulsions comprised of droplets of nematic thermotropic LCs in continuous phases of aqueous nematic DSCG phase (15 wt%) by the sequential vortexing and sonication of mixtures of these two LCs. Subsequently, we confined a thin film (~60 μm in thickness) of the emulsion between rubbed polyimide surfaces that caused a planar orientation and uniform azimuthal alignment of the continuous nematic DSCG (Figure 7-S1). Our initial experiments were performed using 4'-pentyl-4-cyanobiphenyl (5CB) as the thermotropic LC (at room temperature). After emulsification, we optically characterized the orientations assumed by

both the continuous (DSCG) and dispersed (5CB) LCs within the thin films of the emulsions. The emulsions were polydisperse, and our observations below are made with reference to the size of the emulsion droplets within the dispersion.

In general, we observed that nematic 5CB droplets with diameters greater than ~6 μm exhibited bipolar configurations and thus planar anchoring at the interface of the droplet with the continuous nematic DSCG phase. Our observations of the optical textures of the 5CB droplets between crossed polars (Figures 7-1A through 7-1C) as well as the positions of the boojums of the droplets evident in bright field images (Figures 7-1D through 7-1F) confirmed the bipolar configuration. Both boojums of bipolar 5CB droplets were observed in some bright field images (Figure 7-S2). For droplets with diameters smaller than ~6 μm, we found it difficult to determine the configuration of the LC within the droplets due to the birefringence of the encompassing nematic DSCG (Figure 7-S3; see Supporting Information for details). All of the 5CB droplets characterized in our experiments (diameters ranging from 6 μm to 35 μm) exhibited very slow translational and rotational diffusion within the nematic DSCG. For example, we measured a 5CB droplet with diameter ~20 μm to move at less than 0.5 μm/min and to rotate at less than 1°/min in the absence of convective flows within the DSCG phase (Figure 7-S4). This observation is consistent with our theoretical estimates of the root mean square displacement and root mean square angular deviation of a 20 μm-diameter spherical particle within nematic 15 wt% DSCG (see Supporting Information).

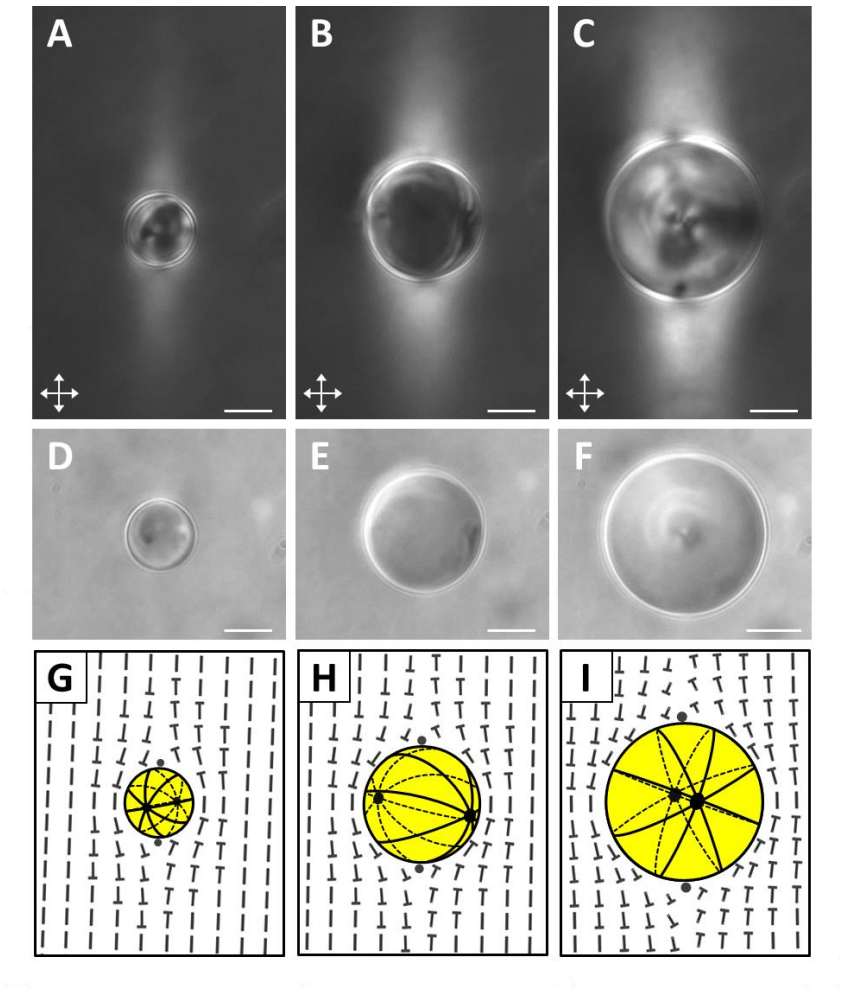

Figure 7-1. Orientations of nematic 5CB emulsion droplets in aligned nematic 15 wt% DSCG. (A-C) Crossed polars and (D-F) bright field micrographs of 5CB droplets with diameters of (A, D) 14.0 µm, (B, E) 24.4 µm, and (C, F) 33.2 µm. (G-I) Corresponding schematics illustrating the director profiles within the 5CB droplets as well as in the encompassing nematic DSCG. The handedness of the twist at the poles of all droplets is arbitrarily depicted to be the same (see text for details). Scale bars = 10 µm.

Within the continuous DSCG phase, distortion of the nematic director around the 5CB droplets generated brightly birefringent "tails" that extended away from the surface of the 5CB droplets parallel to the far-field DSCG director (Figures 7-1A through 7-1C). In addition, we observed four small bright lobes near the surface of the droplets when viewed between crossed polars. Nych *et al.* recently observed similar optical patterns around isotropic water droplets and

synthetic microparticles (planar anchoring) dispersed within nematic 15 wt% DSCG and demonstrated that they are a signature of a twisted DSCG director configuration near the boojum defects located at the poles of the colloids.[20] The twisted director profile is a consequence of the small twist elastic constant (K_2) of this chromonic LC,[20] as K_2 (~1 pN) is approximately an order of magnitude smaller than the elastic constants for splay (K_1) or bend (K_3) (~10 pN).[25] Our observations lead us to conclude that nematic DSCG also forms twisted director configurations around both nematic 5CB droplets (Figures 7-1G through 7-1I) and isotropic silicone oil droplets (Figure 7-S5). This result also leads us to conclude that nematic DSCG exhibits a planar orientation at the interfaces of the 5CB droplets. Similar to the observations of Nych *et al.*, we found (i) the brightness and the length of the birefringent tails in the DSCG to increase with increasing LC droplet size, and (ii) there to be no optical signature indicative of a twisted director configuration around droplets with diameters smaller than ~6 μm (Figure 7-S3).[20] Finally, we note that while our schematic illustrations in Figure 1 all arbitrarily depict the handedness of the twist deformations to be the same at the poles of each LC droplet, the actual twist directions were observed to vary.[20] While the absolute handedness of the twist influences interactions between pairs of 5CB droplets (see below), it does not significantly impact the conclusions that we draw in the remainder of this paper regarding isolated 5CB droplets.

Next, we characterized the orientations of the bipolar 5CB droplets with diameters between 6 and 35 μm within the nematic DSCG phase in order to determine if the droplets aligned in a preferred direction relative to the far-field DSCG director ($\mathbf{n}_{DSCG}$). By measuring the positions of the boojums of a droplet apparent in bright field micrographs (Figures 7-1D through 7-1F), we were able to determine the orientation of the axis of symmetry of the bipolar configuration, as depicted schematically in Figures 7-1G through 7-1I. Significantly, by

quantifying the angle (θ) formed between the symmetry axis of the bipolar 5CB droplets relative to $\mathbf{n}_{DSCG}$ (see Supporting Information for details), we found that the nematic 5CB droplets were oriented in directions that were largely orthogonal to $\mathbf{n}_{DSCG}$ ($\theta \sim 80–90°$) (Figure 7-2A). We note that the bipolar 5CB droplets, while maintaining that orthogonal orientation, were observed to slowly rotate about an axis defined by the far-field orientation of the DSCG phase in our experiments (See arrow in Figure 7-2A; Figure 7-S4).

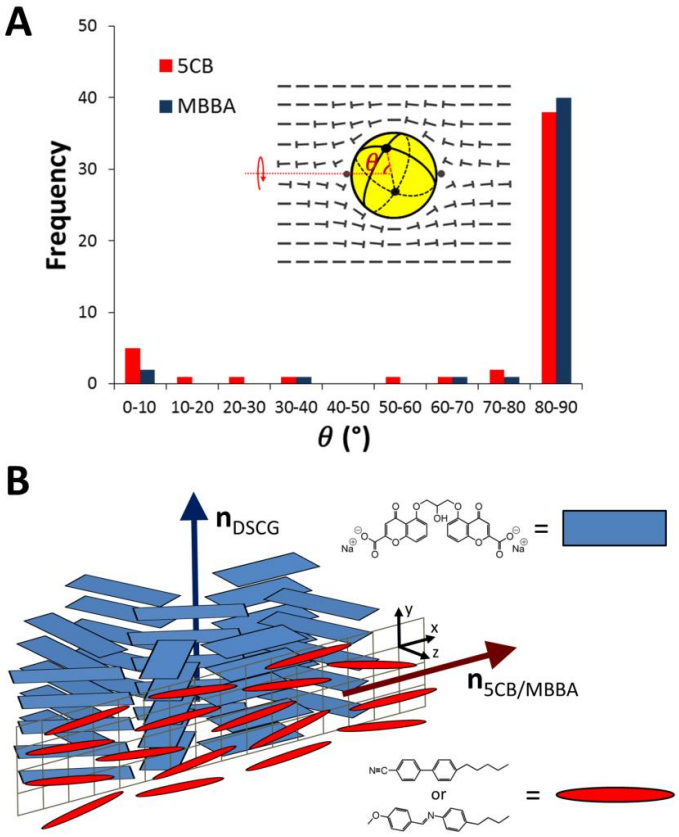

Figure 7-2. Bipolar nematic 5CB droplets align orthogonal to the far-field director of an encompassing nematic DSCG phase.

(A) Quantification of the angle formed between the symmetry axis of bipolar 5CB (N = 50) and MBBA (N = 45) droplets relative to the far-field director of nematic DSCG. (B) Schematic illustrating the preferred orthogonal orientations of the local directors at the interface of the nematic thermotropic LCs and nematic DSCG.

We explored several hypotheses regarding the possible origin of this preferential relative orientation of the bipolar 5CB droplets and nematic DSCG phase. First, we considered the possibility that a slight elongation in the shape of the 5CB droplets might impact their orientation in the nematic DSCG. Elongation of the LC droplets is predicted when the elastic energy within the 5CB droplet and encompassing nematic DSCG (both which scale as $\sim KR$) is similar to or greater in magnitude than the interfacial energy of the droplets (which scales as $\sim \gamma R^2$). For 5CB droplets of R ~ 10 μm, with K ~ 10^{-11} N for DSCG[25] and 5CB[26] and γ of 10^{-3} – 10^{-2} N/m (measured for interfaces between 5CB and either pure water[27] or an aqueous polymer solution[28] (see Supporting Information)), however, the surface energy ($\sim 10^{-13}$ J) is much greater than the bulk elastic energies ($\sim 10^{-16}$ J). Consistent with this prediction, we did not find the 5CB droplets observed in our experiments to measurably depart from a spherical shape. Finally, we note also that ellipsoidal droplets (5CB tactoids) with planar anchoring would be predicted to align with their major axis parallel to the far-field DSCG director in order to minimize the elastic energy of the DSCG.[12] Because our measurements show that the preferred orientation of the symmetry axis of the bipolar 5CB droplets is orthogonal rather than parallel to $\mathbf{n}_{DSCG}$ (see Figure 7-2), we conclude that the orientations of the nematic 5CB droplets and DSCG are not coupled through the elasticity of the nematic DSCG and the anisometric shape of the 5CB droplets.

Second, we considered the possibility that the coupling between the nematic directors of the 5CB and 15 wt% DSCG phases arises from the presence of interfacial electric fields associated with electrical double layers.[29,30] Here we note that electric fields within double layers can generate torques on LCs due to the anisotropic dielectric properties ($\Delta\varepsilon$) of the LC phases.[31,32] In particular, past studies have demonstrated that, due to the positive $\Delta\varepsilon$ of 5CB ($\Delta\varepsilon = +13$)[26], formation of an electrical double layer at an interface of 5CB can cause the

anchoring of 5CB to change from planar to homeotropic.[31,32] We tested the possible role of electrical double layers in the observed coupling of the orientations of the 5CB droplets and DSCG by creating dispersions of nematic N-(4-methoxybenzylidene)-4-butylaniline (MBBA) droplets within nematic DSCG. Since MBBA possesses a negative $\Delta\varepsilon$ ($\Delta\varepsilon = -0.7$)[26], if interfacial electric fields played a key role in the coupling of the orientation of thermotropic LC droplets to the nematic DSCG phase, we would expect the orientation of the MBBA droplets to differ from 5CB droplets. Our measurements of the orientations adopted by bipolar MBBA droplets within aligned DSCG phases (Figure 7-S6), however, revealed that the MBBA droplets also oriented with the axis of symmetry of the bipolar configuration orthogonal to $\mathbf{n}_{DSCG}$ (Figure 7-2A). The result of this experiment leads us to conclude that interfacial ionic phenomena (and the electric fields associated with interfacial adsorption of ions) do not play a dominant role in coupling the orientations of bipolar thermotropic LC droplets and continuous nematic phases of DSCG.

Third, we hypothesized that van der Waals interactions (which arise from anisotropic polarizabilities or refractive indices) between 5CB and nematic DSCG phases may couple their orientations. Past studies have established that van der Waals forces play a central role in determining the orientations adopted by LCs near interfaces, including 5CB near alignment layers such as rubbed polymer films[33,34] and self-assembled alkanethiol monolayers.[35,36] In addition, theoretical studies suggest that anisotropic van der Waals interactions can act over long distances, for example causing the orientation of LCs to be influenced by an anisotropic substrate even when separated from the substrate by a thin (1 – 100 nm) isotropic film.[37–39] In our experiments, on the basis of observations of the LC droplets through crossed polars, we concluded above that both nematic 5CB and DSCG are oriented tangential (or close to

tangential) to the nematic-nematic interface. However, since individual DSCG molecules stack face-to-face into columnar aggregates to form the nematic phase, the polyaromatic cores of the molecules are on average orthogonal to $\mathbf{n}_{DSCG}$ and nematic DSCG exhibits negative optical birefringence ($\Delta n = -0.02$).[10,11,40] Thus, as illustrated in the schematic in Figure 7-2B, although the local director of the DSCG phase ($\mathbf{n}_{DSCG}$) is oriented in a direction tangential to the 5CB/DSCG interface (along the y axis in Figure 7-2B), the orientations of the optical axis with the highest refractive index lie within the plane normal to $\mathbf{n}_{DSCG}$. In contrast, the optical birefringence of nematic 5CB is positive ($\Delta n = +0.18$)[26] and the optical axis with the highest refractive index is tangential to the 5CB/DSCG interface, coinciding with the local director $\mathbf{n}_{5CB}$. Consequently, when $\mathbf{n}_{5CB}$ adopts an in-plane orientation orthogonal to $\mathbf{n}_{DSCG}$ (i.e. $\mathbf{n}_{5CB}$ oriented along the x axis in Figure 7-2B), the optical axes of the two phases with the highest refractive indices are aligned, a mutual orientation that generates the strongest van der Waals coupling between the phases.

At the interface of a LC droplet in a LC-in-LC emulsion, the mutual orientations of the two directors of the LC phases will vary with position across the droplet interface. However, when the symmetry axis of a bipolar 5CB droplet is orthogonal to the far-field director of the nematic DSCG phase, over a significant fraction of the droplet interface, the local directors of the nematic 5CB and DSCG phases are orthogonal (or nearly orthogonal) to one another. In contrast, when the symmetry axis of a bipolar LC droplet is aligned parallel to the far-field director of the DSCG phase, the directors of the two LC phases are largely parallel at the droplet interface. Our observation that the symmetry axis of both bipolar 5CB and MBBA ($\Delta n = +0.21$)[26] droplets aligns orthogonal to the far-field director of nematic DSCG is thus consistent with the hypothesis that the orientations of the nematic thermotropic and lyotropic LCs are

coupled to one another through anisotropic van der Waals interactions in our experiments. We comment also that the twisted DSCG director field[20] around a 5CB droplet will also influence the relative orientations of the nematic phases at the droplet interface and thus the strength of coupling of the two LC phases.

To obtain an estimate of the strength of the orientational coupling between the 5CB droplets and nematic DSCG continuum, we applied a magnetic field parallel to the orientation of the far-field director of the DSCG phase (Figures 7-3A through 7-3C). We found that a magnetic field strength of ~0.3 T was sufficient to rotate the axis of the bipolar 5CB droplets towards the direction of the applied magnetic field (Figures 7-3D through 7-3F), a result that is consistent with the positive diamagnetic anisotropy of 5CB ($\Delta\chi = +1.7 \times 10^{-7}$ (cgs))[26]. Upon removal of the magnetic field, we observed the 5CB droplets to relax back towards their initial orientation over the course of minutes (Figures 7-3D through 7-3P; see Figure 7-S7 for additional examples). We did not observe the nematic DSCG to realign during the application of the magnetic field in our experiments (a result consistent with a small magnitude of the diamagnetic anisotropy of DSCG), nor did we observe 5CB droplets dispersed in an isotropic phase to relax to a preferred orientation following removal of an applied magnetic field (Figure 7-S8; see Supporting Information for details). The driving force for the relaxation of the orientation of the 5CB droplet following the removal of the magnetic field in the experiment described above, according to our hypothesis, is a torque due to anisotropic dispersion forces (Γ_{vdw}) acting across the 5CB-DSCG interface. During the relaxation process, Γ_{vdw} is balanced by a torque that arises from rotational drag on the 5CB droplet of radius R, which can be evaluated as $\Gamma_{drag} = 8\pi\eta R^3\omega$, where ω is the rotational velocity of the droplet. We estimate $\omega \sim 0.36°/s$ (0.006 rad/s) from the slope of the approximately linear portion of the plot in Figure 7-3P (between 0 and 60s) as the

droplet relaxes from $\theta_1 \sim 52°$ to $\theta_2 \sim 74°$. Using $\eta \sim 0.7$ Pa·s for the viscosity of the nematic DSCG phase[21], we calculate $\Gamma_{drag} \sim 2 \times 10^{-16}$ J/rad for the droplet in Figure 7-3 (the diameter of the droplet was ~24 μm). The energy dissipated during the rotation of the droplet is estimated as $E_{rotation} = \Gamma_{drag}(\theta_2 - \theta_1)$, which we calculate to be $\sim 8 \times 10^{-17}$ J ($\sim 2 \times 10^4$ kT). We conclude, therefore, that the orientations of the nematic 5CB droplets and DSCG are coupled through an energy of $\sim 8 \times 10^{-17}$ J.

To determine whether the above-described estimate of the energy that couples the orientations of the 5CB and DSCG phases is consistent with the presence of anisotropic van der Waals interactions, we performed a simple theoretical estimate of the orientation-dependent van der Waals interaction between two semi-infinite planar slabs of uniformly aligned nematic 5CB and nematic DSCG using the expression[41]:

$$E_{aniso} = \frac{-kT}{64\pi d^2}\gamma_{5CB}\gamma_{DSCG}\cos^2\theta. \qquad (7\text{-}1)$$

In this expression, γ_i is evaluated as $\gamma_i = \frac{\sqrt{\varepsilon_\perp^i \varepsilon_\parallel^i}(\varepsilon_\perp^i - \varepsilon_\parallel^i)}{2\varepsilon_\parallel^i\left(\sqrt{\varepsilon_\perp^i \varepsilon_\parallel^i} + \varepsilon_m\right)}$, where $\varepsilon_\parallel^i$ and $\varepsilon_\perp^i$ are the dielectric response functions parallel and perpendicular to each LC director, respectively, and ε_m is the dielectric response of an isotropic medium that separates the two LC slabs at a distance d. When the relative orientations of the nematic directors of 5CB and DSCG (with surface area equal to the interfacial area of the droplet in the experiment described above) changes from $\theta \sim 52°$ to $\theta \sim 74°$, we estimate that the free energy of the system is lowered by $\sim 1 \times 10^{-16}$ J (see Supporting Information for details). Although this value is obtained using a geometry that is simplified relative to our experiment, its close agreement to the estimate obtained from our experiment ($\sim 8 \times 10^{-17}$ J) provides support for our hypothesis that a torque due to anisotropic dispersion forces couples the orientations of the 5CB and DSCG phases.

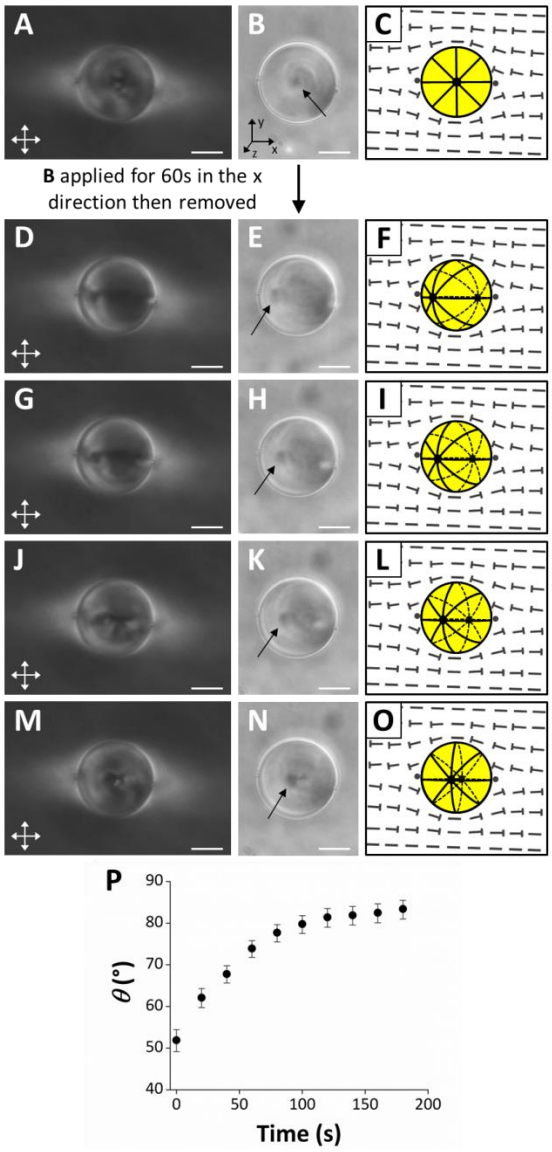

Figure 7-3. Rotation of 5CB droplets following application and removal of a magnetic field.

(A, D, G, J, M) Crossed polars, (B, E, H, K, N) bright field (with arrows indicating the locations of boojums), and (C, F, I, L, O) schematic illustrations of a bipolar 5CB droplet in an aligned region of nematic DSCG. (A-C) Initial configuration of the droplet. (D-O) Configuration of the droplet after application of a magnetic field (B ~ 0.3 T) in the x direction (see coordinate system in B) and removal at t = 0s. (D-F) Configuration of droplet at t = 0s, (G-I) t = 20s, (J-L) t = 40s, and (M-O) t = 120s. (P) Plot of the angle formed between the symmetry axis of the 5CB droplet depicted in (D-O) relative to the far-field director of nematic DSCG ($\boldsymbol{\theta}$) as a function of time following removal of the applied magnetic field. Error bars represent uncertainty in the calculation of $\boldsymbol{\theta}$ associated with estimating the positions of the 5CB droplet center and one of the boojums of the droplet. Scale bars = 10 μm.

We note that the magnitude of the energy arising from anisotropic van der Waals interactions that couples the orientations of the nematic 5CB and nematic DSCG phases is large compared to kT and thus it leads us to predict that 5CB droplets, if at equilibrium, should not be observed to deviate from an orientation that is orthogonal to $\mathbf{n}_{DSCG}$. We speculate that our experimental observation of several 5CB and MBBA droplets oriented at $\theta < 80°$ (Figure 7-2A) may be the result of (i) the slow relaxation of droplets to an equilibrium orientation (Figure 7-3P), (ii) proximity of other droplets altering the near-field alignment of DSCG, or (iii) interactions between the droplets and the polyimide alignment layer.

We also performed experiments using an applied external field to demonstrate that it was possible to use the field to select a unique droplet orientation from the family of degenerate orientations defined by rotation of the symmetry axis of the bipolar 5CB droplet about the axis defined by $\mathbf{n}_{DSCG}$ in the nematic DSCG (Figure 7-4). By applying a magnetic field in a direction orthogonal to both $\mathbf{n}_{DSCG}$ and the initial axis of symmetry of a 5CB droplet (Figures 7-4A through 7-4C), we found that we could orient the symmetry axis of the bipolar 5CB droplet parallel to the direction of the applied field. Due to slow rotational diffusion in DSCG ($< 1°$/min, see above), the droplet retained this orientation for the duration of our observations (5 min) following removal of the field (Figures 7-4D through 7-4I). By repeating this sequence but with the magnetic field rotated to the initial orientation of the LC droplet, the droplet returned to its initial orientation (Figures 7-4J through 7-4O). In this manner, we were able to rotate bipolar 5CB droplets between energetically degenerate orientations orthogonal to $\mathbf{n}_{DSCG}$. These results demonstrate the

ability to direct the orientations of 5CB droplets in aligned nematic DSCG through the transient application of an external field.

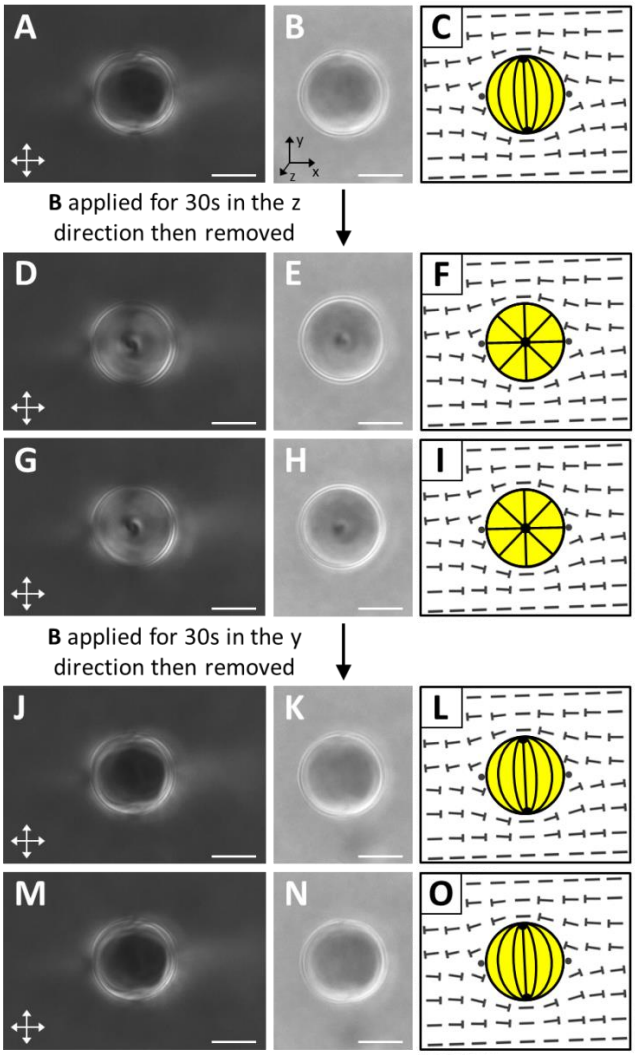

Figure 7-4. Selection of unique orientations of a 5CB droplet dispersed in nematic DSCG using a transient magnetic field.

(A, D, G, J, M) Crossed polars, (B, E, H, K, N) bright field, and (C, F, I, L, O) schematic illustrations of a 5CB droplet in an aligned region of nematic DSCG. (A-C) Initial configuration of the droplet. (D-I) Configuration of the droplet after the application and removal of a magnetic field (**B** ~ 0.3 T) in the z direction (see coordinate system in B). (D-F) Configuration of the droplet 30s and (G-I) 300s after the field was removed. (J-O) Configuration of the droplet after the application and removal of a magnetic field (**B** ~ 0.3 T) in the y direction. (J-L) Configuration of the droplet 30s and (M-O) 300s after the field was removed. Scale bars = 10 μm.

We end our paper by making some observations regarding interactions between the 5CB droplets that are mediated by the DSCG phase. Similar to the inverted LC emulsions studied previously (i.e., isotropic water droplets dispersed in nematic 5CB[3,16,17]), we observed pairs of nematic 5CB droplets dispersed in nematic DSCG to exhibit attractive interactions. In particular, we found that droplets adhered upon approaching one another (Figure 7-5), consistent with the effects of the elasticity of the nematic DSCG phase on inter-droplet interactions.[3,16,17,20] We occasionally observed adhered nematic droplets to coalesce (Figure 7-S9), but more often we found that droplets remained adhered to one another for long times. Although the elasticity of nematic droplets has been reported to create a barrier that inhibits coalescence of nematic droplets in an isotropic continuous phase,[42] we also found that isotropic silicone oil droplets dispersed in DSCG adhered to one another without coalescing (Figure 7-S10). This leads us to conclude that the barrier to coalescence arises from either elastic forces mediated by the DSCG or potentially other colloidal forces such as electrical double layer forces arising from charging of the interface of the 5CB in the DSCG.[32]

We found that the alignment of pairs of 5CB droplets relative to the far field director of the DSCG phase depended upon the diameters (d_1 and d_2) of the two interacting 5CB droplets. When the difference in size was large ($d_1 > 3d_2$), we found that the droplets aligned parallel to $\mathbf{n}_{DSCG,}$ with the smaller droplet positioned at the site of one of the boojums in the nematic DSCG near the large droplet. We observed this arrangement when the smaller droplet ($d_2 < 3$ μm) did not noticeably deform the DSCG (Figure 7-5A) and when it was large enough ($d_2 > 6$ μm) to induce observable twist in the DSCG (Figures 7-5B and 7-S11). However, when $d_1 < 3d_2$, we found the 5CB droplets instead to align at a small angle from $\mathbf{n}_{DSCG}$, with the angle approaching a maximum value of ~30° for the case of $d_1 \sim d_2$ (Figure 7-5C), consistent with recent

observations of isotropic droplets in nematic DSCG[20] as well as spherical colloids that induced strain with a quadrupolar symmetry in LCs[16]. We note that whenever both d_1 and d_2 were $>$ 6 µm, attraction between the droplets only occurred when the chirality of the twisted distortions in adjacent "tails" was the same, while repulsion was observed in cases when the chirality was opposite.[20]

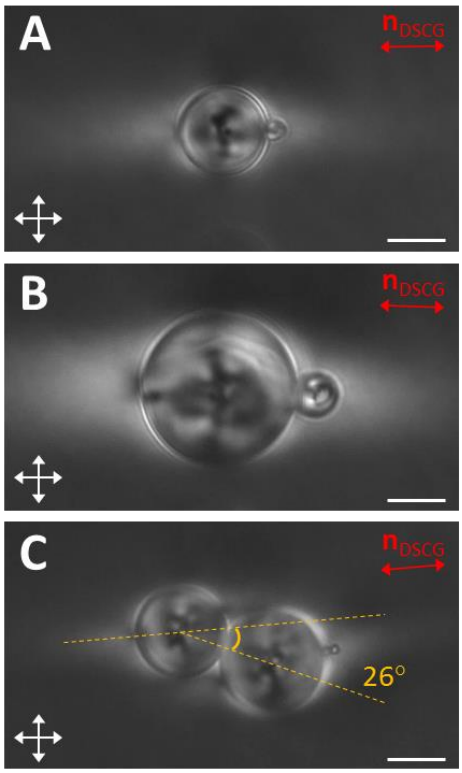

Figure 7-5. Organization of pairs of 5CB droplets in nematic DSCG.
Micrographs of adhered 5CB droplets (crossed polars) (A) with diameters of 15.3 µm and 3.7 µm, (B) 26.9 µm and 7.9 µm, and (C) 18.5 µm and 16.0 µm within aligned regions of nematic DSCG. The far-field orientation of the nematic DSCG is indicated by a double headed red arrow. Scale bars = 10 µm.

7.4 Conclusions

In conclusion, this paper reports the formation and characterization of hierarchical ordering present in LC-in-LC emulsions, specifically with nematic thermotropic LC droplets

dispersed within a nematic LCLC. Most interestingly, we demonstrate that the orientations of the LCs in the dispersed and continuous phases are coupled, and report a series of experiments that support our hypothesis that the coupling reflects anisotropic van der Waals interactions (and not, for example, anisometric LC droplet shapes). This coupling of the local directors of the LC phases leads to a hierarchy of organization in the system. For example, the coupling induces the symmetry axis of micrometer-sized bipolar nematic thermotropic LC droplets to align orthogonal to the far-field director of the nematic LCLC phase, which itself is aligned by the rubbed polyimide substrates in our experiments. In addition, we show that the LCLC phase can mediate interactions that lead to clustering of the aligned, thermotropic LC droplets. By analyzing the dynamics of the response of the orientations of the LC droplets to an applied magnetic field, we conclude that the orientations of the 5CB and DSCG phases are coupled through interaction energies of order $\sim 10^4$ kT for 5CB droplets with R $\sim$ 10 μm. These results and others reported in this paper involving assemblies of multiple droplets suggest that the hierarchical organization of LC-in-LC emulsions and their responsiveness to weak external perturbations (e.g., magnetic fields) makes them fertile territory for fundamental soft matter research as well as technologically promising (e.g., for the creation of novel photonic devices that can be driven by weak fields). We envision that these studies could be extended to include investigations of the coupling of LC orientations within LC-in-LC emulsions in which the dispersed LC phase is confined within droplets having higher geometrical complexity, such as handlebody-shaped thermotropic LC droplets of non-zero genus (e.g., toroids) within a nematic LCLC[43–45] or faceted columnar phase LCLC droplets[15] dispersed in a thermotropic LC. The results also suggest that interfaces defined by thermotropic LC materials may offer the basis of a general and facile approach to control of the surface anchoring of chromonic LC phases.

Acknowledgements

This work was supported by the National Science Foundation (under awards DMR-1121288 (MRSEC) and CBET-1263970), the National Institutes of Health (CA108467 and AI092004), and the Army Research Office (W911-NF-11-1-0251 and W911-NF-14-1-0140). The authors would like to thank Daniel S. Miller and Xiaoguang Wang for helpful discussions.

7.5 Supporting Information

Configurations of small 5CB droplets (diameters less than ~6 μm) dispersed in nematic DSCG

The internal configurations of 5CB droplets with diameters smaller than ~6 μm are difficult to determine when dispersed within the DSCG films (~60 μm in thickness) because the optical retardance of the DSCG ($\Delta n = -0.02$) film is comparable to or exceeds the optical retardance of the 5CB ($\Delta n = +0.18$) droplets with diameters less than ~6 μm. That is, the birefringence of the encompassing DSCG phase obscures the optical appearance of the small 5CB droplets (Figure 7-S3). We also note that nematic DSCG does not appear to adopt a twisted configuration around 5CB droplets less than ~6 μm in diameter (in agreement with the observations of Nych *et al.* of the alignment of nematic DSCG around isotropic droplets of this size[20]).

Theoretical estimates of root mean square displacement and angular deviation

We estimated diffusion coefficients for translational ($D_t = \frac{k_B T}{6\pi\eta R} \sim 0.002$ μm^2/min) and rotational ($D_r = \frac{k_B T}{8\pi\eta R^3} \sim 0.05$ deg^2/min)[46] motion of a spherical particle with R = 10 μm within nematic 15 wt% DSCG. In making these estimates, we note that we have neglected the anisotropy of the viscosity of the DSCG phase, and approximated it as an isotropic medium with an effective viscosity ($\eta \sim 0.7$ Pa s)[21]. Using these diffusion coefficients, we arrived at theoretical estimates for the root mean square displacement in two dimensions ($\sqrt{\langle x^2 \rangle} = \sqrt{4D_t t} \sim 0.1$ μm) and the root mean square angular deviation about a single axis ($\sqrt{\langle \phi^2 \rangle} = \sqrt{2D_r t} \sim 0.3°$) expected over one minute. These values are consistent with our experimental

measurements that a 5CB droplet with radius R $\sim$ 10 μm translated at $<$ 0.5 μm/min and rotated at $<$ 1°/min in the absence of convective flows within the nematic DSCG phase (Figure 7-S4).

Experimental measurement of θ

To determine the angle formed between the symmetry axis of 5CB/MBBA droplets in bipolar configurations and the far-field nematic DSCG director (θ), we imaged the bipolar droplets (in crossed polar and bright field modes) with the focal plane adjusted to the midplane of the droplet. ImageJ software was used to determine the radius of the droplet, the position of the center of the droplet, as well as the position of the projection of one of the boojums of the bipolar droplet on the droplet's midplane in the bright field micrograph. Using trigonometry, the locations of the boojums of the 5CB/MBBA droplet were determined from this information. The orientation of the far-field director of the nematic DSCG phase was determined using the images obtained through crossed polars and used to determine the locations of the boojums in the DSCG phase at the surface of the droplets. Through knowledge of the positions of both the DSCG and 5CB/MBBA boojums, trigonometric relations could be employed to calculate θ.

Estimation of interfacial tension between 5CB and nematic DSCG phases

Our estimate of the interfacial tension between 5CB and the aqueous DSCG phase is based on prior measurements of water-5CB interfacial tensions. We believe this estimate is reasonable because DSCG is not amphiphilic. Specifically, at room temperature, an interfacial tension of 2.6×10^{-2} N/m was measured between 5CB and pure water[27] and an interfacial tension of 6×10^{-3} N/m was reported between 5CB and an aqueous solution containing 30 wt% $CaCl_2$ and 1 wt% polyvinyl alcohol[28]. By approximating the interfacial energy of a 5CB droplet

in nematic DSCG (which scales as $\sim\gamma R^2$) as $\gamma \sim 10^{-3}$ N/m, and for 5CB droplets of R ~ 10 μm, we estimate the interfacial energy ($\sim 10^{-13}$ J) to be much larger than the bulk elastic energies ($\sim 10^{-16}$ J). We note that if we instead used $\gamma \sim 10^{-2}$ N/m in our scaling argument, it would only serve to strengthen our conclusion that the interfacial energy of droplets of R ~ 10 μm exceeds the bulk elastic energies.

Experimental test to determine if interactions with the polyimide alignment layer influence droplet relaxation

To determine if interactions involving the rubbed polyimide alignment layer contributed to the observed relaxation of the droplet orientations in our experiment, we applied a magnetic field parallel to the direction of rubbing to a dispersion of 5CB droplets in isotropic 98 wt% glycerol, which has a viscosity similar to nematic DSCG. The 5CB droplets were observed to reorient in the magnetic field, however, we did not observe the droplets to relax to an orientation orthogonal to the direction of rubbing (as was observed when the continuous phase was nematic DSCG (Figure 7-3)) when the magnetic field was removed (Figure 7-S8).

Theoretical estimation of E_{aniso}

We calculated the orientation-dependent van der Waal's interaction between two semi-infinite planar slabs of uniformly aligned nematic 5CB and nematic DSCG. When the directors of both LCs are oriented parallel to the interface and at an angle θ relative to one another, and when the planar LC slabs are separated from one another at a distance d across an isotropic medium, the anisotropic part of the van der Waal's interaction can be evaluated as: $E_{aniso} =$

$\frac{-kT}{64\pi d^2}\gamma_{5CB}\gamma_{DSCG}\cos^2\theta$.[41] In this expression, $\gamma_i = \frac{\sqrt{\varepsilon_\perp^i \varepsilon_\parallel^i}(\varepsilon_\perp^i - \varepsilon_\parallel^i)}{2\varepsilon_\parallel^i\left(\sqrt{\varepsilon_\perp^i \varepsilon_\parallel^i} + \varepsilon_m\right)}$, where $\varepsilon_\parallel^i$ and $\varepsilon_\perp^i$ are the dielectric response functions parallel and perpendicular to the LC director, respectively, which are related to the refractive indices of the LCs by $\varepsilon_\parallel \sim n_\parallel^2$ and $\varepsilon_\perp \sim n_\perp^2$. The dielectric response of the isotropic medium, ε_m, is also related to the refractive index of the medium by $\varepsilon_m \sim n_m^2$. Employing $n_\parallel = 1.71$ and $n_\perp = 1.53$ for 5CB[26] and $n_\parallel = 1.35$ and $n_\perp = 1.37$ for DSCG (private communication from O. Lavrentovich), we calculate $E_{aniso} \sim 2 \times 10^{-7} \cos^2\theta$ J/m^2 for nematic 5CB and DSCG slabs separated by a thin layer (d = 0.2 nm) of water ($n_m = 1.33$). We note that we chose d = 0.2 nm in our calculation. However, the conclusions arising from our calculation are not changed by using other values of d (e.g., d = 0.5 nm). If the two slabs each have a surface area equal to the interfacial area of the droplet in Figure 7-3 (the diameter of the droplet was ~ 24 μm), this estimate of E_{aniso} leads to the prediction that a change in the relative orientation of the nematic directors of 5CB and DSCG from $\theta \sim 52°$ to $\theta \sim 74°$ results in a lowering of the free energy of the system by $\sim 1 \times 10^{-16}$ J. This value is in close agreement with the value obtained ($\sim 8 \times 10^{-17}$ J) via analysis of the dynamics of relaxation of the orientations of a 5CB droplet following removal of an applied magnetic field (Figure 7-3).

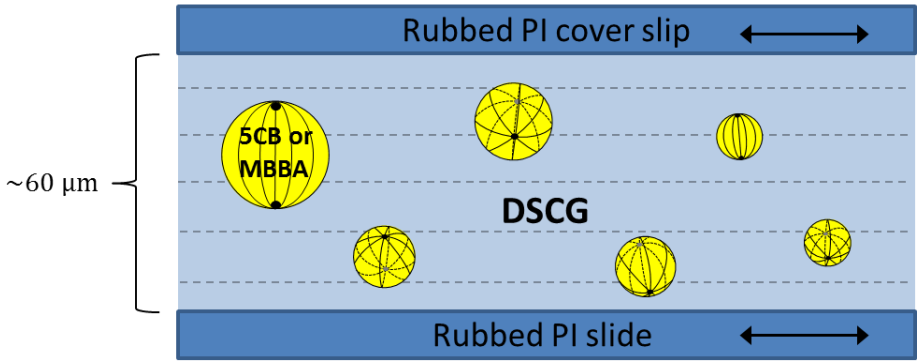

Figure 7-S1. Experimental setup.

Schematic illustration of the imaging chamber used to characterize LC-in-LC emulsions. The double headed arrows indicate the direction of rubbing of the polyimide (PI) substrates.

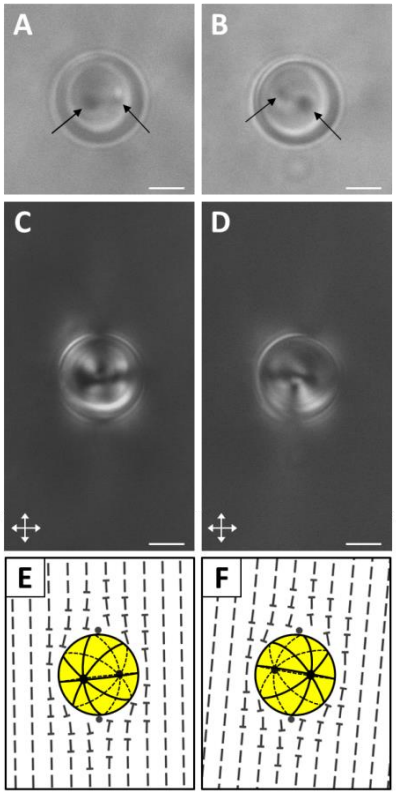

Figure 7-S2. Additional examples of bipolar 5CB droplets dispersed in nematic 15 wt% DSCG.

Optical micrographs (A, B, bright field) and (C, D, crossed polars) of 5CB droplets with diameters of (A, C) 12.4 µm and (B, D) 12.0 µm. Both boojums (indicated by arrows) of the bipolar droplet configurations can be observed in (A) and (B). (E, F) Corresponding schematic illustrations of the director profiles within the 5CB droplets as well as in the encompassing nematic DSCG. Scale bars = 5 µm.

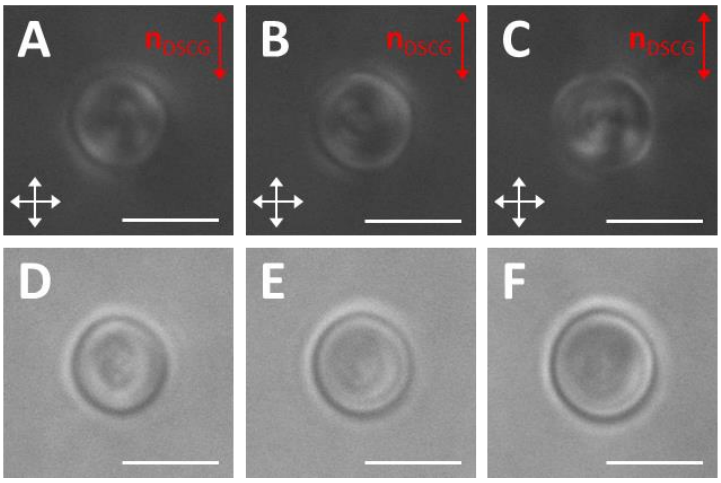

Figure 7-S3. Small (diameter < 6 µm) 5CB droplets dispersed in nematic 15 wt% DSCG.
Optical micrographs (A-C, crossed polars) and (D-F, bright field) of 5CB droplets with diameters of (A, D) 4.9 µm, (B, E) 5.1 µm, and (C, F) 5.4 µm dispersed within aligned regions of nematic DSCG. The far-field orientation of the DSCG is indicated in (A-C). Scale bars = 5 µm.

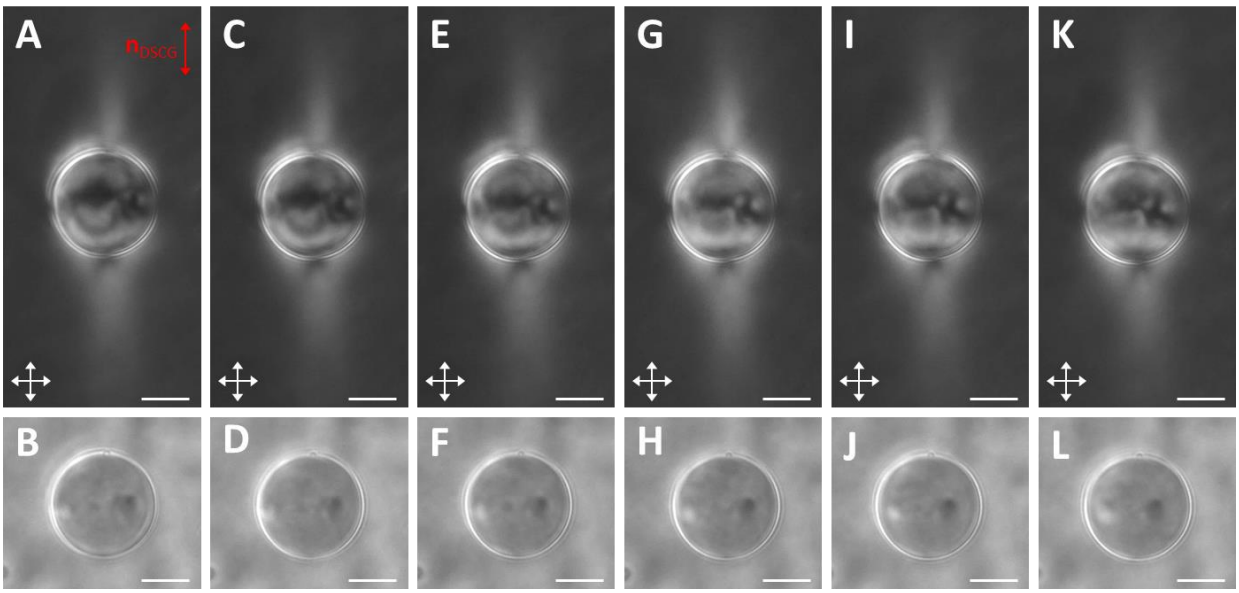

Figure 7-S4. Rotational diffusion of a 5CB droplet in nematic 15 wt% DSCG.
Optical micrographs (A, C, E, G, I, K, crossed polars; B, D, F, H, J, L, bright field) of a 21.7 µm diameter nematic 5CB droplet suspended in nematic 15 wt% DSCG. Images acquired after (A, B) 0 min, (C, D) 3 min, (E, F) 6 min, (G, H) 9 min, (I, J) 12 min, and (K, L) 15 min. The far-field orientation of the DSCG is indicated in (A). Scale bars = 10 µm.

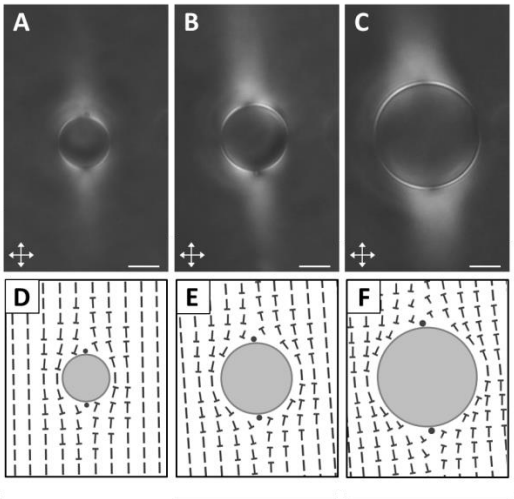

Figure 7-S5. Orientation of nematic 15 wt% DSCG near silicone oil droplets.
(A-C) Optical micrographs (crossed polars) of silicone oil droplets with diameters of (A) 15.9 µm, (B) 21.3 µm, and (C) 33.5 µm. (D-F) Corresponding schematic illustrations of the director profiles in the nematic DSCG. Scale bars = 10 µm.

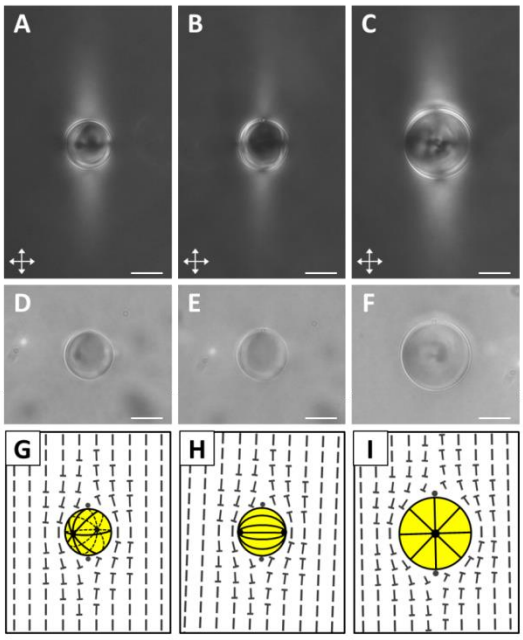

Figure 7-S6. Orientations of nematic MBBA emulsion droplets in nematic 15 wt% DSCG films.
(A-F) Optical micrographs (A-C, crossed polars) and (D-F, bright field) of MBBA droplets with diameters of (A, D) 14.9 µm, (B, E) 15.6 µm, and (C, F) 21.2 µm. (G-I) Corresponding schematic illustrations of the director profiles within the MBBA droplets as well as in the encompassing nematic DSCG. Scale bars = 10 µm.

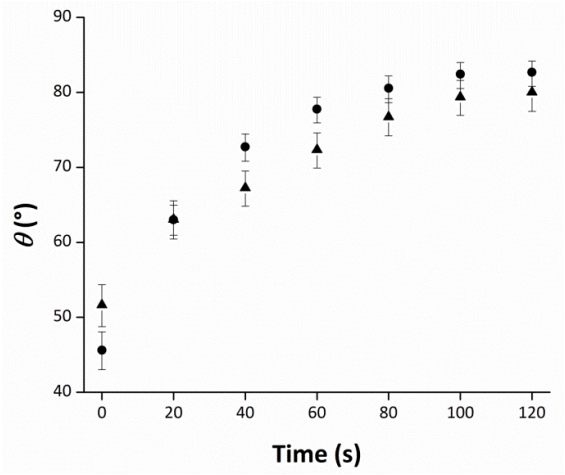

Figure 7-S7. Additional examples of the rotation of bipolar 5CB droplets following application and removal of a magnetic field.

Plot of the angle formed between the axis of symmetry of bipolar 5CB droplets (with diameters of 27.3 μm (●) and 23.6 μm (▲)) and to the far-field director of nematic DSCG (***θ***) as a function of time following removal of a magnetic field (**B** ~ 0.3 T) applied parallel to n_{DSCG} for 60s. Error bars represent uncertainty in the calculation of ***θ*** associated with estimating the positions of the 5CB droplet center and one of the boojums of the droplet.

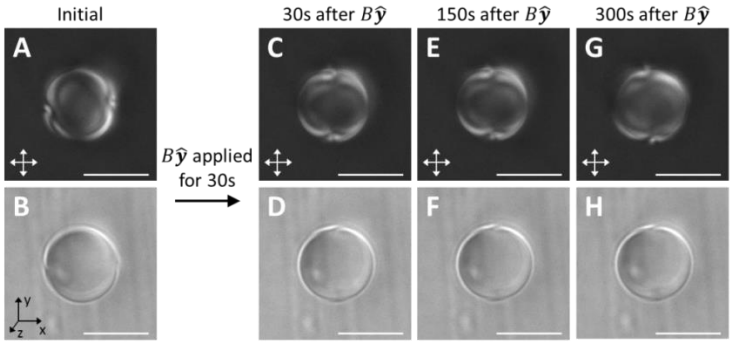

Figure 7-S8. Dynamics of a bipolar 5CB droplet in an isotropic 98 wt% glycerol solution following application and removal of a magnetic field.

Optical micrographs (crossed polars (A, C, E and G) and bright field (B, D, F and H)) of a nematic 5CB droplet dispersed within an isotropic 98 wt% glycerol solution between polyimide substrates both (A, B) before and (C-H) after application of a magnetic field (**B** ~ 0.3 T). The magnetic field was applied in the $\hat{\boldsymbol{y}}$ direction (see coordinate system in (B)), parallel to the direction of rubbing of the polyimide substrate. The 5CB droplet is 11.2 μm in diameter. Scale bars = 10 μm.

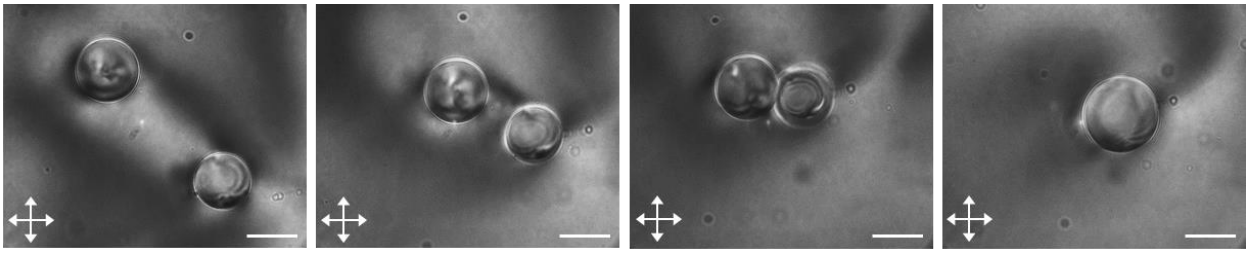

Figure 7-S9. Coalescence of nematic 5CB droplets in nematic 15 wt% DSCG.

Optical micrographs (crossed polars) showing the coalescence of two nematic 5CB droplets dispersed in a region of nematic DSCG that does not exhibit uniform azimuthal alignment. Scale bars = 20 μm.

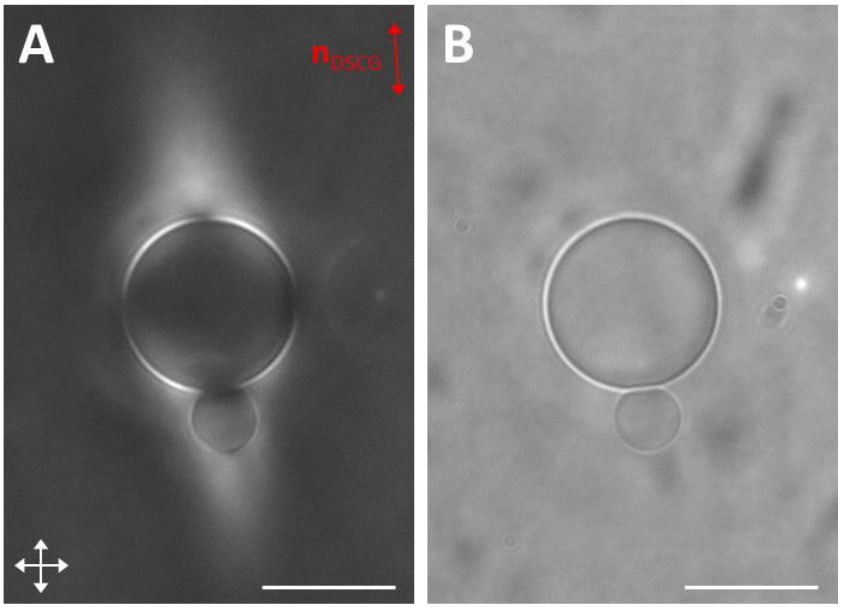

Figure 7-S10. Interaction between two isotropic silicone oil droplets dispersed in nematic 15 wt% DSCG.

(A, B) Optical micrographs (crossed polars, A and bright field, B) of two silicone oil droplets that adhered to one another within an aligned region of nematic DSCG. The far-field orientation of the nematic DSCG is indicated in (A). Scale bars = 20 μm.

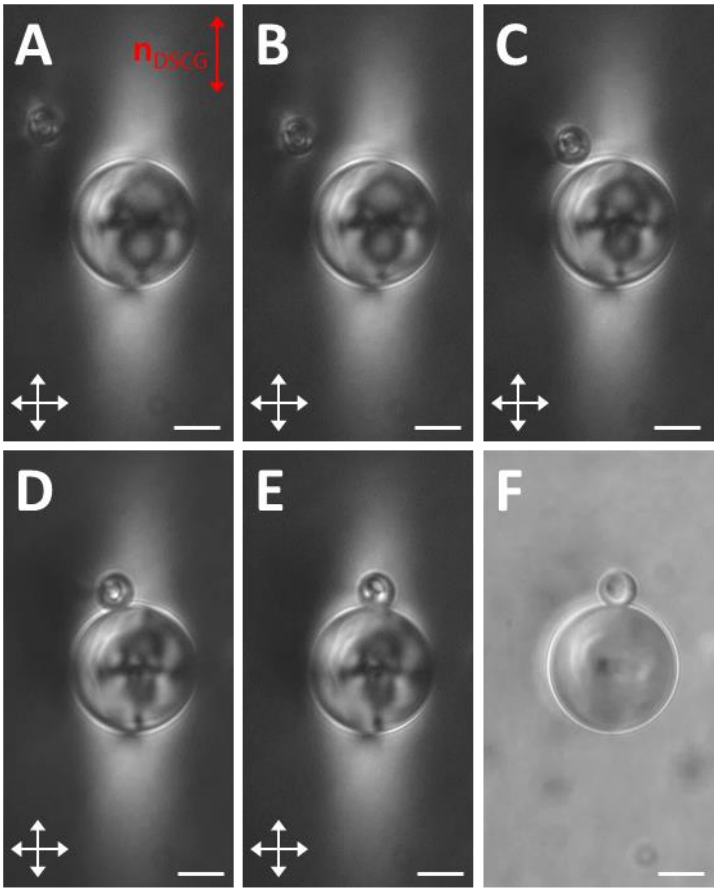

Figure 7-S11. Migration of a small 5CB droplet to the boojum in the nematic 15 wt% DSCG phase located near the surface of a large 5CB droplet .

Sequence of optical micrographs (crossed polars (A-E) and bright field (F)) showing the migration of a 7.9 µm diameter 5CB droplet within an aligned region of nematic DSCG to the DSCG boojum located near the surface of a 26.9 µm diameter 5CB droplet. The far-field orientation of the nematic DSCG is indicated in)A). The micrographs were taken at (A) 0 min, (B) 5 min, (C) 10 min, (D) 13 min, (E) 16 min, and (F) 17 min. Scale bars = 10 µm.

7.6 References

*This chapter was prepared as a Full Paper reporting original research in the journal *Soft Matter*. Reprinted (adapted) with permission from: Mushenheim, P.C.; Abbott, N. L. Hierarchical Organization in Liquid Crystal-in-Liquid Crystal Emulsions. *Soft Matter* **2014**, 10, 8627-8634.

1. Volovik, G. E.; Lavrentovich, O. D. Topological Dynamics of Defects: Boojums in Nematic Drops. *Sov. Phys. JETP* **1983**, 58, 1159–1166.
2. Drzaic, P. S. *Liquid Crystal Dispersions*; World Scientific: Singapore, 1995.
3. Poulin, P.; Stark, H.; Lubensky, T. C.; Weitz, D. A. Novel Colloidal Interactions in Anisotropic Fluids. *Science* **1997**, 275, 1770–1773.
4. Lavrentovich, O. D. Topological Defects in Dispersed Liquid Crystals, or Words and Worlds around Liquid Crystal Drops. *Liq. Cryst.* **1998**, 24, 117–125.
5. Loudet, J.-C.; Barois, P.; Poulin, P. Colloidal Ordering from Phase Separation in a Liquid-Crystalline Continuous Phase. *Nature* **2000**, 407, 611–613.
6. Gupta, J. K.; Sivakumar, S.; Caruso, F.; Abbott, N. L. Size-Dependent Ordering of Liquid Crystals Observed in Polymeric Capsules with Micrometer and Smaller Diameters. *Angew. Chem. Int. Ed. Engl.* **2009**, 48, 1652–1655.
7. Miller, D. S.; Wang, X.; Abbott, N. L. Design of Functional Materials Based on Liquid Crystalline Droplets. *Chem. Mater.* **2014**, 26, 496–506.
8. Lockwood, N. A.; Gupta, J. K.; Abbott, N. L. Self-Assembly of Amphiphiles, Polymers and Proteins at Interfaces between Thermotropic Liquid Crystals and Aqueous Phases. *Surf. Sci. Rep.* **2008**, 63, 255–293.
9. Carlton, R. J.; Hunter, J. T.; Miller, D. S.; Abbasi, R.; Mushenheim, P. C.; Tan, L. N.; Abbott, N. L. Chemical and Biological Sensing Using Liquid Crystals. *Liq. Cryst. Rev.* **2013**, 1, 29–51.
10. Lydon, J. Chromonic Liquid Crystalline Phases. *Liq. Cryst.* **2011**, 38, 1663–1681.
11. Agra-Kooijman, D. M.; Singh, G.; Lorenz, A.; Collings, P. J.; Kitzerow, H.-S.; Kumar, S. Columnar Molecular Aggregation in the Aqueous Solutions of Disodium Cromoglycate. *Phys. Rev. E* **2014**, 89, 062504.
12. Nastishin, Y.; Liu, H.; Schneider, T.; Nazarenko, V.; Vasyuta, R.; Shiyanovskii, S.; Lavrentovich, O. Optical Characterization of the Nematic Lyotropic Chromonic Liquid Crystals: Light Absorption, Birefringence, and Scalar Order Parameter. *Phys. Rev. E* **2005**, 72, 041711.
13. Simon, K. A.; Sejwal, P.; Gerecht, R. B.; Luk, Y.-Y. Water-in-Water Emulsions Stabilized by Non-Amphiphilic Interactions: Polymer-Dispersed Lyotropic Liquid Crystals. *Langmuir* **2007**, 23, 1453–1458.
14. Kim, Y.-K.; Shiyanovskii, S. V; Lavrentovich, O. D. Morphogenesis of Defects and Tactoids during Isotropic-Nematic Phase Transition in Self-Assembled Lyotropic Chromonic Liquid Crystals. *J. Phys. Condens. Matter* **2013**, 25, 404202.
15. Jeong, J.; Davidson, Z. S.; Collings, P. J.; Lubensky, T. C.; Yodh, A. G. Chiral Symmetry Breaking and Surface Faceting in Chromonic Liquid Crystal Droplets with Giant Elastic Anisotropy. *Proc. Natl. Acad. Sci. U. S. A.* **2014**, 111, 1742–1747.
16. Poulin, P.; Weitz, D. A. Inverted and Multiple Nematic Emulsions. *Phys. Rev. E* **1998**, 57, 626–637.

17. Poulin, P.; Cabuil, V.; Weitz, D. Direct Measurement of Colloidal Forces in an Anisotropic Solvent. *Phys. Rev. Lett.* **1997**, 79, 4862–4865.
18. Nazarenko, V. G.; Nych, A. B.; Lev, B. I. Crystal Structure in Nematic Emulsion. *Phys. Rev. Lett.* **2001**, 87, 075504.
19. Smalyukh, I.; Chernyshuk, S.; Lev, B. I.; Nych, A. B.; Ognysta, U.; Nazarenko, V. G.; Lavrentovich, O. D. Ordered Droplet Structures at the Liquid Crystal Surface and Elastic-Capillary Colloidal Interactions. *Phys. Rev. Lett.* **2004**, 93, 117801.
20. Nych, A.; Ognysta, U.; Muševič, I.; Seč, D.; Ravnik, M.; Žumer, S. Chiral Bipolar Colloids from Nonchiral Chromonic Liquid Crystals. *Phys. Rev. E* **2014**, 89, 062502.
21. Mushenheim, P. C.; Trivedi, R. R.; Tuson, H. H.; Weibel, D. B.; Abbott, N. L. Dynamic Self-Assembly of Motile Bacteria in Liquid Crystals. *Soft Matter* **2014**, 10, 88–95.
22. Champion, J. V; Meeten, G. H. Conformation of Sodium Cromolyn in Aqueous Solution Using Light Scattering and Magnetic Birefringence. *J. Pharm. Sci.* **1973**, 62, 1589–1595.
23. Nastishin, Y. A.; Liu, H.; Shiyanovskii, S. V.; Lavrentovich, O. D.; Kostko, A. F.; Anisimov, M. A. Pretransitional Fluctuations in the Isotropic Phase of a Lyotropic Chromonic Liquid Crystal. *Phys. Rev. E* **2004**, 70, 051706.
24. Kinsinger, M. I.; Buck, M. E.; Abbott, N. L.; Lynn, D. M. Immobilization of Polymer-Decorated Liquid Crystal Droplets on Chemically Tailored Surfaces. *Langmuir* **2010**, 26, 10234–10242.
25. Zhou, S.; Neupane, K.; Nastishin, Y. A.; Baldwin, A. R.; Shiyanovskii, S. V; Lavrentovich, O. D.; Sprunt, S. Elasticity, Viscosity, and Orientational Fluctuations of a Lyotropic Chromonic Nematic Liquid Crystal. *Soft Matter* **2014**, 10, 6571–6581.
26. Blinov, L. M.; Chigrinov, V. G. *Electrooptic Effects in Liquid Crystal Materials*; Springer: New York, 1994.
27. Proust, J.; Perez, E.; Ter-Minassian-Saraga, L. Films Minces de Cristal Liquide Nematique Sur Support Liquide. *Colloid Polym. Sci.* **1978**, 256, 666–681.
28. Gharbi, M. A.; Seč, D.; Lopez-Leon, T.; Nobili, M.; Ravnik, M.; Žumer, S.; Blanc, C. Microparticles Confined to a Nematic Liquid Crystal Shell. *Soft Matter* **2013**, 9, 6911–6920.
29. Hiemenz, P. C.; Rajagopalan, R. *Principles of Colloid and Surface Chemistry*, 3rd ed.; CRC Press: Boca Raton, FL, 1997.
30. Leunissen, M. E.; Zwanikken, J.; van Roij, R.; Chaikin, P. M.; van Blaaderen, A. Ion Partitioning at the Oil–water Interface as a Source of Tunable Electrostatic Effects in Emulsions with Colloids. *Phys. Chem. Chem. Phys.* **2007**, 9, 6405–6414.
31. Shah, R. R.; Abbott, N. L. Coupling of the Orientations of Liquid Crystals to Electrical Double Layers Formed by the Dissociation of Surface-Immobilized Salts. *J. Phys. Chem. B* **2001**, 105, 4936–4950.
32. Carlton, R. J.; Gupta, J. K.; Swift, C. L.; Abbott, N. L. Influence of Simple Electrolytes on the Orientational Ordering of Thermotropic Liquid Crystals at Aqueous Interfaces. *Langmuir* **2012**, 28, 31–36.
33. Jerome, B. Surface Effects and Anchoring in Liquid Crystals. *Reports Prog. Phys.* **1991**, 54, 391–451.
34. Nishikawa, M.; Taheri, B.; West, J. L. Mechanism of Unidirectional Liquid-Crystal Alignment on Polyimides with Linearly Polarized Ultraviolet Light Exposure. *Appl. Phys. Lett.* **1998**, 72, 2403–2405.

35. Miller, W. J.; Abbott, N. L. Influence of van Der Waals Forces from Metallic Substrates on Fluids Supported on Self-Assembled Monolayers Formed from Alkanethiols. *Langmuir* **1997**, 7463, 7106–7114.
36. Gupta, V. K.; Abbott, N. L. Design of Surfaces for Patterned Alignment of Liquid Crystals on Planar and Curved Substrates. *Science* **1997**, 276, 1533–1536.
37. Smith, E. R.; Ninham, B. W. Response of Nematic Liquid Crystals to van Der Waals Forces. *Physica* **1973**, 66, 111–130.
38. Dubois-Violette, E.; de Gennes, P. G. Effects of Long Range van Der Waals Forces on the Anchoring of a Nematic Fluid at an Interface. *J. Colloid Interface Sci.* **1976**, 57, 403–410.
39. Bernasconi, J.; Strassler, S.; Zeller, H. R. Van Der Waals Contribution to the Surface and Anchoring Energies of Nematic Liquid Crystals. *Phys. Rev. A* **1980**, 22, 276–281.
40. Tortora, L.; Park, H.-S.; Kang, S.-W.; Savaryn, V.; Hong, S.-H.; Kaznatcheev, K.; Finotello, D.; Sprunt, S.; Kumar, S.; Lavrentovich, O. D. Self-Assembly, Condensation, and Order in Aqueous Lyotropic Chromonic Liquid Crystals Crowded with Additives. *Soft Matter* **2010**, 6, 4157–4167.
41. Parsegian, V. A. *Van Der Waals Forces*; Cambridge University Press: Cambridge, 2005.
42. Terentjev, E. M. Stability of Liquid Crystalline Macroemulsions. *Europhys. Lett.* **1995**, 32, 607–612.
43. Senyuk, B.; Liu, Q.; He, S.; Kamien, R. D.; Kusner, R. B.; Lubensky, T. C.; Smalyukh, I. I. Topological Colloids. *Nature* **2013**, 493, 200–205.
44. Pairam, E.; Vallamkondu, J.; Koning, V.; van Zuiden, B. C.; Ellis, P. W.; Bates, M. A.; Vitelli, V.; Fernandez-Nieves, A. Stable Nematic Droplets with Handles. *Proc. Natl. Acad. Sci. U. S. A.* **2013**, 110, 9295–9300.
45. Campbell, M. G.; Tasinkevych, M.; Smalyukh, I. I. Topological Polymer Dispersed Liquid Crystals with Bulk Nematic Defect Lines Pinned to Handlebody Surfaces. *Phys. Rev. Lett.* **2014**, 112, 197801.
46. Bird, R. B.; Stewart, W. E.; Lightfoot, E. N. *Transport Phenomena*, 2nd ed.; John Wiley & Sons: New York, NY, 2007.

Chapter 8: Elastically Strained Giant Unilamellar Vesicles in Liquid Crystals*

8.1 Introduction

Dispersions of micro- and nanometer-sized colloidal particles in nematic liquid crystals (LCs) have been demonstrated to hold great promise for the creation of self-assembled structures for applications including photonic crystals and metamaterials.[1–6] These opportunities largely arise because the long range ordering and elasticity of the nematic LC phase lead to direction-dependent interparticle forces that depend sensitively on the director distortions and topological defects that form around particles. By varying the physical properties of particles including their sizes and shapes,[7–11] in addition to manipulating the chemistry of the particles to modify the preferential alignment of LCs at the particle surfaces (i.e. "surface anchoring"),[3,12,13] a diverse range of self-assembled structures and colloidal crystals can be created.

Whereas the studies described above address colloids dispersed in LCs that are rigid and preserve their shape in LCs, in this paper we move to consider the more complex situation in which flexible colloids are dispersed in LCs and a coupling emerges between the colloid shape and LC strain. Specifically, we report on highly flexible, micrometer-sized synthetic giant unilamellar vesicles (GUVs) prepared in LCs. We hypothesize that elastic stresses arising due to the confinement of the LC will deform the GUVs, possibly giving rise to anisometric GUV shapes, expansion of the surface area of GUV membranes, or even inducing the rupture of the vesicles. To perform these experiments, we employ the lyotropic chromonic LC phase formed by aqueous solutions of disodium cromoglygate (DSCG), since DSCG is non-amphiphilic and thus will not disrupt the lipid bilayers of GUVs. We note here that the configurations adopted by

nematic DSCG and other chromonic LCs have been explored in confined spherical[14] and cylindrical geometries[15] as well as when encompassing spherical inclusions[16].

In support of our hypothesis that elastic LC-mediated stresses might induce GUVs to adopt non-spherical shapes, we note that previous studies have demonstrated that at temperatures in lyotropic LCs at which nematic and isotropic phases coexist, the dispersed phase domains adopt elongated and cusped shapes.[17–21] These anisometric domains, called "tactoids", form as a result of interplay between the energy associated with the nematic-isotropic interface and LC elastic energy. Also, a recent study has shown that elastic stresses imparted by an LC phase can bend the bodies of rod-shaped bacteria that are tens of micrometers in length.[22]

In addition to providing fundamental insight, investigating how elastic stresses couple to particle shape in synthetic systems also may reveal opportunities for the design of novel LC-based responsive, reconfigurable materials or active systems driven either by application of external fields[23,24] or dissipation of energy.[25–29] In addition, because recent experiments suggest curvature strain within the membranes of rod-shaped bacteria induce localization of certain lipids to the regions of highest membrane curvature at the cell poles, we envision that elastically strained GUVs might be a useful experimental platform to further investigate biophysical questions relating to membrane curvature strain.[30,31]

8.2 Experimental Section

Materials. 1,2-dioleoyl-*sn*-glycero-3-phosphocholine (DOPC), 1,2-dioleoyl-*sn*-glycero-3-phosphoethanolamine-N-[methoxy(polyethylene glycol)-2000] (ammonium salt) (DOPE-PEG2000), and 1,2-distearoyl-*sn*-glycero-3-phosphoethanolamine-N-[poly(ethylene glycol)2000 -N'-carboxyfluorescein] (ammonium salt) (DSPE-PEG2000-CF) were purchased from Avanti

Polar Lipids, Inc. (Alabaster, AL). *N*-(4,4-difluoro-5,7-dimethyl-4-bora-3a,4a-diaza-*s*-indacene-3-propionyl)-1,2-dihexadecanoyl-*sn*-glycero-3-phosphoethanolamine triethylammonium salt (BODIPY-DHPE) was obtained from Molecular Probes (Eugene, OR). Disodium cromoglycate (DSCG) was purchased from Sigma-Aldrich (Milwaukee, WI) and used as received. Chloroform was obtained from Sigma-Aldrich (St. Louis, MO). Fisher's Finest Premium grade glass slides and cover glass and amber glass vials (O.D. = 15 mm) were purchased from Fisher Scientific (Pittsburgh, PA). Deionization of a distilled water source was performed with a Milli-Q system (Millipore, Bedford, MA) to give water with a resistivity of 18.2 MΩ cm.

Lyotropic LC preparation. Lyotropic LCs containing DSCG were prepared by mixing 15 wt% of DSCG with 85 wt% water. The mixture was shaken for at least 12 h to ensure complete solubility and homogeneity. Prior to experimentation, the DSCG solution was heated at 65°C for 10 min to avoid possible time dependence of the properties of the mixture.[32,33]

GUV preparation. GUVs were prepared via the gentle hydration of a dried DOPC lipid film based on previously published procedures.[34,35] Briefly, 100 μL of a phoshpolipid mixture (1 mM total lipid concentration) in chloroform was added to the bottom of a small glass vial. In our experiments, we employed lipid mixtures containing a small amount (0.2 – 2 mol%) of DOPE-PEG2000 (or DSPE-PEG2000-CF) and up to 0.5 mol% of a fluorescent probe (BODIPY-DHPE). The solvent was subsequently evaporated using a stream of nitrogen prior to the vial being placed under vacuum for at least 2 h, leaving dried lipid films on the vial walls. The vial was then immersed in a water bath at 48°C. To promote GUV formation, we next performed a pre-incubation step in which 2 μL of water was added to the vial and incubated for 5 minutes.

Then 200 μL of 15 wt% DSCG solution (heated into its isotropic phase) was added to the glass vial in the hot water bath. GUVs formed over the course of an incubation period of at least 1.5 h. Care was taken to minimize agitation of the vial during this incubation step to maximize GUV yield. Consistent with a previous report,[35] we found that our GUV yield was significantly improved when PEG-lipids, which facilitate GUV formation by promoting steric repulsions between lipid layers deposited on the glass vial, were included in the lipid mixture.

Preparation of experimental chambers. To investigate GUVs prepared in 15 wt% DSCG, we added a small volume (~ 4.5 μL) of the GUV mixture to a cavity created using sheets of Mylar film (~ 60 μm in thickness) between two glass substrates. Following assembly, the chamber was immediately sealed with epoxy to prevent water evaporation. Generally as we performed these steps, the temperature of the GUV mixture was rapidly quenched from 48°C (in which 15 wt% DSCG is in the isotropic phase) to room temperature (25°C) (in which 15 wt% DSCG is in the nematic phase). In order to investigate the dynamical shape changes of GUVs that accompany this phase transition, some experimental chambers were prepared on a hot plate (INSTEC, Inc., Boulder, CO) set at ~ 48°C such that the DSCG remained in the isotropic phase. In this way, we could image the GUV mixture as the temperature of the sample was subsequently quenched to 25°C.

Microscopy. GUVs prepared in 15 wt% DSCG were investigated using an Olympus IX71 inverted microscope (Center Valley, PA) equipped with a 100× oil-immersion objective, a 60× objective, crossed polarizers, and a 100W mercury lamp. Bright field, polarized light, and fluorescence micrographs of the GUVs were collected with a Hamamatsu 1394 ORCAER CCD

camera (Bridgewater, NJ) connected to a computer and controlled through SimplePCI imaging software (Compix, Inc., Cranberry Twp., NJ). BODIPY and carboxyfluorescein fluorescence were both imaged using a fluorescence filter cube with an excitation filter of 480 nm and an emission filter of 535 nm. An Olympus BX60 microscope equipped with crossed polarizers was also used to analyze GUVs. Images were captured using a digital camera (Olympus C-2040 Zoom) mounted on the microscope and set to an f-stop of 2.8 and a shutter speed of 1/25 s.

8.3 Results

First, we sought to characterize the shapes of GUVs that formed upon hydrating a dried lipid film (consisting of a ternary mixture of DOPC/DOPE-PEG2000/BODIPY-DHPE) within a 15 wt% DSCG solution in its isotropic phase at 48°C (as detailed in the Experimental section). At this concentration, we measured DSCG to form a nematic phase below ~30°C and an isotropic phase above ~42°C, with two phase coexistence at intermediate temperatures. A small amount ($\leq$ 2 mol%) of PEG-lipids was included in the lipid mixtures to increase steric repulsions between lipid layers within the film upon hydration and facilitate the formation of GUVs.[35] Upon inspecting the distribution of the fluorescent probe (BODIPY-DHPE) in samples at 48°C (prepared such that the DSCG remained in its isotropic phase at all times), we found many approximately spherical domains encapsulated by lipids (Figure 8-1A), consistent with the formation of GUVs. We confirmed the DSCG solutions both inside and outside of the GUVs were in the isotropic phase at this temperature by characterizing the samples between crossed polars and observing extinction of transmitted light (Figure 8-1B). We note here that we frequently observed small regions exhibiting heightened fluorescence near the membranes of GUVs that we attribute to the presence of small lipid aggregates that become associated with the

GUVs. We also note that we did not observe these fluorescent aggregates to influence the shapes of the GUVs. Apart from these domains, we measured an approximately uniform fluorescence signal from the lipid bilayers of GUVs in both nematic and isotropic DSCG, suggesting that the fluorescent probe is homogenously dispersed in the bilayer. Inspection of the distribution of fluorescently-labeled PEG-lipids in GUVs revealed these lipids to be completely miscible, as well (Figure 8-S1).

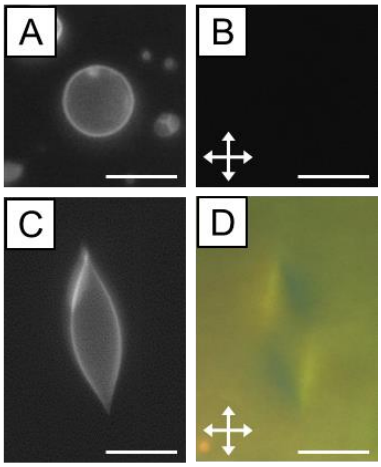

Figure 8-1. Elongation of GUVs within the nematic phase of a lyotropic LC.
(A, B) Fluorescence and crossed polars micrographs, respectively, of a GUV (DOPC/BODIPY-DHPE/DOPE-PEG-2000) in 15 wt% DSCG at 48ºC (isotropic phase). (C, D) Fluorescence and crossed polars micrographs, respectively, of a GUV in 15 wt% DSCG following a quench to 25ºC (nematic phase). Scale bars = 10 µm.

We note that a polydisperse population of spherical GUVs was formed in isotropic DSCG by this gentle hydration method. We measured the GUVs to have diameters ranging from 2 µm to 20 µm, although we occasionally found GUVs as large as 50 µm in diameter in our samples. The sizes and shapes of GUVs in 15 wt% DSCG at 48°C were similar to those adopted by GUVs that we prepared in other isotropic solutions, such as water and 5.5 wt% DSCG (Figure 8-S2). We also note that we observed some vesicles to adopt non-spherical shapes in the isotropic solution and to possess "onion-like" structures (Figures 8-S3 through 8-S5; see Supporting

Information for discussion). In this paper, however, we focus on results obtained with unilamellar vesicles exhibiting spherical shapes in isotropic DSCG and their products in nematic DSCG.

While the majority of GUVs adopted spherical shapes in 15 wt% DSCG in its isotropic phase, we hypothesized that the GUVs would be deformed upon cooling of the DSCG solution into its nematic phase due to elastic stresses associated with the confinement of the LC by each GUV. To explore this hypothesis, we quenched a dispersion of vesicles in a 15 wt% DSCG solution at a rate of ~10°C/min from 48°C to 25°C from its isotropic phase into its nematic phase (see Video S1 in the online Supporting Information). Upon investigating the sample at 25°C, we indeed found the GUVs within the nematic phase had adopted non-spherical, sometimes highly elongated shapes (Figure 8-1C). Additionally, by inspecting these samples with polarized light (between crossed polarizers), we observed birefringent textures consistent with a nematic LC phase present both inside and outside the GUVs (Figure 8-1D; discussed in further detail below). By heating samples back to 48ºC into the isotropic phase of DSCG, we found that elongated GUVs reverted to spherical shapes (see Video S2 in the online Supporting Information). We observed the return of the spherical shape of GUVs to always coincide with the phase transition of the DSCG into the isotropic phase.

In addition to the highly elongated GUVs of the type shown in Figures 8-1C and 8-1D, we also observed a population of GUVs in nematic DSCG with only slightly elongated shapes and approximately rounded poles. Examples of these two populations are provided in Figures 8-2A through 8-2C and Figures 8-2D through 8-2F, respectively. By performing confocal microscopy, we confirmed GUVs in both populations possessed prolate shapes and were symmetric with respect to rotation around the major axis (see Video S3 in the online Supporting

Information). To quantitatively characterize the shapes adopted by these GUVs in nematic DSCG in our samples, we analyzed fluorescence micrographs using a custom MATLAB code (see Supporting Information for details). Specifically, for each GUV, we quantified the aspect ratio (R/r, where R is the semi-major axis and r is the semi-minor axis), surface area, volume, and cusp angle (α) from micrographs taken at the GUV mid-plane. Inspection of the distribution of GUV cusp angles in nematic DSCG measured through this procedure (Figure 8-2G) supports our conclusion we reached based on visual inspection above that two distinct populations of GUVs form in our samples. From this histogram, these two populations appear to be separated by a critical cusp angle of $\alpha \sim 130°$.

We also quantified the change in aspect ratio of the vesicles with size by plotting R/r as a function of surface area for GUVs in nematic 15 wt% DSCG in Figure 8-2H. In this plot, we distinguish between the population of GUVs possessing sharp cusps $\alpha < 130°$ and the population exhibiting approximately rounded poles $\alpha > 130°$. Whereas Figure 8-2H reveals a clear trend that GUV aspect ratio increases with decreasing GUV size within the population of GUVs with $\alpha > 130°$, there is far greater scatter within the data for GUVs with $\alpha < 130°$. Moreover, our analysis demonstrates that while small GUVs (surface area < 50 μm^2) typically adopt highly elongated shapes with sharp cusps in nematic DSCG, larger GUVs (surface area > 500 μm^2) generally adopt slightly elongated shapes with approximately rounded poles. Interestingly, GUVs with surface areas intermediate to these values commonly exhibit either cusped poles or rounded poles. We note that Figure 8-2H includes data obtained from analysis of GUVs prepared with both 2 mol% and 0.2 mol% PEG-lipids, plotted as filled and unfilled circles, respectively. Although the effective rigidity of lipid bilayers increases with increasing PEG-lipid content,[36,37] we did not observe this difference in rigidity to lead to any significant changes to the shapes

adopted by GUVs in nematic DSCG. These trends discussed above in the context of Figure 8-2H are also apparent in a plot of α versus GUV surface area (Figure 8-S6).

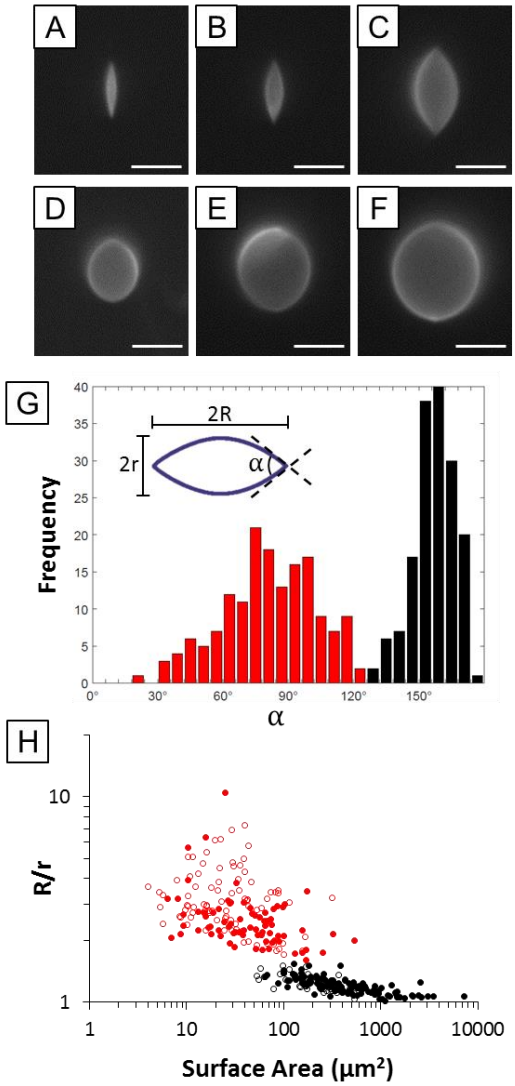

Figure 8-2. Two populations of GUVs with distinct shapes form in nematic 15 wt% DSCG.
(A–C) Fluorescence micrographs of highly elongated, cusped GUVs in 15 wt% DSCG at 25ºC. (D–F) Fluorescence micrographs of slightly elongated GUVs with approximately rounded poles. (G) Histogram depicting the distribution of cusp angles (α) measured for GUVs in nematic 15 wt% DSCG. (H) Plot of GUV aspect ratio (R/r) as a function of surface area for GUVs in nematic 15 wt% DSCG. In G and H, data in red denote GUVs with cusp angles $\alpha < 130^{o}$ (e.g., the GUVs depicted in A-C) and data in black denote GUVs with cusp angles $\alpha > 130^{o}$ (e.g., the GUVs depicted in D-F). In H, filled points denote GUVs containing 2 mol% PEG-lipid and unfilled points denote GUVs containing 0.2 mol% PEG-lipid. Scale bars are 5 μm.

Overall, the results above provide evidence that elongated GUVs form in the nematic phase of 15 wt% DSCG, consistent with our initial hypothesis regarding the influence of LC elastic stresses. However, the observation of two distinct types of non-spherical shapes was not anticipated. Based on this observation, we organize the remainder of the Results section into two parts focusing on each population in turn.

8.3.1 Slightly elongated GUVs with $\alpha > 130°$

First we sought to develop insight regarding the processes leading to the formation of the population of slightly elongated GUVs with $\alpha > 130^{o}$. The GUVs in this population all exhibited aspect ratios of $R/r < 1.54$. To do this, we considered that in order for a spherical GUV in isotropic DSCG to adopt an elongated shape upon quenching into the nematic phase of DSCG, the surface area of the GUV and/or the volume encapsulated by the GUV must change. Previous studies have employed micropipette aspiration experiments to measure that the apparent surface area of GUVs prepared in isotropic aqueous solutions and comprised of DOPC can expand up to $\sim$ 5% through suppression of thermal undulations and an increase in the average area per lipid molecule prior to rupturing at a critical tension of τ^{*} = 10 mN/m.[38–40] To assess the likelihood that elastic stresses associated with the nematic LC dilate the GUV surface area in order to give rise to this population of slightly elongated GUVs, we calculated the fractional expansion in surface area, $\varepsilon_{SA} = (SA_2 - SA_1)/SA_1$, required for an elongated GUV measured in the nematic phase (with surface area SA_2) to encapuslate the same volume as a spherical GUV (with surface area SA_1) (Figure 8-3A). This plot reveals a modest 3% expansion in membrane surface area is necessary to give rise to the most asymmetric GUVs in this population ($R/r \sim 1.54$). This result

suggests that it is possible that internal volume is approximately conserved in GUVs during the DSCG phase transition to lead to formation of this population.

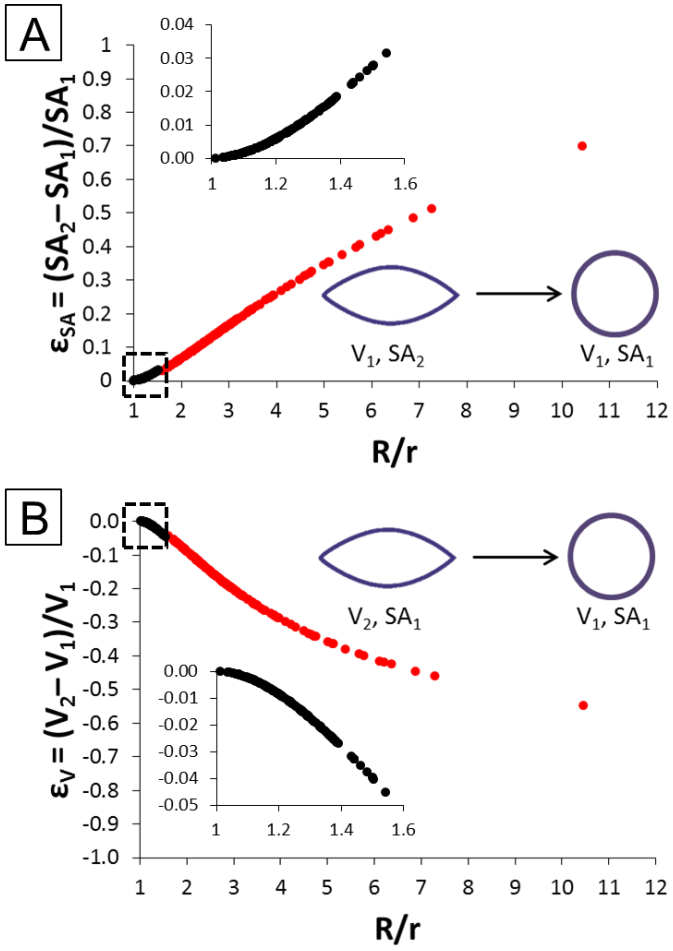

Figure 8-3. Changes in surface area and volume potentially accompanying LC-induced GUV shape transformations.

(A) Surface area expansion (ε_{SA}) required if volume is conserved as GUVs transform from spherical shapes in isotropic DSCG to elongated shapes in nematic DSCG. (B) Decrease in internal volume (ε_V) required if surface area is instead conserved during the GUV shape transformation that accompanies the DSCG phase transition. Data in red denote GUVs with cusp angles $\alpha < 130^o$ and data in black denote GUVs with cusp angles $\alpha > 130^o$.

If GUV volume is indeed conserved during the transformation from a spherical shape to a slightly elongated shape accompanying the DSCG phase transition, then there should be no change in composition of the DSCG phase within and outside the GUVs and thus the termperatures at which phase transitions take place should be approximately the same in both the DSCG solution inside and outside each GUV. To determine whether this is the case, we compared the phase behavior exhibited by the DSCG solutions inside and outside GUVs upon heating and cooling. First, we heated a GUV-containing sample from 26ºC to 50ºC at a rate of ~0.5ºC/min. In Figures 8-4A through 8-4F, we provide an example of the sequence of phase transitions we observed inside and outside a GUV with an initial aspect ratio of R/r ~ 1.14 in the nematic phase (see Video S4 in the online Supporting Information). We found that isotropic phase domains nucleated near the surface of GUVs at temperatures approximately 1ºC lower than those at which isotropic domains first appeared in the bulk of the continuous nematic DSCG solution outside of GUVs (N = 5) (Figures 8-4C and 8-4D). (Note that these isotropic domains do not appear dark between crossed polarizers due to the birefringence of the nematic DSCG outside of the GUVs.) It was difficult for us to determine whether these domains intially formed on the inside and/or the outside of the GUV membrane. Upon heating the sample through the range of temperatures in which nematic and isotropic phase domains coexisted within the DSCG solution inside and outside the GUVs (see Supporting Information for additional discussion), the DSCG solution throughout the sample (both inside and outside of GUVs) transitioned to the isotropic phase and GUVs adopted spherical shapes (Figures 8-4E and 8-4F).

Upon cooling the sample from 50ºC (Figures 8-4G through 8-4L; also see Video S5 in the online Supporting Information), nematic domains appeared outside of GUVs at temperatures ~2.5ºC higher than inside the GUVs (N = 4) (Figures 8-4I and 8-4J). Additional cooling of the

sample led to the growth of nematic phase domains both inside and outside of GUVs (see Supporting Information for additional discussion) followed by the eventual disappearance of remaining isotropic phase domains (Figures 8-4K and 8-4L). We note that we also occasionally observed coexistence between isotropic and columnar phase domains in our samples at temperatures above 41ºC when performing these experiments.[41]

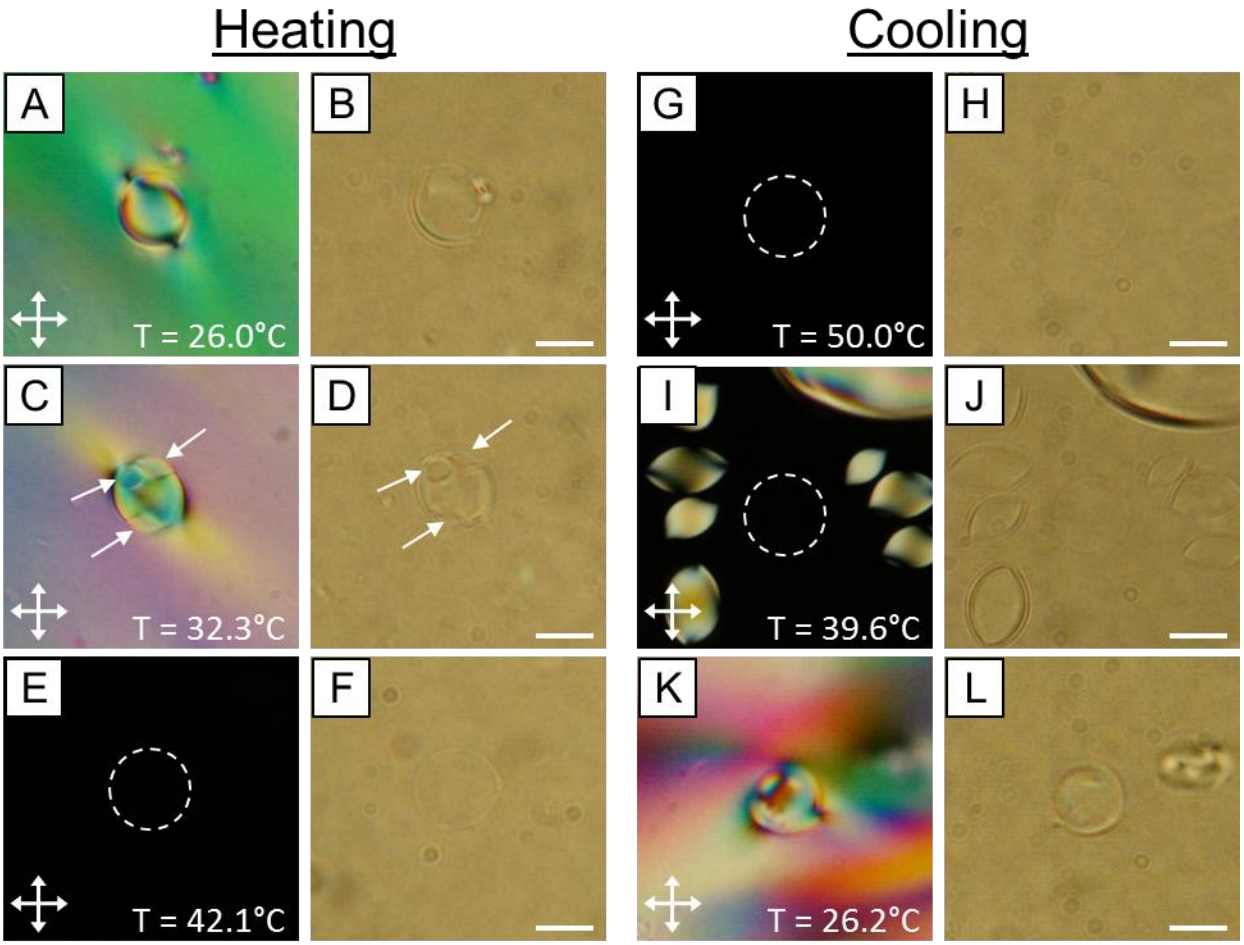

Figure 8-4. DSCG phase transitions inside and outside GUVs.

Crossed polars and corresponding bright field micrographs obtained while (A–F) heating a GUV-containing sample from 26ºC to 50ºC and (G–L) subsequently cooling the sample from 50ºC to 26ºC at a rate of ~0.5ºC/min. Micrographs were collected at the temperatures indicated in the figure. Dotted lines outline the GUV in crossed polars micrographs when the internal DSCG solution is largely in its isotropic phase. In C and D, isotropic phase domains are indicated with arrows. Scale bars = 20 µm.

The lack of an increase in the phase transition temperatures of the internal DSCG solution in these experiments compared to the external DSCG solution suggests that the DSCG concentration inside GUVs in the nematic phase is not enriched relative to the outside solution. We hypothesize that the observed shift of phase transitions to lower temperatures inside the GUVs might reflect i) heightened elastic strain associated with confinement of LCs inside GUVs or ii) local depletion of DSCG near the surface of the GUV membrane. Although the origin of the shift in DSCG phase transitions within GUVs to lower temperatures remains unclear, our measurements are consistent with the hypothesis that slightly elongated GUVs form in the nematic DSCG phase as a result of surface area expansion rather than volume reduction.

Based on these experimental observations, we hypothesize that the population of large, slightly elongated GUVs with rounded poles likely forms via stetching and expansion of the lipid membrane in nematic 15 wt% DSCG. Moreover, because this GUV shape transition occurs in concert with the DSCG phase transition into the nematic phase, we hypothesize that elastic stresses imparted by the nematic LC phase might induce this expansion. To gain insight into the nature of the LC elastic energy (E_{LC}) and interfacial energy of the GUV (E_s) acting in our system, we analyzed how an interplay of these energies might give rise to the equilibrium shapes adopted by GUVs with $\alpha > 130^{o}$. For this population of slightly elongated GUVs,[19]

$$E_{LC} = CKR\left(\frac{r}{R}\right)^2 \qquad (8-1)$$

where K is an average elastic constant of the LC (K ~ 10 pN for 15 wt% DSCG[42]) and C is a constant. Given our conclusion that this population of GUVs forms at constant volume, the major and minor axis of each slightly elongated GUV is related to R_1, the radius of the initially spherical GUV in the isotropic phase of DSCG, by the expression

$$R_1 = (Rr^2)^{1/3}. \quad (8-2)$$

On the other hand, the interfacial energy is given by

$$E_s = \tau SA_2 \quad (8-3)$$

where SA_2 is the surface area of the slightly elongated GUV in nematic DSCG and τ is a parameter that might be a function of many factors, including R/r, ε_{SA}, and SA_2.

Previously, Prinsen and van der Schoot demonstrated that the optimal aspect ratio of nematic tactoids that form at temperatures within the two-phase nematic-isotropic coexistence range of lyotropic chromonic LCs is given by

$$\frac{R}{r} = CK^{3/5}\,\tau^{-3/5}V^{-1/5} \quad (8-4)$$

by minimizing the total free enegy $E = E_{LC} + E_s$ at constant volume (V), where C is a constant and E_{LC} is given by Equation 8-1.[19] For the case of tactoids, τ is defined as the interfacial tension between the coexisting nematic and isotropic phases and thus is a constant. In order to determine if Equation 8-4 might also describe the equilibrium shapes of GUVs in nematic DSCG for some constant value of τ, we solved Equation 8-4 for τ. For our case, we found the constant in Equation 8-4 to be $C \sim 15$ by solving the Ericksen-Leslie equations with strong tangential anchoring for nematic LC inside and outside of prolate spheroidal bodies with aspect ratios matching those we observed experimentally. Then, by using our experimental data, we were able to investigate whether the value of τ that leads to the optimal GUV aspect ratio ($\tau = \tau_{optimal}$) based on this expression varies with ε_{SA}, the fractional extension in GUV surface area (at constant volume). Inspection of Figure 8-5A reveals that $\tau_{optimal}$ is nearly constant over the entire range of ε_{SA} values we calculate for the population of GUVs with $\alpha > 130^o$. In contrast, if the interfacial energy of the GUV is predominantly dictated by the elastic energy associated with stretching the GUV membrane, given by[43]

$$E_k \sim \frac{K_s}{2} SA_1 {\varepsilon_{SA}}^2 \qquad (8-5)$$

where K_s is the elastic stretch modulus ($K_s \sim 300$ mN/m for DOPC[38]) and $SA_1 = 4\pi R_1^2$, we instead would expect $\tau \propto {\varepsilon_{SA}}^2$. This relationship between $\tau = \tau_{elastic}$ and ε_{SA} is also plotted in Figure 8-5A.

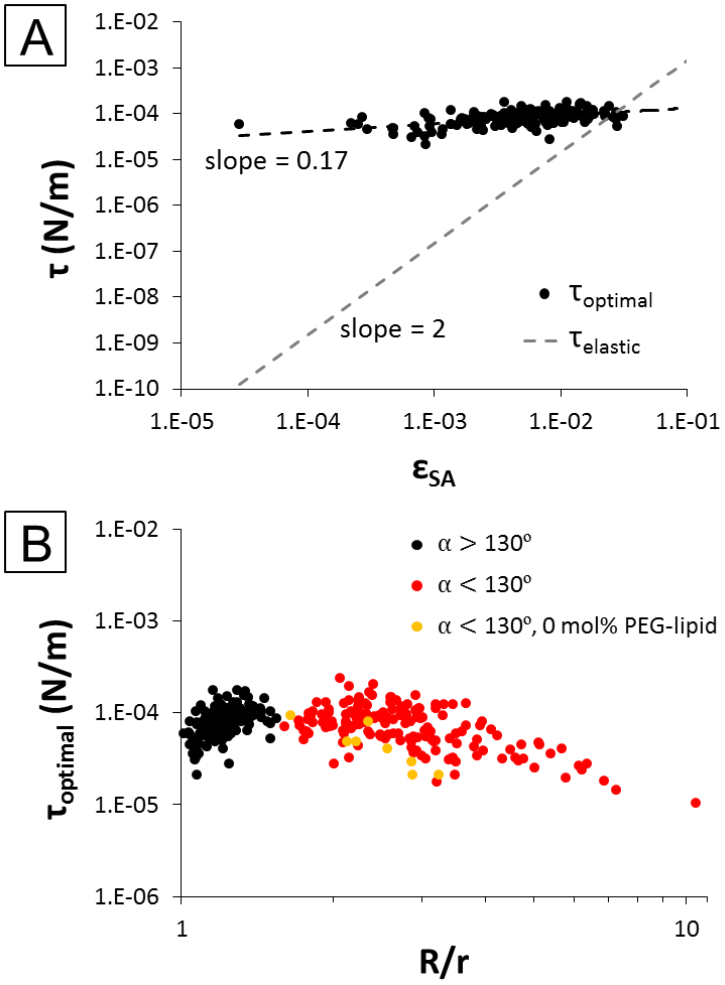

Figure 8-5. Plots of τ as a function of fractional surface area expansion (ε_{SA}) and GUV aspect ratio (R/r).

(A) Log-log plot of $\tau_{optimal}$ as a function of ε_{SA} for the population of GUVs with $\alpha > 130°$. The slope of a power law fit to the data is indicated in the figure. The relationship between $\tau_{elastic}$ and ε_{SA} is also provided in the figure. (B) Log-log plot of $\tau_{optimal}$ as a function of R/r. Data in red and black denote GUVs with cusp angles $\alpha < 130°$ and $\alpha > 130°$, respectively, prepared with 0.2 – 2 mol% PEG-lipid. Data in yellow denote GUVs prepared with 0 mol% PEG-lipid, all of which had $\alpha < 130°$.

Our calculation of $\tau_{optimal}$ based on our experimental data and comparison to $\tau_{elastic}$ thus somewhat surprisingly leads to the suggestion that the interfacial energy of GUVs in our system is dominated not by an energy penalty associated with stretching the GUV membrane but rather by a surface energy resembling that present in the case of nematic tactoids considered by Prinsen and van der Schoot. Moreover, $\tau_{optimal}$ remains approximately constant with a magnitude of $\sim$ 0.1 mN/m across the entire range of experimental values of ε_{SA} for this population of GUVs, which is the same order of magnitude as the interfacial tension previously measured between coexisting nematic and isotropic DSCG phases.[21] We comment further on this apparent coupling between LC elastic energy and a surface energy due to interfacial tension that appears to influence the shapes adopted by this population of GUVs in the following section.

Next, in order to better understand the nature of the LC-mediated elastic stresses acting on GUVs in the population of slightly elongated GUVs with approximately rounded poles, we sought to characterize the anchoring and configurations adopted by the nematic 15 wt% DSCG inside and outside the GUVs. We found birefringent "tails" to extend outward from the poles of these GUVs when examined between crossed polars in the direction parallel to the orientation of the far-field director in the continuous nematic LC phase (Figures 8-6A through 8-6C). These tails, which have previously been observed around spherical particles and emulsion droplets with diameters greater than 6 μm and that anchor DSCG tangentially,[16,44] are indicative of a twisted configuration of the LC that is favored due to the small twist elastic constant (K_2) of nematic DSCG.[45] Our observation of these optical signatures (and other observations reported below) leads us to conclude that nematic DSCG is also anchored tangentially on the lipid bilayers of GUVs in our experiments. Consistent with past studies, we found that the tails extending from the poles of a GUV could exhibit the same handedness of twist (Figure 8-6A) or opposite

handedness of twist (Figure 8-6B). However, we did not measure the shapes of GUVs to measurably differ depending on the handedness of the twisted tails.

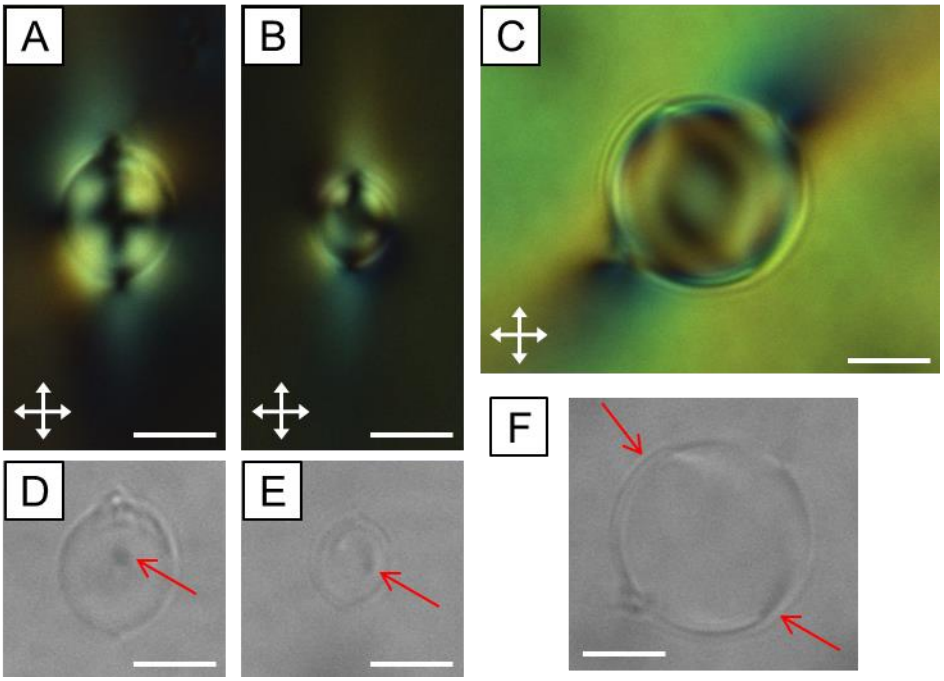

Figure 8-6. Configuration of nematic DSCG inside and outside of slightly elongated GUVs ($\alpha >$ 130º).

(A-C) Crossed polars micrographs and (D-F) corresponding bright field micrographs of slightly elongated GUVs in nematic 15 wt% DSCG at 25ºC. Boojums are indicated in the bright field images using arrows. Scale bars = 10 µm.

While the configuration of the nematic DSCG outside of GUVs is readily inferred from polarized light micrographs, assessing the configuration of DSCG inside GUVs is less straightforward since birefringence from the DSCG phase outside of each GUV contributes to the optical appearance of the GUVs in these micrographs. However, surface defects ("boojums") associated with the internal configuration of the DSCG were evident in bright field micrographs of these GUVs (Figures 8-6D through 8-6F). We found each GUV to have two boojums diametrically opposed from one another, reminiscent of a bipolar configuration (although depending on the orientation of the GUV, only one defect can be clearly observed in

micrographs). However, we were surprised to find that the two surface defects commonly were positioned on or near a minor axis of each GUV (Figures 8-6D through 8-6F).

Recently, Jeong et al. reported that spherical droplets of another lyotropic chromonic LC, Sunset Yellow (SSY), adopt a twisted bipolar configuration.[14] We wondered whether there also might be twisting in the nematic DSCG phase confined within GUVs in our experiments that perhaps would help to explain the surprising orientation of the symmetry axis. A twisted director configuration is energetically favored over an untwisted configuration within a spherical droplet when the elastic constants of the LC meet the Williams condition: $K_{33}/K_{11} \leq 2.32(1 - K_{22}/K_{11})$.[46,47] While the elastic constants of SSY satisfy this criterion,[48] those of nematic DSCG do not.[45] Thus, based on this calculation, we do not expect the LC confined inside nearly spherical GUVs to relax via twist distortions.

Our analysis above reveals that in this population of slightly elongated GUVs with approximately rounded poles, there appear to be two boojums commonly located along the minor axis of the GUVs and that twisting of the internal director field is not expected. Based on this information, we cannot yet make a definite determination of the exact configuration(s) adopted by nematic DSCG inside GUVs in this population and additional studies are required.

8.3.2 Highly elongated GUVs with $\alpha < 130°$

Next, we turn our attention to characterizing and elucidating the formation of the population of highly elongated GUVs ($R/r > 1.54$) with cusped poles ($\alpha < 130^{o}$) that also forms upon quenching into the nematic phase of DSCG. First, we considered whether the highly anisometric GUV shapes in this population might also develop as a result of LC elasticity-induced expansion of the GUV surface area at constant GUV volume, similar to the population

of slightly elongated GUVs described above. However, inspection of Figure 8-3A reveals that this is not likely to occur, as such a process would require greater than a 50% expansion of membrane surface area for the most asymmetric GUVs in this population, which is far greater than the ~5% expansion that DOPC membranes are expected to tolerate.[38–40]

Since the internal volume of DSCG solution in this population of GUVs does not appear to be conserved during the transition from the isotropic phase to the nematic phase, we considered whether the loss of internal volume might be accomplished via an efflux of pure water from the GUVs since lipid bilayers are highly permeable to water[40] but may be relatively impermeable to polyaromatic DSCG molecules. This process would give rise to an osmotic stress acting on the GUV membrane and, based on phase diagrams of aqueous solutions of DSCG, lead to a shift in the phase transition temperatures of the internal DSCG solution to higher values relative to the external DSCG solution.[41,49] To determine whether this might be the case, we compared the volume of each elongated GUV in the nematic phase (V_2) to the volume of a spherical GUV (V_1) possessing the same surface area and noted that this shape transformation would require a 50% reduction in volume for GUVs with the highest aspect ratios within this population (Figure 8-3B). Such a large change in volume would be expected to lead to a very large increase in the phase transition temperatures of the internal DSCG solution and possibly even to the condensation of higher order phases.[49,41] However, inconsistent with the hypothesis that this volume change reflects efflux of pure water, we found that phase transitions in the DSCG solution inside of elongated and cusped GUVs occurred at the same or lower temperatures than in the continuous DSCG phase (see, for example, Videos S1 and S2 in the online Supporting Information).

The results described above are consistent with the hypothesis that efflux of both water and DSCG leads to the formation of this population of highly elongated and cusped GUVs. Since lipid bilayers are much more permeable to water than polyaromatic molecules,[39,50] we expect that the efflux of 15 wt% DSCG solution likely does not occur simply by permeation through intact GUV membranes. Instead, we hypothesize that in response to some critical level of tension within the membrane imparted by LC elastic stresses, the lipid bilayer may partically rupture, leading to the formation of transient pores within the membrane.[51–54] In this way, 15 wt% DSCG solution might efflux from GUVs until the membrane relaxes sufficiently to allow the pores to dynamically reseal.[53–56] Such a decrease in the internal volume of 15 wt% DSCG solution from the GUVs thus could allow for the significant elongation of GUVs we measure in this population.

Inspection of Figure 8-5A reveals that while $\tau_{optimal} \gg \tau_{elastic}$ for most GUVs within the population of slightly elongated GUVs with $\alpha > 130^{o}$, we calculate $\tau_{elastic}$ to become comparable in magnitude to $\tau_{optimal}$ for the smallest and most highly deformed GUVs in this population. This suggests that the heightened energy penalty associated with stretching the lipid membranes of GUVs smaller in size might indeed lead these vesicles to partially rupture and give rise to the population of small, highly elongated and cusped GUVs in nematic DSCG. Moreover, the fact that E_{LC} and E_s scale with GUV size as $\frac{E_{LC}}{E_s} \sim \frac{1}{R}$ is consistent with our suggestion that GUVs smaller than some critical size may be elongated to the point of rupture due to LC elastic stresses. In addition, several other experimental observations support the physical picture we have described above. First, we note that whereas Figure 8-2H reveals a clear trend between aspect ratio and surface area in the population of slightly elongated GUVs with $\alpha > 130^{o}$, there is far greater scatter in the data for the population of highly elongated and

cusped GUVs. This scatter could arise due to the potentially stochastic nature of the pore formation and dynamic resealing processes that we hypothesize gives rise to this population of GUVs.[57] It also allows us to understand why there could be coexisting populations of slightly elongated and highly elongated GUVs exhibiting surface areas within the range of 50 μm^2 to 500 μm^2, as depending on the configurations adopted by the nematic LC phase, varying amounts of elastic stresses are imparted on the membrane. We provide information regarding the configurations adopted by LCs inside and outside of GUVs with $\alpha < 130^o$ later in this section.

We next sought to determine if the equilibrium shapes adopted by GUVs with $\alpha < 130^o$ following the efflux of 15 wt% DSCG solution appear to be set by an interplay between the LC elastic energy and a surface area arising due to interfacial tension, as was found for the population of GUVs with $\alpha > 130^o$ described in the previous section. To do this, we used our experimental data in conjunction with Equation 8-4 to generate a plot of $\tau_{optimal}$ versus R/r (Figure 8-5B). We found that $\tau_{optimal}$ varied weakly as a function of R/r for the population of GUVs with $\alpha < 130^o$ (similar to the population of GUVs with $\alpha > 130^o$) with values that ranged between 0.01 mN/m and 0.1 mN/m, suggesting the same coupling between LC elastic energy and a surface energy due to interfacial tension dictates the shapes adopted by all of the GUVs we observe in nematic 15 wt% DSCG.

These results hint that the local concentration of DSCG may be depleted near the surface of GUV membranes in our experiments, effectively creating an "interface" between DSCG-rich and DSCG-poor solutions that influences the bending of the membrane. Consistent with this hypothesis that DSCG becomes locally depleted near the GUV membrane, we note that upon heating GUV-containing samples, we observed isotropic domains to form first near the surface of GUVs (Figures 8-4C and 8-4D). In particular, we hypothesized that depletion of DSCG near

membrane surfaces might be promoted in our experiments by the presence of PEG-lipids within the lipid bilayer, as a previous study has reported that the addition of PEG to bulk DSCG solutions leads to condensation of higher order DSCG domains at a given temperature compared to DSCG solutions without PEG.[58] Condensation of these domains was attributed to depletion interactions, as PEG molecules likely become expelled from high order DSCG phases. To test this hypothesis, we created GUVs from lipid mixtures that did not contain any PEG-lipids (99.5 mol% DOPC/0.5 mol% BODIPY-DHPE). Although the yield of GUVs was very low in these nematic 15 wt% DSCG samples, the few GUVs we did observe all had $\alpha < 130^{o}$. Moreover, the values of $\tau_{optimal}$ calculated with Equation 8-4 for these GUVs with 0 mol% PEG-lipid were approximately independent of R/r with values of $\sim$ 0.1 mN/m, similar to what we measured for GUVs containing PEG-lipids (Figure 8-5B). This result suggests that DSCG becomes locally depleted near the surface of GUV membranes even in the absence of PEG-lipids and that the presence of small amounts ($\leq$ 2 mol%) of PEG-lipids in the GUVs does not dramatically change the physical properties of the membranes.

To provide insight regarding the LC elastic stresses acting on highly elongated GUVs with $\alpha < 130^{o}$, we characterized the configurations of the nematic DSCG phases inside and outside these GUVs (Figure 8-7). Whereas pronounced birefringent tails were found extending from the approximately rounded poles of GUVs with $\alpha > 130^{o}$ in the surrounding nematic LC, we did not observe this same optical signature in polarized light micrographs of highly elongated and cusped GUVs (Figures 8-7A through 8-7C). In fact, there typically were no discernable distortions in the continuous DSCG phase, suggesting that due to the slender shape of these GUVs and the tangential anchoring condition, the nematic DSCG outside the GUV is forced to deviate minimally away from the orientation of the far-field director. We note that Nych, et al.

also did not observe distortions of a nematic DSCG phase outside small (< 2 μm diameter) spherical inclusions.[16]

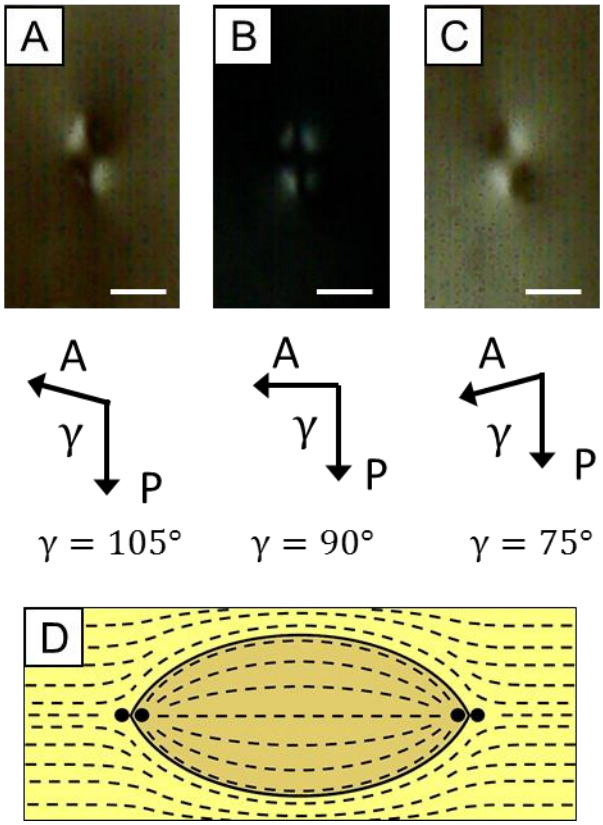

Figure 8-7. Configuration of nematic DSCG inside and outside of highly elongated GUVs (α < 130º).

(A-C) Polarized light micrographs of a GUV in which the angle between the polarizer and the analyzer is varied. (D) Schematic depicting the orientation of the LC inside and outside elongated and cusped GUVs. Scale bars = 5 μm.

We expected that inside the elongated and cusped GUVs, nematic DSCG would adopt a configuration similar to that previously observed in nematic tactoids. Almost exclusively, nematic tactoids have been reported to adopt a bipolar configuration with boojum defects located at the cusped poles,[17,21,28,59] although one report of a twisted configuration appearing in sessile tactoids exists.[60] In order to determine whether the LC inside these GUV twists, we collected polarized light micrographs with the polarizers oriented at various angles relative to each other

and observed the intensity of light transmission in the center of the GUV (Figures 8-7A through 8-7C). Consistent with an internal untwisted bipolar DSCG configuration, we only observed extinction of the light in this central region when the polarizers were set at 90 degrees relative to one another (Figure 8-7B).[60] Given that we did not observe twist distortions in the more nearly spherical GUVs above, this result is in agreement with the theoretical calculation of Prinsen and van der Schoot that twist distortions are less likely to develop in elongated, tactoid-shaped droplets than in spherical droplets of the same size.[61] We also note that we did not observe boojum defects positioned along the minor axis in bright field micrographs of these elongated and cusped GUVs as we did in the case of GUVs with approximately rounded poles. Based on these results, we conclude that nematic DSCG adopts configurations inside and outside these GUVs as depicted schematically in Figure 8-7D.

While most GUVs in our samples (and all of those analyzed above) exhibited a largely uniform fluorescence signal at their boundaries, consistent with an approximately "smooth" lipid bilayer, a smaller population of elongated and cusped GUVs had a striated appearance in fluorescence and optical micrographs (Figures 8-8A through 8-8D), consistent with the formation of folds or wrinkles in the lipid bilayer. These wrinkles in the lipid bilayer were always oriented along the elongated axis of the GUV. Others have previously reported the formation of wrinkles in GUVs possessing excess surface area[62,63] as well as in elastic, polymeric sheets stretched over millimeter-sized liquid droplets[64,65]. In our system, an excess of membrane area and a subsequent wrinkling instability could result in cases where long-lived pores in the membrane allow substantial amounts of 15 wt% DSCG solution to efflux from GUVs. In addition, we observed what we interpret to be lipid tubes[66,67] occasionally extending from the cusped poles of elongated and cusped GUVs (both wrinkled and unwrinkled) (Figure 8-

8E). Formation of lipid tubes, which can occur, for example, when an extensional force is applied to GUVs under high membrane tensions[68–71], might occur in our system as a consequence of LC-mediated elastic stresses driving the transformation of spherical GUVs to a highly elongated and cusped shape.

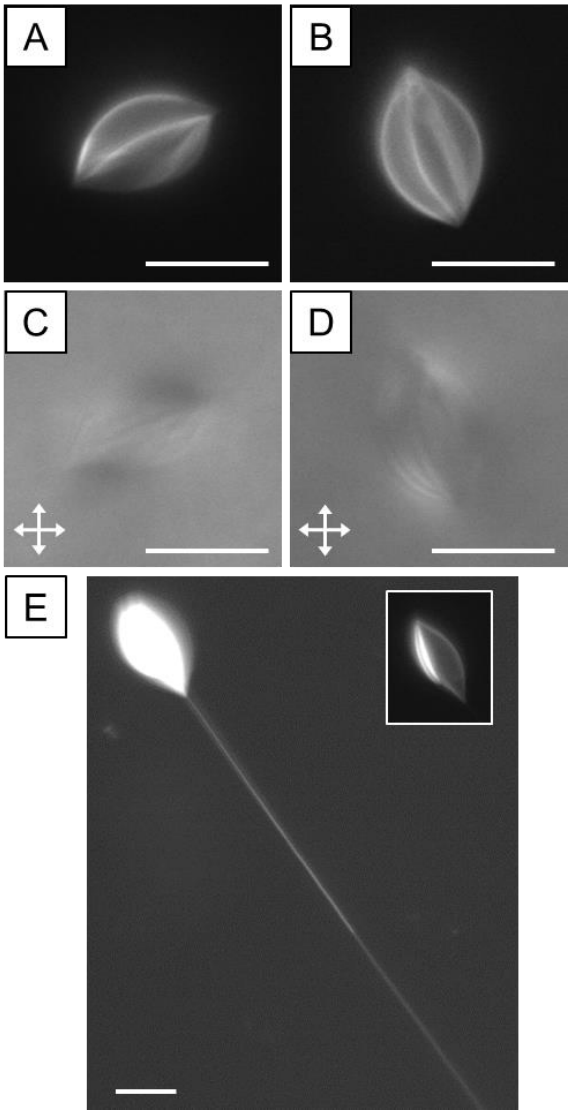

Figure 8-8. Wrinkled GUVs and GUV-associated lipid tubes in nematic 15 wt% DSCG.
(A, C) Fluorescence micrographs and (B, D) corresponding optical micrographs (crossed polarizers) of 2 mol% PEG-lipid GUVs in nematic 15 wt% DSCG at 25ºC. (E) Fluorescence micrograph of a cusped GUV with a lipid tube extending from its pole. The inset is a micrograph collected using a shorter exposure time. Scale bars = 10 μm.

8.4 Discussion

The results presented in this paper show that GUVs prepared in isotropic 15 wt% DSCG are deformed into elongated, non-spherical shapes upon quenching the solution into the nematic phase. The observation that these shape transformations accompany the DSCG phase transition suggests that elastic stresses imparted by the LC drive the GUV elongation. This conclusion is also supported by our demonstration that GUVs revert to a spherical shape upon heating the DSCG solution back into the isotropic phase. Moreover, our results indicate that two distinct populations of GUVs form in the nematic DSCG phase. We hypothesize that these two populations might emerge depending on whether or not elastic stresses imparted by the LC are sufficient in magnitude to lead to partial rupture and transient formation of pores in the GUVs.

The population of slightly elongated GUVs characterized by cusp angles of $\alpha > 130^{o}$ appears to form via a process involving the expansion of GUV surface area due to elastic stresses upon quenching from the isotropic to the nematic phase of DSCG while the GUV maintains constant volume. Given this hypothesis, we expected the equilibrium shapes of GUVs within this population in the nematic LC phase to reflect interplay between bulk LC elastic energy and the energy associated with stretching an elastic GUV membrane. However, our analysis of τ_{optimal} revealed it to be only a weak function of the fractional surface area expansion ε_{SA} (Figure 8-5A). Given this result, the energetic coupling appearing to underlie the shapes adopted by GUVs in this population seems to more closely resemble that which leads to the formation of elongated nematic tactoids in lyotropic LCs – coupling between LC elastic energy and a surface energy due to interfacial tension. We hypothesize that this unexpected result could be a consequence of local depletion of DSCG from the region near the surface of GUV membranes, although we note that

our analysis suggests that this depletion is not induced solely as a result of the presence of PEG-lipids.

On the other hand, our results suggest that the population of GUVs with $\alpha < 130^{o}$ likely forms through a process in which GUVs partially rupture due to high levels of strain within the membrane imparted by the nematic DSCG phase, allowing 15 wt% DSCG solution to efflux from the GUVs through transient pores in the membrane. This process allows GUVs to adopt highly elongated shapes that give rise to configurations of confined nematic DSCG that are distinct from those observed in the population of GUVs with $\alpha > 130^{o}$. Several experimental observations support this hypothesis, including our measurement that the elastic energy penalty associated with stretching a GUV membrane grows to become comparable to the surface energy arising due to interfacial tension for the smallest and most highly deformed GUVs in the population with $\alpha > 130^{o}$ (Figure 8-5A). Additionally, our analysis suggests that following the efflux of 15 wt% DSCG solution, the equilibrium shapes adopted by the population of highly elongated and cusped GUVs are influenced by the same balance between LC elastic energy and surface energy arising due to interfacial tension that sets the shapes of the population of GUVs with $\alpha > 130^{o}$ (Figure 8-5B). We note that although this coupling is reminiscent of that which gives rise to the equilibrium shape of nematic tactoids dispersed in continuous isotropic phases in lyotropic LCs, we measure the aspect ratios of GUVs in our system to vary more dramatically as a function of GUV size than what has been reported for nematic tactoids. Specifically, whereas a recent study reports the aspect ratios of tactoids that form in dispersions of carbon nanotubes in chlorosulfonic acid to vary between 2 and 6 for tactoids characterized by major axes ranging from 5 to 200 μm in length,[72] in our system we measure the aspect ratios of GUVs to vary between 1 and 10 for GUVs with major axis lengths between 2.5 μm and 50 μm.

On extremely rare occasions, while analyzing GUVs in nematic 15 wt% DSCG solutions, we observed that GUVs could spontaneously undergo sudden transformations in shape. Specifically, we have observed one example in which a slightly elongated GUV with $\alpha > 130^{o}$ transformed into a highly elongated and cusped shape with $\alpha < 130^{o}$ as well as one example of the inverse transformation. We note that in both of these instances, the surface area of these shape-changing GUVs was between 50 μm^2 and 500 μm^2, the range of GUV sizes in which we commonly found GUVs to exhibit cusp angles of both $\alpha > 130^{o}$ and $\alpha < 130^{o}$ in our samples (Figure 8-2H). These isolated observations hint that our system may exhibit bistability.

In a previous study by Varghese, et al.,[73] it was shown that the addition of certain anionic and nonionic surfactants at very high concentrations (> 6 wt%) gave rise to surfactant-decorated nematic domains when dispersed in 5.5 wt% DSCG solutions at room temperature, conditions at which DSCG solutions ordinarily exhibit an isotropic phase. The authors suggest that the formation of these nematic domains, which were both tactoidal and spherical in shape, might proceed through the formation of lipid bilayers surrounding these domains. However, reports that the addition of similar high concentrations of non-amphiphilic molecules, such as PVA,[74] PEG,[58] and spermine[58] condense DSCG solutions and lead to the formation of nematic and columnar phase domains suggest the nematic domains observed by Varghese, et al.[73] are not GUVs. Condensation of DSCG into higher order phases by polymers is likely the result of depletion effects while electrostatic interactions also may contribute in the case of spermine.[58] We suspect that these effects may also contribute to condensation of nematic DSCG domains in the study of Varghese, et al.[73] In contrast, we note that a very small amount of lipid (~ 0.04 wt%) is dispersed in DSCG solutions in our experimental procedure, hinting that nematic domains form in our experiments via a mechanism distinct from any of these past studies. We also note that we did

not observe nematic LC phases to form inside or outside GUVs prepared via gentle hydration of lipid films with 5.5 wt% DSCG (Figure 8-S2).

We note before concluding that our GUV samples in nematic 15 wt% DSCG were frequently marked by additional heterogeneity beyond the two most common GUV populations that we focused on above. For example, we often observed that domains exhibiting heightened fluorescence were localized near one or both of the poles of slightly elongated GUVs (Figures 8-9A and 8-9B). Similar regions displaying a heightened fluorescence signal rarely were localized near the cusped poles of highly elongated GUVs. We note that we observed these domains of heightened fluorescence near the poles of GUV poles with $\alpha > 130^{o}$ both when the fluorescently-tagged lipid species was BODIPY-DHPE as well as DSPE-PEG-2000-CF. We hypothesize that the polar localization of these domains may be the result of aggregates of lipid partitioning to the sites of defects in the nematic DSCG phase outside the GUV to reduce strain in the LC within these highly strained regions,[75,76] although curvature strain within the GUV membrane might be responsible if this phenomenon instead reflects phase separation within the lipid bilayer.[30,31] We also identified examples of multiple GUVs interacting with one another in nematic DSCG (Figures 8-9C and 8-9D). It was unclear in these examples whether these interactions were the result of a “budding” process or the association and fusing of two initially separated GUVs.

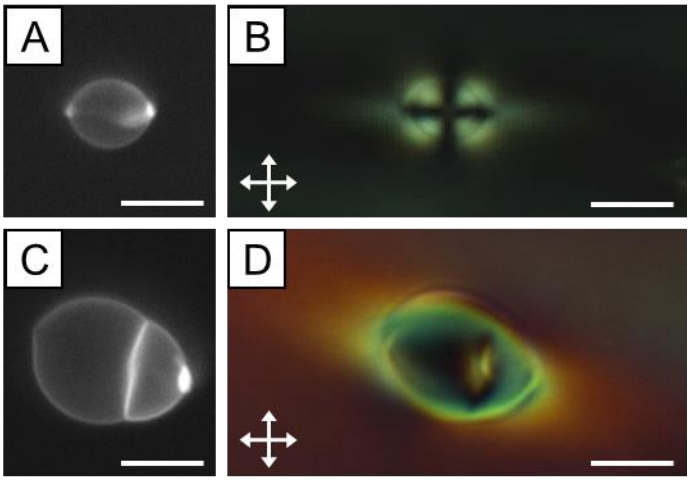

Figure 8-9. "Exotic" structures of GUVs in nematic 15 wt% DSCG.
(A, B) Fluorescence and crossed polars micrographs, respectively, of a GUV with regions of enhanced fluorescence signal at the poles. (C, D) Fluorescence and crossed polars micrographs, respectively, of two GUVs that are either fused together or in which a smaller GUV is budding from the larger GUV. Scale bars = 10 μm.

8.5 Conclusions

In conclusion, this paper reports a facile method to create elongated, non-spherical GUVs by utilizing an aqueous lyotropic chromonic LC. Specifically, we demonstrate that the GUV membranes are deformed from initially spherical shapes into two distinct classes of non-spherical shapes by elastic stresses imparted by the nematic LC phase. Whereas we find the formation of a population of slightly elongated GUVs with $\alpha > 130^{o}$ to be consistent with expansion of lipid membrane surface area at constant GUV volume, our results suggest formation of highly elongated GUVs with $\alpha < 130^{o}$ involves a loss of 15 wt% DSCG from GUVs, perhaps through transient pores that form in the membrane.

Our analysis of the interplay between LC elastic energy and the interfacial energy of GUVs that dictates the shapes adopted by GUVs leads to the surprising conclusion that the

interfacial energy of the GUVs is dominated by some surface energy arising due to an interfacial tension rather than an energy associated with stretching the GUV membrane. This result, in addition to our observation that isotropic domains nucleate near the surface of GUVs at temperatures ~1ºC lower than in the bulk 15 wt% DSCG solution, suggests a local depletion of DSCG near the GUV membrane surface. This depletion of DSCG appears to significantly influence the energetic coupling that sets the shapes adopted by elastically strained GUVs in our experiments. Overall, these insights and others regarding the coupling between LC elastic strain and strain within flexible lipid membranes developed in this study should guide future fundamental studies of GUVs and other soft, deformable particles in LCs.

In addition, the demonstrated coupling between particle shape and strain within nematic LCs suggests new possibilities for the design of LC-based systems that exhibit potentially useful dynamical and equilibrium behaviors. In particular, we envision that these elastically strained GUVs might be attractive model cell membranes and could serve as versatile synthetic platforms to investigate further, for example, how curvature strain influences localization of lipids and proteins in biological membranes. We also note that the possibility to dynamically and reversibly switch GUVs between isometric and anisometric shapes simply by adjusting the temperature to change the phase of the DSCG solution is a unique and attractive feature of this system that might be employed in biophysical studies or in other potential applications.

Acknowledgements

This work was supported by the National Science Foundation (under awards DMR-1121288 (MRSEC) and CBET-1263970), the National Institutes of Health (CA108467 and AI092004), and the Army Research Office (W911-NF-11-1-0251 and W911-NF-14-1-0140).

8.6 Supporting Information

GUVs in isotropic 15 wt% DSCG at 50ºC

Prior to quenching experimental samples containing vesicles formed in 15 wt% DSCG solution from 50ºC to 25ºC, although a majority of vesicles were spherical in shape, we also observed a significant number of non-spherical vesicles as well as vesicles that possessed more than one lamellae (Figure 8-S3). Such non-spherical and oligolamellar vesicles also appeared when we prepared and characterized vesicles in other isotropic solutions, such as pure water (Figures 8-S4 and 8-S5). Included in the diverse GUV shapes we observed were slightly elongated prolate and oblate GUVs, fused GUVs comprised of multiple compartments, and tubular membranes (that we occasionally observed to exhibit pearling instabilities[77]. Moreover, the membranes of these non-spherical GUVs are highly "floppy" and exhibit dynamic undulations and shape changes as a result of thermal fluctuations. Such fluctuating, non-spherical GUVs have been shown to form in isotropic solutions when GUVs possess excess membrane area as a result of osmotic pressure differences or fusion events between multiple GUVs and also when a mismatch exists between the number of lipids comprising the inner and outer leaflets of a lipid bilayer forming a GUV.[66,78–80] We suspect this apparent diversity of GUV shapes in isotropic 15 wt% DSCG might contribute to the resulting varied landscape of shapes GUVs adopt upon quenching the solution into the nematic phase. For example, we hypothesize that the excess surface area exhibited by non-spherical GUVs in the isotropic phase might lead to the formation of wrinkles (Figures 8-8A through 8-8D) upon quenching to the nematic DSCG phase. We note, however, that it is not exclusively this population of initially non-spherical GUVs that adopts elongated shapes in the nematic LC (see, for example, Video S1 in the online Supporting Information). In addition, we note that such thermal shape fluctuations were entirely suppressed

in GUVs upon quenching into the nematic DSCG phase, consistent with previous studies showing that shape fluctuations vanish upon application of even small (~0.001 mN/m) tensions to GUVs[81,82].

Quantitative analysis of GUVs

The analysis of the GUVs was performed in MATLAB using a custom analysis script. First, the user inputs the objective lens utilized (60× or 100×) to collect the image to be used later to convert from pixels to μm. Next, the image was imported and the region with the GUV to be analyzed is selected using a graphical user interface (GUI). The selected GUV is thresholded to be used to perform edge detection and a user drawn line is input on the thresholded image to bisect the GUV from one cusp to the other. Using a GUI, the user may choose to erase regions around the GUV boundary that the threshold was unable to remove due to intensity gradients within the microscope image. High intensity regions that might cause overexposure within the image and blur the boundary are masked, if necessary, so that the pixels are not included in the edge data when performing the fit. The boundary of the GUV is then detected, the high intensity masked pixels are removed, and each half of the bisected GUV is fit to a circle, where the center and radius are determined by the fit (Figure 8-S7). The major and minor axes of the GUV are determined respectively from the point of intersection of the two circles and the points where a line connecting the circle centers intersect with each circle. These lengths are used to calculate the aspect ratio of the GUV. Finally, the cusp angles of the GUV are calculated from the circular fit of the GUV by the angle between the tangent lines of both circles at each intersection point.

From this analysis, we found that two distinct populations of GUVs formed in our samples: slightly elongated GUVS with rounded poles ($\alpha > 130^{o}$) and highly elongated and

cusped GUVs ($\alpha < 130^{o}$) (see main text for details). The GUVs in the population with $\alpha > 130^{o}$ were approximately prolate spheroidal in shape. So, to quantify the surface area and volume of these GUVs, we used the expressions

$$SA_{\alpha > 130^{\circ}} = 2\pi r^2 \left[1 + \frac{R}{r\delta}\sin^{-1}(\delta)\right]$$

$$V_{\alpha > 130^{\circ}} = \frac{4}{3}\pi R r^2$$

where $\delta^2 = 1 - \frac{r^2}{R^2}$. The semi-major axis (R) and semi-minor axis (r) of GUVs were measured using the MATLAB script.

Alternatively, the shapes of GUVs in the population with $\alpha < 130^{o}$ were best described as bodies of revolution of parabolic curves. Thus, we quantified the surface area and volume of these GUVs using the expressions

$$SA_{\alpha < 130^{\circ}} = \frac{\pi}{16r^2}\left[2r(8r^2 - R^2)\sqrt{4r^2 + R^2} + (16r^2R^2 + R^4)\sinh^{-1}\left(\frac{2r}{R}\right)\right]$$

$$V_{\alpha < 130^{\circ}} = \frac{16}{15}\pi R r^2$$

where R and r are again the semi-major and semi-minor axis of GUVs, respectively.

<u>Observations of GUV-containing samples at temperatures within the two-phase coexistence range of DSCG</u>

In Figure 8-S8, additional micrographs collected at tempetaures within the two-phase nematic-isotropic coexistence range during the temperature ramp and quench experiments described in the main text (Figure 8-4) are presented. During the heating of the GUV-containing sample, following the nucleation of isotropic domains near the surface of a GUV membrane (Figures 8-4C and 8-4D), isotropic domains subsequently also appeared within the bulk of the

continuous DSCG phase. As these isotropic domains grew in size, we found GUVs to be pushed along by the advancing nematic-isotropic interfaces defined by the domains (Figures 8-S8A and 8-S8B). Interestingly, as we continued to increase the temperature within the two phase coexistence range of DSCG, we frequently observed a circular disc-shaped nematic domain to form inside of GUVs separating two isotropic domains (Figures 8-S8C and 8-S8D) prior to the DSCG solution throughout the sample transitioning to the isotropic phase (Figures 8-4E and 8-F).

Upon cooling the sample, nematic domains nucleated inside of GUVs (Figures 8-S8E and 8-S8F) at temperatures approximately 2.5ºC lower than outside of the GUVs (Figures 8-4I and 8-4J). As the temperature of the sample was further reduced, the nematic phase domains grew inside and outside of the GUVs (Figures 8-S8G and 8-S8H) until no isotropic domains remained (Figures 8-4K and 8-4L).

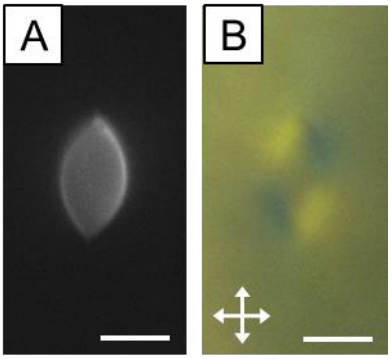

Figure 8-S1. Uniform distribution of PEG-lipid in GUVs prepared in 15 wt% DSCG.

(A, B) Fluorescence and crossed polars micrographs, respectively, of a DOPC/DSPE-PEG-2000-CF GUV in nematic 15 wt% DSCG at 25ºC. We observed the encapsulating lipid bilayer of each GUVs prepared with this lipid mixture to exhibit a uniform fluorescence signal, suggesting that PEG-lipids do not phase separate within the bilayers. Scale bars = 5 µm.

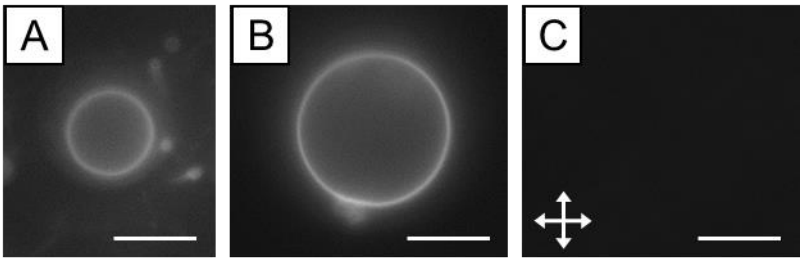

Figure 8-S2. GUVs prepared in isotropic solutions at 25ºC.

(A) Fluorescence micrograph of a DOPC/DOPE-PEG2000/BODIPY-DHPE GUV in water. (B, C) Fluorescence and crossed polars micrographs, respectively, of a DOPC/DOPE-PEG2000/BODIPY-DHPE GUV in 5.5 wt% DSCG. Scale bars = 10 µm.

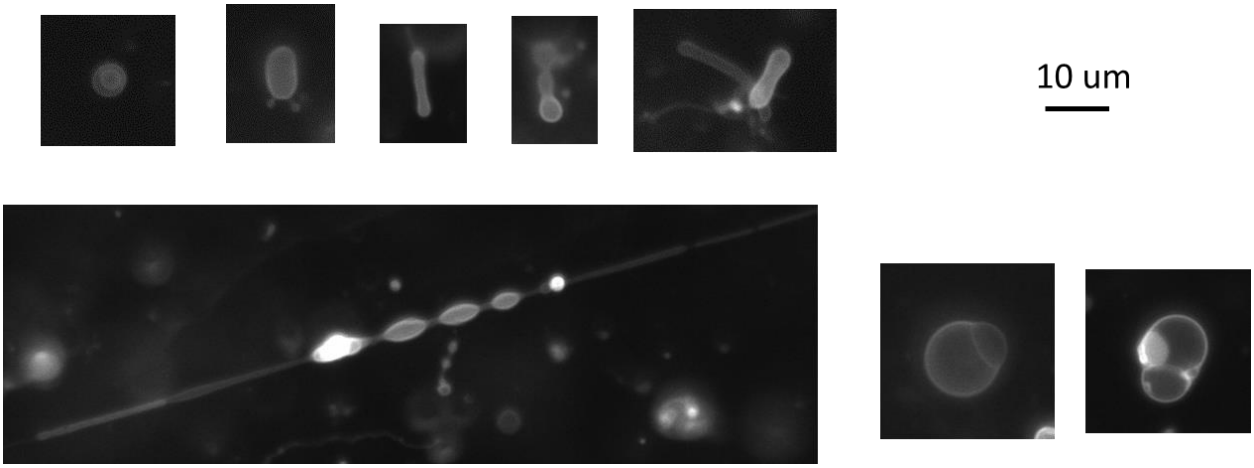

Figure 8-S3. Examples of non-spherical GUVs as well as vesicles exhibiting "onion-like" structures in isotropic 15 wt% DSCG at 50ºC.

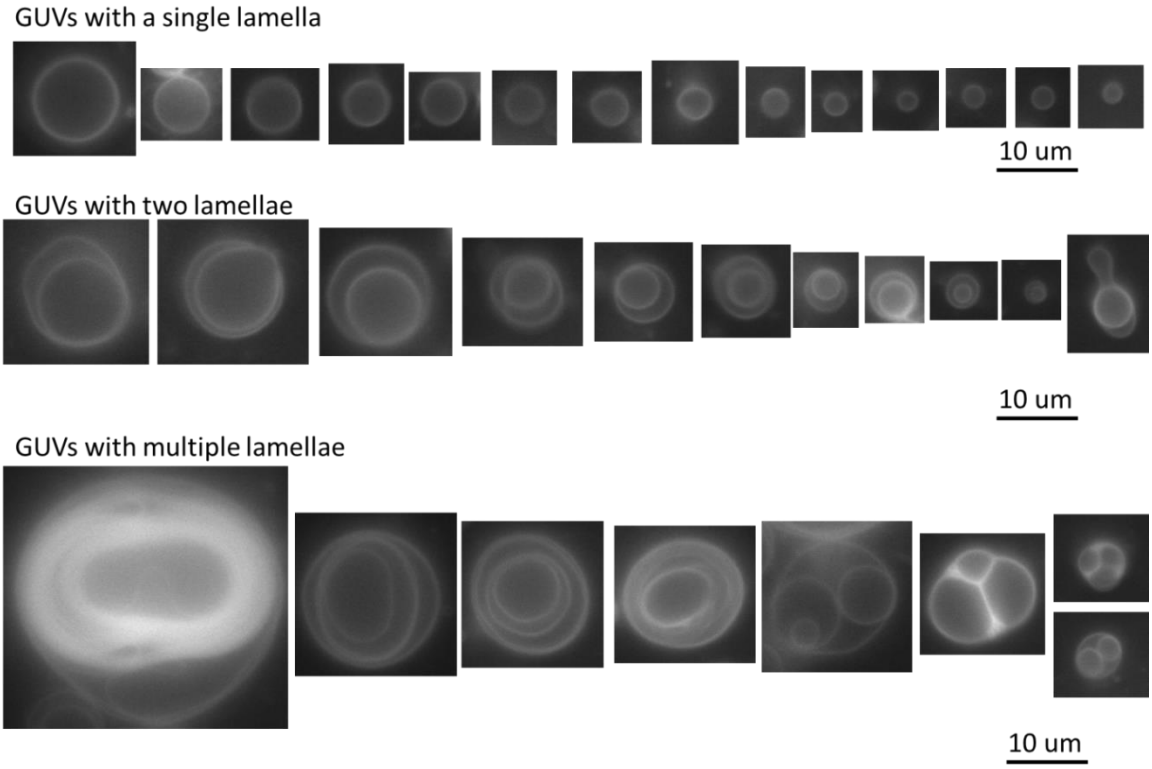

Figure 8-S4. Examples of spherical unilamellar GUVs as well as vesicles exhibiting "onion-like" structures in DI water at 25ºC.

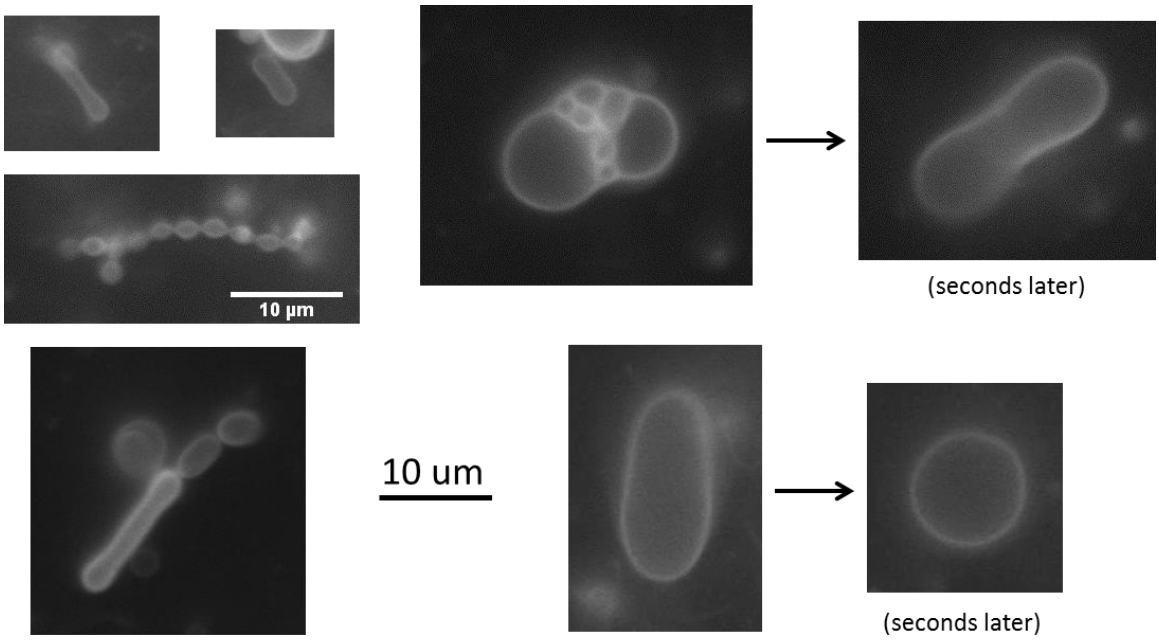

Figure 8-S5. Examples of non-spherical GUVs prepared in DI water at 25ºC.

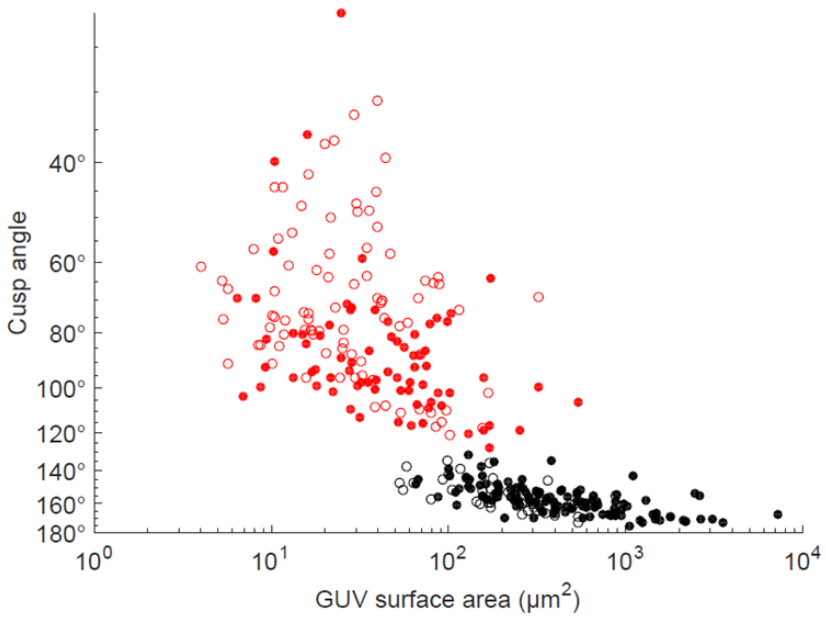

Figure 8-S6. Plot of GUV cusp angle (α) as a function of surface area for GUVs in nematic 15 wt% DSCG.

Data in red denote GUVs with cusp angles $\alpha < 130^{o}$ and data in black denote GUVs with cusp angles $\alpha > 130^{o}$. Filled points denote GUVs containing 2 mol% PEG-lipid and unfilled points denote GUVs containing 0.2 mol% PEG-lipid.

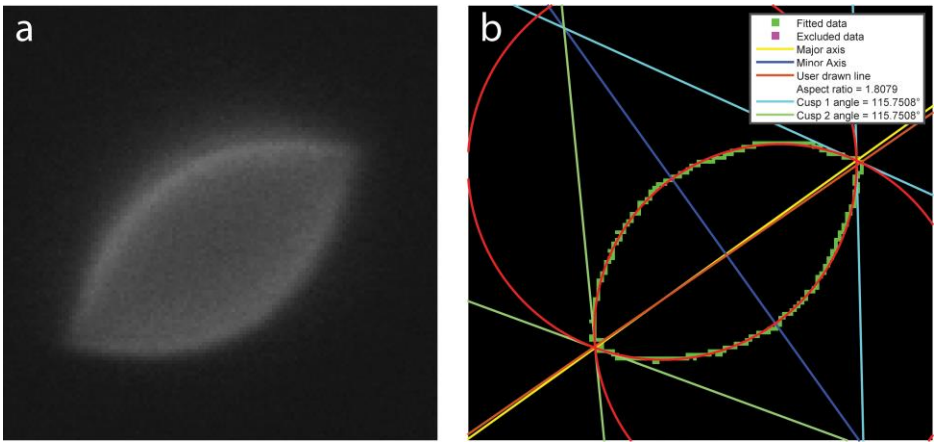

Figure 8-S7. Quantitative analysis of GUVs.

(a) Fluorescence micrograph of a GUV in nematic 15 wt% DSCG and (b) the resulting fit from the GUV perimeter (pixels in green), including both circular fits (red lines), the user drawn line (orange line), the major and minor axes of the GUV calculated from the circular fits (yellow and blue lines respectively), and the cusp angles calculated as the angle between the light green lines and separately the light blue lines. The aspect ratio is calculated using the major and minor axis lengths of the GUV.

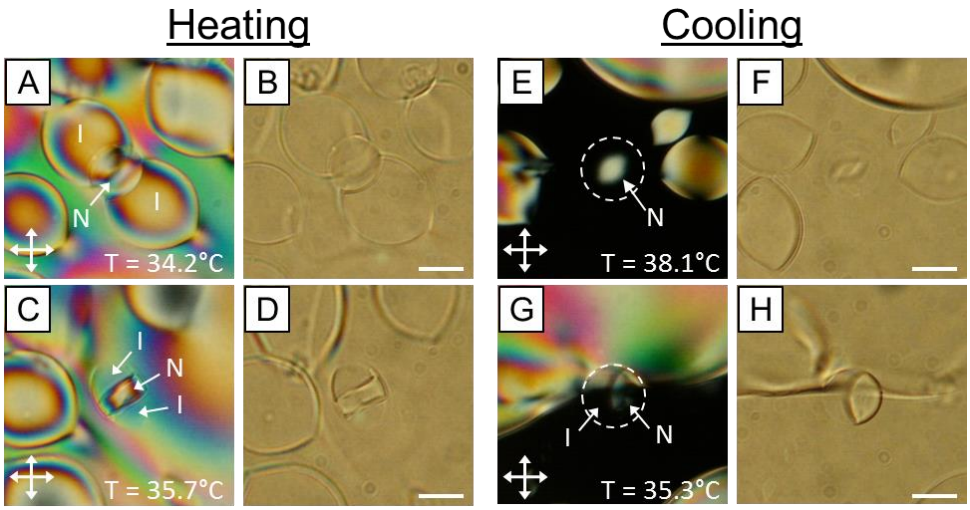

Figure 8-S8. Micrographs of a GUV-containing sample obtained at temperatures within the two-phase nematic-isotropic coexistence range of DSCG.

Crossed polars and corresponding bright field micrographs were collected at the temperatures indicated in the figure while (A – D) heating the sample from 26ºC to 50ºC and (E – H) subsequently cooling the sample from 50ºC to 26ºC at a rate of ~0.5ºC/min. Dotted lines outline the GUV in crossed polars micrographs when the internal DSCG solution is largely in its isotropic phase. The phase (nematic (N) or isotropic (I)) of selected DSCG domains is indicated in the figure. Scale bars = 20 µm.

Supplementary Video Captions

Following the publication of this manuscript, supporting videos will be available in the online SI.

Video S1. Bright field microscopy video of a GUV changing shape in 15 wt% DSCG as the sample is quenched from 50°C to 25°C . Played at 20X speed.

Video S2. Bright field microscopy video of a GUV changing shape in 15 wt% DSCG as the sample is heated from 25°C to 50°C. Played at 10X speed.

Video S3. Z-stack of fluorescence images obtained via confocal microscopy of a GUV in nematic 15 wt% DSCG at 25°C.

Video S4. Z-stack of fluorescence images obtained via confocal microscopy of a GUV in nematic 15 wt% DSCG at 25°C.

Video S5. Polarized light (crossed polarizers) microscopy video of a GUV in 15 wt% DSCG as the sample is quenched from 50°C to 26°C at 0.5ºC/min. Field of view has width = 350 µm.

8.7 References

*This chapter was in preparation for submission to a peer-reviewed journal as a Full Paper reporting original research at the time of publication of this thesis. Joel Pendery wrote the MATLAB code to analyze experimental data. Saverio Spagnolie performed mathematical modeling of GUVs in nematic LCs.

1. Khoo, I. C.; Werner, D. H.; Liang, X.; Diaz, A. Nanosphere Dispersed Liquid Crystals for Tunable Negative-Zero-Positive Index of Refraction in the Optical and Terahertz Regimes. *Opt. Lett.* **2006**, 31, 2592–2594.
2. Musevic, I.; Škarabot, M.; Tkalec, U.; Ravnik, M.; Žumer, S. Two-Dimensional Nematic Colloidal Crystals Self-Assembled by Topological Defects. *Science* **2006**, 313, 954–958.
3. Škarabot, M.; Ravnik, M.; Žumer, S.; Tkalec, U.; Poberaj, I.; Babič, D.; Muševič, I. Hierarchical Self-Assembly of Nematic Colloidal Superstructures. *Phys. Rev. E* **2008**, 77, 061706.
4. Lev, B.; Chernyshuk, S.; Yamamoto, T.; Yamamoto, J.; Yokoyama, H. Photochemical Switching between Colloidal Photonic Crystals at the Nematic-Air Interface. *Phys. Rev. E* **2008**, 78, 020701.
5. Senyuk, B.; Smalyukh, I. I. Elastic Interactions between Colloidal Microspheres and Elongated Convex and Concave Nanoprisms in Nematic Liquid Crystals. *Soft Matter* **2012**, 8, 8729–8734.
6. Draper, M.; Saez, I. M.; Cowling, S. J.; Gai, P.; Heinrich, B.; Donnio, B.; Guillon, D.; Goodby, J. W. Self-Assembly and Shape Morphology of Liquid Crystalline Gold Metamaterials. *Adv. Funct. Mater.* **2011**, 21, 1260–1278.
7. Lapointe, C. P.; Mason, T. G.; Smalyukh, I. I. Shape-Controlled Colloidal Interactions in Nematic Liquid Crystals. *Science* **2009**, 326, 1083–1086.
8. Senyuk, B.; Evans, J. S.; Ackerman, P. J.; Lee, T.; Manna, P.; Vigderman, L.; Zubarev, E. R.; van de Lagemaat, J.; Smalyukh, I. I. Shape-Dependent Oriented Trapping and Scaffolding of Plasmonic Nanoparticles by Topological Defects for Self-Assembly of Colloidal Dimers in Liquid Crystals. *Nano Lett.* **2012**, 12, 955–963.
9. Senyuk, B.; Liu, Q.; He, S.; Kamien, R. D.; Kusner, R. B.; Lubensky, T. C.; Smalyukh, I. I. Topological Colloids. *Nature* **2013**, 493, 200–205.
10. Liu, Q.; Senyuk, B.; Tasinkevych, M.; Smalyukh, I. I. Nematic Liquid Crystal Boojums with Handles on Colloidal Handlebodies. *Proc. Natl. Acad. Sci.* **2013**, 110, 9231–9236.
11. Tkalec, U.; Škarabot, M.; Muševič, I. Interactions of Micro-Rods in a Thin Layer of a Nematic Liquid Crystal. *Soft Matter* **2008**, 4, 2402–2409.
12. Chandran, S. P.; Mondiot, F.; Mondain-Monval, O.; Loudet, J. C. Photonic Control of Surface Anchoring on Solid Colloids Dispersed in Liquid Crystals. *Langmuir* **2011**, 27, 15185–15198.
13. Conradi, M.; Ravnik, M.; Bele, M.; Zorko, M.; Žumer, S.; Muševič, I. Janus Nematic Colloids. *Soft Matter* **2009**, 5, 3905–3912.
14. Jeong, J.; Davidson, Z. S.; Collings, P. J.; Lubensky, T. C.; Yodh, A. G. Chiral Symmetry Breaking and Surface Faceting in Chromonic Liquid Crystal Droplets with Giant Elastic Anisotropy. *Proc. Natl. Acad. Sci.* **2014**, 111, 1742–1747.

15. Jeong, J.; Kang, L.; Davidson, Z. S.; Collings, P. J.; Lubensky, T. C.; Yodh, A. G. Chiral Structures from Achiral Liquid Crystals in Cylindrical Capillaries. *Proc. Natl. Acad. Sci.* **2015**, 112, E1837-E1844.
16. Nych, A.; Ognysta, U.; Muševič, I.; Seč, D.; Ravnik, M.; Žumer, S. Chiral Bipolar Colloids from Nonchiral Chromonic Liquid Crystals. *Phys. Rev. E* **2014**, 89, 062502.
17. Kaznacheev, A. V; Bogdanov, M. M.; Taraskin, S. A. The Nature of Prolate Shape of Tactoids in Lyotropic Inorganic Liquid Crystals. *J. Exp. Theor. Phys.* **2002**, 95, 57–63.
18. Kaznacheev, A. V; Bogdanov, M. M.; Sonin, A. S. The Influence of Anchoring Energy on the Prolate Shape of Tactoids in Lyotropic Inorganic Liquid Crystals. *J. Exp. Theor. Phys.* **2003**, 97, 1159–1167.
19. Prinsen, P.; van der Schoot, P. Shape and Director-Field Transformation of Tactoids. *Phys. Rev. E* **2003**, 68, 021701.
20. Nastishin, Y. A.; Liu, H.; Schneider, T.; Nazarenko, V.; Vasyuta, R.; Shiyanovskii, S. V; Lavrentovich, O. D. Optical Characterization of the Nematic Lyotropic Chromonic Liquid Crystals: Light Absorption, Birefringence, and Scalar Order Parameter. *Phys. Rev. E* **2005**, 72, 041711.
21. Kim, Y.-K.; Shiyanovskii, S. V; Lavrentovich, O. D. Morphogenesis of Defects and Tactoids during Isotropic-Nematic Phase Transition in Self-Assembled Lyotropic Chromonic Liquid Crystals. *J. Phys. Condens. Matter* **2013**, 25, 404202.
22. Mushenheim, P. C.; Trivedi, R. R.; Roy, S. S.; Arnold, M. S.; Weibel, D. B.; Abbott, N. L. Effects of Confinement, Surface-Induced Orientations and Strain on Dynamical Behaviors of Bacteria in Thin Liquid Crystalline Films. Submitted for publication.
23. Lavrentovich, O. D.; Lazo, I.; Pishnyak, O. P. Nonlinear Electrophoresis of Dielectric and Metal Spheres in a Nematic Liquid Crystal. *Nature* **2010**, 467, 947–950.
24. Lazo, I.; Lavrentovich, O. D. Liquid Crystal-Enabled Electrophoresis of Spheres in a Nematic Medium with Negative Dielectric Anisotropy. *Philos. Trans. R. Soc. London, Ser. A* **2013**, 371, 20120255.
25. Kumar, A.; Galstian, T.; Pattanayek, S. K.; Rainville, S. The Motility of Bacteria in an Anisotropic Liquid Environment. *Mol. Cryst. Liq. Cryst.* **2013**, 574, 33–39.
26. Zhou, S.; Sokolov, A.; Lavrentovich, O. D.; Aranson, I. S. Living Liquid Crystals. *Proc. Natl. Acad. Sci.* **2014**, 111, 1265–1270.
27. Mushenheim, P. C.; Trivedi, R. R.; Tuson, H. H.; Weibel, D. B.; Abbott, N. L. Dynamic Self-Assembly of Motile Bacteria in Liquid Crystals. *Soft Matter* **2014**, 10, 88–95.
28. Mushenheim, P. C.; Trivedi, R. R.; Weibel, D. B.; Abbott, N. L. Using Liquid Crystals to Reveal How Mechanical Anisotropy Changes Interfacial Behaviors of Motile Bacteria. *Biophys. J.* **2014**, 107, 255–265.
29. Sokolov, A.; Zhou, S.; Lavrentovich, O. D.; Aranson, I. S. Individual Behavior and Pairwise Interactions between Microswimmers in Anisotropic Liquid. *Phys. Rev. E* **2015**, 91, 013009.
30. Renner, L. D.; Weibel, D. B. Cardiolipin Microdomains Localize to Negatively Curved Regions of *Escherichia coli* Membranes. *Proc. Natl. Acad. Sci.* **2011**, 108, 6264–6269.
31. Renner, L. D.; Eswaramoorthy, P.; Ramamurthi, K. S.; Weibel, D. B. Studying Biomolecule Localization by Engineering Bacterial Cell Wall Curvature. *PLoS One* **2013**, 8, e84143.

32. Nastishin, Y. A.; Liu, H.; Shiyanovskii, S. V.; Lavrentovich, O. D.; Kostko, A. F.; Anisimov, M. A. Pretransitional Fluctuations in the Isotropic Phase of a Lyotropic Chromonic Liquid Crystal. *Phys. Rev. E* **2004**, 70, 051706.
33. Champion, J. V; Meeten, G. H. Conformation of Sodium Cromolyn in Aqueous Solution Using Light Scattering and Magnetic Birefringence. *J. Pharm. Sci.* **1973**, 62, 1589–1595.
34. Akashi, K.; Miyata, H.; Itoh, H.; Kinosita, K. Preparation of Giant Liposomes in Physiological Conditions and Their Characterization under an Optical Microscope. *Biophys. J.* **1996**, 71, 3242–3250.
35. Yamashita, Y.; Oka, M.; Tananka, T.; Yamazaki, M. A New Method for the Preparation of Giant Liposomes in High Salt Concentrations and Growth of Protein Microcrystals in Them. *Biochim. Biophys. Acta* **2002**, 1561, 129–134.
36. Marsh, D. Elastic Constants of Polymer-Grafted Lipid Membranes. *Biophys. J.* **2001**, 81, 2154–2162.
37. Marsh, D.; Bartucci, R.; Sportelli, L. Lipid Membranes with Grafted Polymers : Physicochemical Aspects. *Biochem. Biophys. Acta* **2003**, 1615, 33–59.
38. Rawicz, W.; Olbrich, K. C.; Mcintosh, T.; Needham, D.; Evans, E. Effect of Chain Length and Unsaturation on Elasticity of Lipid Bilayers. *Biophys. J.* **2000**, 79, 328–339.
39. Olbrich, K.; Rawicz, W.; Needham, D.; Evans, E. Water Permeability and Mechanical Strength of Polyunsaturated Lipid Bilayers. *Biophys. J.* **2000**, 79, 321–327.
40. Rawicz, W.; Smith, B. A.; Mcintosh, T. J.; Simon, S. A.; Evans, E. Elasticity, Strength, and Water Permeability of Bilayers That Contain Raft Microdomain-Forming Lipids. *Biophys. J.* **2008**, 94, 4725–4736.
41. Agra-Kooijman, D. M.; Singh, G.; Lorenz, A.; Collings, P. J.; Kitzerow, H.-S.; Kumar, S. Columnar Molecular Aggregation in the Aqueous Solutions of Disodium Cromoglycate. *Phys. Rev. E* **2014**, 89, 062504.
42. Zhou, S.; Neupane, K.; Nastishin, Y. A.; Baldwin, A. R.; Shiyanovskii, S. V; Lavrentovich, O. D.; Sprunt, S. Elasticity, Viscosity, and Orientational Fluctuations of a Lyotropic Chromonic Nematic Liquid Crystal. *Soft Matter* **2014**, 10, 6571–6581.
43. Idiart, M. A.; Levin, Y. Rupture of a Liposomal Vesicle. *Phys. Rev. E* **2004**, 69, 061922.
44. Mushenheim, P. C.; Abbott, N. L. Hierarchical Organization in Liquid Crystal-in-Liquid Crystal Emulsions. *Soft Matter* **2014**, 10, 8627–8634.
45. Zhou, S.; Neupane, K.; Nastishin, Y. A.; Baldwin, A. R.; Shiyanovskii, S. V; Lavrentovich, O. D.; Sprunt, S. Elasticity, Viscosity, and Orientational Fluctuations of a Lyotropic Chromonic Nematic Liquid Crystal. *Soft Matter* **2014**, 10, 6571–6581.
46. Williams, R. Two Transitions in Tangentially Anchored Nematic Droplets. *J. Phys. A Math. Gen.* **1986**, 19, 3211–3222.
47. Lavrentovich, O. D.; Sergan, V. V. Parity-Breaking Phase Transition in Tangentially Anchored Nematic Drops. *Nuovo Cim. D* **1990**, 12, 1219–1222.
48. Zhou, S.; Nastishin, Y. A.; Omelchenko, M. M.; Tortora, L.; Nazarenko, V. G.; Boiko, O. P.; Ostapenko, T.; Hu, T.; Almasan, C. C.; Sprunt, S. N.; Gleeson, J. T.; Lavrentovich, O. D. Elasticity of Lyotropic Chromonic Liquid Crystals Probed by Director Reorientation in a Magnetic Field. *Phys. Rev. Lett.* **2012**, 109, 037801.
49. Lee, H.; Labes, M. M. Phase Diagram and Thermodynamic Properties of Disodium Cromoglycate-Water Lyomesophases. *Mol. Cryst. Liq. Cryst.* **1983**, 91, 53–58.

50. Marmottant, P.; Biben, T.; Hilgenfeldt, S. Deformation and Rupture of Lipid Vesicles in the Strong Shear Flow Generated by Ultrasound-Driven Microbubbles. *Proc. R. Soc. A* **2008**, 464, 1781–1800.
51. Taupin, C.; Dvolaitzky, M.; Sauterey, C. Osmotic Pressure Induced Pores in Phospholipid Vesicles. *Biochemistry* **1975**, 14, 4771–4775.
52. Needham, D.; Nunn, R. S. Elastic Deformation and Failure of Lipid Bilayer Membranes Containing Cholesterol. *Biophys. J.* **1990**, 58, 997–1009.
53. Sandre, O.; Moreaux, L.; Brochard-Wyart, F. Dynamics of Transient Pores in Stretched Vesicles. *Proc. Natl. Acad. Sci.* **1999**, 96, 10591–10596.
54. Nourian, Z.; Roelofsen, W.; Danelon, C. Triggered Gene Expression in Fed-Vesicle Microreactors with a Multifunctional Membrane. *Angew. Chem. Int. Ed. Engl.* **2012**, 51, 3114–3118.
55. Brochard-Wyart, F.; de Gennes, P. G.; Sandre, O. Transient Pores in Stretched Vesicles : Role of Leak-Out. *Physica A* **2000**, 278, 32–51.
56. Ohno, M.; Hamada, T.; Takiguchi, K.; Homma, M. Dynamic Behavior of Giant Liposomes at Desired Osmotic Pressures. *Physica A* **2009**, 25, 17669–17674.
57. Levin, Y.; Idiart, M. A. Pore Dynamics of Osmotically Stressed Vesicles. *Physica A* **2004**, 331, 571–578.
58. Tortora, L.; Park, H.-S.; Kang, S.-W.; Savaryn, V.; Hong, S.-H.; Kaznatcheev, K.; Finotello, D.; Sprunt, S.; Kumar, S.; Lavrentovich, O. D. Self-Assembly, Condensation, and Order in Aqueous Lyotropic Chromonic Liquid Crystals Crowded with Additives. *Soft Matter* **2010**, 6, 4157–4167.
59. Nastishin, Y.; Liu, H.; Schneider, T.; Nazarenko, V.; Vasyuta, R.; Shiyanovskii, S.; Lavrentovich, O. Optical Characterization of the Nematic Lyotropic Chromonic Liquid Crystals: Light Absorption, Birefringence, and Scalar Order Parameter. *Phys. Rev. E* **2005**, 72, 041711.
60. Tortora, L.; Lavrentovich, O. D. Chiral Symmetry Breaking by Spatial Confinement in Tactoidal Droplets of Lyotropic Chromonic Liquid Crystals. *Proc. Natl. Acad. Sci.* **2011**, 108, 5163–5168.
61. Prinsen, P.; van der Schoot, P. Parity Breaking in Nematic Tactoids. J. Phys. Condens. *Matter* **2004**, 16, 8835–8850.
62. Kantsler, V.; Segre, E.; Steinberg, V. Vesicle Dynamics in Time-Dependent Elongation Flow: Wrinkling Instability. *Phys. Rev. Lett.* **2007**, 99, 178102.
63. Knorr, R. L.; Staykova, M. Wrinkling and Electroporation of Giant Vesicles in the Gel Phase. *Soft Matter* **2010**, 6, 1990–1996.
64. King, H.; Schroll, R. D.; Davidovitch, B.; Menon, N. Elastic Sheet on a Liquid Drop Reveals Wrinkling and Crumpling as Distinct Symmetry-Breaking Instabilities. *Proc. Natl. Acad. Sci.* **2012**, 109, 9716–9720.
65. Hohlfeld, E.; Davidovitch, B. Sheet on a Deformable Sphere : Wrinkle Patterns Suppress Curvature-Induced Delamination. *Phys. Rev. E* **2015**, 91, 012407.
66. Mui, B. L.-S.; Dobereiner, H.-G.; Madden, T. D.; Cullis, P. Influence of Transbilayer Area Asymmetry on the Morphology of Large Unilamellar Vesicles. *Biophys. J.* **1995**, 69, 930–941.
67. Bagatolli, L. A.; Parasassi, T.; Gratton, E. Giant Phospholipid Vesicles: Comparison among the Whole Lipid Sample Characteristics Using Different Preparation Methods A Two Photon Fluorescence Microscopy Study. *Chem. Phys. Lipids* **2000**, 105, 135–147.

68. Sorre, B.; Callan-Jones, A.; Manneville, J.; Nassoy, P.; Prost, J.; Goud, B.; Bassereau, P. Curvature-Driven Lipid Sorting Needs Proximity to a Demixing Point and Is Aided by Proteins. *Proc. Natl. Acad. Sci.* **2009**, 106, 5622–5626.
69. Sorre, B.; Callan-jones, A.; Manzi, J.; Goud, B.; Prost, J. Nature of Curvature Coupling of Amphiphysin with Membranes Depends on Its Bound Density. *Proc. Natl. Acad. Sci.* **2011**, 109, 173–178.
70. Heinrich, V.; Boz, B.; Sventina, S.; Zeks, B. Vesicle Deformation by an Axial Load : From Elongated Shapes to Tethered Vesicles. *Biophys. J.* **1999**, 76, 2056–2071.
71. Frenkel, D.; Dogterom, M. Force Barriers for Membrane Tube Formation. *Phys. Rev. Lett.* **2005**, 94, 068101.
72. Jamali, V.; Behabtu, N.; Senyuk, B.; Lee, J. A.; Smalyukh, I. I.; van der Schoot, P.; Pasquali, M. Experimental Realization of Crossover in Shape and Director Field of Nematic Tactoids. *Phys. Rev. E* **2015**, 91, 042507.
73. Varghese, N.; Shetye, G. S.; Bandyopadhyay, D.; Gobalasingham, N.; Seo, J.; Wang, J.-H.; Theiler, B.; Luk, Y.-Y. Emulsion of Aqueous-Based Nonspherical Droplets in Aqueous Solutions by Single-Chain Surfactants: Templated Assembly by Nonamphiphilic Lyotropic Liquid Crystals in Water. *Langmuir* **2012**, 28, 10797–10807.
74. Simon, K. A.; Sejwal, P.; Gerecht, R. B.; Luk, Y.-Y. Water-in-Water Emulsions Stabilized by Non-Amphiphilic Interactions: Polymer-Dispersed Lyotropic Liquid Crystals. *Langmuir* **2007**, 23, 1453–1458.
75. Mondiot, F.; Wang, X.; de Pablo, J. J.; Abbott, N. L. Liquid Crystal-Based Emulsions for Synthesis of Spherical and Non-Spherical Particles with Chemical Patches. *J. Am. Chem. Soc.* **2013**, 135, 9972–9975.
76. Whitmer, J. K.; Wang, X.; Mondiot, F.; Miller, D. S.; Abbott, N. L.; de Pablo, J. J. Nematic-Field-Driven Positioning of Particles in Liquid Crystal Droplets. *Phys. Rev. Lett.* **2013**, 111, 227801.
77. Bar-Ziv, R.; Moses, E. Instability and Pearling States Produced in Tubular Membranes by Competition of Curvature and Tension. *Phys. Rev. Lett.* **1994**, 73, 1392–1395.
78. Miao, L.; Seifert, U.; Wortis, M.; Dobereiner, H.-G. Budding Transitions of Fluid-Bilayer Vesicles: The Effect of Area-Difference Elasticity. *Phys. Rev. E* **1994**, 49, 5389–5407.
79. Dobereiner, H.-G.; Evans, E.; Kraus, M.; Seifert, U.; Wortis, M. Mapping Vesicle Shapes into the Phase Diagram: A Comparison of Experiment and Theory. *Phys. Rev. E* **1997**, 55, 4458–4474.
80. Baumgart, T.; Hess, S.; Webb, W. Imaging Coexisting Fluid Domains in Biomembrane Models Coupling Curvature and Line Tension. *Nature* **2003**, 425, 821–824.
81. Evans, E.; Rawicz, W. Entropy-Driven Tension and Bending Elasticity in Condensed-Fluid Membranes. *Phys. Rev. Lett.* **1990**, 64, 2094–2097.
82. Evans, E. Entropy-Driven Tension in Vesicle Membranes and Unbinding of Adherent Vesicles. *Langmuir* **1991**, 7, 1900–1908.

Chapter 9: Summary and Future Directions

9.1 Summary

The first three studies presented in this thesis describe a new class of active and anisotropic soft matter formed by dispersing motile bacteria (*Proteus mirabilis*) within a biocompatible nematic lyotropic chromonic LC phase. Specifically, in the first study, we found that the anisotropic elasticity of the nematic LC phase orients *P. mirabilis* cells and directs their motion parallel to the direction of LC alignment when dispersed in nematic DSCG films exhibiting a uniform planar alignment. In addition, the elasticity of the LC generates inter-bacterial forces that drive the formation of bacteria into linear multi-cellular assemblies. These assemblies form reversibly due to the interplay of forces generated by the flagella of bacteria and the elasticity of the LC, both of which are comparable in magnitude (tens of pN) for motile *P. mirabilis* cells.

The second study revealed motile bacteria to adsorb to the interfaces of tactoids, which form at temperatures where nematic and isotropic DSCG phases coexist, and also to orient and move parallel to the local director due to the influence of the nematic elasticity. Interestingly, we observed that adsorption to the nematic-isotropic interfaces was reversible, as bacteria generated sufficient propulsive forces to escape from tactoids near one of the two surface topological defects of the tactoids into the encompassing phase. Whereas individual bacteria could escape from nematic tactoids into the continuous isotropic phase, for isotropic tactoids in a continuous nematic phase, the elasticity of the LC generally prevented single bacteria from escaping. Instead, in these cases, assemblies of bacteria escaped through a cooperative, multicellular phenomenon also mediated by defects. In this study, we also demonstrated that the combined

effects of nematic elasticity and topological defects can be thermally tuned to dynamically corral and release bacteria from isotropic domains.

The third study uncovered additional changes to the dynamical behaviors of motile bacteria that emerge when the bacteria are dispersed in LC films confined by pairs of substrates that cause either uniform homeotropic or hybrid anchoring of the LC. Moreover, by employing two different *P. mirabilis* cell types (short vegetative cells approximately 3 μm in length and swarm cells 10 – 60 μm in length), we demonstrated how the motility of the cells changes in limits where the cells are small and large compared to the thickness of the confining LC film. Specifically, we showed that while short vegetative cells align and move perpendicular to the bounding surfaces of homeotropic films due to the elastic suppression of a wall-induced hydrodynamic torque that typically reorients motile bacteria near confining surfaces of isotropic solutions, steric constraints force swarm cells to orient and move in directions orthogonal to the far-field director. We also established that the elastic strain stored in hybrid LC films can be used to rectify the motion of vegetative cells and to impart elastic stresses that deform the bodies of long swarm cells in a predictable manner within the film.

These studies, which unmask a range of colloid and interfacial phenomena involving motile bacteria in a nematic LC, establish principles for the design of active and anisotropic soft matter that may be extended in the future to systems involving synthetic self-propelling active particles in complex fluids. In addition, they define new methods that permit manipulation of bacteria in ways that are not possible in isotropic fluids. Because nematic LCs recapitulate key physical properties of certain native bacterial environments that can exhibit viscoelasticity and long-lived anisotropic states, this series of investigations also provides new insight into the

manner in which fundamental dynamical behaviors of bacteria might change in these biological environments.

In the last two studies reported in this thesis, we revealed two experimental approaches leading to the formation of emulsions comprised of multiple LC phases and demonstrated several unique and interesting properties of the resulting emulsion systems. First, we established that stable LC-in-LC emulsions comprised of micrometer-sized droplets of nematic thermotropic LCs (e.g., 5CB) dispersed in a continuous nematic lyotropic chromonic LC (DSCG) phase can be prepared due to the immiscibility of these two LC phases. Significantly, we found the directors of the continuous and dispersed LC phases to be coupled, as revealed by the preferential alignment of the symmetry axis of bipolar nematic 5CB droplets orthogonal to the far-field director of the nematic DSCG phase. Through experiments involving perturbations of the alignment of the droplets using magnetic fields and comparison to a simple theoretical model, we showed that this coupling of orientations is consistent with the influence of van der Waal's interactions between the two phases that arise from the anisotropic polarizabilities of nematic 5CB ($\Delta n = +0.18$) and DSCG ($\Delta n = -0.02$).

Finally, we demonstrated that by hydrating dry lipid films with an aqueous DSCG solution, we can create GUVs that both encompass and are encompassed by nematic DSCG. Whereas GUVs prepared with isotropic aqueous solutions, including isotropic phase DSCG, typically adopt spherical shapes, we found that elastic stresses imparted on the GUVs by nematic DSCG lead them to adopt non-spherical, sometimes highly elongated shapes. Specifically, we measured two distinct populations of GUVs to form in the nematic DSCG. Whereas formation of a population of slightly elongated GUVs with approximately rounded poles was consistent with expansion of lipid membrane surface area due to LC elastic stresses while GUV volume is

conserved, our results suggested that formation of a population of highly elongated GUVs with sharp cusps instead involves a loss of 15 wt% DSCG from GUVs, perhaps through transient pores that form in the membrane. Surprisingly, information regarding the interplay between LC elastic energy and the interfacial energy of the GUVs obtained through analysis of the equilibrium shapes adopted by GUVs in our experiments led to the conclusion that the interfacial energy of the GUVs is dominated by some surface energy arising due to an interfacial tension rather than an energy associated with stretching the GUV membrane, suggesting DSCG may be locally depleted near the GUV surface. In this study, we also demonstrated the ability to transform elongated GUVs in nematic DSCG back into spherical shapes simply by heating the DSCG back into its isotropic phase.

The LC-in-LC emulsions described in these final two studies define exciting new classes of materials characterized by emergent properties arising due to the presence of multiple, spatially separated LC phases. While we report on the method of formation and present initial characterization of two such LC-in-LC emulsions, there remain a number of opportunities, as described below, for further investigation. Moreover, due to the biocompatibility of aqueous lyotropic chromonic LC phases, such as DSCG, these emulsion systems also may be well-suited for investigating research questions posed by the biochemical and biophysics communities.

9.2 Future Directions

The research described in this thesis as well as several preliminary experimental observations I describe below suggest many avenues for future investigation. In this section, I briefly outline and recommend a few future directions based on my research.

First, while the results described in Chapters 4 through 6 define a number of new methods and approaches to manipulate the motility and organization of bacteria in non-trivial ways due to interplay between elasticity-mediated LC forces and flagella-derived forces, no devices or platforms have yet been developed to truly leverage these phenomena in a technological context. In general, such efforts have been hampered by the relative difficulty of aligning lyotropic chromonic LC phases in desired orientations (especially orthogonal to a surface) relative to more conventional thermotropic LCs. However, recent research in this area[1] as well as additional advances that are likely to arise as a result of burgeoning interest in lyotropic chromonic LC phases in the soft matter community should support creation of LC-based platforms for sensitively controlling bacteria dynamics. Future research efforts could be focused on developing, for example, LC-filled microfluidic devices that direct the motion of bacteria and facilitate quantification and/or spatial concentration of the cells. In addition, the observation reported in Chapter 6 that elastic stresses imparted by hybrid LC films deform *P. mirabilis* swarm cells could serve as the basis for a new means to measure mechanical properties of bacteria, such as cell rigidity and bending stiffness. In order for this to occur, though, a more precise theoretical model must first be developed to estimate and compare energies associated with bending the cell body and locally straining the LC phase.

Second, ongoing preliminary experimental studies that I have performed in collaboration with Dr. Joel S. Pendery and Rishi R. Trivedi suggest that coupling between the chiral propulsion mechanism of bacteria (which involves the rotation of a helical flagella bundle) and the chirality of a twisted DSCG film produces forces that induce motile bacteria to accumulate over time near one of the two bounding substrates (depending on the handedness of the twist cell). We currently are working with Prof. Saverio E. Spagnolie to describe this phenomenon

theoretically. This coupling could serve as the basis of a novel method to separate and spatially concentrate bacteria.

Third, while LC elasticity-mediated, dynamical inter-bacterial interactions in uniform planar nematic LC films and at nematic-isotropic interfaces were discussed in detail in Chapters 4 and 5, respectively, interactions between bacteria in thin hybrid and homeotropic films were not covered in Chapter 6. However, I have made preliminary observations that groups of vegetative *P. mirabilis* cells can dynamically form two-dimensional, rotating, hexagonally-packed assemblies near the graphene substrates of homeotropic, and especially, hybrid DSCG films. This phenomenon appears qualitatively similar to the recent report that nearly spherical *Thiovulum majus* self-organize into rotating, two-dimensional "bacterial crystals" when dispersed in an isotropic fluid and dynamically bound to a surface as a result of hydrodynamic and steric interactions between cells.[2] In light of this recent report, it could be particularly interesting to further investigate the rotating crystals of vegetative *P. mirabilis* cells that form in hybrid LC films and document how they compare to the bacterial crystals observed by Petroff et al.[2]

Fourth, the research in Chapters 4 through 6 of this thesis was performed entirely with rod-shaped *P. mirabilis* bacteria that propel through biocompatible nematic LC phases using a rotating bundle of flagella (so-called "pushers"[3]). It would be interesting in the future to investigate how the fundamental behaviors of motile bacteria differing from *P. mirabilis* in terms of shape (e.g., spherical or helical)[4] or propulsion mechanism (e.g., "pullers" that use flagella to draw fluid in along the long axis of the cell body and expel it from the sides)[3] change when dispersed in a nematic LC. As a result of differences in the elastic distortions of LCs around bacteria with alternative shapes or in the interactions between LCs and the flagella of "pullers",

the dynamic behaviors of these bacteria in nematic DSCG phases could be distinct from those of *P. mirabilis*.

Fifth, the principles uncovered in Chapters 4 through 6 for the design of active and anisotropic soft matter were based entirely upon studies of biological active particles (i.e. bacteria) dispersed within a nematic LC phase. These studies could be extended and their implications potentially broadened by the development and investigation of a purely synthetic analogue to this experimental system. With the assistance of two undergraduate students, Eddie B. Ramos Hernández and Chaval Punyatanasakchai, I have performed preliminary experiments on such an experimental system involving 3 μm-diameter synthetic Palladium/silica "Janus" microparticles sedimented onto the interface between a thermotropic LC (5CB) and an aqueous solution containing hydrogen peroxide. These synthetic active particles exhibit spontaneous motion when in contact with aqueous hydrogen peroxide solutions as a consequence of the asymmetric, metal-catalyzed decomposition of hydrogen peroxide at the particle surface.[5,6] We hypothesized that when adsorbed at the nematic LC interface, these particles (which anchor 5CB tangential to the particle surface) would actively move preferentially parallel to the nematic director (planar anchoring at the 5CB-aqueous interface), similar to the motion exhibited by bacteria at interfaces of nematic tactoids discussed in Chapter 5. Although we found in our initial experiments that the Janus particles deposited on the LC-aqueous interface actively propelled upon addition of hydrogen peroxide to the aqueous phase, the motion of the particles was not strikingly direction-dependent. Correspondingly, the diffusion coefficients we measured for these particles (in the absence of hydrogen peroxide in the aqueous phase) lacked anisotropy and had magnitudes consistent with the particles being located almost entirely on the aqueous side of the interface. Future investigations of this experimental system might employ silica particles

functionalized with DMOAP,[7] a surface treatment which should allow the Janus particles to immerse into the LC to a greater extent and thus give rise to anisotropic particle motion. In addition, one potential experimental realization of synthetic active particles propelling within bulk LC, as opposed to an LC interface, might involve dispersing rolled up polymer microtubes with an interior catalytic platinum layer[8,9] in a nematic aqueous DSCG phase containing hydrogen peroxide.

Sixth, the generality of the observation reported in Chapter 7 of coupling between immiscible LC phases could be established through investigations of emulsion droplets of lyotropic chromonic LCs within a continuous thermotropic LC phase. Although the high birefringence of most thermotropic LCs relative to lyotropic chromonic LCs makes it difficult to determine the internal configuration of droplets of lyotropic chromonic LC using polarized light microscopy in this type of emulsion, techniques such as fluorescence confocal polarizing microscopy[10] may instead be leveraged to examine this system. In addition, investigations of the coupling between LC orientations when the dispersed LC phase has higher geometrical complexity (e.g., dispersions of toroidal thermotropic LC droplets[11] or faceted columnar phase lyotropic chromonic LC droplets[12]) or at planar interfaces formed between two immiscible LC phases could be performed to extend research in this area and generate additional insights.

Seventh, creating elastically strained GUVs in LCs as detailed in Chapter 8 is an exciting and promising new technique that should open the door for several new avenues of research in the future. For instance, these DSCG GUVs could be prepared using biologically-relevant lipid mixtures in order to create minimal synthetic model cell membranes. The GUVs could then be employed, for example, to investigate the hypothesis that differences in membrane curvature can induce microphase separation of certain lipid species.[13,14] In addition, because these elastically

strained GUVs as well as the elastically deformed *P. mirabilis* swarm cells in hybrid LC films represent, to my knowledge, some of the first reports of the deformation of flexible objects by LC elastic stresses, these experimental systems should be of great fundamental interest to the liquid crystal community. Further examination of the equilibrium shapes adopted by GUVs and the accompanying LC configurations as well as investigations of the dynamic responses of this system to the application of external electric and magnetic fields or osmotic stresses promise to produce novel and interesting results, especially if accompanied by theoretical and computational studies. In particular, these studies should initially aim to more fully elucidate details regarding the unexpected coupling between LC elastic energy and the interfacial energy of GUVs uncovered in Chapter 8 as well as to determine the LC director configuration within slightly elongated GUVs. Preparation of GUVs such that the LC phase is only present on one side of the vesicles with an isotropic solution chosen to match the osmolality of the DSCG solution on the other side represents another intriguing future direction to explore. Besides simply exchanging the aqueous solution used to form GUVs via gentle hydration, such GUVs also could be prepared through the use of a continuous emulsion transfer technique.[15]

9.3 References

1. Jeong, J.; Han, G.; Johnson, A. T. C.; Collings, P. J.; Lubensky, T. C.; Yodh, A. G. Homeotropic Alignment of Lyotropic Chromonic Liquid Crystals Using Noncovalent Interactions. *Langmuir* **2014**, 30, 2914–2920.
2. Petroff, A. P.; Wu, X.-L.; Libchaber, A. Fast-Moving Bacteria Self-Organize into Active Two-Dimensional Crystals of Rotating Cells. *Phys. Rev. Lett.* **2015**, 114, 158102.
3. Lauga, E.; Powers, T. R. The Hydrodynamics of Swimming Microorganisms. *Reports Prog. Phys.* **2009**, 72, 096601.
4. Young, K. D. The Selective Value of Bacterial Shape. *Microbiol. Mol. Biol. Rev.* **2006**, 70, 660–703.
5. Gibbs, J. G.; Zhao, Y.-P. Autonomously Motile Catalytic Nanomotors by Bubble Propulsion. *Appl. Phys. Lett.* **2009**, 94, 163104.
6. Ebbens, S. J.; Howse, J. R. Direct Observation of the Direction of Motion for Spherical Catalytic Swimmers. *Langmuir* **2011**, 27, 12293–12296.
7. Abras, D.; Pranami, G.; Abbott, N. L. The Mobilities of Micro- and Nano-Particles at Interfaces of Nematic Liquid Crystals. *Soft Matter* **2012**, 8, 2026–2035.
8. Solovev, A. A.; Mei, Y.; Bermúdez Ureña, E.; Huang, G.; Schmidt, O. G. Catalytic Microtubular Jet Engines Self-Propelled by Accumulated Gas Bubbles. *Small* **2009**, 5, 1688–1692.
9. Mei, Y.; Solovev, A. A.; Sanchez, S.; Schmidt, O. G. Rolled-up Nanotech on Polymers: From Basic Perception to Self-Propelled Catalytic Microengines. *Chem. Soc. Rev.* **2011**, 40, 2109–2119.
10. Smalyukh, I. I.; Shiyanovskii, S. V; Lavrentovich, O. D. Three-Dimensional Imaging of Orientational Order by Fluorescence Confocal Polarizing Microscopy. *Chem. Phys. Lett.* **2001**, 336, 88–96.
11. Pairam, E.; Vallamkondu, J.; Koning, V.; van Zuiden, B. C.; Ellis, P. W.; Bates, M. A.; Vitelli, V.; Fernandez-Nieves, A. Stable Nematic Droplets with Handles. *Proc. Natl. Acad. Sci. U. S. A.* **2013**, 110, 9295–9300.
12. Jeong, J.; Davidson, Z. S.; Collings, P. J.; Lubensky, T. C.; Yodh, A. G. Chiral Symmetry Breaking and Surface Faceting in Chromonic Liquid Crystal Droplets with Giant Elastic Anisotropy. *Proc. Natl. Acad. Sci. U. S. A.* **2014**, 111, 1742–1747.
13. Renner, L. D.; Weibel, D. B. Cardiolipin Microdomains Localize to Negatively Curved Regions of *Escherichia coli* Membranes. *Proc. Natl. Acad. Sci. U. S. A.* **2011**, 108, 6264–6269.
14. Renner, L. D.; Eswaramoorthy, P.; Ramamurthi, K. S.; Weibel, D. B. Studying Biomolecule Localization by Engineering Bacterial Cell Wall Curvature. *PLoS One* **2013**, 8, e84143.
15. Abkarian, M.; Massiera, G. Continuous Droplet Interface Crossing Encapsulation (cDICE) for High Throughput Monodisperse Vesicle Design. *Soft Matter* **2011**, 7, 4610–4614.